Experimental Investigation of Viscoelastic Cavitating and Turbulent Channel Flows Subjected to Different Pressure Gradients

by

Reza Azadi

A thesis submitted in partial fulfillment of the requirements for the degree of

Doctor of Philosophy

Department of Mechanical Engineering

University of Alberta

Abstract

Steam-assisted gravity drainage is a common method for oil production in Alberta, Canada. Production wells are equipped with inflow control devices to improve production efficiency. These devices utilize nozzle-type constrictions to enhance oil production by hindering water and gas breakthroughs. The relatively large pressure drop of the turbulent flow passing the nozzle can lead to chaotic cavitation that deteriorates the production rate and damages the equipment.

In this research, adding minute amounts of polyacrylamide (PAM) drag-reducing additives to the flow was suggested as a viable method to control cavitation and turbulence drag in nozzle flows. A flow facility and an optical setup based on high-speed imaging and microscopic particle image velocimetry (PIV) were developed to scrutinize this hypothesis.

The cavitation process was studied in a converging-diverging nozzle with water and PAM solutions of concentrations from 50 p.p.m. to 400 p.p.m. Rheological measurements demonstrated that solutions were shear-thinning and viscoelastic. Statistical analysis of the instantaneous images showed that polymer additives noticeably relaxed the mean cavitation collapse and growth rate and their fluctuations. A reduction of 65 % was measured in the 400 p.p.m. flow relative to water flow at the highest tested flow rate, where its inception shedding frequency was reduced by 70 %.

The flow's turbulence was studied using PIV in a channel with a bump resembling the profile of the converging-diverging nozzle used in the cavitation studies. Water, and 200 p.p.m., and 400 p.p.m. PAM flows were examined at three flow rates at regions subjected to zero, favorable and adverse pressure gradients (ZPG, FPG, and APG) and local curvature effects.

A drag reduction (DR) of 30.4 % and 38.6 % were obtained in the fully-developed ZPG 200 p.p.m. and 400 p.p.m. flows at the highest tested flow rate. As the flow rate or the solution concentration increased, the mean velocity profiles approached the ultimate profile, but maximum

DR was not achieved. Mean Reynolds shear stress and wall-parallel Reynolds stress were attenuated and enhanced in the PAM solutions.

The accelerating flows were transferred to a fully relaminarized regime, where the turbulent activities were significantly damped relative to a ZPG flow. The velocity profiles were pushed below the logarithmic profile at positions with a stronger FPG or weaker APG. Under FPG, the mean outer-normalized Reynolds shear stress was attenuated compared to ZPG flows. In APG flows, shear stresses showed intensity levels similar to that of a ZPG flow.

Inner-normalized velocity profiles of the accelerating 200 p.p.m. flows deviated from the logarithmic law, depending on the local FPG and curvature strength, and were elevated above the ultimate profile in the accelerating 400 p.p.m. flow at positions with a minimum friction factor. The turbulence production was reduced up to 70 % and 78 % in the accelerating 200 p.p.m flow relative to the ZPG PAM and FPG water flows. Substantial attenuation of the turbulence production in the accelerating 400 p.p.m. flow generated negative Reynolds shear stress zones.

The mean velocity profiles of the decelerating 200 p.p.m. flows deviated above the log-law at positions with small friction factors and collapsed to the ultimate profile where friction was minimum. At the same position and the highest flow rate, the velocity profile of the 400 p.p.m. flow elevated above the ultimate profile.

APG intensified stronger mean Reynolds shear stress in both solutions and attenuated the weaker ones to the extent that negative counter-gradient zones emerged over the boundary layer. The turbulence production was reduced by up to ≈ 58 % in the PAM solutions compared to the water flow. Compared to the APG water flow, the semi-dilute solutions indicated intensified wall-parallel and wall-normal fluctuations.

This study elucidated that adding PAM to the flow can be utilized as an efficient cavitation-controlling method. A novel methodology was presented for quantitative analysis of the cavitation reduction mechanisms from high-speed images. Polymer additives generated significant DR in the fully-developed ZPG PAM solutions. Under pressure gradient and wall curvature effects, flows indicated substantial streamwise dependence. The high spatial resolution and accuracy of the PIV-based flow statistics make the data unique and an important foundation for model development. Another novelty of this research is that, for the first time, the viscoelastic polymer solutions were examined under pressure gradient effects.

Preface

This thesis reports the original research work by Reza Azadi, which was conducted at the Applied ThermoFluids Lab at the Department of Mechanical Engineering, Faculty of Engineering, University of Alberta, under the direct supervision of Professor David S. Nobes.

The design and construction of the flow facility, calibration of the pressure sensors and optical systems, set up of the numerical simulations, code developments, pressure, high-speed imaging, and velocimetry measurements, data collection, analysis, and interpretation of the results were carried out by Reza under the supervision of Professor David S. Nobes and using the equipment of the Applied ThermoFluids Lab and Compute Canada's cluster computers. The rheology tests were carried out by Reza at the institute for oil sands innovation at the University of Alberta.

In collaboration with Professor David S. Nobes as the supervisory author, this research work resulted in the publication of several peer-reviewed journal papers (denoted by letter *p*) and conference papers (denoted by letter *c*) as listed here:

*p*1- **Azadi, R.**, Nobes, D.S., 2022. Hydrodynamic cavitation reduction in semidilute turbulent polymer solution flows. *J. Fluid Mech.* **952**, A29. [*Chapters* 4 & 5].

*p*2- **Azadi, R.**, Nobes, D.S., 2021. Local flow dynamics in the motion of slug bubbles in a flowing mini square channel. *Int. J. Heat Mass Transf.* **178**, 121588. [*Appendix G*].

*p*3- **Azadi, R.**, Nobes, D.S., 2021. On the three-dimensional features of a confined slug bubble in a flowing square capillary. *Phys. Fluids* **33**, 033327. [*Appendix F*].

*p*4- **Azadi, R.**, Wong, J., Nobes, D.S., 2021. Determination of fluid flow adjacent to a gas/liquid interface using particle tracking velocimetry (PTV) and a high-quality tessellation approach. *Exp. Fluids* **62**, 48. [*Appendix E*].

*p*5- **Azadi, R.**, Wong, J., Nobes, D.S., 2020. Experimental and analytical investigation of mesoscale slug bubble dynamics in a square capillary channel. *Phys. Fluids* **32**, 083304. [*Appendix D*].

*c*1- **Azadi, R.**, Nobes, D.S., 2022. Experimental investigation of a cavitating water flow with the addition of drag-reducing agents, in: *20th International Symposium on the Application of Laser and Imaging Techniques to Fluid Mechanics*. Lisbon. [*Chapters* 4 & 5].

*c*2- **Azadi, R.**, Nobes, D.S., 2021. Pressure calculation for flows with moving surface boundaries from particle tracking velocimetry (PTV), in: *14th International Symposium on Particle Image Velocimetry*. Chicago.

*c*3- **Azadi, R.**, Nobes, D.S., 2019. On the detachment mechanisms of monodisperse bubbles flowing through a wavy channel, in: *13th International Symposium on Particle Image Velocimetry (ISPIV)*. Munich.

*c*4- **Azadi, R.**, Soltani, H., Sabbagh, R., Nobes, D.S., 2018. Experimental and numerical investigation of bubble dynamics rising through rectangular confinement, in: 5th International Conference on Experimental Fluid Mechanics (ICEFM).

The author has also been involved in other research projects, which led to the following conference papers:

1- Saffar, Y., Ansari, S., **Azadi, R.**, Raffel, J., Nobes, D., Sabbagh, R., 2021. Determination of the Near Wall Flow of a Multi-Stage Tesla Diode Using PIV and PTV, in: *14th International Symposium on Particle Image Velocimetry*. Chicago.

2- Soltani, H., **Azadi, R.**, Baldygin, A., Ansari, S., Nobes, D.S., 2018. Developing quantitative information of oil droplets rising through rectangular confinement, in: *5th International Conference on Experimental Fluid Mechanics (ICEFM)*. Munich.

To my dear parents,

To the love of my life, my wife, Samira, and

To the brave women and men of Iran who fight for their freedom

Acknowledgments

I express my deepest gratitude to my supervisor and mentor, Professor David S. Nobes, for his endless guidance, support, patience, and advice.

I appreciate the readers of my work: Dr. Rui Ni from the Department of Mechanical Engineering, Johns Hopkins University, Professor Mark Loewen from the Department of Civil and Environmental Engineering, University of Alberta, and Professor C. R. (Bob) Koch and Dr. Carlos Lange from the Department of Mechanical Engineering, University of Alberta.

I am always thankful to my dear parents and family for their enduring consideration and to my lovely wife, Samira, who is a real-life partner and supporter, without whom crossing this road was impossible. Thank you for always being there.

I am grateful to all my friends and former and current colleagues for their support and help during my research and lab experiments.

I am also thankful to the Government of Alberta for two periods of the *Alberta Graduate Excellence Scholarship*, the Department of Mechanical Engineering and Faculty of Engineering at the University of Alberta for the *Sadler Graduate Scholarship*, and the *Donald Lougheed Engineering Graduate Scholarship*.

Contents

List of Tables

List of Figures

Nomenclature

Unless otherwise mentioned, notations are defined in Euclidian space and the Eulerian frame.

Upper-case Roman

Symbol	Explanation	Units
$\mathcal{A}$	Amplitude	
$\mathcal{B}$	Arbitrary body in the Euclidian space	
$\mathcal{L}$	Some characteristic length scale of the flow system	m
$\boldsymbol{\mathcal{M}}(\boldsymbol{x}, t)$	Linear momentum vector	kg m s^{-1}
$\mathcal{P}$	Probability	
$\mathcal{U}_{\phi}$	Uncertainty of variable ϕ	
$\widetilde{U}$	Generalized velocity	m s^{-1}
$\dot{V}$	Volumetric flow rate	m^3 s^{-1}
A	Cross-sectional area	m^2
A_G ($\boldsymbol{x}$, t)	Vapor ratio field	
AR	Aspect ratio	
$\boldsymbol{B}$	Summation of all body acceleration forces acting on a unit volume	kg m^{-2} s^{-2}
C_s	Solution concentration	p.p.m.
$\boldsymbol{D}$ ($\boldsymbol{x}$, t)	Rate of strain tensor; $\boldsymbol{D} = (\boldsymbol{L} + \boldsymbol{L}^{\mathrm{T}})/2$	s^{-1}
D	Diameter	m
DR	Drag reduction percentage	
E (k)	Energy spectrum function	m^3 s^{-2}
$\boldsymbol{F}$ ($\boldsymbol{x}$, t)	Force vector field	kg m s^{-2} (N)
Fr	Froude number	
G	Defect (or Clauser) shape factor	
G'	Storage (elastic) modulus	Pa
G''	Loss (viscous) modulus	Pa
H	Shape factor	
$\boldsymbol{I}$	Identity tensor	
I	Image intensity	
K	Acceleration parameter	
$\boldsymbol{L}$ ($\boldsymbol{x}$, t)	Velocity gradient tensor; $\boldsymbol{L} = \nabla \boldsymbol{U}$	s^{-1}
L	Length	m
M	Magnification	
N	Number of samples	
N_A	Numerical aperture	
N_t	Total number of samples	
P ($\boldsymbol{x}$, t)	Pressure scalar field	N m^{-2} (Pa)
P_e	Local mean pressure of the boundary layer edge	N m^{-2} (Pa)
P_r	outlet-to-inlet pressure ratio	
R	Radius	m
R_{cd}	Coefficient of determination	
Re	Reynolds number	
St	Strouhal number	
St_k	Stokes number	
T	Temperature	℃
$\boldsymbol{U}$ ($\boldsymbol{x}$, t)	Velocity vector field in the Eulerian reference frame	m s^{-1}

U_e	Local mean wall-parallel velocity of the boundary layer edge	m s^{-1}
$\boldsymbol{U}_i$ ($\boldsymbol{x}$, t)	The i'th component of the velocity vector $\boldsymbol{U}(\boldsymbol{x}, t)$	m s^{-1}
U_{zs}	Zagarola-Smits velocity	m s^{-1}
V	Volume	m^3
$\boldsymbol{X}$	Position vector in the Lagrangian frame (reference configuration)	m

Lower-case Roman

Symbol	Explanation	Units
a_G ($\boldsymbol{x}$, t)	Fluctuating vapor ratio field	
c_0^+	Law of the wall constant	
c_p	Pressure coefficient	
c_f	Skin friction coefficient	
d	Diameter	m
$\boldsymbol{e}_i$	Unit coordinate vector in the i'th direction	
$\|e\|$	Camera's sensor size	m
$\boldsymbol{e}_R$	Random error of measurement	
f	Frequency	s^{-1} (Hz)
$f_\#$	F-number	
f_c	Camera's frame rate	s^{-1} (Hz)
$\boldsymbol{g}$	Gravity vector	m s^{-2}
g	Gravitational acceleration	m s^{-2}
h	Height	m
k	Wavenumber	m^{-1}
l	Length	m
m	Mass	kg
$\boldsymbol{n}$	Normal outward vector applied to a surface s	
n	Local wall-normal position	m
n_{tot}	Total refractive index	
p ($\boldsymbol{x}$, t)	Fluctuating pressure scalar field	N m^{-2} (Pa)
r	Pearson correlation coefficient	
s	Local wall-parallel position	m
$\boldsymbol{t}(\boldsymbol{n})$	Traction force applied to a surface area s	N m^{-3}
t	Time	s
t_{ed}	Eddy-turnover time	s
t_p	Particle's response time	s
t_R	Relaxation time	s
t_v	Inner (viscous) time scale; $t_v = \nu_w/u_\tau^2$	s
$\boldsymbol{u}$ ($\boldsymbol{x}$, t)	Fluctuating velocity vector field in the Eulerian reference frame	m s^{-1}
u_i ($\boldsymbol{x}$, t)	The i'th fluctuating component of the velocity vector	m s^{-1}
u_p	Particle's settling velocity	m s^{-1}
u_τ	Friction velocity; $u_\tau = \sqrt{\tau_w/\rho}$	m s^{-1}
w	Width	m
$\boldsymbol{x}$	Position vector in the Eulerian frame (current configuration)	m
x, y, z	Coordinate positions of a point in the flow field relative to the origin	m

Upper-case Greek

Symbol	Explanation	Units
Δ	Defect displacement thickness or Clauser length scale	m
Δ_p	Non-dimensional FPG parameter	
Δ_τ	Non-dimensional shear stress gradient	
$\Phi(\boldsymbol{x}, t)$	A scalar, vector, or tensor field in the Eulerian frame	

Lower-case Greek

Symbol	Explanation	Units
α	Angle	°
β	Rotta-Clauser pressure gradient parameter	
$\dot{\gamma}$	Shear strain rate	s^{-1} (Hz)
δ	Boundary layer thickness	m
$\delta\phi$	Infinitesimal segment of a scalar variable ϕ	
δ^+	Kármán number	
δ^*	Displacement thickness	m
δ_{zs}	Defect boundary layer thickness based on Zagarola-Smits velocity	m
δz	Depth of field	m
ε	Rate of dissipation of turbulent kinetic energy per unit mass	$m^2\ s^{-3}$
ε_{ijk}	Permutation (alternator) function	
ζ	Indicator function	
θ	Momentum thickness	m
θ_c, θ_d	Convergence and divergence angles	°
κ	Von Kármán constant	
λ	Wavelength	m
λ_b	Bulk viscosity	Pa s
λ_v	Inner (or viscous) length scale; $\lambda_v = \nu_w/u_\tau$	m
$\mu(\boldsymbol{D})$	Shear viscosity scalar field	N s m^{-2} (Pa.s)
μ_0	Zero shear viscosity	N s m^{-2} (Pa.s)
μ_3	Skewness	
μ_4	Kurtosis (or flatness)	
μ_∞	Infinite shear viscosity	N s m^{-2} (Pa.s)
ν	Kinematic viscosity; $\nu = \mu / \rho$	$m^2\ s^{-1}$
ξ	Second viscosity; $\xi = \lambda + (2\mu/3)$	Pa s
$\rho(\boldsymbol{x}, t)$	Density field in the Eulerian frame, $\rho = \lim_{dV \to 0} dm/dV$	kg m^{-3}
ς	Digital resolution	µm $pixel^{-1}$
$\boldsymbol{\sigma}(\boldsymbol{x}, t)$	Cauchy stress tensor in the Eulerian frame	N m^{-2} (Pa)
σ	Cavitation number	
σ_i	Cavitation inception number	
σ_ϕ	Root mean square of an arbitrary variable ϕ	
$\boldsymbol{\tau}(\boldsymbol{x}, t)$	Shear stress tensor in the Eulerian frame	N m^{-2} (Pa)
τ	Shear stress	N m^{-2} (Pa)
$\phi(\boldsymbol{x}, t)$	Scalar field in the Eulerian frame	
$\boldsymbol{\omega}$	Vorticity field; $\boldsymbol{\omega} = \nabla \wedge \boldsymbol{U}$	s^{-1} (Hz)
ω	Angular frequency	s^{-1} (Hz)
ω_i	The i'th component of the vorticity vector field	s^{-1} (Hz)

Subscripts

Symbol	Explanation
0	Denotes the base case, for instance ρ_0 is the base density
a	Air
ac	Acrylic
b	Bump
c	Convergence
ca	Cavitation
CFD	Computational fluid dynamics
CY	Carreau-Yasuda
d	Divergence or downstream
def	Defocus
diff	Diffraction
e	Edge
en	Entrance
exp	Exposure
geo	Geometrical
h	Hydraulic
in	Inlet
L	Liquid
m	Mean
n	Local wall-normal direction
out	Outlet
p	Particle
PIV	Particle image velocimetry
PK	Prandtl Kármán
r	Reference
s	Local wall-parallel direction
sat	Saturation
t	Current
ta	Target
th	Throat
tu	Tube
v	Vapor
vs	Viscous sublayer
w	Wall
wat	Water

Symbols

Symbol	Explanation
$\boldsymbol{a}\otimes\boldsymbol{b}$	Tensor product between vectors $\boldsymbol{a}$ and $\boldsymbol{b}$
$\mathcal{A}\cap\mathcal{B}$	Intersection of sets $\mathcal{A}$ and $\mathcal{B}$
$\mathcal{A}\cup\mathcal{B}$	Union of sets $\mathcal{A}$ and $\mathcal{B}$
$\mathcal{A}\in\mathcal{B}$	$\mathcal{A}$ is an element of $\mathcal{B}$
$\dot{\Phi}$	Material (or total) derivative of a scalar, vector or tensor field Φ
$\nabla\Phi$	Gradient of a field Φ; $d\Phi = \nabla\Phi\cdot d\boldsymbol{x}$

$\nabla^2\Phi$	Laplacian of a field Φ
$\nabla\cdot\Phi$	Divergence of a field Φ
$\partial\mathcal{P}$	Surface area enclosed by body part $\mathcal{P}$
$\boldsymbol{a}\wedge\boldsymbol{b}$	Vector product of vectors $\boldsymbol{a}(\boldsymbol{x},t)$ and $\boldsymbol{b}(\boldsymbol{x},t)$
$\boldsymbol{A}^{\mathbf{T}}$	Transpose of a tensor $\boldsymbol{A}$
tr$\{\boldsymbol{A}\}$	Trace of a tensor $\boldsymbol{A}$
$\langle\phi\rangle$	Ensemble average (mean) of a scalar field $\phi(\boldsymbol{x},t)$
$\bar{\bar{\phi}}$	Average over a surface area (usually the cross-sectional area)
ϕ^+	Inner normalized variable ϕ

Acronyms & Abbreviations

Symbol	Explanation
2D	Two-dimensional
APG	Adverse pressure gradient
AR	Aspect ratio
BL	Boundary layer
CCL	Cavitation collapse level
CFD	Computational fluid dynamics
CGL	Cavitation growth level
CT	Computed tomography
CWT	Continuous wavelet transform
DR	Drag reduction
FDM	Frame difference method
FFT	Fast Fourier transform
FOV	Field of view
FPG	Favorable pressure gradient
PAM	Polyacrylamide
PIV	Particle image velocimetry
PK	Prandtl Kármán
p.p.m.	Parts per million
PSD	Power spectral density
PTV	Particle tracking velocimetry
QAS	Quaternary ammonium salt
r.m.s.	Root mean square
REC	Recovery
ROI	Region of interest
SOC	Sum of correlation
X-PCI	X-ray phase-contrast imaging
ZPG	Zero pressure gradient

1. Introduction

1.1. Motivation

Steam-assisted gravity drainage (SAGD) is a popular enhanced recovery oil extraction process, shown schematically in Figure 1-1(*a*). This process injects high-temperature steam into the underground oil sand to reduce the viscosity of the stored highly viscous bitumen to make it flow by gravity (Butler, 2008). As Figure 1-1(*a*) illustrates, slotted liners and wire wrap screens are used on the production well to minimize the production of sand (Pallares et al., 2018). The oil sand reservoirs also contain substantial amounts of gas, water, and condensed steam that can flow into the production well and significantly reduce oil production. Assuming an ideal slotted liner, the concentration of the sand particles in the highly viscous bitumen flow through the slotted liners is inconsequential. Therefore, as shown in Figure 1-1(*b*), the flow through the slotted liners can be simplified as a laminar two-phase flow of a viscous bulk liquid, as a mixture of water and bitumen, carrying dispersed gas bubbles of different sizes.

Inflow control devices (ICDs) can improve oil production by delaying the water and gas breakthrough and are frequently utilized in Canada's SAGD wells (Oyeka et al., 2014). As illustrated in Figure 1-1(*b*), a constriction such as an orifice or nozzle is fitted into ICDs to inhibit water and gas production by generating a large pressure drop. Nevertheless, the large pressure drop can lead the high-speed water flow to cavitate or flash and choke the flow path, resulting in a drop in production efficiency. This multiphase flow passes through a vertical constriction and pours into the production well, which is pumped to the surface.

Under particular conditions, turbulent water flow can experience a bulk or local phase change due to an increase in temperature or a sudden pressure drop. Phase change starts with the local advent of nano to microscale vapor bubbles in the flow. This *nucleation* process can originate from thermal or mechanical non-equilibrium in the system (Pinhasi et al., 2005). Subjecting the flow to a strong acceleration can reduce the local flow pressure well below its saturation pressure at a prescribed temperature and initiate the formation of vaporous bubbles in that region, which are then carried by the bulk liquid flow downstream of the nucleation region.

With the downstream pressure well above the saturation pressure, the cavitation bubbles recover their pressure, immediately collapse, and change into liquid water. This flow process is called *cavitation* (Brennen, 2013). In contrast to cavitation, if the operating conditions of the flow

system are set to keep the downstream pressure well below the saturation pressure, the vapor bubbles continue their growth to a determined size at a lower rate. As a result, a more intense two-phase mixture is generated downstream of the flow domain (Ishii and Hibiki, 2006). This flow process is called *flashing*.

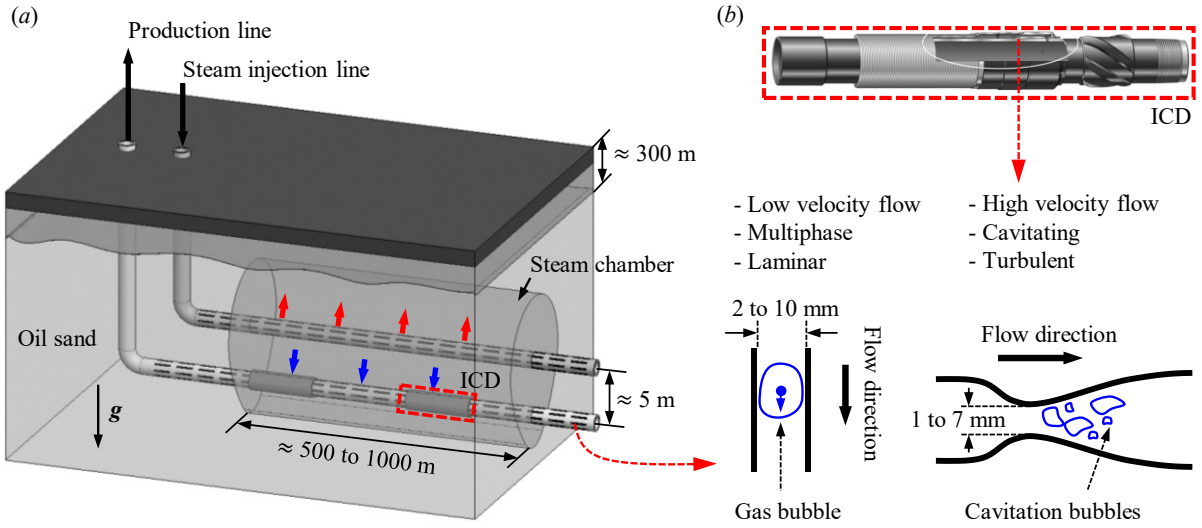

Figure 1-1 (*a*) Schematic representation of the SAGD process. (*b*) Regions of interest in the current study with their associated flow phenomena: low velocity, multiphase flow through slotted liners, and high velocity, cavitating and turbulent flow through the ICDs. Blue curves highlight the dispersed gas phase interface with its surrounding bulk liquid. The ICD image in (*b*) is retrieved from (Oyeka et al., 2014).

A sudden constriction or expansion in the flow path commonly causes the pressure difference that leads to cavitation. Any industrial application or natural phenomenon with liquids flowing through has the potential for cavitation. Refrigerant systems with valves and capillary tubes (Simões-Moreira and Bullard, 2003), atomization of fuel spray in engines (Tong et al., 2017), liquid flow through cracked steam generators in power plants (Feburie et al., 1993), leakage of toxic chemicals through dissemination vessels (Spicer and Miller, 2018) and mixtures of oil-gas-water flow through ICDs during oil extraction (Banerjee and Hascakir, 2018), all are examples of processes where cavitating flow is present.

Cavitating flows can be significantly destructive to equipment. In the past decades, extensive research has been undertaken to understand the fundamental concepts of cavitation and to procure a relevant technology to protect devices and equipment from the potentially detrimental effects of cavitating and flashing flows (Casal, 2008). Due to a large pressure drop across the ICDs, they are

vulnerable to the eroding effects of cavitating flow, and their practical design demands a deep understanding of this physical phenomenon (Banerjee and Hascakir, 2018).

Long-chain polymers have shown significant drag reduction (DR) effects in turbulent flows since the discovery by Toms (1948). Minute amounts of polymer additives, in parts per million (p.p.m.), can result in DR as high as 60 % in a turbulent pipe flow (Owolabi et al., 2017). Numerous experimental and numerical studies on single-phase turbulent channel flows have proven that after the onset of DR, the polymer agents enhance the streamwise and mitigate the wall-normal and spanwise velocity fluctuations (Den Toonder et al., 1997; Lumley, 1973, 1969; Owolabi et al., 2017; Shah and Yarusevych, 2020; Toonder et al., 1995; Virk, 1975, 1971; Virk et al., 1970; Warholic et al., 1999, 2001; White et al., 2012; Xi, 2019).

On the other hand, the fundamental reason behind hydrodynamic cavitation in a turbulent water flow after its onset is the fluctuations of the local flow pressure around the saturation pressure of the flow at a known temperature, which is usually exerted by an alternative strong acceleration and deceleration of the flow. Hence, it is viable to postulate that drag-reducing polymers might be capable of controlling the cavitation intensity as they can control the turbulence drag. Except for a handful of studies available, where the impacts of polymer additives were mostly investigated on unbound cavitating jets (Brennen, 1970; Brujan, 2011; Hasegawa et al., 2009; Hoyt, 1976; Ōba et al., 1978; Ting, 1978), there is a lack of information on the effects of polymer additives on the hydrodynamics of cavitation in wall-bounded flows. Also, while abundant studies are available that investigated developing turbulent boundary layers (BLs) under pressure gradients (Balin and Jansen, 2021; Baskaran et al., 1991, 1987; Bobke et al., 2017; Clauser, 1954; Jones and Launder, 1972; Joshi et al., 2014; Krogstad and Skåre, 1995; Patel and Head, 1968; Vinuesa et al., 2017b; Volino, 2020), there is no available information that examines the combined effect of polymers' viscoelasticity and pressure gradients on the turbulence statistics of the flow.

The design of the next generation of high-efficiency ICDs requires an advanced understanding of the complex multi-scale, multi-physics, and multiphase flow phenomena occurring in these devices and exploring innovative methods to control the flow's turbulence and attenuate the erosive effects of cavitation by attenuating its intensity. For this aim, cavitating and turbulent flow fields were experimentally examined under a wide range of flow conditions in a nozzle flow path mimicking common ICD nozzles. The feasibility of mitigating the intensity of hydrodynamic

cavitation by drag-reducing polymer additives was examined in detail. Also, the fundamental physics of developing turbulent BLs under the combined effect of varying pressure gradients and the viscoelasticity of added polymer additives were investigated.

1.2. Objectives

This research study aims to investigate and describe the physics behind the hydrodynamic cavitating and developing turbulent flow phenomena occurring over a converging-diverging nozzle bump and examine the effect of drag-reducing polymer additives on them. It was hypothesized that (1) drag-reducing polymer additives could attenuate the cavitation intensity and lead to cavitation flow patterns different from the cavitating pure water, and (2) the viscoelasticity effects of long-chain polymer additives on non-equilibrium developing turbulent BLs under pressure gradient could alter the flow's near-wall turbulence behavior and mean statistics.

The main objectives of the research were (1) to develop an experimental mesoscale test setup to obtain instantaneous cavitation structures and turbulent velocity fields over wall surfaces with strong pressure gradients, (2) to investigate the possible cavitation-reduction effects of polymer additives, and (3) to elucidate the effects of strong pressure gradients and viscoelasticity of polymer additives on near-wall turbulence flow.

1.3. Impact of the COVID-19 pandemic on the research progress

The main focus of the current Ph.D. research was to investigate the cavitating turbulent flow through the ICDs, shown in Figure 1-1(*b*). However, during the COVID-19 shutdown, when lab access was restricted, research was undertaken to understand the multiphase dynamics of single bubbles flowing concurrently in a viscous flow through a constricted rectangular path. This flow mirrored the laminar multiphase flow through the slotted liners shown in Figure 1-1(*b*). Before the shutdown, some preliminary experimental velocimetry data was acquired to understand the dynamics of this flow phenomenon. The low flow velocity made it possible to develop some analytical approaches to study the flow and carry on the research during the lockdown. Also, having remote access to Compute Canada's cluster computers, the flow was simulated numerically using an open-source CFD toolbox (OpenFOAM V2006, OpenCFD Ltd).

Combining the obtained experimental, analytical, and numerical results led to a detailed understanding of the laminar two-phase flow through the slotted liners and a wider appreciation of the flow phenomena occurring in a SAGD process as a complementary part of the main focus of the research work. The results of these studies were published as four peer-reviewed journal and three conference papers. The front pages of the journal papers are shown in Appendix D to Appendix G, which also comprises the links to the publishers' websites.

1.4. Overview

This thesis comprises **8** Chapters and **7** Appendices and is organized as follows:

Chapter 2 provides the necessary background on the main governing equations and clear definitions of the variables used throughout the thesis.

Chapter 3 discusses the details of the developed experimental methodology to investigate the flow phenomena of interest. The designed wall geometries, flow facility, and optical settings for high-speed imaging and velocimetry are explained in detail.

Chapter 4 investigates the rheological measurement results and determines the viscoelastic properties of the tested non-Newtonian semi-dilute polymer solution flows.

Chapter 5 explains the mechanisms of the hydrodynamic cavitation reduction in semi-dilute polymer solutions by investigating the results obtained from high-speed imaging and fast single-point pressure measurements.

Chapter 6 describes the statistical behavior of Newtonian developing turbulence flow under favorable and adverse pressure gradients based on the planar velocity fields obtained from particle image velocimetry (PIV) measurements. This chapter highlights the significant effects of pressure gradient on near-wall turbulence and the development of BLs.

Chapter 7 advances the understanding of the combined effect of pressure gradient and flow viscoelasticity on the near-wall turbulence, and non-equilibrium BLs in semi-dilute polymer solution flows on flat and curved wall surfaces.

Chapter 8 provides a concise summary of the key findings of the present research work, highlights its main contribution to the knowledge base, and discusses possible future works.

Appendix A provides the formulations of the essential statistical parameters utilized in this work to better understand the details of calculating turbulence statistics.

Appendix B describes the details of the numerical simulation setup utilized as an ancillary tool to approximate the wall shear stress distribution in a Newtonian turbulent flow.

Appendix C provides the formulation to calculate the particle image size.

Appendix D describes the paper “Experimental and analytical investigation of mesoscale slug bubble dynamics in a square capillary channel.”

Appendix E describes the paper “Determination of fluid flow adjacent to a gas/liquid interface using particle tracking velocimetry (PTV) and a high-quality tessellation approach.”

Appendix F describes the paper “On the three-dimensional features of a confined slug bubble in a flowing square capillary”

Appendix G describes the paper “Local flow dynamics in the motion of slug bubbles in a flowing mini square channel.”

2. Background

This chapter provides a concise review of the main definitions, symbols, and flow variables used throughout the thesis for coherence and consistency in the discussions.

2.1. Governing equations

This thesis defines variables in the Eulerian frame (or current configuration). An instantaneous scalar field is noted by an uppercase italic letter, e.g., U; vectors and tensors are denoted by italic, bold letters, e.g., $\boldsymbol{U}$. A stationary Cartesian coordinate system is used to describe the flow field globally. The position of a point in the flow domain is shown by $\boldsymbol{x} = x\,\boldsymbol{e}_x + y\,\boldsymbol{e}_y + z\,\boldsymbol{e}_z$, where $\boldsymbol{e}$ is the unit vector in the i'th direction. The instantaneous velocity vector field is defined as $\boldsymbol{U}(\boldsymbol{x}, t) = U_x\,\boldsymbol{e}_x + U_y\,\boldsymbol{e}_y + U_z\,\boldsymbol{e}_z$, where each component is also a function of time and space, i.e., $U_i \equiv U_i(\boldsymbol{x}, t)$, where $i = x, y, z$. Similarly, instantaneous pressure is shown by $P(\boldsymbol{x}, t)$. At time t, the vapor ratio, $A_G(\boldsymbol{x}, t)$, is defined as the vapor (gas) volume ratio to the total volume. For a 2D plane, constricted to an explicit region of interest (ROI), volume is replaced with the limited area on the planar ROI.

The instantaneous fluctuation field of a scalar field U is defined as $u(\boldsymbol{x}, t) = U(\boldsymbol{x}, t) - \langle U\rangle(\boldsymbol{x})$, where $\langle U\rangle$ denotes the mean of the flow field, given in equation (A-1) and equation (A-8) of Appendix A. For a statistically stationary flow field, $\langle U\rangle \equiv \langle U\rangle(\boldsymbol{x})$. Hence, velocity fluctuation fields, pressure, and vapor ratio are, respectively, shown by u_i, p, and a_G, where $i = x, y, z$.

Any selected material segment with a volume of $\delta V > 1$ μm^3 is assumed to be continuous, for which the theories of continuum mechanics are valid. For such a material, the general mass conservation and Cauchy's momentum equations are:

$$\frac{\partial \rho}{\partial t} + \nabla \cdot (\rho \boldsymbol{U}) = 0, \tag{2-1}$$

$$\frac{\partial (\rho \boldsymbol{U})}{\partial t} + \nabla \cdot (\rho \boldsymbol{U} \otimes \boldsymbol{U}) = -\nabla P + \nabla \cdot \boldsymbol{\tau} + \rho \boldsymbol{B}, \tag{2-2}$$

where ρ is the density of the flow, '$\nabla\cdot$' and '∇' are the divergence and gradient operators, $P(\boldsymbol{x}, t)$ is the pressure field, $\boldsymbol{\tau}$ is the shear stress tensor, and $\boldsymbol{B}$ is the summation of all body acceleration forces acting on a unit volume of the continuum. Here, t is time and tensor product of velocity vectors $\boldsymbol{U}$ and $\boldsymbol{U}$ can be rewritten as $\boldsymbol{U} \otimes \boldsymbol{U} = \boldsymbol{U}\boldsymbol{U}^{\mathrm{T}}$, where $\boldsymbol{U}^{\mathrm{T}}$ is the transpose of $\boldsymbol{U}$.

A linear constitutive equation can be driven for $\boldsymbol{\tau}$ in a non-Newtonian fluid as:

$$\boldsymbol{\tau} = 2\boldsymbol{D}\nabla\mu + \mu\nabla^2\boldsymbol{U}, \tag{2-3}$$

where $\boldsymbol{D} = (\boldsymbol{L} + \boldsymbol{L}^{\mathrm{T}})/2$ is the rate of strain rate, and $\boldsymbol{L} = \nabla\boldsymbol{U}$ is the velocity gradient tensor. The vorticity vector is defined as the vector product of the gradient operator and the velocity vector field, i.e., $\boldsymbol{\omega} = \nabla\wedge\boldsymbol{U}$. In an orthonormal coordinate system with a basis of $\{\boldsymbol{e}_i\}_{i=1}^3$,

$$\boldsymbol{\omega} = \varepsilon_{ijk}\frac{\partial U_j}{\partial x_i}\boldsymbol{e}_k, \tag{2-4}$$

where ε_{ijk} is the permutation (alternator) function. In a Cartesian coordinate system with base $\{\boldsymbol{e}_x, \boldsymbol{e}_y, \boldsymbol{e}_Z\}$, vorticity vector is $\boldsymbol{\omega} = \omega_x\boldsymbol{e}_x + \omega_y\boldsymbol{e}_y + \omega_z\boldsymbol{e}_z$, where

$$\omega_x = \frac{\partial U_z}{\partial y} - \frac{\partial U_y}{\partial z}, \qquad \omega_y = \frac{\partial U_z}{\partial y} - \frac{\partial U_y}{\partial z}, \qquad \omega_z = \frac{\partial U_y}{\partial x} - \frac{\partial U_x}{\partial y}. \tag{2-5}$$

Introduction of the Reynolds decomposition $U(\boldsymbol{x}, t) = \langle U\rangle(\boldsymbol{x}) + u(\boldsymbol{x}, t)$ into equation (2-2) in a Cartesian coordinates system and taking a time average, with the assumption of a stationary Newtonian incompressible flow field, results in:

$$\rho\langle U_j\rangle\frac{\partial\langle U_i\rangle}{\partial x_j} = \frac{\partial}{\partial x_j}\left[-\langle P\rangle\delta_{ij} + \mu\left(\frac{\partial\langle U_i\rangle}{\partial x_j} + \frac{\partial\langle U_j\rangle}{\partial x_i}\right) - \rho\langle u_i u_j\rangle\right] + \rho\langle B_i\rangle, \tag{2-6}$$

where the indices i and j denote the coordinates in Einstein notation and δ_{ij} is the Kronecker delta. The term $-\rho\langle u_i u_j\rangle$ is known as the Reynolds stress tensor. Since the density of the flow studied in this work was assumed to be constant, the components $\langle u_x^2\rangle$ and $\langle u_y^2\rangle$ are referred to as wall-parallel and wall-normal Reynolds stresses, and $-\langle u_x u_y\rangle$ is the Reynolds shear stress.

2.2. Boundary layer

A mid-span view of a turbulent channel flow with a bump on its lower wall is schematically illustrated in Figure 2-1(*a*). A fully developed flow with a mean streamwise velocity profile $\langle U_{in} \rangle$ and BL thickness of $\delta = 0.5\ h_{in}$ enters the flow domain. Here, h_{in} is the entrance height of the channel. As the flow approaches the bump, δ alters locally with a varying pressure gradient across the channel. Dashed blue curves depict the edge of the BL in Figure 2-1. A global Cartesian coordinate system aligned with the free-stream flow is fixed at the midspan's centerline, attached to the divergence section's start point. As shown in Figure 2-1(*b*), a moving tangent-normal coordinate system (s, n, z) is attached to the wall to define the velocity vector field in terms of wall-parallel and wall-normal velocity components, i.e., $\boldsymbol{U} = U_s\ \boldsymbol{e}_s + U_n\ \boldsymbol{e}_n$. The mean pressure and velocity of the BL's edge are denoted by U_e (s) and P_e (s), respectively.

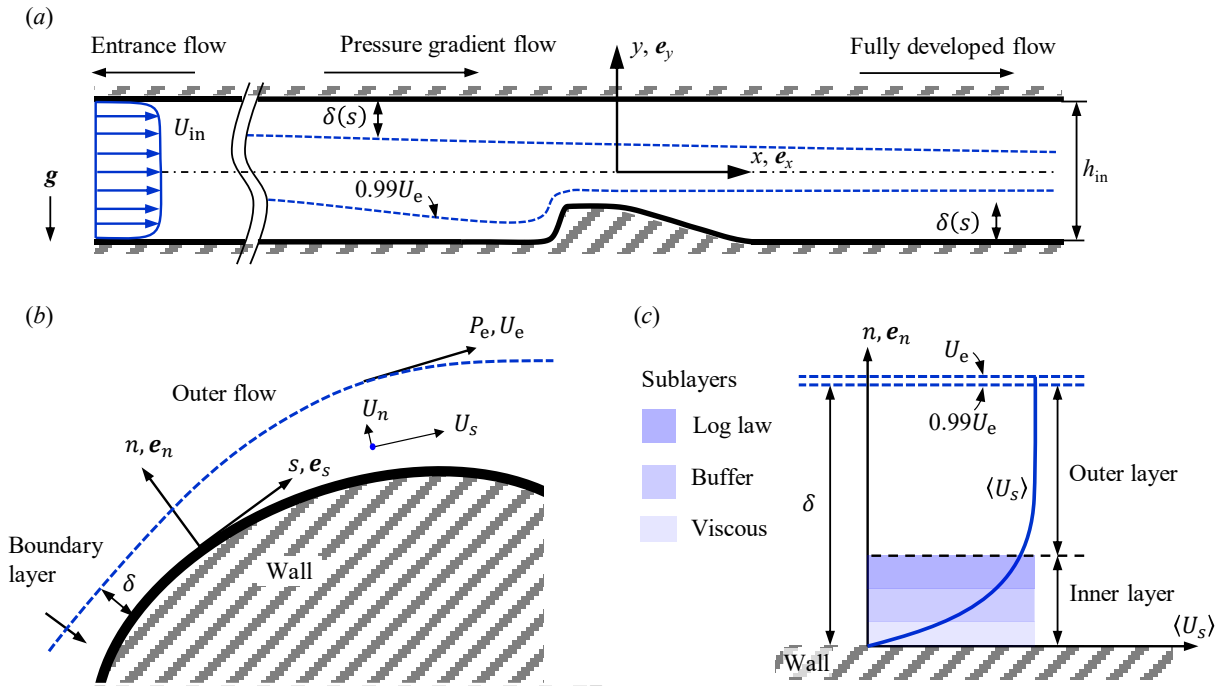

Figure 2-1 (*a*) Schematic representation of the wall and BL profiles of a turbulent channel flow with a bump. A fully developed flow with a mean streamwise velocity $\langle U_{in} \rangle$ and BL thickness of $\delta \approx 0.5\ h_{in}$ enters the channel. BL thickness starts to vary locally as the flow approaches the pressure gradient region, i.e., $\delta \neq$ Const. Dashed blue curves schematically depict the edge of the BL. A free-stream-aligned Cartesian coordinate system (x, y, z) is fixed at the center of the channel, at the starting point of the diverging section of the channel. (*b*) Schematic illustration of the BL over an arbitrary, smoothly curved, 2D solid wall. U_e and P_e, respectively, show the BL's edge velocity and pressure. A tangent-normal moving coordinate system (s, n, z), with its origin attached to the wall, defines the wall-parallel s, wall-normal n, and spanwise z coordinates at each point in space. In this curve-aligned coordinate system, the velocity vector field is defined as $\boldsymbol{U} = U_s\ \boldsymbol{e}_s + U_n\ \boldsymbol{e}_n$ where $\boldsymbol{e}_s$ and $\boldsymbol{e}_n$ are the unit vectors in s and n

directions, respectively. [*After* Çengel and Cimbala (2013)]. (*c*) Figurative representation of the mean wall-parallel velocity profile adjacent to the wall and corresponding sublayers. Not to scale.

The displacement and momentum thickness, δ^* and θ, respectively, are defined as:

$$\delta^* = \int_0^\infty \left(1 - \frac{\langle U_s \rangle}{U_\mathrm{e}}\right) dn, \tag{2-7}$$

$$\theta = \int_0^\infty \frac{\langle U_s \rangle}{U_\mathrm{e}} \left(1 - \frac{\langle U_s \rangle}{U_\mathrm{e}}\right) dn, \tag{2-8}$$

where U_e is the wall-parallel BL edge velocity. It is important to note that across a channel with nonuniform curved walls, U_e is not necessarily constant. A more realistic way of calculating integral quantities, as proposed by Spalart and Watmuff (1993), is by defining a generalized velocity as:

$$\langle \widetilde{U} \rangle (s,n) = -\int_0^n \langle \omega_z \rangle (s,n')\, dn', \tag{2-9}$$

where, $\langle \omega_z \rangle (s,n)$ is the mean spanwise vorticity component (see equation (2-5)). Here, $\langle \omega_z \rangle$ can be calculated using the mean wall-parallel and -normal components of velocity as:

$$\langle \omega_z \rangle = \frac{\partial \langle U_n \rangle}{\partial s} - \frac{\partial \langle U_s \rangle}{\partial n}. \tag{2-10}$$

Using equation (2-9), $\widetilde{U}_\mathrm{e}$ is:

$$\widetilde{U}_\mathrm{e}(s) = -\int_0^\infty \langle \omega_z \rangle (s,n)\, dn. \tag{2-11}$$

Accordingly, the generalized integral quantities are defined as:

$$\tilde{\delta}^*(s) = -\frac{1}{\widetilde{U}_\mathrm{e}(s)} \int_0^\infty n \langle \omega_z \rangle\, dn, \tag{2-12}$$

$$\tilde{\theta}(s) = -\frac{2}{\widetilde{U}_\mathrm{e}^2(s)} \int_0^\infty n \langle \widetilde{U} \rangle \langle \omega_z \rangle\, dn - \tilde{\delta}^*(s). \tag{2-13}$$

This method was utilized by Balin and Jansen (2021) and Coleman et al. (2018), among others, for the DNS of turbulent flows over bumps, where the computed velocity fields had a high spatial resolution, and it was straightforward to calculate high-accuracy $\langle \omega_z \rangle$ fields. However,

experimentally obtained velocity fields, even the ones from PIV, lack sufficient resolution and make it challenging to calculate. This issue was also noted by (Maciel et al., 2018). In this thesis, equations (2-7)-(2-8) were used primarily to calculate the integral quantities, and wherever applicable integral quantities based on the generalized velocity were also evaluated for comparison. At each wall-parallel position s, the BL thickness, δ, was defined as the wall-normal position where $U_s(s, \delta) \equiv 0.99\, U_e(s)$. The shape factor is defined as the ratio of displacement to the momentum thickness, i.e., $H = \delta^* / \theta$.

When the local radius of curvature of the wall, R_w, is much larger than the local δ, i.e., $R_w \gg \delta$, the normal pressure gradient is negligible through a BL, i.e., $\partial P / \partial n \cong 0$. Simplifying the mean momentum equation, given in (2-2), for an incompressible steady flow in the wall-parallel s-direction inside a BL reads as:

$$U_s \frac{\partial U_s}{\partial s} + U_n \frac{\partial U_s}{\partial n} = -\frac{1}{\rho}\frac{dP}{ds} + \nu \frac{\partial^2 U_s}{\partial n^2}. \tag{2-14}$$

Applying the Bernoulli equation to the outer flow, shown in Figure 2-1(b), at the edge of the BL, yields: $P_e/\rho + U_e^2/2 = \text{Const}$. Since, $P_e \equiv P_e(s)$ and $U_e \equiv U_e(s)$, then

$$\frac{1}{\rho}\frac{dP_e}{ds} = -U_e \frac{dU_e}{ds}. \tag{2-15}$$

From $\partial P / \partial n \cong 0$ condition, $P \approx P_e$, and $dP/ds \approx dP_e/ds$. Introducing equation (2-15) to equation (2-14) leads to

$$U_s \frac{\partial U_s}{\partial s} + U_n \frac{\partial U_s}{\partial n} = U_e \frac{dU_e}{ds} + \nu \frac{\partial^2 U_s}{\partial n^2}. \tag{2-16}$$

The no-slip boundary condition implies that the velocity is zero at the wall. Hence, equation (2-16) reduces to

$$\nu_w \left.\frac{\partial^2 U_s}{\partial n^2}\right|_{n=0} = -U_e \frac{dU_e}{ds} = \frac{1}{\rho}\frac{dP_e}{ds}, \tag{2-17}$$

where $\nu_w(s) = \mu_w(s)/\rho$ is the kinematic viscosity at the wall. As shown in Figure 2-2(a), the velocity profile is concave upward as it approaches the outer flow, implying that the second derivative of the velocity profile relative to the wall-normal direction is negative at the edge of the BL, i.e., $\partial^2 U_s/\partial n^2|_{n\to\delta} < 0$.

The mean wall shear stress τ_w, is directly proportional to the wall-normal gradient of $\langle U_s \rangle$ as

$$\tau_{\mathrm{w}} = \mu_{\mathrm{w}} \left. \frac{\partial \langle U_s \rangle}{\partial n} \right|_{n=0}, \tag{2-18}$$

where μ_{w} is the wall shear (or dynamic) viscosity. For a zero pressure gradient (ZPG) flow, outer flow acceleration is zero, and equation (2-17) suggests that $\partial^2 \langle U_s \rangle / \partial n^2|_{n=0} = 0$. As shown in Figure 2-2(*a*), with the velocity profile having a concave upward shape, the inflection point, where $\partial^2 \langle U_s \rangle / \partial n^2 = 0$, coincides with the wall for a ZPG flow. The velocity profile is linear near the wall with a positive slope in the entire BL. The slope is quantified as $\tan \alpha \approx \delta n / \delta \langle U_s \rangle$, which is reversely proportional to the shear stress τ, i.e., $\tan \alpha \propto \tau^{-1}$. As shown in Figure 2-2(*a*), slope starts at a minimum at the wall ($\tau_{\max} \equiv \tau_{\mathrm{w}}$) and smoothly increases in the entire BL and approaches infinity at the edge of the BL ($\tau \to 0$).

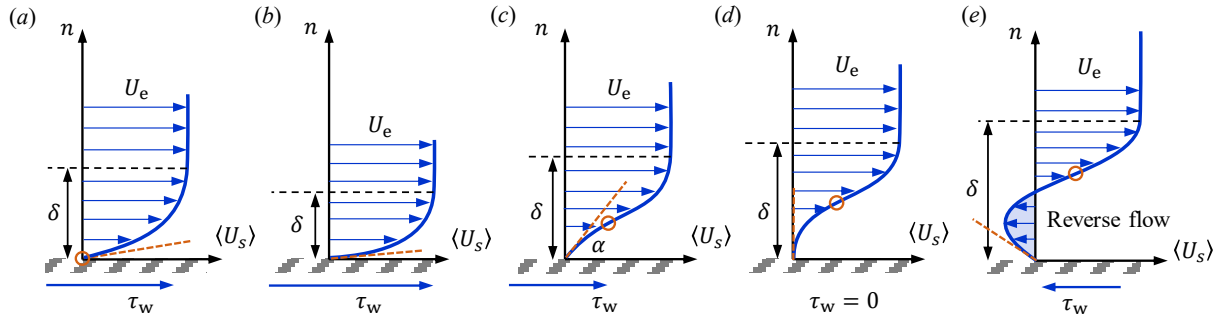

Figure 2-2 Schematic representation of the BL profiles with (*a*) zero, $dP_e / ds = 0$, (*b*) favorable, $dP_e / ds < 0$, (*c*) mildly adverse $dP_e / ds > 0$, (*d*) critically adverse, $dP_e / ds \gg 0$, and (*e*) largely adverse pressure gradients. Separation initiates at flow conditions shown in (*d*). Reverse flow occurs in (*e*). On each diagram, the velocity profile is depicted by a solid blue line, and the edge of BL thickness δ is shown by a black horizontal dashed line parallel to the wall, where $\langle U_s \rangle \equiv 0.99\, U_e$. A line tangent to the velocity profile at the origin of the mean $\langle U_s \rangle$-n diagram is shown by a dashed orange line, representing the slope $\tan \alpha \approx \delta n / \delta \langle U_s \rangle \propto \tau^{-1}$. For each condition, wall shear stress τ_{w} acts on the s-z plane in the positive s-direction, which is exerted on the wall by the flowing fluid. Here, the shear stress component of the tensor field, $\tau_{\mathrm{w}} \boldsymbol{e}_n \otimes \boldsymbol{e}_s$, is demonstrated by a solid blue vector. The magnitudes of the wall shear stresses are scaled relative to that of the ZPG flow shown in (*a*). Inflection points, where $\partial^2 \langle U_s \rangle / \partial n^2 = 0$ are shown by orange circles. [*After* Yunus A. Çengel and Cimbala (2013)].

As depicted in Figure 2-2(*b*), in a favorable pressure gradient (FPG) flow, the outer flow accelerates ($dU_e/ds > 0$ and $dP_e/ds < 0$) and $\partial^2 \langle U_s \rangle / \partial n^2|_{n=0} < 0$. This implies that the velocity profile of a flow with FPG has a stronger concave shape relative to the flow with ZPG and approaches the outer flow at a smaller δ for a similar U_e, i.e., $\delta_{\mathrm{ZPG}} < \delta_{\mathrm{FPG}}$. At the wall, flow with FPG has a smaller slope relative to the ZPG flow, which means the wall shear stress of FPG flow is larger than the ZPG flow for a similar U_e, i.e., $\tau_{\mathrm{w,FPG}} > \tau_{\mathrm{w,ZPG}}$.

For a decelerating flow ($dU_e / ds < 0$), the outer flow's pressure gradient in the s-direction is positive and unfavorable. For adverse pressure gradient (APG) flows, where $dP_e / ds > 0$, equation (2-17) implies that $\partial^2\langle U_s\rangle/\partial n^2|_{n=0} > 0$, which means the velocity profile has a concave downward shape near the wall. As discussed before, near the edge of the BL $\partial^2\langle U_s\rangle/\partial n^2|_{n\to\delta} < 0$. Therefore, as shown in Figure 2-2(*c*-*e*), there should be an inflection point on the velocity profile somewhere inside the BL and away from the wall with $\partial^2\langle U_s\rangle/\partial n^2 = 0$. The shear stress distribution changes in APG regions, which can *separate* the BL from the solid wall. As shown in Figure 2-2(*c*), for a flow with a mild APG, the slope of the velocity profile at the wall is steeper than the flow with a ZPG, implying that APG enforces smaller shear stress to the wall compared to a ZPG flow of equal U_e. The inflection point drifts away from the wall in an APG flow, and the BL thickens.

Increasing APG leads to a critical flow condition, where the slope of the velocity profile at the wall becomes very large, which implies that wall shear stress approaches a zero value. This condition is illustrated in Figure 2-2(*d*). A point with $\tau_w \approx 0$ (or equivalently $\partial\langle U_s\rangle/\partial n|_{n=0} \approx 0$) is called the *separation* point, beyond which a separation bubble and reverse flow occur, as shown in Figure 2-2(*e*). Reverse flow occurs near the wall in strong APG flow conditions, where the direction of the shear stress exerted on the wall changes.

2.2.1 Law of the wall

Generally, the flow field near a solid wall with ZPG can be divided into an *inner* and *outer* layer. The effect of flow viscosity is of less importance in the outer layer. Figure 2-1(*c*) shows that the inner layer comprises viscous, buffer, and log-law sublayers. In the viscous sublayer, viscous diffusion and dissipation are dominant, and the mean velocity profile $\langle U_s\rangle(n)$ changes linearly with the wall-normal location n. The velocity gradient $\partial\langle U_s\rangle/\partial n$ is relatively large in the viscous sublayer and contains the largest shear stress values over the entire BL. The buffer sublayer follows the viscous sublayer and is the near-wall region where the viscous and turbulent shear stresses are relatively dominant. Shear flow is strongly unstable in the buffer layer, where turbulent kinetic energy production and turbulent energy dissipation rate are maximum. As illustrated in Figure 2-1(*c*), the log-law region is the last sublayer of the inner layer in a ZPG flow, where velocity changes linearly with the wall-normal direction n, scaled logarithmically.

2.2.2 Normalization

Based on the application, turbulence parameters are usually normalized using 'outer' or 'inner' scales. Both scaling constants are used in wall-bounded turbulent flow studies. The outer length, velocity, and time scales are usually the BL thickness δ, mean edge velocity U_e, and δ/U_e. Friction velocity is defined as the squared root of the ratio of the wall-shear stress τ_w and the flow's density ρ, i.e., $u_\tau = \sqrt{\tau_w/\rho}$. Friction velocity is used as the inner velocity scale to normalize turbulence parameters. The inner length scale is defined as $\lambda_v = \nu_w/u_\tau$, which is also called 'wall unit' or 'viscous length scale.' Accordingly, the inner time scale is $t_v = \nu_w/u_\tau^2$. Here, μ_w and ν_w are the wall dynamic and kinematic viscosities.

Using the inner scales, the mean velocity $\langle U_s \rangle$ and n positions are normalized as $\langle U_s \rangle^+ = \langle U_s \rangle/u_\tau$, and $n^+ = n/\lambda_v$. The inner normalization of the BL thickness results in $\delta^+ = u_\tau\, \delta\, /\, \nu_w$, which is commonly called the Kármán number. The superscript '+' denotes normalization using inner scales. The inner-normalized velocity profile of a ZPG flow has a universal distribution as:

$$\begin{aligned} \langle U_s \rangle^+ &= n^+, && n^+ < 5, \\ \langle U_s \rangle^+ &\neq n^+, \langle U_s \rangle^+ \neq \frac{1}{\kappa}\ln n^+ + c_0^+, && 5 < n^+ < 30, \\ \langle U_s \rangle^+ &= \frac{1}{\kappa}\ln n^+ + c_0^+, && n^+ > 30. \end{aligned} \tag{2-19}$$

Here κ is the von Karman constant, and c^+ is the wall-law constant. For a turbulent liquid flow in a channel with smooth solid walls, $\kappa \approx 0.41$ and $c_0^+ \approx 5.5$. It is important to note that the ranges of n^+ given in equation (2-19) are approximate. The velocity profiles of the viscous sublayer and the log-law region given in equation (2-19) intersect at $n^+ = 11.45$.

The defect displacement thickness or length scale of Clauser (1954), Δ, and defect shape factor, G, are respectively defined as (Clauser, 1954; Rotta, 1953):

$$\Delta(s) = \int_0^\delta \frac{U_e(s) - \langle U_s \rangle(s,n)}{u_\tau(s)}\, dn = \delta^* \frac{U_e}{u_\tau}, \tag{2-20}$$

$$G(s) = \int_0^\delta \left(\frac{U_e - \langle U_s \rangle}{u_\tau}\right)^2 dn \Big/ \int_0^\delta \frac{U_e - \langle U_s \rangle}{u_\tau}\, dn = \frac{U_e}{u_\tau}\left(1 - \frac{1}{H}\right). \tag{2-21}$$

As discussed by (Clauser, 1954) and (Mellor and Gibson, 1966) and recently by Maciel et al. (2018), *G* is less dependent on the Reynolds number than the shape factor, *H*, and is ill-defined at separation or reattachment points, where $u_\tau \to 0$.

The friction velocity Reynolds number is defined as:

$$Re_\tau = \frac{u_\tau \delta}{\nu_\mathrm{w}}. \tag{2-22}$$

and is equal to Kármán number δ^+. The Reynolds numbers based on the edge velocity and the mean velocity are respectively formulated as:

$$Re_\mathrm{e} = \frac{U_\mathrm{e} \delta}{\nu_\mathrm{w}}, \tag{2-23}$$

$$Re_\mathrm{m} = \frac{U_\mathrm{m} 2\delta}{\nu_\mathrm{w}}. \tag{2-24}$$

Similarly, the skin friction coefficient based on the BL edge and mean velocities are respectively defined as:

$$c_\mathrm{f,e} = \frac{\tau_\mathrm{w}}{\frac{1}{2}\rho U_\mathrm{e}^2}, \tag{2-25}$$

$$c_\mathrm{f,m} = \frac{\tau_\mathrm{w}}{\frac{1}{2}\rho U_\mathrm{m}^2}. \tag{2-26}$$

2.3. Conclusion

This Chapter reviewed the main governing equations, the definitions of the mean flow variables, and boundary layer terminology used throughout the thesis. The statistical formulations used to calculate the mean parameters are given in Appendix A.

3. Methodology

Two main wall geometries were designed for (1) cavitating flow and (2) non-equilibrium turbulent flow experiments, which are explained in this Chapter. Details of the developed flow facility and the imaging and velocimetry techniques used are also discussed in this Chapter.

3.1. Wall geometry for cavitating flow

As Figure 3-1 illustrates, the wall geometry for the hydrodynamic cavitation tests was designed as a converging-diverging path, which produces a sudden drop in the local pressure well below the saturation pressure and initiates cavitation at the throat region. Cavitation geometry (CG), shown in Figure 3-1, has a throat length of L_{th} to allow the initial cavitation structures to develop on the channel walls before expanding downstream into the divergence region.

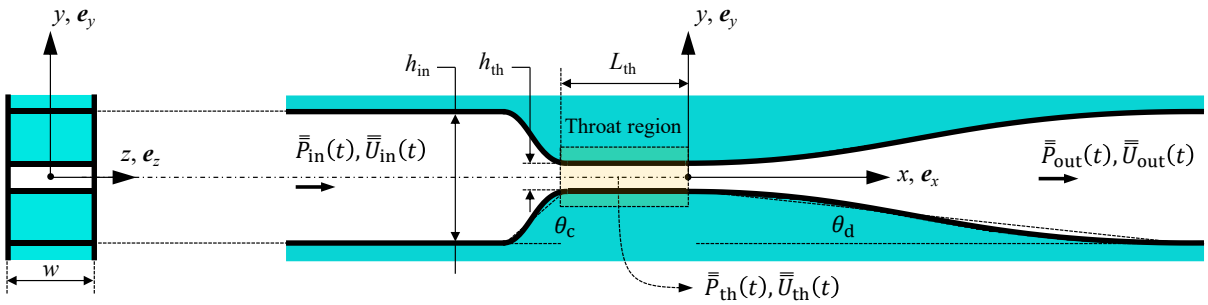

Figure 3-1 Main variables associated with the cavitation geometry (CG). Solid body is colored turquoise.

A parametric numerical study was conducted to find an optimum nozzle geometry using the Flow Simulation toolbox of commercial software (SOLIDWORKS 2021, Dassault Systèmes). Details of the numerical setup are given in Appendix B. Figure 3-1 illustrates the main variables affecting the nozzle shape's design. The cross-sectional area averaged inlet velocity $\overline{\overline{U}}_{in}$, throat height h_{th} and convergence angle θ_c were varied. The inlet height h_{in}, length of the throat L_{th}, channel thickness w, and divergence angle θ_d were defined as $h_{in} = 5\ h_{th}$, $L_{th} = 2\ h_{th} + 1$, $w = 2.5\ h_{th}$, and $\theta_d = \theta_c / 5$. At the inlet, the volumetric flow rate $\dot{V} = A_{in}\overline{\overline{U}}_{in}$ was prescribed, and a fully developed flow condition was enforced. The outlet pressure was set at the atmospheric pressure, i.e., $\overline{\overline{P}}_{out} = P_{atm}$, and no-slip boundary condition was applied to all interior wall surfaces. In the parametric study, h_{th} and θ_c were varied in the range of 1 mm $\leq h_{th} \leq$ 4 mm and 30° $\leq \theta_c \leq$ 80°, respectively, with increments of Δh_{th} = 0.5 mm and $\Delta\theta_c$ = 5°. The set of 77 different flow scenarios was simulated for $\dot{V}$ = 15 lit min^{-1} on an intermediate mesh. Optimum values of h_{th} = 2 mm, and

$\theta_c = 60°$ were obtained, considering the limitations of the pump capacity, inlet pressure threshold, and minimum channel height for optical access.

The final geometrical parameters of the flow path used for the cavitation experiments are listed in Table 3-1. The channel's height decreases over 5.2 mm in the convergence region, is constant for a length of $L_{th} = 5$ mm in the throat region and starts to increase smoothly again at $\theta_d = 12$ ° over a length of 42.3 mm and reaches a slope of zero before the outlet. The converging and diverging profiles of the flow path were generated based on a third-order polynomial curve, with their starting and ending points tangent to the horizontal flow path. The hydraulic diameter of the channel throat is $D_{h,th} = 2\ (h_{th}\ w)\ /\ (h_{th} + w) = 2.86$ mm. The throat Reynolds number is defined as $Re_{th} = \rho \bar{\bar{U}}_{th} D_{h,th} \mu_w^{-1}$, where ρ and μ_w are the density and wall dynamic viscosity of the fluid.

Table 3-1 Geometrical properties of the designed converging-diverging nozzle profile.

h_{in} (mm)	w (mm)	h_{th} (mm)	L_{th} (mm)	θ_c (°)	θ_d (°)
10	5	2	5	60	12

3.2. Wall geometry for non-equilibrium turbulent flow

The designed turbulent geometry (TG) is illustrated in Figure 3-2. It has a converging-diverging bump on the channel's lower wall to produce successive favorable and adverse pressure gradients in the turbulent flow. As listed in Table 3-2, the flow path has an inlet height of $h_{in} = 8$ mm. The bump profile increases in height with a constant slope over $L_c = 2.3$ mm at a convergence angle of $\theta_c = 60$ ° to produce a bump height of $h_b = 2$ mm, which is extended for $L_b = 3.4$ mm downstream, with a zero slope. Fillets of radius $r_c = 1$ mm were applied to the convergence profile to make its start and end lines tangent to the horizontal flow path.

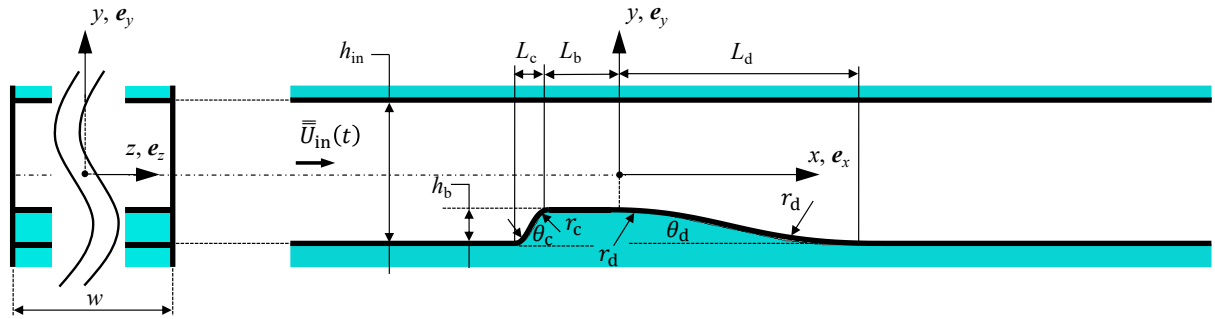

Figure 3-2 Main variables associated with turbulent geometry (TG). Solid body is colored turquoise.

A fixed Cartesian coordinate system is attached at the end point of the flat surface of the bump on the midspan plane. The bump profile starts to decrease in height, from the origin of the coordinate system, with a constant slope at a divergence angle of $\theta_d = 12°$ over a length of $L_d = 11.5$ mm until it meets the downstream's flat surface. Fillets of radius $r_d = 10$ mm were applied to the starting and end lines of the divergence profile to make it tangent to the horizontal flow path. By examining a wide range of experimental data, Dean (1978) suggested that an aspect ratio (AR) of ≈ 7 in rectangular channels is the minimum threshold to avoid significant 3D disturbance and assume a 2D central flow. In this study, the width of the TG channel is $w = 60$ mm, which results in a minimum AR of $AR = w / h_{in} = 7.5$ at the inlet and a maximum $AR = 10$ at the flat surface of the bump. Therefore, the investigated turbulent flow can be assumed to be 2D.

Table 3-2 Geometrical properties of the designed converging-diverging bump profile on the lower wall of TG.

h_{in} (mm)	w (mm)	L_c (mm)	θ_c (°)	r_c (mm)	L_b (mm)	h_b (mm)	L_d (mm)	θ_d (°)	r_d (mm)
8.0	60.0	2.3	60	1.0	3.4	2.0	11.5	12	10.0

3.3. Flow facility

A mesoscale flow loop was designed to examine the cavitation and turbulent flows in a converging-diverging channel. A schematic of the flow system is shown in Figure 3-3. A positive displacement pump (Model 33204; Moyno Inc.), equipped with a variable frequency drive, circulated the flow. The flow's mass flow rate, density, and temperature were measured online using a Coriolis flowmeter (Krohne Optimass 7000), which communicated with a computer via RS-485 Modbus protocol. A custom code based on the MODBUS interface of the instrument control toolbox of MATLAB (2021, MathWorks) was developed to read, control, and store flowmeter signals. For each test, flowmeter data was collected for 10 s.

As shown in Figure 3-3, the flow facility was designed so that the channel section can be bypassed from the main loop by closing a gate valve at its inlet. In this way, water-additive mixtures can be circulated in the system at moderate flow rates and for a certain period to generate a more homogeneous solution. At each test, the liquid flow's pressure drop over the straight tube ΔP_{tu} was measured over L_{tu} = 0.92 m in a circular, straight plastic tube with an inner diameter of D_{tu} = 19 mm. A differential pressure transducer (DP15; Validyne Engineering) with a transducer diaphragm (no. 3-26; Validyne Engineering), calibrated for a full-scale (FS) pressure of 2.0 kPa, measured ΔP_{tu} at a scan rate of 500 Hz.

Two differential pressure transducers (DP15; Validyne Engineering) measured the pressure drop ΔP_{ch} over the test sections and the outlet pressure P_{out} at a scanning frequency of 500 Hz. The ΔP_{ch} and P_{out} transducers used a diaphragm (no. 3-48; Validyne Engineering) calibrated for FS = 500 kPa, and a diaphragm (no. 3-20; Validyne Engineering) calibrated for FS = 800 Pa. The accuracy of the pressure measurements was ± 0.5 % FS. Pressure transducers were calibrated with a portable pressure calibrator (DPI 603; Druck, Baker Hughes business) based on 15 discrete measurements for a full-scale output voltage of 10 V and fitting a line to the time-averaged pressure data. The coefficient of determination of the fitted curves was ~ 1. The output voltage signals were conditioned using a multi-channel carrier demodulator (CD280; Validyne Engineering) with a maximum frequency response of 1 kHz.

Figure 3-4 illustrates that two high-frequency quartz pressure sensors (112A05, charge type; P.C.B. Piezotronics) were mounted at the top and bottom of the CG test section, downstream of the flow, to measure the pressure fluctuations of the downstream flow, P_d, during cavitation tests.

The sensitivity of the pressure sensors was 0.172 pc/kPa. A signal conditioner (482C54; P.C.B. Piezotronics) with a charge sensitivity of 10 mV/pc was used to charge the sensors. Full-scale pressure measurement and output voltage were 100 kPa and 10 V, respectively. The gain values were adjusted to produce output sensitivities of 100 mv/kPa. The scanning frequency of the pressure sensors was 125 kHz.

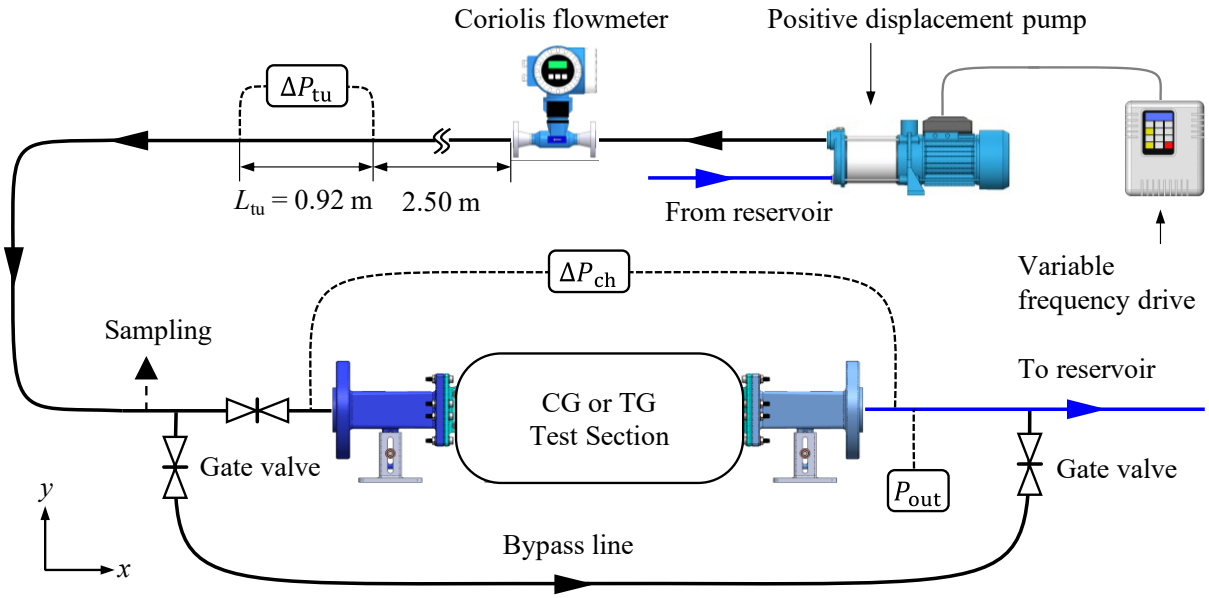

Figure 3-3 Schematic representation of the flow facility and its main components. Not to scale.

A voltage input module (NI-9205; National Instruments) installed on a compact data acquisition chassis (Ni-cDAQ-9188; National Instruments) read the incoming pressure signals and transferred them to the computer via an Ethernet connection. Two resistance temperature detectors (TR40; WIKA Instruments Canada Ltd.) measured the incoming and outgoing flow temperatures. A temperature input module on the same chassis read temperatures at 200 Hz. A custom code based on the data acquisition toolbox of MATLAB (2021, MathWorks) was developed to read, control, and store pressure and temperature signals.

A maximum flow rate of $\dot{V}$ = 25 lit min^{-1} and absolute inlet pressure of P_{in} = 600 kPa were the constricting parameters in the design of the experimental facility. The entry length required for the turbulent flow to be fully developed can be approximated as (Çengel and Cimbala, 2013): $L_{en} = 1.36\, D_h\, Re_{D_h}^{1/4}$. In the CG channel with inlet D_h = 6.67 mm, the flow rate varied in the range of 5 lit min^{-1} $\lesssim \dot{V} \lesssim$ 12 lit min^{-1}, which is equivalent to $1.2 \times 10^4 \lesssim Re_{D_h} \lesssim 3.0 \times 10^4$. For these flow conditions, 95 mm $\lesssim L_{en} \lesssim$ 119 mm. Therefore, as Figure 3-4 illustrates, the test section was

extended by ≈ 230 mm (≈ 23 h_{in} and ≈ 34.5 D_h) upstream of the nozzle to generate a fully developed turbulent flow.

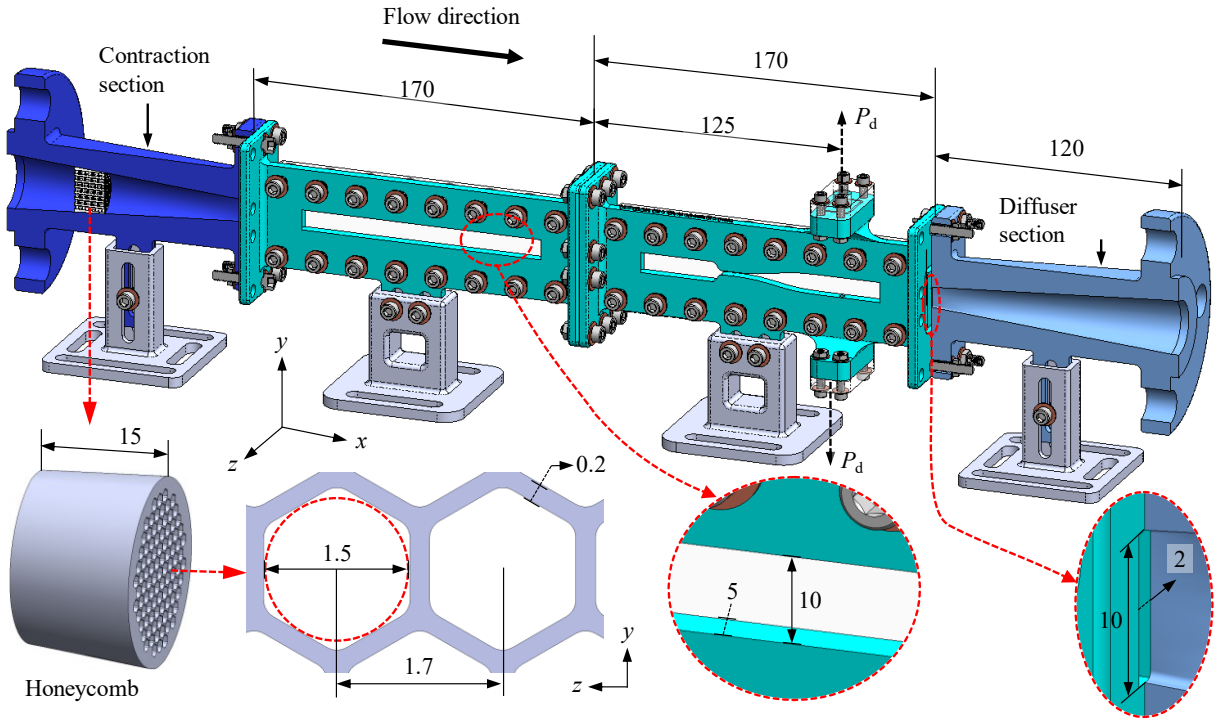

Figure 3-4 Representation of the CG flow channel and its principal dimensions annotated. Left-bottom inserted figure displays the geometry and main dimensions of the honeycomb. Fluid flows in the positive x direction. All dimensions are in mm.

Figure 3-4 illustrates that the flow was delivered to the CG test section via a contraction. It smoothly transformed the flow path's circular cross-section with a diameter of 26.7 mm into a rectangular entrance of 10 × 2 mm^2. A honeycomb was designed to straighten the incoming flow with uniformly distributed hexagonal hollows of inscribed circle diameter of 1.5 mm, with an edge-to-edge distance of 0.2 mm. The honeycomb's length was 15 mm, and its outer face followed the internal topology of the contraction section.

Figure 3-5 shows the TG channel with inlet D_h = 14.12 mm. For turbulent flow tests, the flow rate was 15 lit min^{-1} ≲ $\dot{V}$ ≲ 25 lit min^{-1}, which is equivalent to 8.1 × 10^3 ≲ Re_{D_h} ≲ 1.35 × 10^4. Hence, 182 mm ≲ L_{en} ≲ 207 mm. As discussed, the AR of the TG channel is sufficiently large at the inlet (AR = 7.5) to assume a 2D turbulent flow. Therefore, it is also common to calculate the Reynolds number based on the inlet height (h_{in} = 8 mm). Here, 4.6 × 10^3 ≲ $Re_{h_{in}}$ ≲ 7.63 × 10^3 and 90 mm ≲ L_{en} ≲ 102 mm. The inlet section was further extended by a length of 170 mm to produce

a total inlet length of ≈ 220 mm between the entrance and the nozzle bump to ensure a fully developed turbulent flow field.

As illustrated in Figure 3-5, a contraction of 120 mm length transformed the flow path's circular cross-section into a rectangular entrance of 8×20 mm^2. A honeycomb with hollow patterns similar to the CG test section straightened the incoming flow. The honeycomb length was 31 mm, and its outer face followed the internal topology of the contraction section.

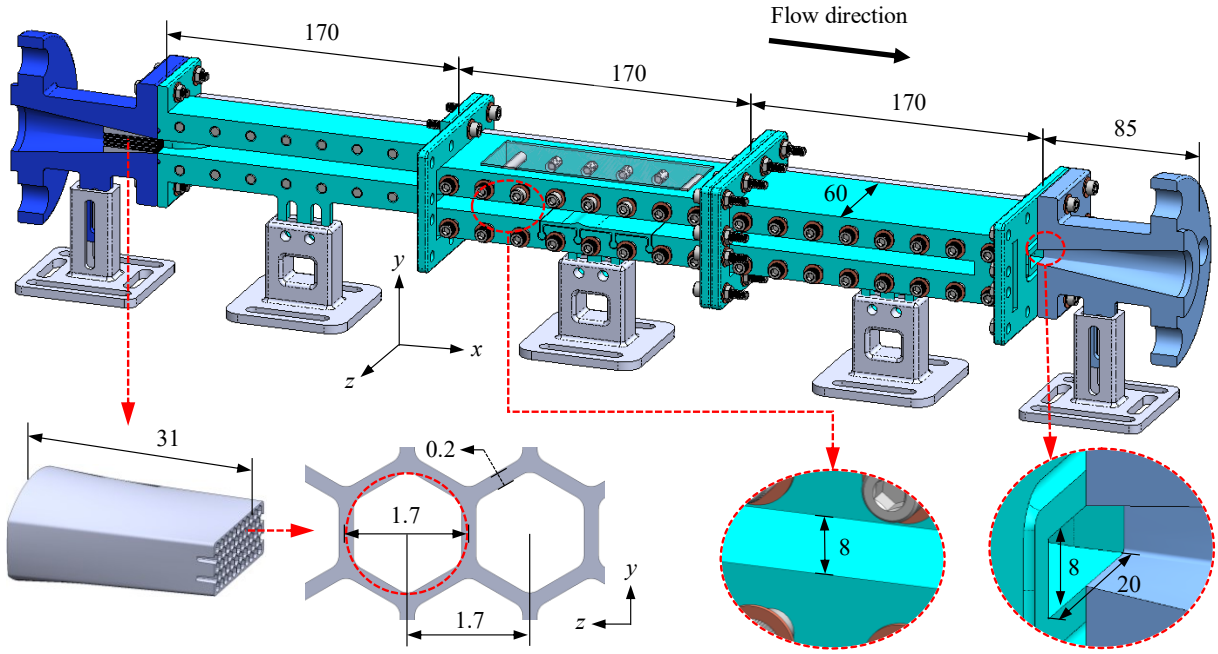

Figure 3-5 Representation of the TG flow channel and its principal dimensions annotated. Left-bottom inserted figure displays the geometry and main dimensions of the honeycomb. Fluid flows in the positive x direction. All dimensions are in mm.

The contraction and diffuser sections shown in Figure 3-4 and Figure 3-5, the honeycombs, the test sections, and the bumps were constructed using a low force stereolithography technology (Form 3; Formlabs Inc.). The print resolution was 50 µm for the bumps and 100 µm for all other parts. Transparent resin (V4; FormLabs Inc.) was used as the base material for printing the test section and the nozzle bumps, and for the other printed components, grey resin (V4; FormLabs Inc.) was utilized. The nozzle sections can be easily separated from the test section and replaced with different shapes to generate different configurations. The bump surfaces were polished using ultra-fine micro-grit sandpapers. Finally, a plastic polish (7100 Plastic Polish Kit; NOVUS Plastic Polish) was used to remove micro-scratches on the surface. The final surface finish was sufficiently smooth and glossy.

Two transparent windows were laser cut from ¼ inch acrylic sheet (Optix acrylic; Plaskolit Inc.) using a commercial laser cutter (VersaLaser V.L.D. Version 3.50; Universal Laser Systems) and were installed on both sides of the channel to give optical access to the interior flow. Figure 3-5 illustrates that a transparent acrylic sheet was also mounted at the channel's top to give spanwise optical access to the flow passing over the bump. The flow left the test section via a diffuser section, identical to the contraction, and returned to the reservoir with a capacity of ≈ 20 liters.

3.4. Optical set-up

As shown in Figure 3-6, the flow field was interrogated using an optical system based on backlit illumination. A green-light high-current light-emitting diode (LED) (iLA.LPS v3; ILA_5150 GmbH) with a maximum frequency of 1 MHz illuminated the field-of-view (FOV). As illustrated in Figure 3-6, two bi-convex lenses were used in sequence. Their distances from the channel's central plane were carefully tuned to focus the light and uniformly distribute it on the relatively small FOVs to achieve the maximum intensity of collimated light rays.

3.4.1 Imaging

A high-speed camera (Phantom VEO 710; Vision Research Inc.) was utilized to record 20 000 instantaneous images of cavitating flow structures at a frame rate of 19 kHz ($\Delta t \approx 52.6$ µs) for each flow scenario. The camera and LED were carefully synchronized and triggered by adjusting the trigger signal's delay, period, and duty using a function generator (AFG 3021B, Tektronix Inc.). The camera's exposure time and the LED's power were adjusted to saturate ≈ 80 % of the camera's sensors in the liquid region (equivalent to ≈ 204/255 image counts). The LED's duty duration was set to 237 ns (≈ 0.45 % of the full cycle) to freeze the fastest motion of cavitation structures. Table 3-3 lists the main optical properties of the imaging system.

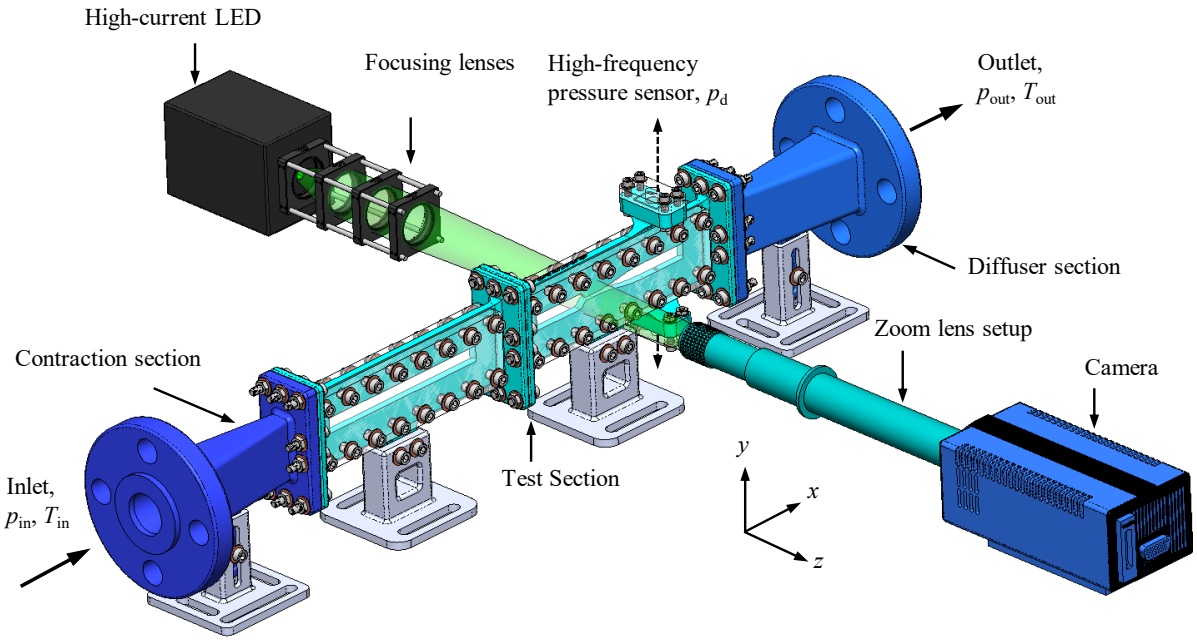

Figure 3-6 Schematic representation of the optical set-up.

A micro-calibration glass plate (MP 50 × 12; LaVision GmbH) was utilized to calibrate the images and focus on the midspan of the channel (plane $z = 0$). Dot targets with diameters of 100 ± 1 µm and equal planar distancing of 300 ± 1 µm of the target plane were found to be suitable for the calibration. Due to the geometrical constrictions of the test section, it was not feasible to put the calibration plate within the channel and adjust its position to calibrate the imaging system. Therefore, the apparent width of the test section was carefully measured, and the position of the channel's midspan relative to the channel's front window was determined with high certainty.

Table 3-3 Main optical properties of the imaging system.

$\|e\|$ (µm)	f_c (kHz)	Δt_{exp} (ns)	$L_x \times L_y$ (pixel^2)	FOV (mm^2)	M	ς (µm pixel^{-1})	δz (µm)
20	19	237	1008 × 320	26.2× 8.3	0.77	25.92	790.70

An average of 1000 images with ≈ 700 target dots was used in a third-order polynomial fit model to map the images to real-world coordinates. The fit's root-mean-square (r.m.s.) was less than 0.1 pixels for all cases. Commercial software (DaVis V8.2; LaVision GmbH) was used for mapping. A zoom lens (12X, 1-50486; Navitar Inc.) with an extension adapter (1X, 1-6015; Navitar) and a lens attachment (0.5X, 1-50012; Navitar Inc.) was used to obtain a magnification of $M \approx 0.77$ and digital resolution of $\varsigma \approx 25.92$ µm pixel^{-1}. Figure 3-7 highlights the interrogated FOV over the CG test section in cavitation measurements. The formulation (Inoué et al., 1997):

$$\delta z = \frac{n_{\text{tot}}\lambda}{(N_A)^2} + \frac{n_{\text{tot}}e}{M(N_A)}, \tag{3-1}$$

was used to calculate the depth of field δz value. Here, $n_{\text{tot}} = 0.9$ is the total refractive index of air, acrylic, and water, the media between the lens and the object under study, $\lambda = 532$ nm is the wavelength of the green light, $|e| = 20$ µm is the discrete sensor size, and $N_A = 0.043$ is the numerical aperture of the zoom lens system. Hence, $\delta z = 790.70$ µm, which covers ± 8 % of the flow field about the midspan plane of the channel, as Figure 3-7 illustrates.

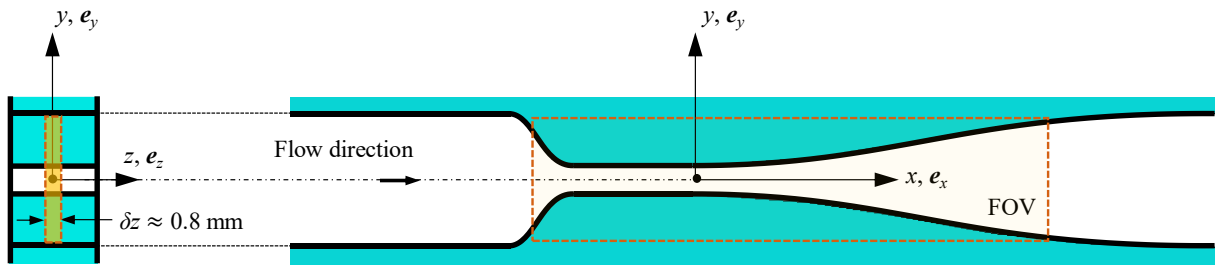

Figure 3-7 Highlighted interrogated FOV over the CG test section in the cavitation measurements. Pale orange rectangles with dashed red borders highlight the imaging system's depth of field.

3.4.2 Determination of the location of the mid-span plane

As illustrated in Figure 3-8, a micro calibration glass target (MP 50 × 12, LaVision GmbH) was utilized to calibrate the images and focus the focal plane of the imaging system on the midspan of the channel (plane $z = 0$). Dot distances and diameters of the micro targets are listed in Table 3-4. Due to the geometrical constrictions of the test section, it was not feasible to put the calibration plate inside the channel and adjust its position to calibrate the imaging system. Therefore, a different calibration process was followed.

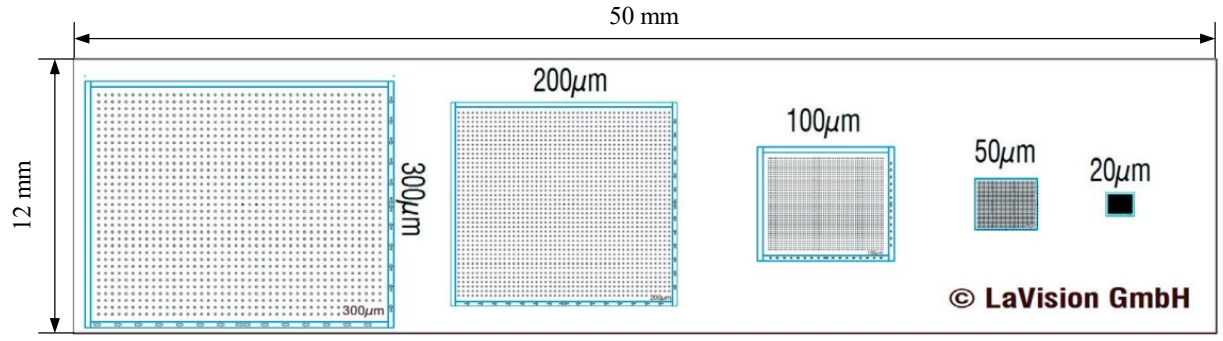

Figure 3-8 A snapshot of the micro calibration plate (MP 50 × 12, LaVision GmbH) used to calibrate the images. The plate thickness is w_{ta} = 15 mm.

Table 3-4 Dot distances and diameters of the utilized micro calibration target plate (MP 50 × 12, LaVision GmbH).

Target name	MP 50 × 12 300	MP 50 × 12 200	MP 50 × 12 100	MP 50 × 12 50	MP 50 × 12 20
Distance (μm)	300 ± 1	200 ± 1	100 ± 1	50 ± 1	20 ± 1
Diameter (μm)	100 ± 1	66.7 ± 1	33.3 ± 1	16.7 ± 1	6.7 ± 1

The first step was to determine the physical location of the focal plane on the target relative to its front or back face. Figure 3-9 represents a schematic of this process. The target was initially mounted on the front window of the test section, with its front plane A facing the camera. Then, the magnification of the imaging system was set to ~ 8 to generate a slender depth of field, $\delta z \approx 50$ μm. Using a combination of a one-axis linear stage (M-460P-X, Newport Corporation) and a Vernier micrometer (SM-25, Newport Corporation), the camera was moved in increments of 1 μm in the negative z-direction to focus on the MP 50 target dots.

Figure 3-9 shows a physical distance z_0 between the front of the lens and the target's plane facing the camera. The distance between the focal plane and the back face of target B is shown by dw. Next, without touching the camera, the target plate was removed and mounted again on the front window of the test section, this time with its back face B facing the camera. Then, the camera was moved to get focus on the MP 50 dots. This process was repeated three times, and the camera's

displacement from Position 1 to 2 was obtained to be $dz = 1.000 \pm 0.002$ mm. The geometrical equality: $z_0 + dw = dz_0 + z_0 + (w_{ta} - dw)$ is true for the settings illustrated in Figure 3-9. Therefore, $dw = (w_{ta} + dz_0) / 2 = 1.250 \pm 0.002$ mm. As was proven, the focal plane has an offset of ~ 0.5 mm from the target's central plane and is *not* centered, which might be due to the non-unity refractive index of the target, $n_{ta} \approx 1.517$.

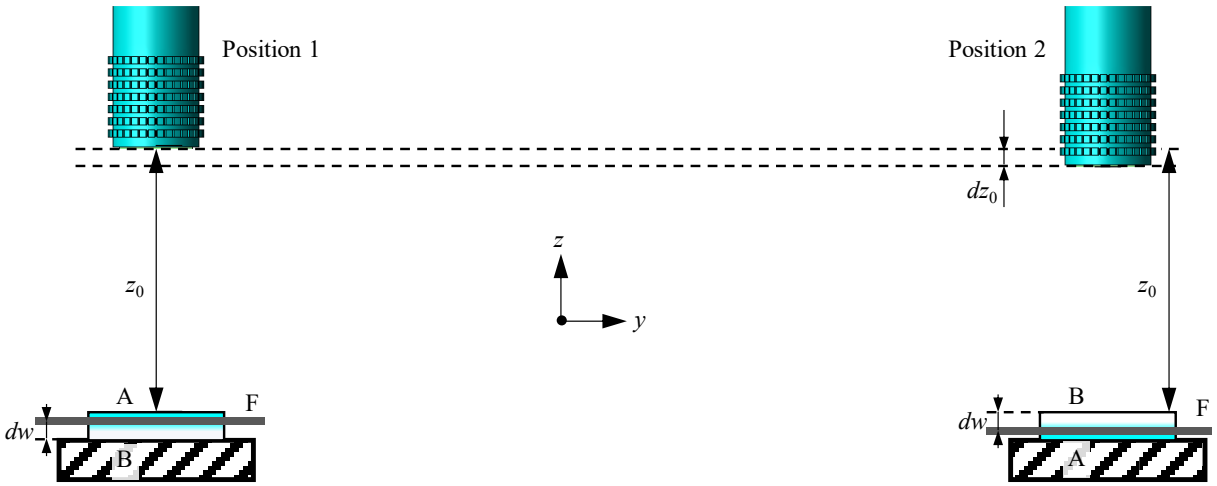

Figure 3-9 Schematic presentation of the process to determine the position of the focal plane relative to the target. The front and back faces of the target are labeled with letters A and B, and the focal plane is shown by a thick dark gray line marked with the letter F. Not to scale.

In the current experiments, illumination light rays pass through media of different refractive indices to reach the camera's sensor. As shown in Figure 3-10, the variation of the refractive indices causes the physical distance of the lens front from the channel's midspan z_1 to differ from its *apparent* counterpart z'_1, which is visualized by the camera. Here, the physical distance is $z_1 = z_0 + w_{ac} + 0.5\ w$, while the apparent distance is $z'_1 = (z_0/n_a) + (w_{ac}/n_{ac}) + (0.5\ w/n_w)$. With $n_a = 1.0$, $n_{ac} = 1.489$, and $n_{wat} = 1.333$, it can be concluded that $z'_1 < z_1$. Therefore, it is essential to account for the variation in the refractive indices to correctly locate the position of the apparent midspan and properly coincide the focal plane with it.

As depicted in Figure 3-11, the following procedure was applied to locate the position of the midspan plane of the flow channel. (1) Initially, the glass target plate with a refractive index of $n_{ta} = 1.517$ was mounted on the front window, with its front plane A facing toward the camera. The magnification was set to ~ 8 ($\delta z \approx 50$ μm), and the camera was focused on the 50 μm dots.

(2) The target was removed and mounted on the test section's rear window, with its front face A facing the camera. With the same magnification of ~ 8, the camera was moved in the negative

z-direction with increments of 1 μm to get it focused on the MP 50 dots. With three repetitions, the physical distance that the camera was displaced from its initial position was found to be $dz = 13.33 \pm 0.002$ mm for the CG test section with $w = 5$ mm. This value can also be determined by calculating the apparent distance between the initial and final positions of the focal plane as $dz = (dw/n_a) + 2\,(w_{ac}/n_{ac}) + w/n_w + ((w_{ta}\text{-}dw)/n_{ta}) = 13.22$ mm. The difference between the calculated and measured dz is only 0.8 %, which may be due to the nominal values used for the refractive indices of the media. This step verifies that the apparent distance concept can be used to determine the position of the midspan plane relative to the initial position of the camera's focus plane on the target.

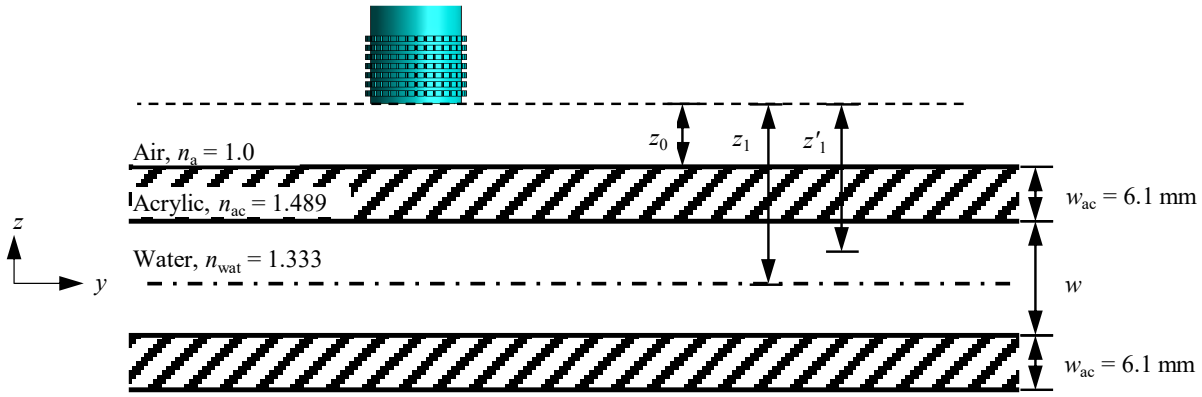

Figure 3-10 Effect of the refractive index variation on the apparent distance visualized by the camera.

(3) The target was removed from the rear window and was mounted again on the front window, with its front face A toward the camera. Then, the camera was moved by dz in the positive z-direction to get a focus on the target. Then, the target was removed without touching the camera. The apparent distance between the CG channel's midspan plane and the initial position of the camera's focal plane was calculated as $h_0 = (dw/n_a) + (w_{ac}/n_{ac}) + [(0.5\,w)/n_w] = 7.15$ mm. Therefore, moving the camera by h_0 in the negative z-direction, the camera's focal plane coincided with the midspan. Repeating the same procedure for the TG channel, the apparent distance was calculated as $h_0 = 27.65$ mm. Table 3-5 lists the physical and apparent distances between the focus plane on the target and the midspan of the CG and TG channels. It was also assumed that adding polymer additives to the water did not change the refractive index of the liquid fluid.

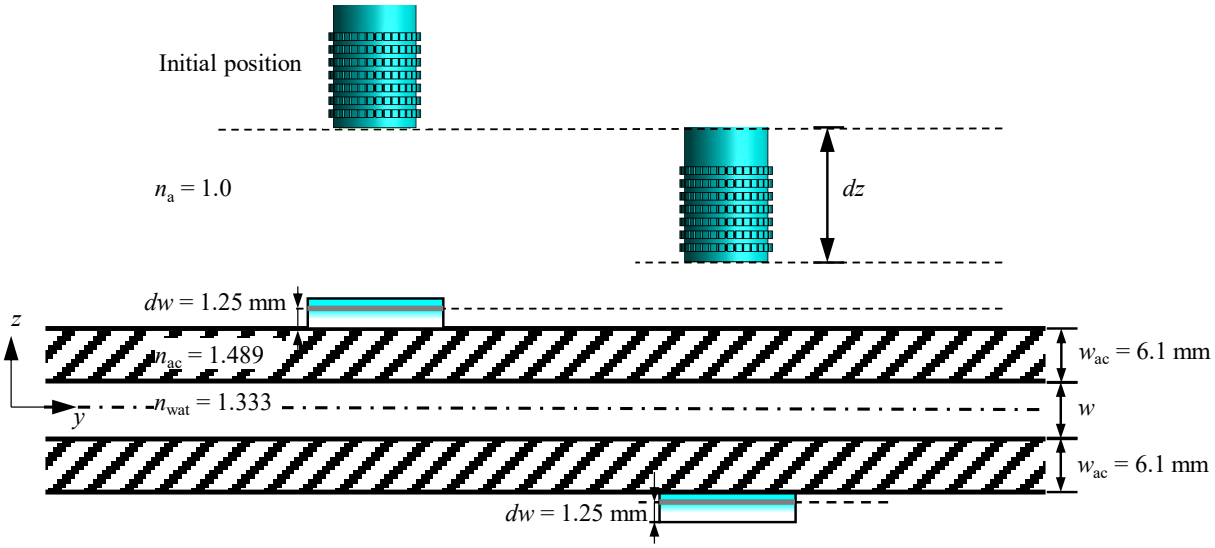

Figure 3-11 Illustration of the calibration procedure applied to locate the accurate position of the midspan plane.

Table 3-5 Physical and apparent distances between the focus plane of the target, attached to the channel's front window, and the midspan plane of the channels.

Distance (mm)	CG channel	TG channel
Physical, H_0	9.85	37.35
Apparent, h_0	7.15	27.65

3.5. Velocimetry

The 2D PIV technique was conducted to measure the turbulent velocity field and determine the characteristics of the developing non-equilibrium BLs on the midspan plane ($z = 0$) over the TG channel walls illustrated in Figure 3-2. A high-speed camera (Phantom VEO 710; Vision Research Inc.) with a minimum exposure time of 300 ns was used in *frame-straddling* recording mode (Adrian and Westerweel, 2011; Wernet, 1991) to capture 11 000 image pairs of the turbulent flow field flowing through the TG test section (see Figure 3-2 and Figure 3-5).

3.5.1 Synchronization procedure

Figure 3-12(*a*) represents a schematic of the trigger signals of the camera and illumination pulses in a frame-straddling recording mode. A synchronization trigger signal, produced internally by the camera, was introduced into a function generator (AFG 3021B; Tektronix Inc.) as a source input signal to define the frequency of the illumination pulses. The black signal shown in Figure 3-12(*a*) represents such a signal. The properties of the illumination trigger signal were precisely controlled to generate two pulses with widths of 1.5 µs and timing of Δt_{PIV} between the pulses, with a signal frequency of $2\Delta t$. Here, $1/\Delta t$ is the recording frame rate of the camera. The camera and the illumination signals were monitored online using an oscilloscope (TDS 2024B; Tektronix Inc.) to ensure the generation of precise pulses.

The generated signal was transferred to a green-light high-current LED (iLA.LPS v3; ILA_5150 GmbH) to illuminate the examined FOV. Figure 3-12(*b*,*c*) shows two snapshots of a sample flow field for $\Delta t_{PIV} = 10$ µs and $\Delta t_{PIV} = 5$ µs. The illumination signal was intentionally altered to generate two pulses on a similar image frame to signify the displacement of similar particles on one image. As the displacement vectors on zoomed-in inserts in Figure 3-12(*b*,*c*) display, reducing Δt_{PIV} by 50 % reduces the displacement of particles by 50 %. This test validated the correct timing and synchronization of the camera and illumination pulses.

This study uses $\Delta t = 500$ µs, i.e., the timing between the PIV image pairs was 1 ms. The velocity data should be averaged over a long time for the flow statistics to converge (Taylor et al., 2003). In the current study, the eddy turnover time, $t_{ed} = \delta\, U_e^{-1}$, was used as a criterion to determine the time required for averaging, where δ is the BL thickness, and U_e is the streamwise velocity at the edge of the BL. For the fully developed turbulent channel flows examined, $\delta = 0.5\, h_{in} = 4$ mm and $U_e > 0.5$ m s^{-1}; therefore, $t_{ed,max} \approx 8$ ms. The total recording time for each flow scenario was

≈ 11 s, which is ≈ 1 375 $t_{ed,max}$; a sufficient time to obtain converged flow statistics. The timing between the PIV frames, Δt_{PIV}, varied between 40 µs to 60 µs in experiments to prevent particles from displacing more than 10 pixels between two frames.

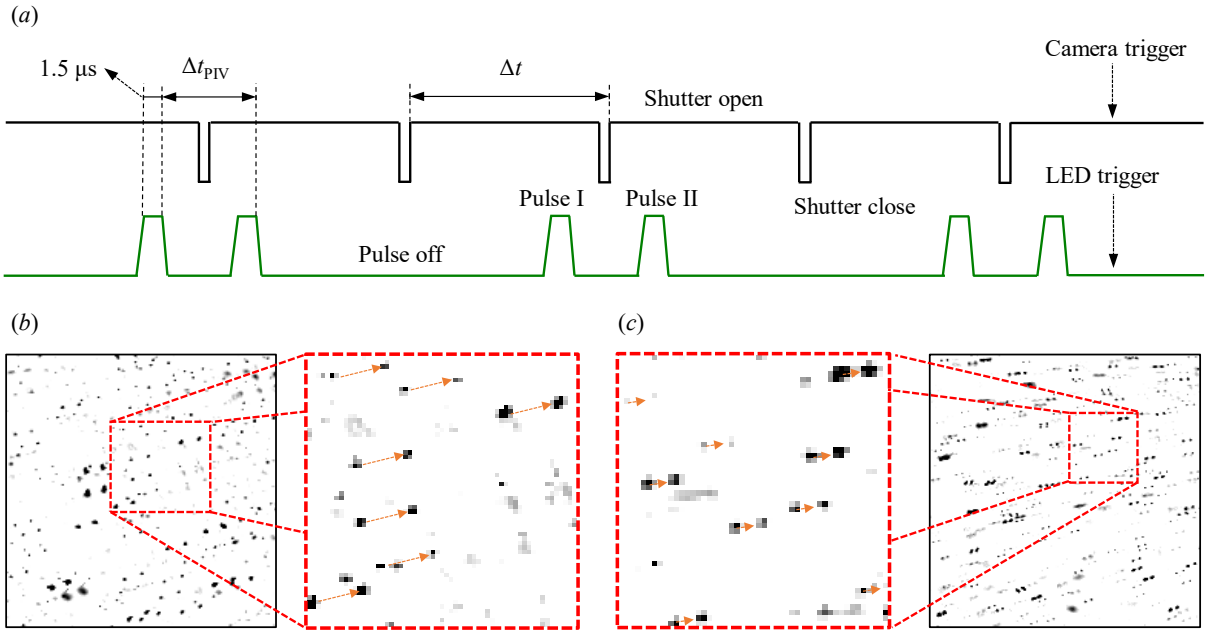

Figure 3-12 (*a*) Schematic representation of a camera and an illumination trigger signals in frame-straddling recording mode. The widths of the light pulses were kept at 1.5 µs to freeze the motion of the moving particles. Here, Δt_{PIV} and $2\Delta t$ are the time interval between two PIV frames and PIV frame pairs. The camera's recording frame rate was $(\Delta t)^{-1}$. Sample snapshots of a seeded flow field, with both illumination pulses applied on a similar frame (single-frame, double exposure recording mode), with (*b*) Δt_{PIV} = 10 µs and (*c*) Δt_{PIV} = 5 µs. In each of (*b*) and (*c*), a zoomed-in view is also displayed beside the main image, where orange arrows illustrate the displacements of sample particles during Δt_{PIV}.

3.5.2 Optical properties

For turbulent flow measurements, the liquid flow was seeded with 10 µm sphere polystyrene particles (Dynoseeds TS10, Microbeads AS). A zoom lens (12X, 1-50486; Navitar Inc.) with an extension adapter (1X; 1-6015, Navitar) was used to obtain a magnification factor of $M \approx 3.3$. These optical settings resulted in focused particle image sizes of 2-4 pixels, which is recommended for PIV (Raffel et al., 2018). The lens system's numerical aperture, N_A, and F-number, $f_\#$, were $N_A = 0.055$ and $f_\# = 8.25$, and the working distance was 86 mm. The introduction of these parameters into the theoretical formulations developed by Olsen and Adrian (2000) and Kähler et al. (2012), given in Appendix C, results in a particle image size of $D_p = 2.83$ pixels. The geometrical particle image size was calculated as $D_{geo} = 1.65$ pixels, and the particle image size generated by the diffraction of light was $D_{diff} = 2.30$ pixels. This calculated D is in excellent

agreement with the experimentally obtained particle image sizes. Equation (3-1) was used to calculate the depth-of-field of the optical system as $\delta z = 263.32$ µm, which covers only 0.44 % of the test section's width. i.e., $(\delta z / w) \times 100\ \% = 0.44\ \%$. It is also important to mention that the system's depth of focus was (Adrian and Westerweel, 2011): $(M\delta z) \approx 870$ µm, covering ≈ 1.45 % of the test section's width.

A micro-target plate (MP 50 × 12 µm; LaVision GmbH) was used to calibrate the images. Details of determining the mid-span position of the channel are discussed in Section 3.4.2. An average of 1000 images of ≈ 700 MP 200 target dots (see Table 3-4) was used in a third-order polynomial fit model to map the images to the real-world coordinates. The fit's root-mean-square (r.m.s.) was less than 0.15 pixels for all cases. Commercial software (DaVis V8.4; LaVision GmbH) was used for image calibration, correction, de-warping and mapping.

Figure 3-13 illustrates that the turbulent flow field was interrogated in three FOVs at the flat (top) surface. These flow regions were selected to cover conditions of zero, favorable, and adverse pressure gradients for each flow condition. The FOVs were 608 pixels × 896 pixels ($L_x \times L_y$), equivalent to 3.6 mm × 5.3 mm. In this study, $M = 3.4$ and $\varsigma = 5.87$ µm pixel^{-1}. Table 3-6 lists the optical properties of the imaging system used for the velocimetry of the turbulent flow field.

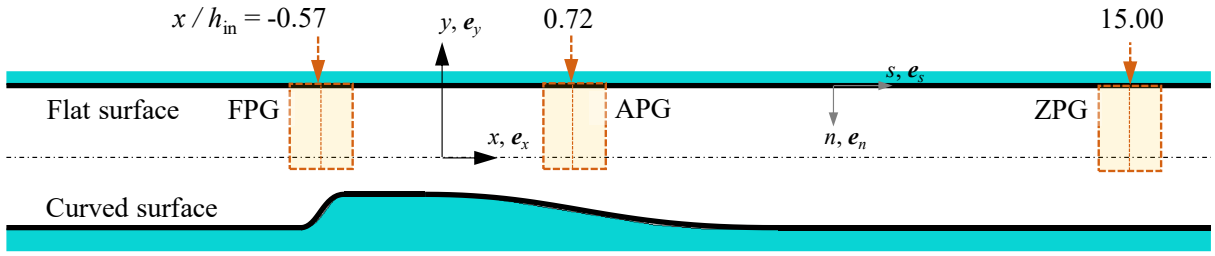

Figure 3-13 Schematic representation of the FOVs, where the turbulent flow was interrogated in the TG channel. ZPG, FPG, and APG stand for the zero, favorable, and adverse pressure gradients.

Table 3-6 Main optical properties of the imaging system used for velocimetry of the turbulent flow.

Δt_{PIV} (µs)	Δt (µs)	Δt_{exp} (µs)	$\|e\|$ (µm)	n_{tot}	N_A	$f\#$	ς (µm pixels^{-1})	M	D_p (pixels)	δz (µm)	L_x (mm)	L_y (mm)
40-60	1000	1.5	20	0.89	0.055	8.05	5.87	3.4	2.86	250	3.6	5.3

3.5.3 Validation of the primary PIV assumptions

One of the primary assumptions in PIV is that the seeding particles follow the flow trajectory (Raffel et al., 2018). The particle's inertia and settling in the flow should be inconsequential for this assumption to hold, which implies that the Stokes (St_k) and Froude (Fr) numbers be of infinitesimal orders, i.e., $St_k \ll 1$ and $Fr \ll 1$ (Raffel et al., 2018). St_k is defined as:

$$\mathrm{St_k} = t_\mathrm{p}/t_\mathrm{v}, \tag{3-2}$$

where, t_p is the particle's response time and is defined as:

$$t_\mathrm{p} = \rho_\mathrm{p} d_\mathrm{p}^2/18\mu_\mathrm{w}, \tag{3-3}$$

where d_p and ρ_p are the particle's mean diameter and density. The fluid's wall shear viscosity is denoted by μ_w and is a function of the wall shear rate $\dot{\gamma}_\mathrm{w}$ (see Chapter 4). The viscous time scale, $t_\mathrm{v} = \nu_\mathrm{w}/u_\tau^2$ (see Section 2.2.2), represents the characteristic fluid response time. Fr is defined as

$$\mathrm{Fr} = u_\mathrm{p}/u_\tau, \tag{3-4}$$

where the particle's settling velocity u_p is defined as

$$u_\mathrm{p} = g\left(\rho_\mathrm{p} - \rho\right)d_\mathrm{p}^2/18\mu_\mathrm{w}. \tag{3-5}$$

The utilized seeding particles had a d_p = 10 µm and ρ_p = 1200 kg m^{-3}. The measured wall shear stresses on the TG channel's midspan plane *xz* vary in the range of 2 Pa < τ_w < 10 Pa. Also, via rheology measurements discussed in Chapter 4, the shear viscosities of the solutions were obtained as a function of $\dot{\gamma}_\mathrm{w}$. The measured density of the solutions and the pure water (see Section 3.3) show that the fluid's density was constant in all experiments, i.e., ρ = 1 000 ± 1.25 kg m^{-3}. With this information, the ranges of the dynamic characteristics of the seeding particles used in this study were calculated and are listed in Table 3-7 for the pure water and different polyacrylamide (PAM) solutions. For the tested solutions and flow conditions, $\mathrm{St_k} \sim \mathcal{O}(10^{-2})$ and $\mathrm{Fr} \sim \mathcal{O}(10^{-5})$, proving that the seeding particles follow the flow and their inertia and settling in the flow are insignificant under the current test conditions.

Table 3-7 Range of dynamic characteristics of the seeding particles under the tested flow conditions with 2 Pa < τ_w < 10 Pa.

C_s (p.p.m.)	μ_w (mPa.s)	t_p (µs)	λ_v (µm)	t_f (µs)	u_p (µm s^{-1})	$\mathrm{St_k} \times 10^2$	$\mathrm{Fr} \times 10^5$
Pure water	0.91	7.3	9.1-20.3	91-455	12.0	1.61-8.05	11.98-26.78
100	1.11	6.0	11.1-24.8	111-555	9.8	1.08-5.41	9.82-21.96
200	8.01-1.40	0.8-4.8	179.1-13.9	139-4005	1.4-7.9	0.02-3.46	1.36-17.56
400	8.40-1.53	0.8-4.4	187.7-15.3	153-4198	1.3-7.1	0.02-2.87	1.30-15.98

3.5.4 Detection of the wall position

Determination of the normal wall position n_w in the PIV images is crucial in estimating the turbulent parameters. As the first step in determining n_w in each data set, the PIV images were averaged over 11 000 frame pairs and then were inverted. A sample mean image, normalized by its maximum value, is shown in Figure 3-14(*a*) for a ZPG FOV on a flat channel wall. The normalized mean intensity values were averaged in the streamwise direction *x*, far from the image

boundaries, and the resultant $\overline{\langle I \rangle}$ profile is shown in Figure 3-14(*b*). The position of $\overline{\langle I \rangle}_{max}$ was chosen to be y_w. If the position of $\overline{\langle I \rangle}_{max}$ was not unique, n_w was calculated as the average of $\overline{\langle I \rangle}_{max}$ positions. This process is highlighted by light blue shaded rectangles in Figure 3-14(*b*). The standard deviation of n_w positions in the *s*-direction was defined as the error of the measured wall position. For the ZPG FOV shown in Figure 3-14(*a*), $n_w = 40 \pm 5$ µm. A similar procedure was applied to other FOVs to determine n_w position in the image frames.

Also, a line was fitted to the velocity data points in the viscous sublayer in each flow scenario, and the wall position was obtained from the normal intercept of the fitted equation. The relative difference between the estimated wall positions from the explained methods was ± 2 % from each other and hence was assumed insignificant.

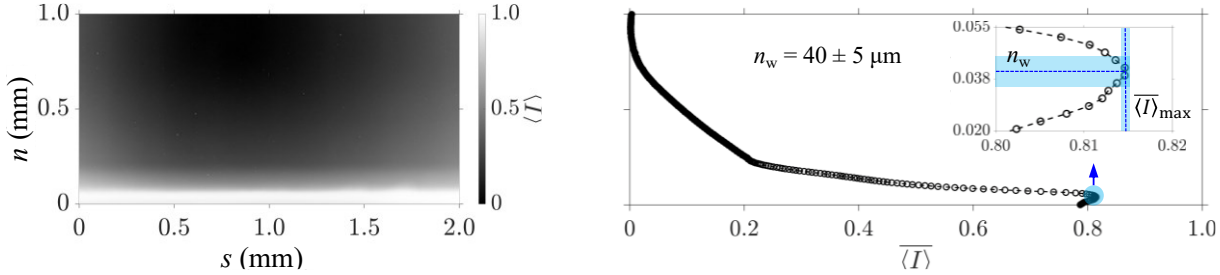

Figure 3-14 (*a*) A sample mean PIV image of the ZPG FOV, inverted, and normalized by its maximum value. The white region shows the channel wall. (*b*) Variation of the normalized intensity profile, averaged in the *s*-direction, with the wall-normal position *y*. The inserted figure shows a close-up view of the intensity variation adjacent to the mean wall position n_w. The light blue shaded rectangles highlight the regions of averaging.

3.5.5 Calculation of the velocity fields

A set of 11 000 image pairs were recorded for each flow scenario using the optical setup explained in Section 3.4. The pairs of PIV frames were inverted based on the local maximum intensity of the image. A sliding background window, based on a Gaussian profile, with a length of 8 pixels was subtracted from the intensity of each pixel. Finally, the particles' intensities were normalized by subtracting the average intensity of each image from it and dividing it by the standard deviation of the image intensity. The processed images were cross-correlated to calculate the instantaneous velocity fields $\boldsymbol{U}(x, y, t)$ on the midplane. Initially, circular 48 × 48 pixels windows, with 50 % overlap, interrogated the flow fields. This step was followed by three passes of interrogation by ellipsoidal 32 × 32 pixels, with an overlap of 75 %. The ellipsoidal windows had an aspect ratio of 2:1, with their longer axes parallel to the lower boundary of the images. After each pass, the resultant velocity field was scanned, and any possible outliers were detected

and removed in a filter region of 9 × 9 pixels using the universal outlier detection technique developed by Westerweel and Scarano (2005). The results show that the total number of the removed outlier vectors was less than 1 % of the total calculated velocity vectors in each PIV velocity field. Commercial software (Davis 8.4.0, LaVision GmbH) was utilized for the velocity calculations. The resultant velocity fields comprised 77 × 113 ($n_x \times n_y$) velocity vectors.

3.6. Conclusion

This Chapter discussed the details of the design of the wall geometries for the cavitating and developing turbulent flows and the developed flow facility to study these phenomena. The optical system utilized for high-speed imaging of instantaneous cavitation structures and velocimetry of the turbulent flow fields subjected to pressure gradient was discussed in detail. The calibration process based on the concept of apparent depth was discussed, and its validity for this study was examined. Calculating the Stokes and Froude numbers for the range of the flow conditions tested and the seeding particles utilized in velocimetry showed that the inertia and settling of the seeding particles were inconsequential. Therefore, the assumption that seeding particles follow the flow is valid for the flow conditions examined in this study. The estimation of the wall position based on the maximum gradient of the mean image intensity near the wall was explained, and it was concluded that the estimated position of the wall using this approach was within the ± 2 % of the wall position determined by fitting a line to the mean wall-parallel velocity profile. Details of the PIV settings utilized to obtain the velocity fields were also described.

4. Flow rheology

The mass of the polyacrylamide (PAM) required to prepare the desired solution concentration was measured using a digital scale (Explorer; Ohaus Corporation) with a 0.1 mg resolution. The additives were gradually added to a 0.5 lit glass beaker filled with water and mixed using a stirrer (1103; Jenway) at a moderate rotational speed. The stirring bar size was selected to cover most of the container's bottom surface to mitigate the adhesion of polymers to the container walls. Each master solution was stirred for 2 hours, and the resultant uniform, highly concentrated solution was then gradually added to the circulating water in the flow loop. Before any tests, the solution was allowed to circulate at a low pump speed for 1 hour, bypassing the test-section line. Samples were obtained from the flow line using a sampling valve installed close to the channel's inlet (see Figure 3-3). Later, in cavitation measurements, an extreme condition was applied to the solution, and another sample was taken to explore the effect of cavitation on the rheology of the solution.

4.1. Shear-thinning behavior of PAM solutions

A short time after taking the samples, the rheological characteristics of the solutions were determined using a rotational rheometer (Kinexus lab+; NETZSCH-Gerätebau GmbH) with a double gap geometry (DG25). The bob's internal and external diameters were 23 mm and 25 mm, respectively, with an interior height of 57.5 mm. Cup had a diameter of 26.25 mm, and an insert diameter of 22 mm. Three independent measurements were performed for each sample at 20 °C with the shear rate controlled during the tests. The average measurement values, with corresponding standard deviations, are reported here.

Figure 4-1(a) shows the variation of the solution viscosities versus the strain rate. The results indicate that the selected PAM solutions in water have a shear-thinning behavior. Such a fluid behaves as a Newtonian fluid at very low, $\mu(\dot{\gamma} \ll 1) \rightarrow \mu_0$, and very high, $\mu(\dot{\gamma} \gg 1) \rightarrow \mu_\infty$, shear rates (Bird et al., 1987). Shear-thinning fluids follow a power-law relation for intermediate $\dot{\gamma}$ values, i.e., $\mu = K\dot{\gamma}^n$ for $1 < \dot{\gamma} < \infty$ (Bird et al., 1987). Here, K and n are correlation constants. The standard deviations of the viscosity measurements were more than 10 % for $\dot{\gamma} < 10$ s^{-1} and $\dot{\gamma} > 500$ s^{-1} and were discarded. This discrepancy is caused by surface tension that produces artifact shear-thickening at low shear rates and the development of unstable secondary flows for higher shears, where viscosity shows a sudden increase (Morrison, 1998). The Carreau-Yasuda (CY) model (Yasuda et al., 1981) was fitted to the measurement data to determine the solution viscosities

at higher strain rates, and the resultant fitted profiles are plotted in Figure 4-1(*a*) as dashed lines. The CY model is formulated as:

$$\mu(\dot{\gamma}) = \mu_\infty + (\mu_0 - \mu_\infty)[1 + (\lambda_t \dot{\gamma})^a]^{(n-1)/a}, \tag{4-1}$$

where μ_0 and μ_∞ are the zero and infinite shear viscosities. Here, λ_t is a time constant, n is the power-law index, and a is a constant parameter suggested by Yasuda et al. (1981).

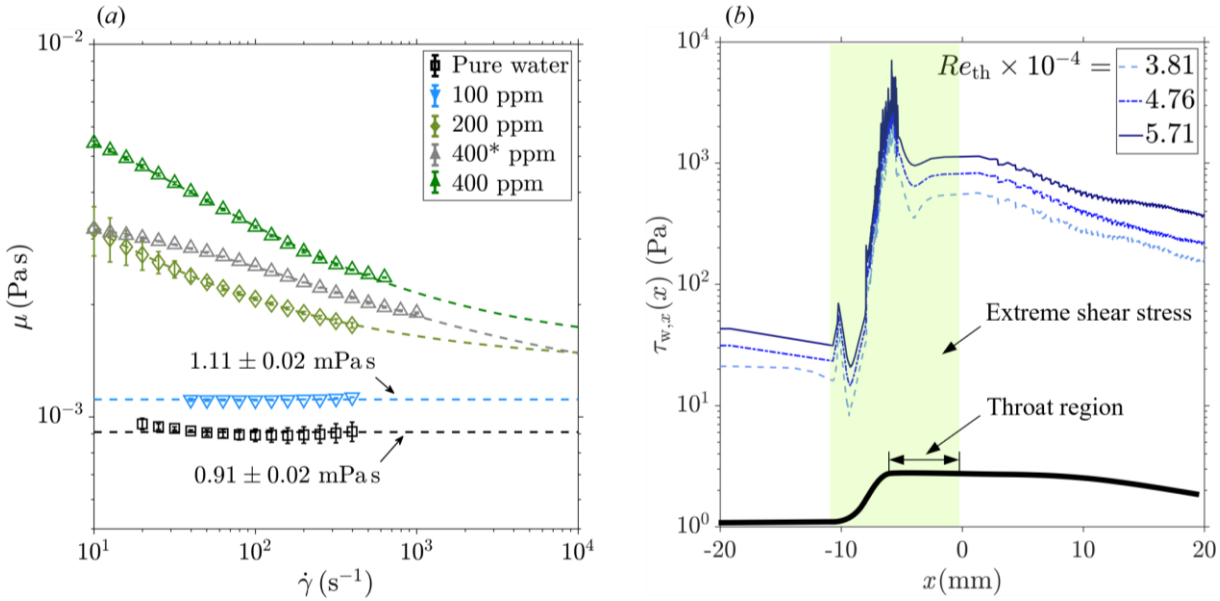

Figure 4-1 (*a*) Variation of the dynamic viscosity of the pure water and PAM solutions versus the shear rate. A dashed line depicts the fitted CY model for each solution with a concentration of more than 100 p.p.m. For pure water and the 100 p.p.m. solution, dashed lines show the average values in the span of the measured shear rates. The error bars indicate the standard deviations of three independent measurements. Here, '*' signifies that the solution has experienced the cavitation process. (*b*) Changes of the numerically determined (see Appendix B) wall shear stress in the streamwise direction $\tau_{w,x}$ (x) on the midspan of the CG channel in the pure water flow, plotted for three different Re_{th}. The inserted thick black curve illustrates the profile of the lower nozzle wall. A pale green rectangle highlights the region of extreme shear stress.

As discussed by Syed Mustapha et al. (1999) and later by Escudier et al. (2001), the Pearson correlation coefficient r should be more than 0.9975 for a rheological model to be valid and reliable. Here, r is (Escudier et al., 2001):

$$r = \frac{N\sum_{i=1}^{N}\mu_{\mathrm{M},i}\mu_{\mathrm{CY},i} - \sum_{i=1}^{N}\mu_{\mathrm{M},i}\sum_{i=1}^{N}\mu_{\mathrm{CY},i}}{\sqrt{\left[N\sum_{i=1}^{N}\mu_{\mathrm{M},i}^2 - \left(\sum_{i=1}^{N}\mu_{\mathrm{M},i}\right)^2\right]\left[N\sum_{i=1}^{N}\mu_{\mathrm{CY},i}^2 - \left(\sum_{i=1}^{N}\mu_{\mathrm{CY},i}\right)^2\right]}}, \tag{4-2}$$

where N denotes the number of viscosity measurements, and the subscript 'M' means 'measured.' Also, the coefficient of determination R_{cd} was calculated for each solution to evaluate the model's accuracy. Table 4-1 lists the obtained coefficients of the CY model for each PAM solution, with

their associated r and R_{cd} coefficients. For all cases, $r > 0.9992$ and $R_{cd} > 0.9985$; hence, the obtained correlations are valid for estimating the viscosity values at higher strain rates.

Table 4-1 CY model constants for the tested PAM solutions, with their corresponding r and R_{cd} coefficients. Here, '*' signifies that the solution has experienced the cavitation process.

C_s (p.p.m.)	μ_0 (mPa.s)	μ_∞ (mPa.s)	λ_t (s)	n	a	r	R_{cd}
200	8.010	1.388	2.287	0.58	3.523	1.0000	0.9999
400*	3.616	1.137	0.033	0.66	0.693	0.9993	0.9983
400	8.395	1.525	0.164	0.53	0.732	0.9993	0.9987

As Figure 4-1(*a*) illustrates, the viscosity of the 400 p.p.m. solution decreases for the entire range of the tested shear strain rates after experiencing violent cavitation conditions. While still showing shear thinning behavior at relatively lower shear strain rates, the results suggest that the cavitation process weakens this behavior. As given in Table 4-1, the solution has an infinite viscosity of ≈ 18 % lower than the 200 p.p.m. solution that was not undergone the cavitation process. This result confirms that the polymer used in this work degrades mechanically due to the molecular scission at relatively large shear strain rates.

4.2. Determination of wall viscosity in cavitation tests

In this study, the mass flow rate was chosen as the independent parameter and was varied for each fluid to produce a range of flow conditions. Hence, in cavitation tests, the throat Reynolds number Re_{th} was matched between different solution flows to investigate the effect of PAM additives on the cavitation process. The Reynolds number based on the hydraulic diameter, $D_{h,th}$, and averaged velocity of the throat, $\langle\overline{\overline{U}}_{th}\rangle$, is defined as $Re_{th} = \langle\rho_L\rangle\langle\overline{\overline{U}}_{th}\rangle D_{h,th}/\mu_w(C_s)$, where $\langle\rho_L\rangle$ was determined using temporal measurements of the Coriolis flowmeter (see Section 3.3). Here, μ_w and C_s are the wall shear viscosity and polymer concentration, discussed in Section 4.1.

As discussed, the tested PAM solutions were shear-thinning, and their local viscosity in the flow domain was a function of the strain rate they experienced and the relaxation time of the solution. Therefore, to determine Re_{th} for PAM solutions, it is crucial to estimate the wall viscosity at the shear rate experienced by the throat wall, i.e., $\mu_{w,th}(\dot{\gamma}_{w,th})$. It was not feasible to resolve the viscous sublayer at the throat using the optical settings described in Section 3.5.2. Therefore, $\dot{\gamma}_{w,th}$ was calculated using: (1) the Prandtl-Karman (PK) friction factor correlation for turbulent water flow in smooth tubes (White, 2011) and (2) a 3D numerical simulation of the turbulent water flow. Details of the numerical setup are given in Appendix B.

The PK friction factor at the throat is defined as:

$$c_f^{-1/2} = 4\log\left(Re_{th}\, c_f^{1/2}\right) - 0.4, \tag{4-3}$$

where $c_f = 2\tau_{w,th}/\langle\rho_L\rangle\langle\overline{\overline{U}}_{th}\rangle^2$ and $\tau_{w,th} = \mu_{w,th}\dot{\gamma}_{w,th}$. It is important to note that $\dot{\gamma}_{w,th}$ might change in a viscoelastic flow (Naseri et al., 2018a), and more accurate simulations based on a non-Newtonian flow model are required to elucidate this conjecture. The effect of this difference is negligible on Re_{th}. As an example, in the 400 p.p.m. solution, $\mu_{w,th}$ (5.0×10^4 s^{-1}) = 1.627 mPa.s and $\mu_{w,th}$ (2.5×10^4 s^{-1}) = 1.667 mPa.s. For this solution, a 50 % reduction in the shear strain rate at a constant flow rate increases the wall shear viscosity and decreases Re_{th} by only 2.5 % in the highest PAM concentration tested. Hence, numerically obtained values of $\dot{\gamma}_{w,th}$ in water flow were used to approximate Re_{th} of PAM solutions.

Figure 4-1(*b*) depicts the variation of the wall shear stress $\tau_{w,x}(x)$ of pure water flow in the streamwise direction x at the midspan of the channel, obtained numerically for three different inlet flow rates. Water flow experiences extreme shear stress in the throat region, which increases for

higher flow rates. Numerical wall shear stress values were averaged over the bottom flat plate of the throat region (see Appendix B) and were used to determine the average shear rate at the throat wall $\left(\dot{\gamma}_{w,th}\right)_{CFD}$. Table 4-2 lists the calculated average shear stresses and their associated shear strain rates for three different Re_{th} of the pure water flow. The estimated values based on the PK friction factor are in the range of ± 10 % of their numerical counterpart. Nevertheless, only the numerical values are used for further calculations.

Table 4-2 Calculated average wall shear stresses for three different throat velocities in pure water flow using the PK friction factor and 3D numerical simulations. Here, ρ_L = 1000 kg m^{-3} and μ_w = 0.91 mPa s, the measured mean water density and viscosity were used in the calculations.

$\overline{\overline{U}}_{th}$ (m/s)	$Re_{th} \times 10^{-4}$	$\left(\tau_{w,th}\right)_{PK}$ (Pa)	$\left(\dot{\gamma}_{w,th}\right)_{PK}$ (s^{-1})	$\left(\tau_{w,th}\right)_{CFD}$ (Pa)	$\left(\dot{\gamma}_{w,th}\right)_{CFD}$ (s^{-1})
13.34	3.8	494	543 000	448	492 300
16.67	4.8	734	807 000	772	848 700
20.01	5.7	1016	1 116 000	1 076	1 183 000

A numerical parametric study was conducted with a similar numerical setup explained in Appendix B for five different inlet conditions in $2 \times 10^4 < Re_{th} < 6 \times 10^4$. The results were used to estimate the wall shear rate and wall viscosity at the throat. Table 4-3 lists the determined viscosities of different solutions at three throat velocities and equal $\dot{\gamma}_{w,th}$, with their associated Re_{th}. At relatively high shear rates experienced by the cavitating flow examined in this work, the largest $\mu_{w,th}$ is ≈ 1.56 mPa s, which is 1.7 × larger than the pure water viscosity and belongs to the 400 p.p.m. solution at $\overline{\overline{U}}_{th}$ = 13.34 m s^{-1}. All the reported Reynolds numbers in this study are calculated based on the mean wall viscosity.

Table 4-3 Numerically estimated mean viscosities at the throat wall and their corresponding Re_{th} for different flow rates of the pure water flow simulations. Here, '*' signifies that the solution has experienced the cavitation process.

C_s (p.p.m.)	200		400*		400	
$\overline{\overline{U}}_{th}$ (m s^{-1})	$Re_{th} \times 10^{-4}$	$\mu_{w,th}$ (mPa s)	$Re_{th} \times 10^{-4}$	$\mu_{w,th}$ (mPa s)	$Re_{th} \times 10^{-4}$	$\mu_{w,th}$ (mPa s)
13.34	2.7	1.41	3.1	1.23	2.4	1.56
16.67	3.4	1.40	3.9	1.21	3.1	1.55
20.01	4.1	1.40	4.8	1.20	3.7	1.55

In turbulent flow tests, the inlet Reynolds number Re_{in} was varied in each flow scenario. The corresponding wall shear viscosity at each examined position was obtained using the calculated wall shear strain rate from the mean wall-normal gradient of the PIV velocity data.

4.3. Viscoelasticity of PAM solutions

A series of oscillation frequency sweep tests using PAM solutions with concentrations of 50 p.p.m. to 400 p.p.m. were conducted, and the resultant elastic (storage) modulus $G'(\omega)$ and viscous (loss) modulus $G''(\omega)$ are plotted in Figure 4-2(a,b) as functions of angular frequency ω. The strain was kept constant at 1 % in all tests. As shown in Figure 4-2(a), the elastic moduli of all tested solutions show a plateau for the range of $0.1 \lessapprox \omega \lessapprox 10$ rad s^{-1} and start to increase as ω increases. An increase in the polymer concentration increases the plateau G'.

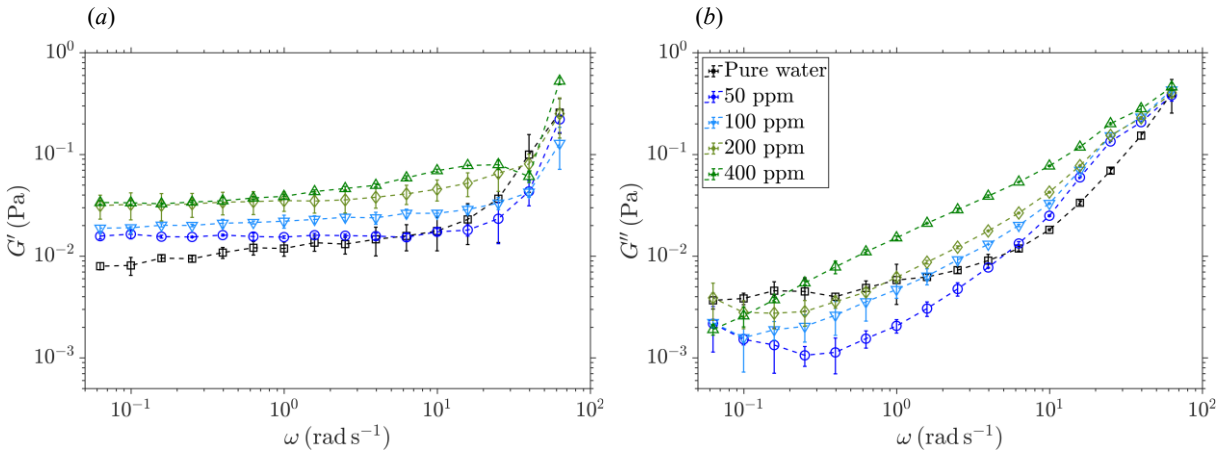

Figure 4-2 Changes of the (a) elastic (storage) modulus G' and (b) viscous (loss) modulus G'' of different PAM solutions with angular frequency ω. The strain rate was kept constant at 1 %, and the temperature was at 20 °C in all tests. The plotted profiles are the average of three independent measurements, and the error bars show the standard deviation of the measurements at each frequency.

As Figure 4-2(b) illustrates, the viscous moduli change almost linearly for $\omega \gtrapprox 10$ rad s^{-1}, which highlights the Newtonian behavior of the fluid in this frequency range, i.e., $G'' = \mu_0\, \omega$, where the viscosity μ_0 shows an increase as the concentration increases. Oscillation tests were also conducted for higher frequencies to obtain the cross-over points of $G'(\omega)$ and $G''(\omega)$ profiles. The cross-over point correlates with the relaxation time t_R of the solution. For 200 p.p.m. and 400 p.p.m. solutions, $t_R \approx 14.5$ ms and $t_R \approx 12.5$ ms were obtained as the average of three independent tests. Due to inertial effects, no consistent cross-over points were obtained for lower concentrations at higher frequencies.

4.4. Drag reduction

In the straight tube section (see Figure 3-3), characteristic velocity was obtained from the time-averaged flow rate $\langle \dot{V} \rangle$ as $\langle \bar{\bar{U}} \rangle_{\mathrm{tu}} = \langle \dot{V} \rangle / A_{\mathrm{tu}}$, where A_{tu} denotes the cross-sectional area. Reynolds number of the straight tube is defined as $Re_{\mathrm{tu}} = \langle \rho_{\mathrm{L}} \rangle \langle \bar{\bar{U}}_{\mathrm{tu}} \rangle D_{\mathrm{tu}} / \mu_{\mathrm{w}}(C_{\mathrm{s}})$. Dimensionless pressure gradient or the Fanning friction factor in a straight tube, such as the one shown in Figure 3-3, is defined as $c_{\mathrm{f}} = 2\tau_{\mathrm{w}} / \langle \rho_{\mathrm{L}} \rangle \langle \bar{\bar{U}}_{\mathrm{tu}} \rangle^2$, where the wall mean shear stress τ_{w} is a function of the time-averaged measured pressure drop $\langle \Delta P_{\mathrm{tu}} \rangle$ over length $L_{\mathrm{tu}} = 0.92$ m of the tube with $D_{\mathrm{tu}} = 19$ mm. Therefore, $\tau_{\mathrm{w}} = D_{\mathrm{tu}} \langle \Delta P_{\mathrm{tu}} \rangle / 4L_{\mathrm{tu}}$. The Fanning friction factor is defined as:

$$c_{\mathrm{f}} = \frac{D_{\mathrm{tu}}}{2\, L_{\mathrm{tu}}} \frac{\langle \Delta P_{\mathrm{tu}} \rangle}{\langle \rho_{\mathrm{L}} \rangle \langle \bar{\bar{U}}_{\mathrm{tu}} \rangle^2}. \tag{4-4}$$

DR is the relative reduction in the pressure drop of an additive solution over a known section of the flow path with a constant cross-sectional area compared to the pressure drop of the pure solvent flow at a similar flow rate and wall viscosity (Lumley, 1973; Virk, 1975). Therefore, the percentage of *DR* can be defined as:

$$DR\% = 1 - \frac{c_{\mathrm{f,s}}}{c_{\mathrm{f,0}}}, \tag{4-5}$$

where subscripts 's' and '0' stand for the additive solution and pure solvent, respectively. Here, c_f was calculated from the measured pressure drops in the turbulent flow of pure water and four different concentrations of PAM solutions in the range of $2\times10^4 \leq Re_{\mathrm{tu}} \leq 3\times10^4$. Each test was repeated three times with a new solution, and the mean values are plotted in Figure 4-3. The maximum standard deviation of the calculated friction factors was 7% of its mean value.

Virk's asymptote correlation for the maximum drag reduction (MDR) in a turbulent pipe flow of dilute polymer solutions over a smooth tube is (Virk et al., 1970):

$$c_{\mathrm{f}}^{-1/2} = 19 \log\left(Re_{\mathrm{tu}}\, c_{\mathrm{f}}^{1/2}\right) - 32.4, \tag{4-6}$$

which is only valid for $4 \times10^3 < Re_D < 40 \times 10^3$. Moderate DR regimes fall between the Newtonian PK friction factor, given in equation (4-3), and Virk's asymptote. The resultant c_f (Re_{tu}) profile of pure water agrees with the Prandtl-Karman equation (White, 2011), shown with a dashed line in Figure 4-3. Virk's asymptote for maximum DR (MDR) (Virk et al., 1970) in dilute polymer solutions in turbulent pipe flow is indicated by a thick black line in Figure 4-3. MDR was not obtained for any of the tested solution concentrations. The 50 p.p.m. solution shows a higher *DR*

(≈ 10 %-20 % more) than the 100 p.p.m. and 200 p.p.m. solutions. Increasing the concentration to 400 p.p.m. did not enhance pressure reduction, and a *DR* % comparable to the 50 p.p.m. solution was obtained for the tested flow rates. All examined concentrations resulted in a similar *DR* ≈ 50 % at the maximum tested flow rate ($Re_{tu} = 3\times10^4$).

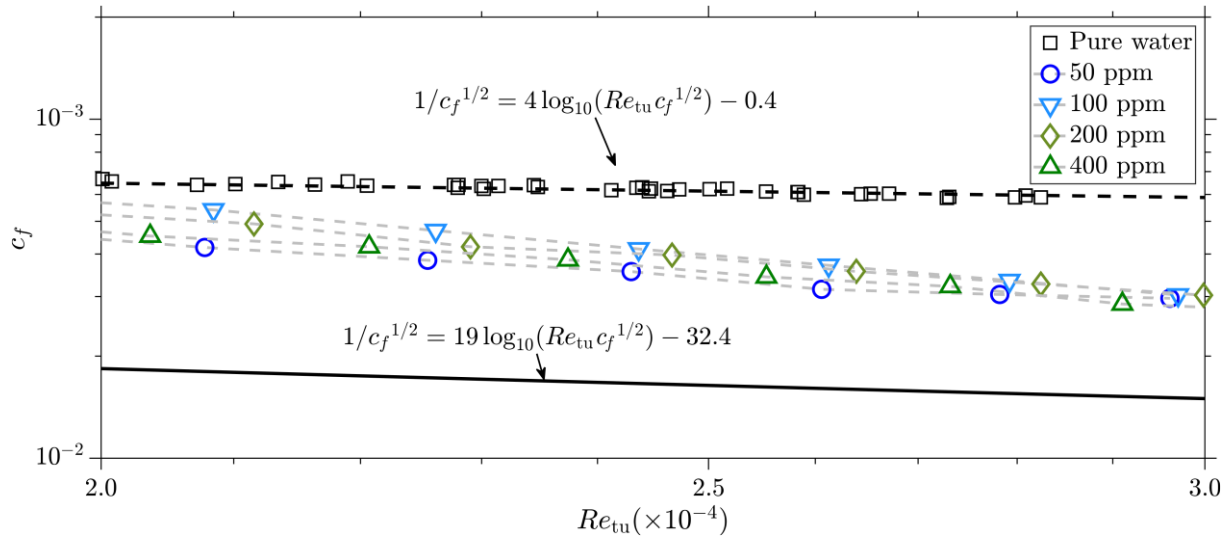

Figure 4-3 Variation of the Fanning friction factor, c_f, as a function of the straight tube's Reynolds number, Re_{tu}, in PAM solutions of various concentrations. The thick dashed line indicates the Prandtl-Karman friction factor (White, 2011) for turbulent water flow in smooth tubes. The solid black line shows Virk's MDR asymptote (Virk et al., 1970) for the turbulent flow of polymer solutions in smooth tubes. Each point on the plot denotes the mean of three independent measurements, with a maximum standard deviation of 7 % of the mean value in all tests.

The percentage ratio of instantaneous drag reduction, $DR(t)$, to the initial steady drag reduction, DR_0, i.e., $(DR(t) / DR_0) \times 100$ %, was probed for 500 s at $Re_{tu} = 3.0 \times 10^4$ to investigate the degradation level of the solutions. The results are plotted in Figure 4-4.

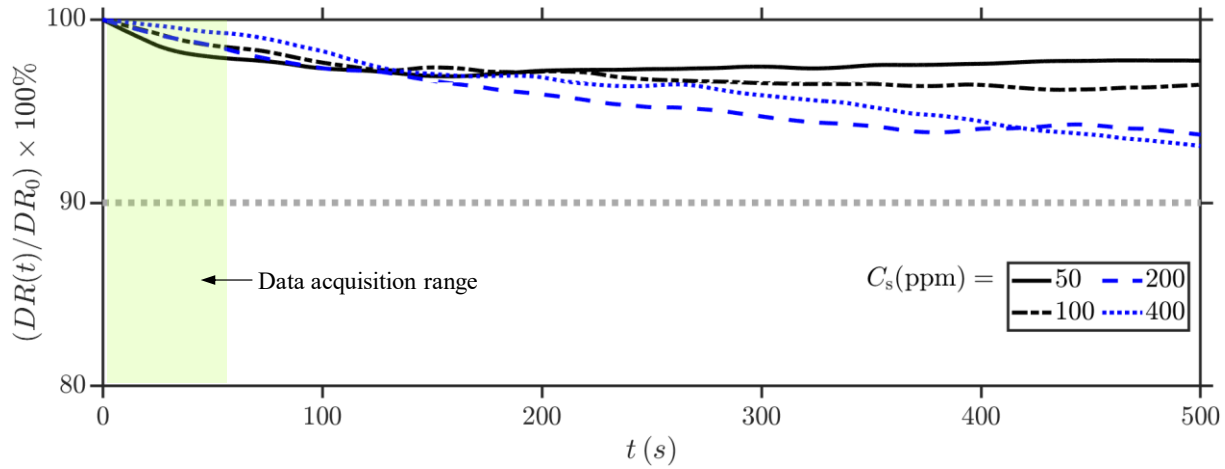

Figure 4-4 Degradation of the PAM solutions in time, defined as the percentage ratio of the instantaneous drag reduction $DR(t)$ to the steady drag reduction of the flow system DR_0. Tests were conducted at $Re_{th} = 3.0 \times 10^4$.

After ≈ 8 minutes, $DR(t)$ drops only by ≈ 5 % at maximum relative to its corresponding DR_0. The data acquisition for each test took nearly 10 s, and each solution was used only for four to five tests. The solution was renewed if further tests were required. A pale green rectangle highlights the maximum data acquisition period with each fresh solution batch (≈ 50 s). The rheology measurements of the samples obtained during the velocimetry tests revealed that due to degradation, the zero and infinite shear viscosities of the 400 p.p.m. solutions, listed in Table 4-1, decreased by ≈ 20 % after 20-30 minutes. This change was considered in calculating the wall viscosities in Chapter 7.

4.5. Conclusion

The results of rheology measurements of the pure water and different semi-dilute PAM solutions of concentrations from 50 p.p.m. to 400 p.p.m. were discussed in this Chapter. The steady shear viscosity measurements demonstrated that the PAM solutions with concentrations higher than 100 p.p.m. have shear-thinning non-Newtonian behavior, where their dynamic viscosity decreases as the shear strain rate increases. The solutions with concentrations lower than 100 p.p.m. illustrated almost constant viscosities and were considered to behave as Newtonian flows. The trends of viscosity changes with the shear strain rate were found to follow the CY rheological model. Therefore, the fitted CY models were used to estimate the wall viscosities at different strain rates and solution concentrations. A parametric numerical simulation, explained in Appendix B, was used as an ancillary tool to approximate the mean shear strain rates at the throat and the flow under cavitation conditions.

A series of oscillation frequency sweep tests were conducted to obtain the elastic modulus G' and viscous modulus G'' for different PAM solutions as a function of the angular frequency ω. Calculating the cross-over point in the 200 p.p.m. and 400 p.p.m. solutions, the relaxation times of these solutions were estimated to be $t_R \approx 14.5$ ms and $t_R \approx 12.5$ ms as the average of three independent tests. Due to inertial effects, no consistent cross-over points were obtained for lower concentrations at higher frequencies. Drag reductions in the PAM solutions were calculated based on the pressure drop changes over a length of $L_{tu} = 0.92$ m in the fully developed pipe flow, shown in Figure 3-3, for a $2\times10^4 \leq Re_{tu} \leq 3\times10^4$. In agreement with the previous studies, increasing the Re_{tu} at a constant solution concentration increased DR. The results showed an intermediate DR of 50 % in all solutions where MDR was not achieved under the defined flow conditions.

5. Hydrodynamic cavitation in semi-dilute polymer solution flows[1]

5.1. Introduction

Flow parameters such as pressure and velocity can show relatively high fluctuation levels in a turbulent flow regime. Under certain circumstances, instantaneous pressure at any point of a wall-bounded turbulent flow, $P(\boldsymbol{x}, t)$, can experience a drop well below the fluid's saturation pressure P_{sat} at a specified temperature T_L, i.e., the condition of $P(\boldsymbol{x}, t) \ll P_{sat}(T_L)$. As a result, a local phase change occurs, and micro-scale vapor (or cavitation) bubbles emerge in the bulk liquid flow. This phenomenon triggers the onset of the cavitation process and is commonly called the *cavitation inception* regime (Rood, 1991). An instant later, the local pressure may recover to a value higher than P_{sat}, which causes the cavitation bubbles to collapse in microseconds (Brennen, 2013). Simultaneous growth and collapse of the cavitation bubbles at different regions of the flow field are intrinsic characteristics of the cavitation phenomenon, and one cannot exist without the other. The higher the pressure fluctuations relative to P_{sat}, the more violent the spatial growth and collapse of the vapor bubbles, resulting in the agglomeration of tiny bubbles and the generation of large-scale cavitation clouds (Arndt, 2002).

The sudden collapse of microbubbles is followed by an extreme increase in local pressures up to 85 MPa and temperatures up to 6 400 °C at the bubble centroid (Fujikawa and Akamatsu, 1980). Extreme pressure gradients near the collapsing bubbles generate local liquid microjets with relatively high momentums. Zeng et al. (2020) investigated the dynamics of such jets in a thin liquid layer confined between two rigid walls and showed that these liquid jets could gain impact speeds up to 200 m s^{-1}. The collapse generates relatively high-momentum shockwaves, which mostly propagate upstream of the flow and modify the dynamics of the incoming liquid flow (Ganesh et al., 2016). The complex interaction of growing and collapsing bubble pockets with the bulk turbulent flow and the wall boundaries, accompanied by the propagating shockwaves, results in different cavitation regimes, which can be qualitatively grouped as inception, sheet, cloud, developing, and supercavitation regimes (Brennen, 2013).

---

[1] Parts of this Chapter were published in the Journal of Fluid Mechanics: [**Azadi, R.**, Nobes, D.S., 2022. Hydrodynamic cavitation reduction in semidilute turbulent polymer solution flows. *J. Fluid Mech.* 952, A29.], in a conference proceeding: [**Azadi, R.**, Nobes, D.S., 2022. Experimental investigation of a cavitating water flow with the addition of drag-reducing agents, in: 20th International Symposium on the Application of Laser and Imaging Techniques to Fluid Mechanics. Lisbon.].

An acoustic or ultrasound field (Curtiss et al., 2013; Murakami et al., 2021) applied to a flow, or sudden acceleration and deceleration of the flow can cause P ($\mathbf{x}$, t) to fluctuate around P_{sat} (T_L) and trigger the cavitation process. In some applications, conditions for cavitation to occur are intentionally created. For instance, micro-sized bubbles can be manipulated to carry antibiotics and cancer-treatment drugs to malignant tissues, where ultrasound fields are externally applied to collapse the bubbles and release the therapeutic drugs in vitro (Stride and Coussios, 2019; Versluis et al., 2020). The generated shockwaves and microjets locally penetrate the cancerous tissues and open a path for the drug molecules to dive into deeper levels of the tissues, which significantly enhances the efficacy of the drug delivery process (Stride et al., 2020).

The collapse of bubbles near solid walls generates relatively high shear stress regions and high moment re-entrant liquid jets adjacent to the fast deforming bubbles where the combined effect is utilized in removing dirt and cleaning surfaces (Chahine et al., 2016; Verhaagen and Fernández Rivas, 2016). Turner et al. (2019) explored the exfoliation of graphene layers using ultrasonication and showed that control and optimization of the acoustic cavitation results in higher rates of exfoliated graphene at shorter sonication periods. Cavitation is also advantageous in destroying microorganisms (Zupanc et al., 2019) and disinfecting water (Mane et al., 2020). Using a hydrodynamic cavitation process, where a low concentration of peppermint oil was added to the flow, Mane et al. (2020) showed that a disinfection rate of more than 99 % could be achieved in relatively short times.

In contrast to the scenarios where cavitation can be advantageous, cavitation can cause noise, vibration, erosion, and noticeable damage to equipment in most industrial applications. Dular et al. (2004) used three different hydrofoil configurations covered with copper foil to examine the impact of hydrodynamic cavitation on surface erosion. Using image processing, they detected and counted the number of pits produced on the copper surfaces that had undergone violent cavitation and correlated this to the cavitation structures they had visualized. In an experimental study on a converging-diverging venturi channel, Xu et al. (2020) showed that the noise level strongly depended on the outlet-to-inlet pressure ratio, $P_r = P_{out} / P_{in}$, and had a peak at $P_r \approx 0.9$.

Any alteration of the wall geometry, thermophysical properties of the fluid, or body forces being applied to the flow field that can avoid or delay the local pressure drop below its saturation pressure, can reduce cavitation intensity. In the past years, researchers used various passive and

active methods to control the inception or intensity of cavitation. Chatterjee and Arakeri (1997) generated synthetic cavitation at the throat of a converging-diverging venturi by injecting electrolysis bubbles at the channel's inlet to act as free-stream nuclei. They applied an acoustic pressure field upstream of the throat using a ring piezoelectric transducer and showed that cavitation was noticeably suppressed at the throat. In their experiments, the synthetic bubbles experienced sudden cavitation and collapsed as they passed the acoustic field and disintegrated into dissolved nuclei in the bulk liquid, mitigating the potential of cavitation inception at the throat.

Kawanami et al. (1997) investigated the feasibility of passively controlling the generation of cloud cavitation on a hydrofoil using small square obstacles attached to the hydrofoil surface. They used straight acrylic obstacles with square cross-sections and tested different configurations relative to the streamwise flow direction. Their results showed that when the obstacle covered the entire spanwise width of the hydrofoil and was positioned at ≈ 37 % of the chord length relative to the leading edge of the hydrofoil, peak pressure fluctuations were damped out by 40 %, and the noise level was reduced by 5-20 dB, indicating that cloud cavitation was suppressed. In a cloud cavitation regime with no obstacles, a continuous layer of re-entrant liquid flows upstream on the wall surface towards the throat, where it cuts off the growing sheet cavities and elevates the cloud cavitation process. Adding an obstacle at this position breaks the chain of events for the cloud cavitation to be maintained. The re-entrant flow stagnates at the obstacle and loses momentum, and only small-scale cavity structures are generated at the closure of the sheet cavities.

Kadivar et al. (2020a) used a series of cylindrical vortex generators (VG) installed with equal predefined distancing on the entire spanwise width of a benchmark hydrofoil CAV2003 to control the unsteady cloud and partial cavitation passively. In another study, Kadivar et al.(2020b) investigated the cavitation control mechanisms by a wedge-type VG covering the entire spanwise width of the same hydrofoil. In their studies, the obstacles had heights comparable to the size of the buffer layer at the installation point. Obstacles were positioned on the hydrofoil surface, where the turbulent detachment occurred. The positioned VG suppressed the laminar separation at that position, stabilized the BL, and delayed the onset of cavitation upstream after the trailing edge of the hydrofoil. They also showed that pressure fluctuations were noticeably reduced.

Following the first study by Toms (1948), it has been well understood in recent years that the addition of minute amounts, in orders of parts per million (p.p.m.), of long-chain polymers to a

turbulent liquid flow has significant drag-reducing effects (White and Mungal, 2008; Xi, 2019), which can be as high as 60 % in a pipe flow (Owolabi et al., 2017). As the polymer solution flow experiences continuous shear stress, such as during the circulation of a fluid in a closed-loop system, the DR effects decay due to the scission of polymer molecules, a phenomenon commonly known as the mechanical degradation of the polymers (den Toonder et al., 1995).

Significant DR effects of polymer additives have also been of interest to researchers in the field of cavitating two-phase flows to explore the feasibility of cavitation reduction (CR) effects of these additives. Brennen (1970) used a variety of bulk bodies, including spheres of different sizes, a cylinder, and a disk, and exposed them to an incoming flow of different additive solutions. Dilute solutions of a surface tension-reducing agent, three types of rigid and flexible polymers, and a cationic surfactant were tested at different free stream velocities. It was shown that a dilute polymer solution did not have any practical effect on the cavity flow behind the disk. In contrast, the attached flow behind the spherical and cylindrical bodies was destabilized in the polymer solution and caused separation line distortion and cavitation interface irregularities.

Hoyt (1976) investigated the effect of polyethylene oxide (PEO) on the cavitation inception number σ_i of a cavitating jet flow. In Hoyt's experiments, $\sigma_i = (P - P_v)/(0.5\,\rho\,U^2)$, where P was defined as the static pressure of the free stream, P_v was the saturation pressure of water at the test temperature, ρ was the density of the solution, and U was denoted as the bulk fluid velocity. The results show that concentrations as low as 8 p.p.m. reduced σ_i by ≈ 40 % relative to the pure water flow. The viscosity and air content were measured to be similar to those in the water and PEO solution. Ting (1978) utilized different concentrations of PEO and polyacrylamide (PAM) solutions in water to study the effect of these additives on the cavitation mechanism on the surface of a rotating disk. Ting (1978) showed that σ_i was reduced by ≈ 65 % in a 500 p.p.m. solution of PEO at the tested flow rate. The author argued that high deceleration rates adjacent to the stagnation point on the disk cause relatively high viscoelastic stresses that suppress the cavitation and reconfigure its topology. Ōba et al. (1978) showed that in a flow through a circular orifice, the desinence cavitation number σ_d decreases significantly for 10 p.p.m. PEO solution in water. Increasing the concentration to 50 p.p.m. proliferated the population of non-spherical cavitation bubbles, attenuated pressure fluctuations, and shifted the dominant shedding frequency to lower values relative to the pure water flow. In an extensive review of the studies conducted before 1997, Fruman (1999) concluded that the polymers have consequential effects on the BLs developed on

the solid bodies and the topology of large-scale vortices interacting with individual cavitating bubbles. It was argued that this complexity was the major obstacle to comprehensively understanding the phenomenon.

Hasegawa et al. (2009) measured the pressure drop over different sizes of orifices, ranging from 5 μm to 400 μm, in submerged jet flows of pure water, 50 w/w mixture of water and glycerol and a 1000 p.p.m. PEO solution in water. For all the tested conditions, they showed relatively large reductions of pressure drop, except in the 400 μm orifice. The authors reported that the viscosity of the PEO solution was similar to water, i.e., ≈ 1 mPa.s. Wall slip and elasticity of the PEO solutions were introduced as the main causes of pressure drop reductions. As discussed by Brujan (2011), dilute polymeric solutions mostly demonstrate shear-thinning behavior, with dynamic viscosities relatively higher than pure water for low and intermediate shear strain rates. Hence, it is essential to measure detailed rheological characteristics of non-Newtonian solutions in an experiment to properly address the role of the fluid's elasticity in the obtained results.

Naseri et al. (2018a) simulated the dynamics of cavitating turbulent Phan-Thien-Tanner (PTT) viscoelastic fluids in a step and an injector nozzle. They used the wall-adapting local eddy viscosity (WALE) subgrid-scale turbulence model adapted for large eddy simulation (LES) to simulate the turbulent flow. PTT and Schnerr, and Sauer models were used to simulate the flow's viscoelasticity and cavitation, respectively. Their results showed that the flow's viscoelasticity suppressed cavitation inside the stepped nozzle relative to the pure water flow. They argued that the main physical causes of cavitation suppression were the annihilation of cavitating micro-vortices in the shear layer and a reduction in the turbulence intensity. They also reported that the viscoelastic suppression of turbulence inside the injector nozzle alleviated the generation of string cavitation structures. In another study, Naseri et al. (2018b) demonstrated that a 1000 p.p.m. concentration of quaternary ammonium salt (QAS) surfactant additives reduced the turbulence intensity and attenuated cavitation growth in a fuel nozzle. Using X-ray micro-computed tomography (micro-CT), they measured the cavitation volume fraction in the QAS solution and showed that as a result of CR, the liquid volume fraction passing the nozzle was enhanced by 10 % relative to the pure fuel. Their X-ray phase-contrast imaging (X-PCI) measurements suggested that the lifetime of string vortex cavities was extended in the QAS solutions. As the authors explained, the QAS additives decayed the formation of small-scale vortices in the flow and mitigated their interaction

with larger longitudinal cavitation vortices, avoiding the collapse of the main cavitating cores. Thus, string cavitation structures were stabilized in the main flow.

The dynamics of the interaction of viscoelastic dilute polymer solutions with micro-sized cavitation bubbles at the inception or with large-scale bubble pockets in a violent regime such as cloud cavitation are not well understood. It is unclear whether these additive agents can suppress or attenuate highly intense cavitation regimes, such as supercavitation, when their molecules experience extreme extensional shears. This Chapter aims to answer these questions by shedding light on the dynamics of the cavitation phenomenon in flowing dilute polymer solutions in a wall-bounded converging-diverging mesoscale channel. Information obtained from high-speed imaging and pressure sensor data was analyzed using various image processing and statistical techniques to elucidate the intricacies of this flow phenomenon.

5.2. Description of the flow field

The CG flow path is schematically illustrated in Figure 3-1. The coordinate system is located at the midspan of the channel, with the x-axis starting at the intersection point of the throat and the divergence zones of the nozzle and the y-axis starting from the channel's centreline and pointing vertically upward. Liquid flow of density ρ_L and temperature T_{in} enters the channel at the pressure P_{in} and streamwise area-averaged velocity $\bar{\bar{U}}_{in}$ and leaves it at P_{out} and $\bar{\bar{U}}_{out}$. Single-point wall pressures at the top and bottom of the downstream flow are denoted as P_d. Main dimensions of the flow path are listed in Table 3-1.

The time average of the vapor ratio field A_G (x, y, t) and its fluctuating component are denoted by $\langle A_G \rangle(x, y)$ and $a_G(x, y, t)$, respectively. The spatial average of A_G in the y-direction and over a plane (cross-section or the midspan) are shown by $\bar{A}_G(x, t)$, and $\bar{\bar{A}}_G(t)$, respectively. For the channel flow over the nozzle, illustrated in Figure 3-1, the characteristic length was chosen to be the hydraulic diameter of the throat, $D_{h,th} = 2.86$ mm, and the characteristic velocity was $\langle \bar{\bar{U}} \rangle_{th} = \langle \dot{V} \rangle / A_{th}$, where $A_{th} = h_{th} \times w = 10$ mm^2 is the throat cross-sectional area. The Reynolds number based on the hydraulic diameter and averaged velocity of the throat is defined as $Re_{th} = \langle \rho_L \rangle \langle \bar{\bar{U}}_{th} \rangle D_{h,th} / \mu_w(C_s)$. The cavitation number is defined as:

$$\sigma = \frac{\langle P_{in} \rangle - P_{sat}(\langle T_L \rangle)}{\frac{1}{2} \rho_L \langle \bar{\bar{U}}_{th} \rangle^2}, \tag{5-1}$$

where, $\langle P_{in} \rangle = \langle \Delta P_{ch} \rangle + \langle P_{out} \rangle$ is the time-averaged absolute pressure of a single point at the channel's inlet wall. Here, $\langle \Delta P_{ch} \rangle$ is the time average of the measured pressure drop over the channel, as illustrated in Figure 3-3, and P_{out} is the mean absolute outlet pressure. Vapor saturation pressure at the liquid's temperature $\langle T_L \rangle$ is denoted by P_{sat}, where $\langle T_L \rangle = 0.5$ $(\langle T_{in} \rangle + \langle T_{out} \rangle)$. Values of P_{sat} were determined using XSteam (Holmgren, 2021), a code developed in MATLAB (MathWorks, 2021). This study used PAM additives (BASF SE; Germany) as cavitation and drag reduction agents. Dilute solutions of PAM and tap water at different concentrations were used as operating fluids in the system. Table 5-1 lists the range of the Re_{th} and σ and their associated values at the cavitation inception for the examined PAM solutions.

High-frequency pressure sensors at the flow downstream (see Figure 3-6) measured the pressure variation relative to an arbitrary initial reference value. Hence, their time-averaged value is of no significance. The r.m.s. of the downstream's fluctuating component of the single-point

pressure signal $p_{\mathrm{d,rms}}$ expounds the intensity of pressure pulsation due to the collapse of cavitation bubbles. For brevity, the results for sensors 1 and 2, as in Figure 3-6, are presented together. The Strouhal number St is defined as:

$$\mathrm{St} = f\mathcal{L}/\langle\overline{\overline{U}}_{\mathrm{th}}\rangle, \tag{5-2}$$

where, f is the maximum dominant pulsation frequency, and $\mathcal{L}$ is the characteristic length scale of the flow system. The current study uses pressure measurement signals to determine f.

Table 5-1 List of the examined PAM solutions with their main characteristics.

C_s (p.p.m.)	Pure water	50	100	200	400
$Re_{\mathrm{th}} \times 10^{-4}$	2.3-5.4	2.1-5.3	2.1-5.2	2.2-5.1	2.1-4.8
$Re_{\mathrm{th,i}} \times 10^{-4}$	2.5	3.0	3.1	3.3	3.7
σ	5.15-3.22	6.26-3.43	6.83-3.56	6.36-3.76	8.82-4.58
σ_{i}	4.71	4.44	4.52	4.42	5.17

5.3. Effect of polymer additives on the pressure drop over the nozzle

As illustrated in Figure 3-3, pressure drop was measured over the nozzle using a differential pressure transducer. The pressure drops were measured for four different concentrations of PAM solution and water in the range of $2 \times 10^4 < Re_{th} < 6 \times 10^4$ to investigate the effect of PAM additives on the nozzle flow. The results are plotted in Figure 5-1(*a-d*) as $\sigma(Re_{th})$ profiles.

For pure water profiles in Figure 5-1(*a-d*), σ decreases exponentially as the flow rate increases. After the onset of cavitation, σ drops with a smaller slope and approaches a value of $\sigma \approx 3.2$ for higher Re_{th}. The gradual decrease of the water flow rate during the ramp-down test results in similar pressure drops over the nozzle. Figure 5-1(*a*) shows that the 50 p.p.m. solution results in a higher σ than the pure water flow at an equal Re_{th}. This difference decreases as the flow rate increases and cavitation intensifies. In the 50 p.p.m. solution, cavitation occurs at a flow rate ≈ 20 % higher than the pure water flow. As shown in Figure 5-1(*b-d*), an increase in the solution concentration shifts σ to even higher values, and cavitation onset occurs at higher flow rates than the pure water flow.

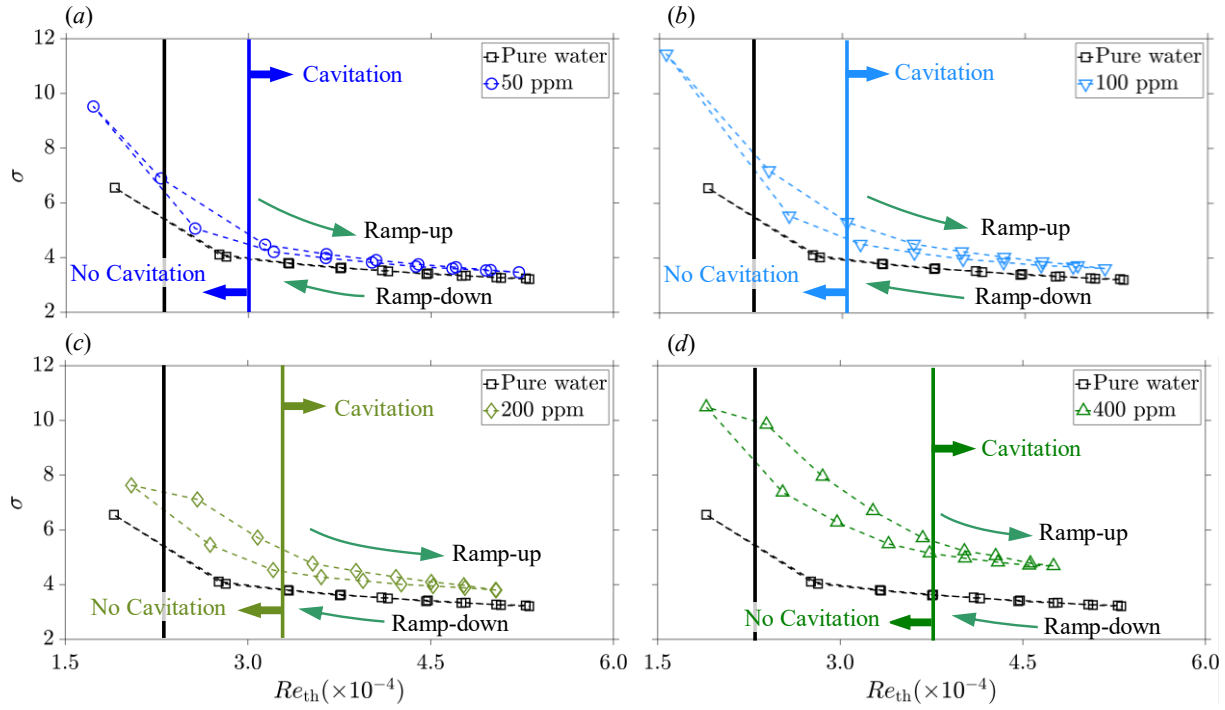

Figure 5-1 Variation of the cavitation number σ versus the throat's Reynolds number Re_{th} for ramp-up (increasing Re_{th}) and ramp-down (decreasing Re_{th}) tests for (*a*) 50 p.p.m., (*b*) 100 p.p.m., (*c*) 200 p.p.m., and (*d*) 400 p.p.m. PAM concentrations. The cavitation onset points are shown by vertical solid lines colored according to the color used to highlight each solution concentration.

For the tested concentrations, solution flows show higher levels of σ during a ramp-up test than a ramp-down test. As Figure 4-4 illustrates, polymers might have experienced mild degradation while recirculating in the flow loop. Relatively, under cavitating flow conditions, it is highly probable that the rate of polymer degradation increased significantly due to the presence of extreme shear stress fields in cavitating regions. At the end of the ramp-up test, the solutions experience relatively high shear stresses during an intense cavitation process. In these extreme conditions, part of the elongated polymer molecules cannot tolerate the exerted shear stresses, degrade, and any entangled polymer molecules straighten. As Figure 4-1(*a*) and Figure 5-1(*a-d*) illustrate, the transmutation of the polymer molecules due to violent cavitation and extreme shears causes a local reduction in viscosity and pressure. Hence, the ramp-down tests show lower pressure drops than the ramp-up measurements.

Figure 5-2(*a*) compares the variation of σ of the solution concentrations examined in this study during the ramp-down test. The inception Reynolds number $Re_{th,i}$ increases as the concentration of PAM polymers increases. For the maximum tested flow rate, corresponding to $Re_{th} \approx 5.4 \times 10^4$, pressure drop over the nozzle increases by ≈ 9 %, ≈ 13 %, ≈ 20 %, and ≈ 50 %, respectively, in the 50, 100, 200, and 400 p.p.m. solution flows relative to the pure water flow. At the inlet of the nozzle channel, the wall shear stress is $\mathcal{O}(10^2$ Pa) (see Figure 4-1*b*), and its corresponding apparent shear viscosity in a PAM solution is higher than the pure water. Therefore, PAM solutions have the potential to produce higher local pressures at low-shear regions in the flow, such as the inlet of the nozzle in this study. This result agrees with the ΔP_{ch} measurements in Figure 5-1(*a-d*).

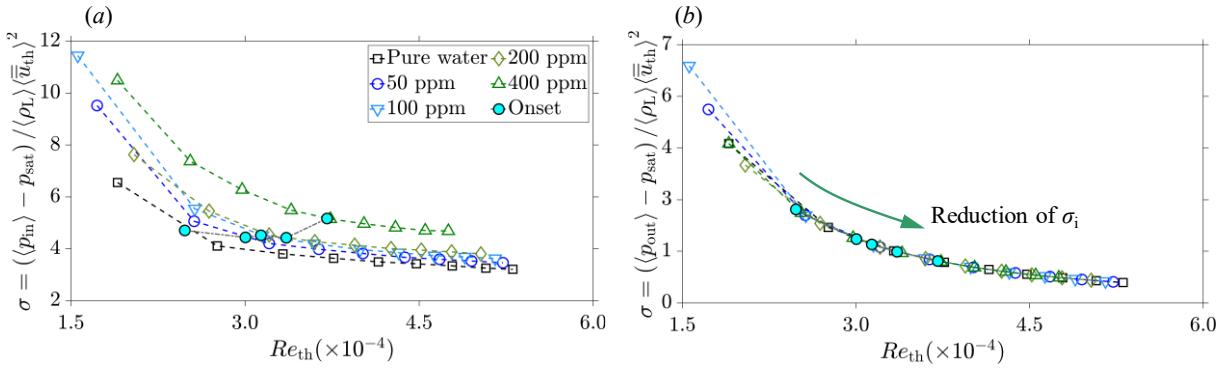

Figure 5-2 Changes of σ as a function of Re_{th} for different concentrations of PAM solutions for the ramp-down tests when (*a*) inlet pressure $\langle P_{in} \rangle$ and (*b*) constant outlet pressure $\langle P_{out} \rangle$ is selected as the reference pressure in equation (5-1). Cyan circles highlight the cavitation onset points.

The PAM concentration increases ΔP_{ch}, and accordingly, inlet pressure P_{in} increases. It is important to note that P_{in} was intentionally chosen as the characteristic pressure in the definition of the cavitation number given in equation (5-1) to demonstrate the physical increase of the pressure drop over the curved nozzle. Nevertheless, most of the previous studies have used a constant reference pressure, such as a free stream or outlet pressure, to define the cavitation number (Hasegawa et al., 2009; Hoyt, 1976; Ōba et al., 1978) and reported reductions in the inception cavitation number σ_i of viscoelastic solutions relative to pure water. Therefore, as Figure 5-2(*b*) shows, if the constant outlet pressure $\langle P_{out} \rangle$ was used in equation (5-1), σ_i would demonstrate a reduction as the concentration increases.

5.4. Temporal evolution of cavitation structures in pure water

The cavitation onset is followed by a complex spatial and temporal evolution of cavitation structures, which expand in size as the pressure drop increases over the nozzle. Figure 5-3(*a-c*) illustrate four instantaneous sample snapshots of vapor ratio fields of cavitating pure water flow for three different flow conditions. These fields are projected on the channel's midspan plane and cover a FOV from approximately the end of the throat region to the vicinity of the end limit of the divergence region (see Figure 3-7). For the current experimental conditions, the incipient cavitation number of pure water was $\sigma_i \sim 4.71$, which was associated with the emergence of tiny cavitation bubbles, detectable by the optical system described in Section 3.4.1.

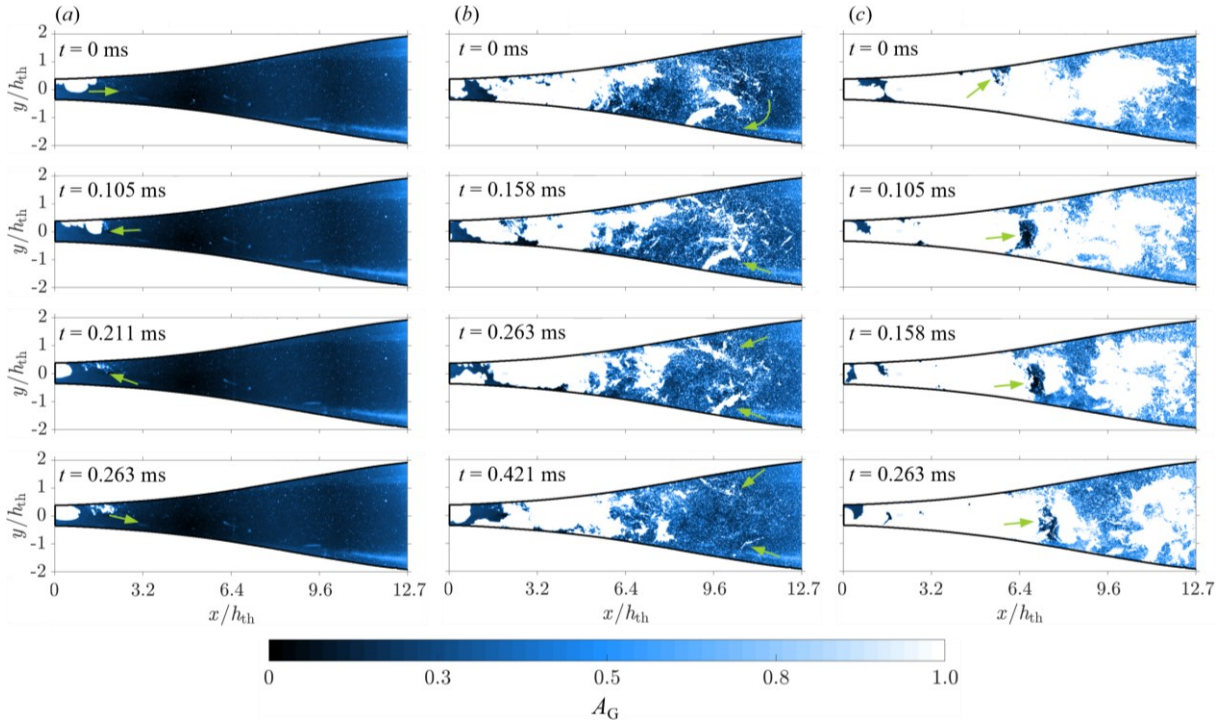

Figure 5-3 Snapshots of cavitating pure water structures at (*a*) $Re_{th} = 2.9 \times 10^4$, $\sigma = 4.23$, (*b*) $Re_{th} = 3.8 \times 10^4$, $\sigma = 3.61$, and (*c*) $Re_{th} = 4.5 \times 10^4$, $\sigma = 3.37$, projected on the channel's midspan (plane $z = 0$). The white color ($A_G = 1$) shows the cavitation areas, and the black color ($A_G = 0$) demonstrates the bulk liquid. Growing and collapsing cavitation structures are annotated using green arrows.

Figure 5-3(*a*) shows the vapor area ratio, A_G (x, y, t), snapshots at $\sigma \approx 4.23$, with a flow rate of ≈ 16 % higher than the inception. Cavitation bubbles are produced cyclically from the throat wall surfaces at this flow condition. As cavities elongate on the upper wall, relatively smaller jet clouds are produced on the lower wall and *vice versa*. Cavities detach from the end of the throat when they reach a length of $\approx 2\ h_{th}$ and flow downstream as they rapidly disintegrate and collapse into micron-sized bubbles. Most tiny micro cavitation bubbles collapse entirely, and any remnants are

carried downstream by the bulk liquid flow. The cavity developed from one wall sporadically interacts with the passing jet cloud originating from the other and generates circular rolling clusters of cavitation bubbles with an equivalent diameter of $\approx h_{th}$. As the bubble clusters flow downstream, they collapse in several microseconds and vanish entirely. Cavity clouds rebound several times during the collapse process and produce radially propagating pressure waves. Interaction of the pressure waves with the growing upstream cavities generates pockets of collapsing bubbles at the front of the cavities, which transmutes the cavity into unstable transient structures.

Further increasing the flow rate enhances cavitation by causing larger pressure drops over the nozzle. Figure 5-3(*b*) illustrates snapshots of the cavitation structures at $\sigma = 3.61$ for the pure water flow. Here, developing cavities gain lengths up to $\approx 5\ h_{th}$ before departing from their origin in the throat. Detached cavities decelerate as they flow downstream and are followed by the next generation of developing cavities. With $P(\boldsymbol{x}, t) \ll P_{sat}$ at almost any position close to the throat, the newborn cavities grow fast and finally bond with the just detached cavities. This bonding further fluctuates the large cavitation structure and may break it off into patches of collapsing streaky clusters of bubbles. These streaky structures exist only for several milliseconds before they entirely vanish or fall apart into micron-sized cavitation bubbles.

The collapse of tilted streaky bubble pockets generates a series of shockwaves that propagate upstream and break the large structures of agglomerated packets of bubbles by modifying their local pressures. This process repeats itself with a particular frequency in time. The pressure field is highly unstable at the throat's downstream region and locally fluctuates around P_{sat}. As a result, smaller scales of bubble pockets emerge and instantly vanish at random positions in the downstream flow field. Chains of bullet-like bubbles are produced at the throat at irregular intervals, separated by liquid slugs of widths of $\approx 0.2\ h_{th}$. Thin films of lubricating liquid were also observed between the cavitation bullet-like bubbles and the channel's walls. As these bubbles travel downstream, they collide with their preceding bubbles, which were decelerated at the divergence region's entrance. As a result, they accumulate in this region and extend the cavitation body from its rear as its front collapses.

Figure 5-3(*c*) is associated with the instantaneous vapor ratio fields of the cavitating water flow with $\sigma = 3.37$. Large pressure drops over the nozzle generate cavitation superstructures with oscillating lengths of $\approx 12\ h_{th}$ in the flow field. Even in this extreme condition, growing wall

cavities cannot entirely occupy the core region of the throat's exit region, which is dominated by a high-speed flow of bulk liquid. Wall cavities expand, merge at the entrance of the divergence region and transform into cavitation superstructures. The interaction of the traveling shockwaves with the front of these huge clouds breaks them off into scattered clouds of cavitation bubbles. The cloud cavitation collapse is chaotic at this flow condition and occurs at random positions in the flow field. As the clouds approach the maximum cross-sectional area, higher pressure levels ($P(\mathbf{x}, t) \gg P_{sat}$) shatter the bubble networks, and the fragmented bubbles vanish as they shrink in size and leave the channel. The chaotic cavitation escalates the pressure fluctuations, which intensifies the cavitation, and this cycle repeats itself as the upstream energy source is present.

As listed in Table 5-1, a series of experiments using varying concentrations of PAM solutions in water were conducted to investigate the effect of PAM additives on the cavitation mechanism and explore the feasibility of the CR effect of these additives. Snapshots of instantaneous vapor ratio fields of the 200 p.p.m. solution on the channel's midspan are plotted in Figure 5-4(*a-c*) for low, medium, and high-intensity cavitation conditions to illustrate the effect of PAM additives on the temporal evolution of cavitation structures. The cavitation process initiates at a Re_{th}, ≈ 32 % higher than the cavitation onset of the pure water flow.

As Figure 5-4(*a*) illustrates, at a condition with a flow rate of only 6 % higher than the onset, the produced cavities form streaky topologies with wiggling outlines in the 200 p.p.m. solution. The instantaneous length of the streaky bubbles increases to ≈ 2 h_{th}, with a length-to-width ratio of ≈ 6. At infrequent periods, the dominant core liquid flow is discontinued instantly by the merging wall cavities at the region where the wall profiles begin to diverge. As the front of the cavities breaks off, relatively uniform structures of detached cavities are generated. They oscillate, partially rebound and collapse as lumps of densely packed cavities, which emerge as continuous cavitation structures in the recorded images. Long polymer molecules act as flexible dampers in the flow field and relax extreme pressure field oscillations adjacent to the collapsing bubbles by releasing their stored energy under tension and storing energy under compression. This effect eases the cavitation process and increases the rebounding period of cavitating bubbles. As a result, lower pressure fluctuations are imposed on the surrounding bulk flow.

For the flow condition with $Re_{th} = 3.6 \times 10^4$ and $\sigma = 4.37$, shown in Figure 5-4(*b*), the core liquid flow exists only to a length of ≈ 2.5 h_{th}, the position where the growing wall cavities merge.

A high-velocity thin layer of lubricating liquid flows upstream between the channel walls and the growing cavities. These continuous film flows possess high levels of momentum, and as they approach the throat, they come to a complete stop near the oncoming growing cavity. The interaction of the front of the lubricating films with the cavities transfers momentum to the cavities, lifts them in the positive wall-normal direction, and separates them from the channel walls. This phenomenon accelerates the merging of the cavities. The recirculating flow regions trap the detached collapsing cavities at irregular periods in the downstream flow field. As a result, the collapse rate is enhanced in regions with a recovered pressure, where the cavities attune to the pressure distribution patterns in the recirculating region by altering their topology.

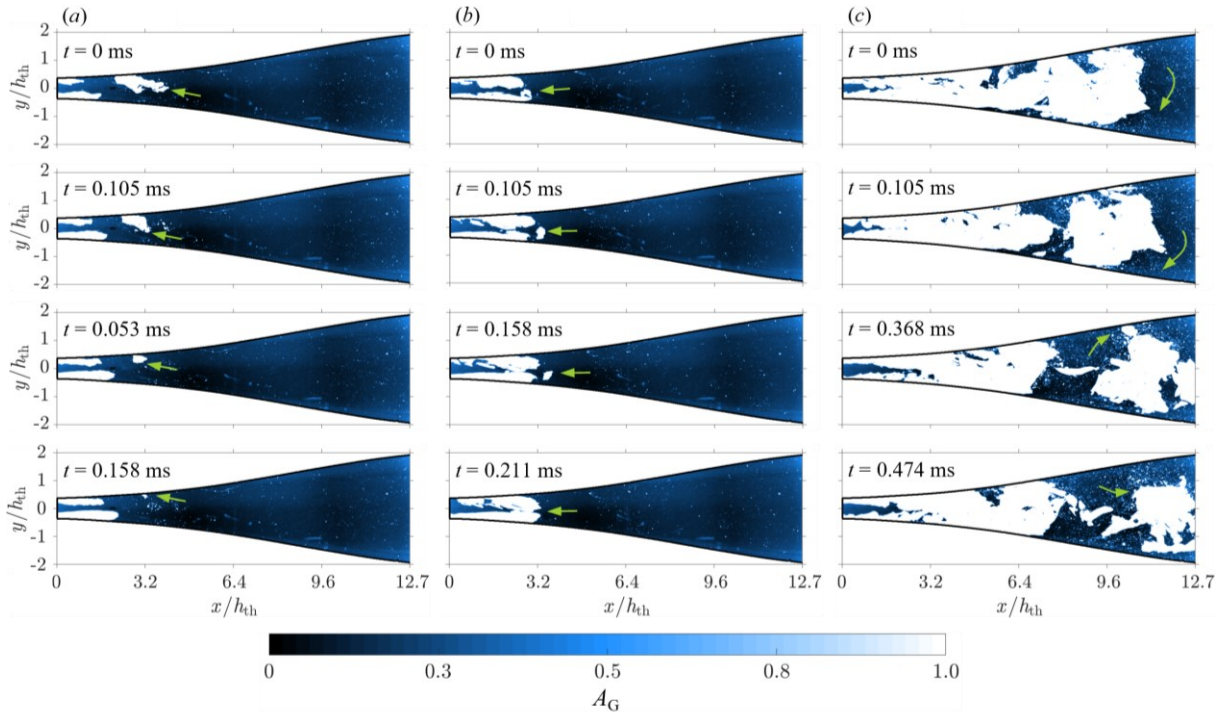

Figure 5-4 Snapshots of cavitating structures in 200 p.p.m. PAM solution flow at (*a*) $Re_{th} = 3.5 \times 10^4$, $\sigma = 4.48$, (*b*) $Re_{th} = 3.6 \times 10^4$, $\sigma = 4.37$, and (*c*) $Re_{th} = 4.3 \times 10^4$, $\sigma = 4.00$, projected on the channel's midspan (plane $z = 0$). The white color ($A_G = 1$) shows the cavitation areas, and the black color ($A_G = 0$) demonstrates the bulk liquid. Growing and collapsing cavitation structures are annotated using green arrows.

As Figure 5-4(*c*) illustrates, cavitation clouds develop into immense structures downstream at a higher cavitation level. The visualization results indicated that the developed cavities remained attached to the wall surfaces during the recording. Under this condition, small-scale clouds were produced due to the break-off and chaotic collapse of the front of the developed cavities, which shed downstream. These clouds show random topologies and generate mesoscale clusters of cavitation bubbles as they collapse. In contrast to water flow (see Figure 5-3*c*), where the collapse

of small-scale cavitation clouds produced consistent micron-sized bubbles, the 200 p.p.m. solution flow produced mesoscale bubble networks with sizes in the range of ≈ 0.2-0.5 mm.

Instantaneous snapshots of cavitating flow structures at the convergence and throat regions of different PAM solution flows are illustrated in Figure 5-5(*a-c*) at three different Re_{th}. As seen, cavitation structures emerge on the walls at about $x/h_{th} \approx -1$, adjacent to the midway of the throat region, oscillating on both walls cyclically as they grow downstream. As expected, increasing the PAM concentration reduces the cavitation intensity and suppresses it at higher concentrations for the tested flow conditions.

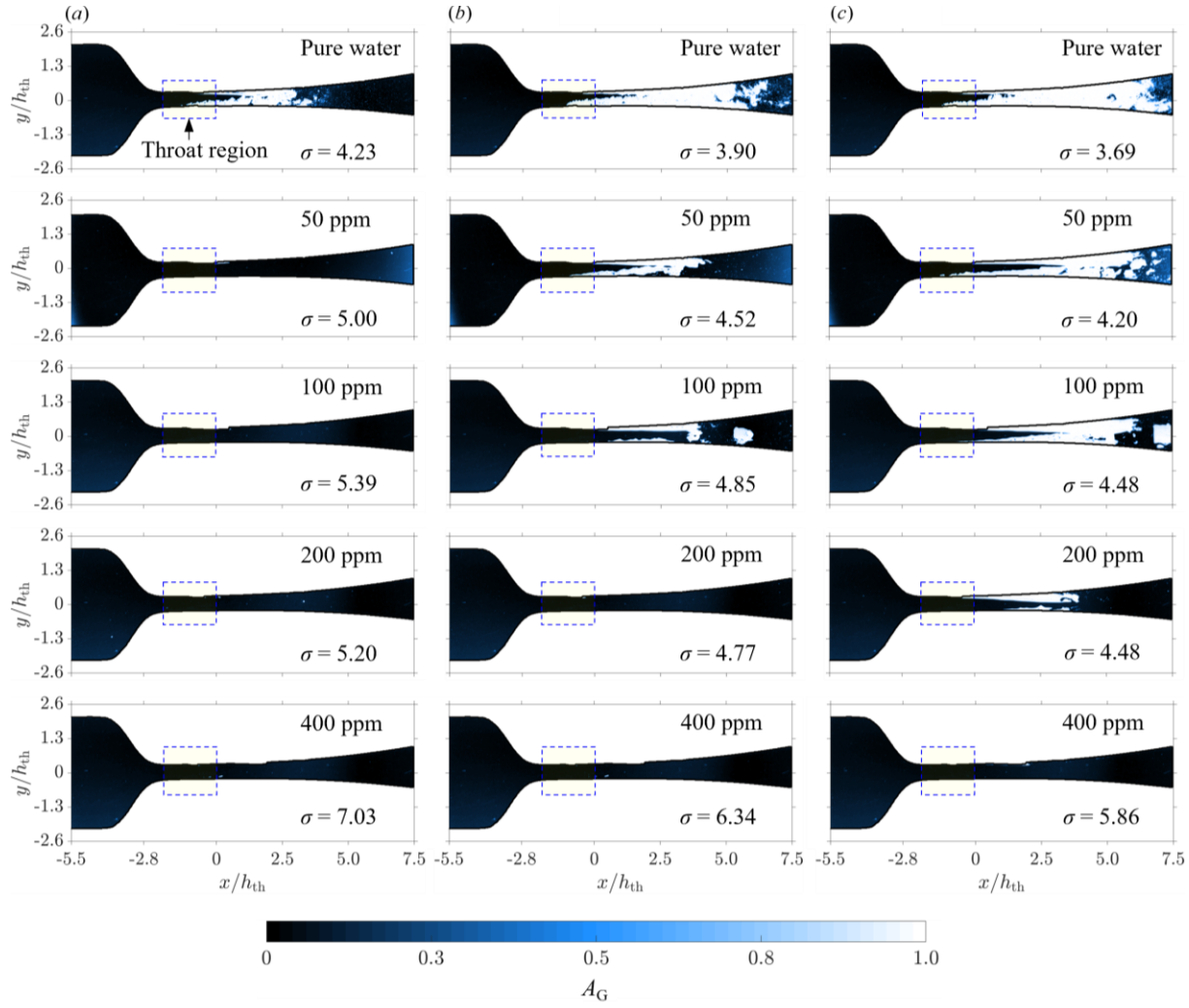

Figure 5-5 Snapshots of instantaneous vapor ratio fields in different PAM solution flows at the convergence and throat regions for (*a*) $Re_{th} = 2.6 \times 10^4$, (*b*) $Re_{th} = 3.0 \times 10^4$, and (*c*) $Re_{th} = 3.4 \times 10^4$, projected on the channel's midspan (plane $z = 0$). The white color ($A_G = 1$) shows the cavitation areas, and the black color ($A_G = 0$) demonstrates the bulk liquid. The flow direction is from left to right, and a rectangle with dashed blue borders signifies the throat region on each figure.

Figure 5-6 schematically demonstrates the approach used to evaluate the spatiotemporal maps of the cavitating flow structures. Each instantaneous vapor ratio field, A_G ($\boldsymbol{x}$, t), was averaged in the y-direction at each streamwise position x / h_{th}, which resulted in a total of ≈ 20 000 $\bar{A}_G(x,t)$ profiles. Then, the values of $\bar{A}_G$ were stacked into columns of a 2D matrix, where each column corresponds to a different instant. The result is a 2D spatiotemporal map, as shown in Figure 5-6. Here, the results of only 1000 images are demonstrated, equivalent to ≈ 45 ms of the total imaging time of T = 0.895 s.

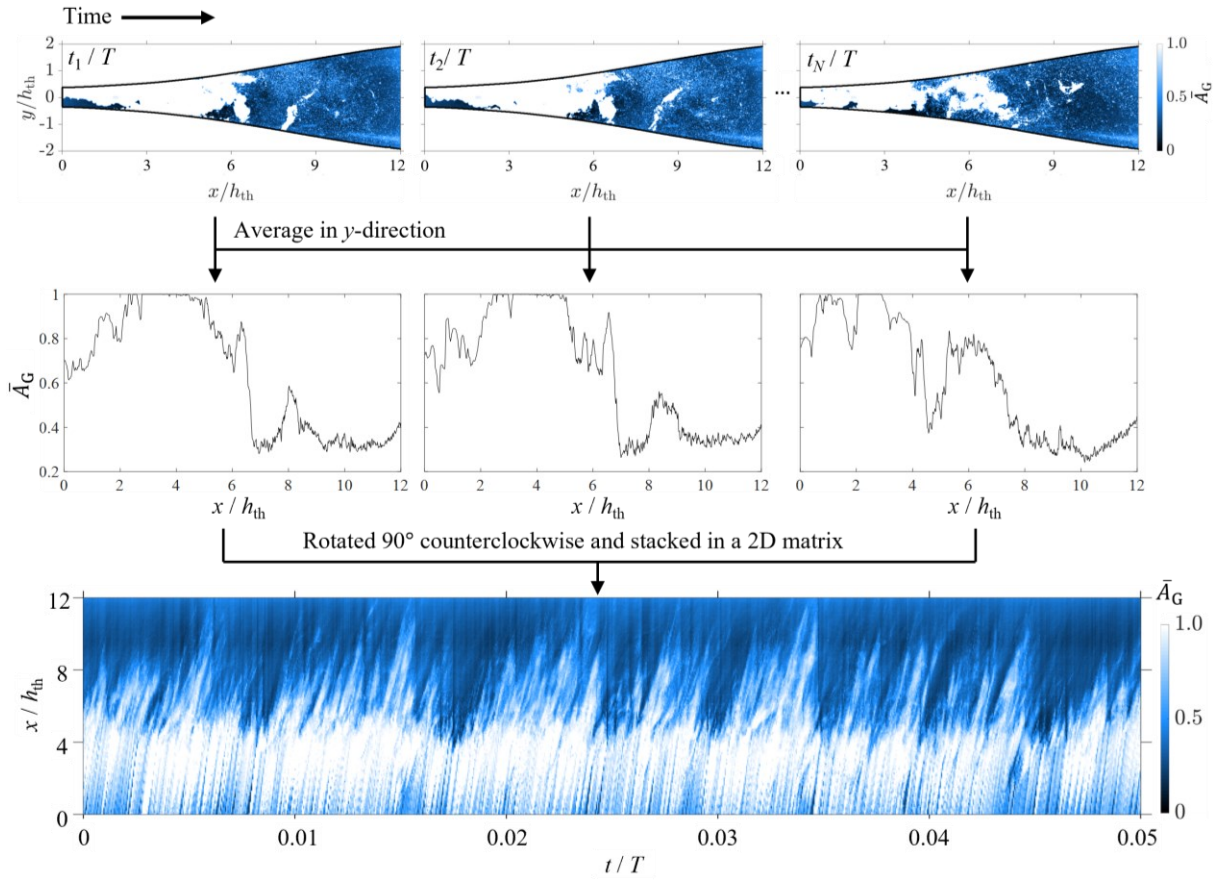

Figure 5-6 Schematic representation of the approach utilized to evaluate the spatiotemporal maps of the cavitating flow fields, illustrated in Figure 5-7(*a*,*b*). The white color (A_G = 1) shows the cavitation areas, and the black color (A_G = 0) demonstrates the bulk liquid. The flow direction is from left to right.

Spatiotemporal maps of cavitating flow fields were evaluated to demonstrate the CR effect of PAM additives on the temporal evolution of cavitation structures. The results are shown in Figure 5-7(*a*,*b*) for an intermediate and a high flow rate of pure water flow and four different concentrations of PAM additives for 45 ms. PAM additives demonstrate significant CR effects by strongly relaxing the chaotic unstable cavity fronts, attenuating their growth downstream, and

suspending the cavitation onset to higher Re_{th}. As given in Table 5-1, cavitation initiates at $Re_{th,i} \approx 3.7 \times 10^4$ in the 400 p.p.m. solution flow, which is ≈ 50 % higher than $Re_{th,i}$ of water flow.

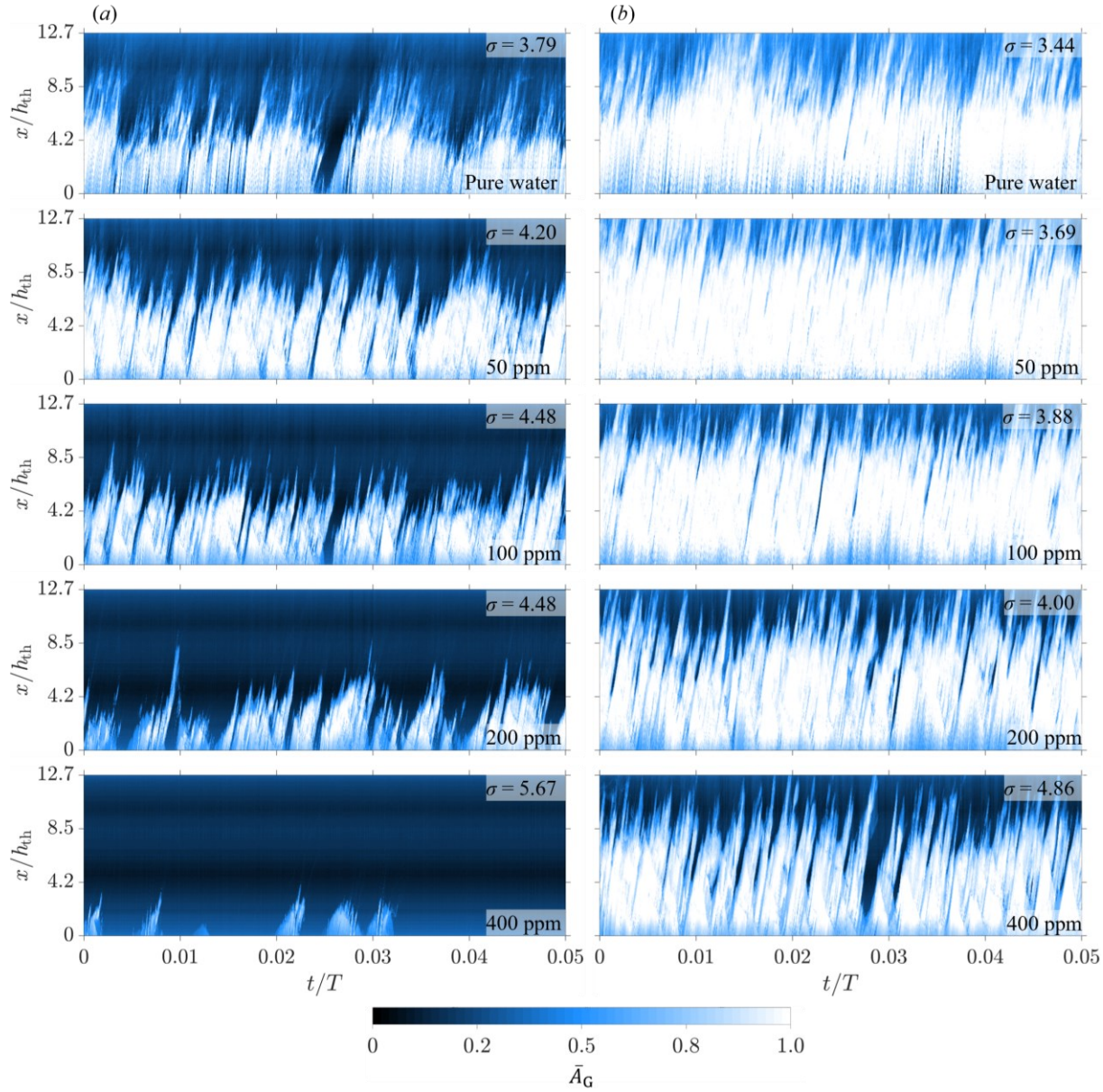

Figure 5-7 Spatiotemporal maps of cavitating PAM solutions for (*a*) $Re_{th} = 3.4 \times 10^4$ and (*b*) $Re_{th} = 4.4 \times 10^4$. From top to bottom, results for pure water, 50 p.p.m, 100 p.p.m, 200 p.p.m, and 400 p.p.m. solutions are illustrated in each row. From the total imaging period of $T = 0.895$ s, results for only 45 ms is illustrated.

In Figure 5-7(*a*), the front of the vaporous structures in the 50 p.p.m. solution flow oscillates with a mean length similar to that in pure water. The population of the miniature cavitation bubbles swimming at the closure of the cavity in the pure water flow is strongly alleviated in the 50 p.p.m. solution. In pure water, the footprints of these tiny bubbles are visible as irregular fading regions

of $\bar{A}_G$ at the cavity closure, which are moderated in the 50 p.p.m. solution flow, as shown in Figure 5-7(*a*). At $Re_{th} = 3.4 \times 10^4$, a further increase in the PAM concentration suppresses the cloud cavitation by damping the growth of the wall cavities and retarding them to sheet cavities. Cavitation is entirely suppressed for a 400 p.p.m. solution, with the only infrequent appearance of small evanescent cavities.

Under extreme cavitation conditions, as shown in Figure 5-7(*b*), pure water flow cavitates violently and generates supercavitation structures that shed downstream, filling almost the entire visualized FOV. At this relatively high flow rate, the 50 p.p.m. solution displays an even more intense cavitation process than the pure water, enhancing the cavitation instead of reducing it. As the concentration increases to 100 p.p.m., the tiny cavitation bubbles adjacent to the oscillating cloud fronts fade out. Growing cavities maintain lengths of similar scales to that in the water flow while oscillating periodically, with lower fluctuations relative to the average cavity length.

As Figure 5-7(*b*) illustrates, increasing the concentration to even 400 p.p.m. cannot suppress the vivacious cavitation structures at this flow condition and only linearize the growth rate of the cloud cavities in time. Once a cavity begins to grow, it expands at an almost constant rate to its maximum length, comparable with the entire length of the divergence region downstream, then it dwindles at a constant and relatively steeper rate, and this process repeats itself in time. Conversely, as the vaporous structures grow in the water flow, they shrink and grow sporadically, at a time-dependent random rate, and produce significant batches of micron-sized dispersed bubbles, which swim in their vicinity and dispense in the entire downstream region.

5.5. Cavitation length

The r.m.s of the fluctuating component of the vapor ratio field $a_{G,rms}$ was calculated for each flow condition to quantify the cavitation intensity. A set of ≈ 17,000 images were analyzed for each flow case to ensure the values converged statistically. Figure 5-8(*a-d*) shows the variation of $a_{G,rms}$ for different flow conditions and PAM solutions in the streamwise direction downstream of the throat on the $y = 0$ centerline of the midspan plane. Each $a_{G,rms}$ ($y = 0$) profile demonstrates a peak, which is associated with the mean position of the oscillating cavitation front. The streamwise distance of this point relative to the origin at $x = 0$ characterizes an appropriate length scale for cavitation structures, denoted by L_{ca} in this study. Dular et al. (2004) and Zhang et al. (2019), among others, used a similar approach to measure the cavitation length. The loci of the peak points are highlighted by cyan circles on the plots in Figure 5-8(*a-d*). There is another peak in each $a_{G,rms}$ ($y = 0$) profile in the $x < 2\ h_{th}$ region. This point corresponds to the mean streamwise position, where cavities detach from the wall surfaces. In Figure 5-8(*a-d*), these detachment regions are highlighted by green dashed rectangles.

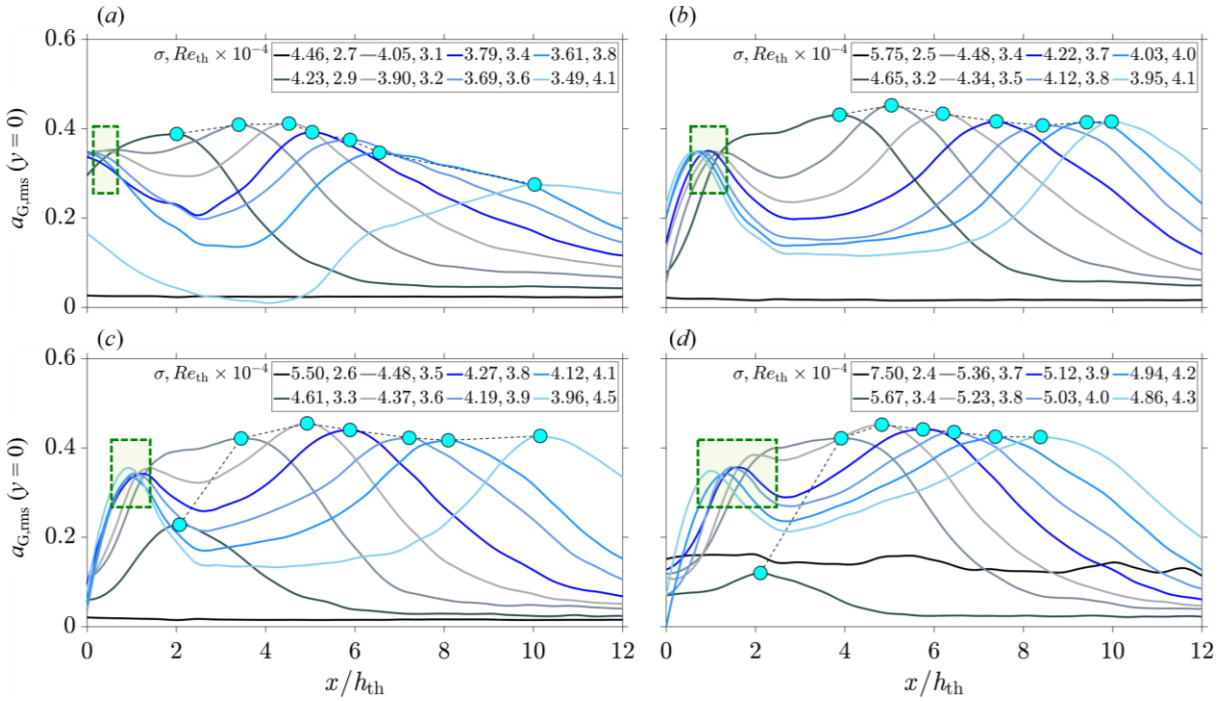

Figure 5-8 Variation of the cavitation intensity $a_{G,rms}$ on the midspan plane $z = 0$ and at the channel's centerline $y = 0$, for the selected range of flow conditions with increasing Re_{th} and decreasing σ for (*a*) pure water, (*b*) 100 p.p.m., (*c*) 200 p.p.m., and (*d*) 400 p.p.m. solution flows. The positions of $[a_{G,rms}\ (y = 0)]_{max}$ are highlighted with cyan circles on each figure and connected with a black dashed line to demonstrate the variation of the maxima. The regions of cavitation detachment adjacent to the throat are emphasized using rectangles colored in pale green with dashed dark green outlines.

Figure 5-8(*a*) shows that as the flow rate (equivalently, the pressure drop) of the pure water flow increases, cloud cavitation structures develop into a wider region downstream while maintaining a maximum of $a_{G,rms} \approx 0.42$ until $Re_{th} = 3.9 \times 10^4$ and $\sigma = 3.2$. After this point, the maximum intensity decays linearly with increasing Re_{th}. This reduction in the maximum intensity reveals that the cavitation cloud's oscillating front is more stable at higher flow rates. For water flows with $\sigma > 3.2$, the growing cavities detach from the wall surface after a partial expansion and are transferred by the bulk liquid flow further downstream, where they collapse due to pressure recovery. At the same time, new cavities are generated and develop from the throat when bulk liquid fills the collapse region. Therefore, a_G shows high fluctuations in this region, resulting in a higher $a_{G,rms}$ at the cloud's closure region. The detachment and collapse periods are longer for larger, more violent structures. For $\sigma > 3.90$, the flow region is repeatedly filled with newly growing cavitation bubbles, which statistically increases the probability of the existence of bubble pockets of a similar population in the same region. Therefore, the flow experiences lower fluctuation levels of a_G at the edge of the cavitation structures.

Similar to the pure water flow shown in Figure 5-8(*a*), intensity values on the centerline of PAM solutions, given in Figure 5-8(*b-d*), show two peaks: (1) in the close vicinity of the throat, where the clouds detach from the surface, and (2) at the edge of the cavitation clouds, where the cavity closure oscillates periodically. Maximum cavitation intensity is maintained for the full range of the examined Re_{th} and σ for PAM solutions tested, while its position is shifted further downstream as Re_{th} increases. As a result, the addition of PAM polymers intensifies the fluctuations of the cavitation edge at higher flow rates, while relative to the pure water, they delay the cavitation onset to larger Re_{th}, and damp the expansion of the cavitation structures in the streamwise direction. Figure 5-8(*a*) reveals that the cavitation detachment position remains almost constant for the entire range of the tested flow rates for pure water at $x / h_{th} \sim 0.4$. Conversely, as shown in Figure 5-8(*b-d*), raising the concentration level in the solution generally shifts the detachment position downstream, respectively, to $x / h_{th} \approx 1$, $x / h_{th} \sim 1.2$, and $x / h_{th} \approx 1.8$. However, as Re_{th} increases, the mean detachment position reverses towards upstream.

The estimated cavitation lengths based on the loci of $[a_{G,rms}(y = 0)]_{max}$ are plotted in Figure 5-9(*a*,*b*) for varying Re_{th} and σ and different solutions of PAM in water. As shown in Figure 5-9(*a*), the occurrence of the minimum cavitation length $L_{ca,min} \approx 2\ h_{th}$ is shifted towards higher Re_{th} as the concentration increases. For the 400 p.p.m. solution, this happens at a Re_{th} of

≈ 18 % higher than pure water. For all examined solutions, L_{ca} increases almost linearly with Re_{th}. At relatively higher flow rates, $3.2 \times 10^4 < Re_{th} < 4.0 \times 10^4$, 50 p.p.m., and 100 p.p.m. solutions expand to longer cavitation structures than pure water, enhancing the growth of streaky and cloud cavities. Solutions with concentrations of more than 100 p.p.m. decelerate the expansion of the cavitation clouds and shrink their size in the streamwise direction. For instance, at $Re_{th} = 4 \times 10^4$, L_{ca} in the 400 p.p.m. solution is reduced by 30 % relative to pure water.

As shown in Figure 5-9(*b*), cavitation length increases almost linearly with the reduction of σ for all examined solutions. A similar L_{ca} is generated at a higher σ in PAM solutions relative to pure water. A cavity of $L_{ca,min} \sim 2\ h_{th}$ occurs at $\sigma \approx 5.7$ in the 400 p.p.m. solution, which is ≈ 34 % higher than its counterpart in pure water. There is a noticeable shift (≈ 11 %) in the L_{ca} (σ) profile for the 50 p.p.m. solution compared to pure water. Increasing the mixture concentration from 50 p.p.m. to 200 p.p.m. does not indicate a significant shift in L_{ca} (σ). As the PAM concentration increases to 400 p.p.m., L_{ca} (σ) shifts ≈ 23 % towards higher σ compared to the 50 p.p.m.-200 p.p.m. profiles. These shifts follow the increase of the inlet pressure due to the local increase of the solution's shear viscosity discussed in Section 4.

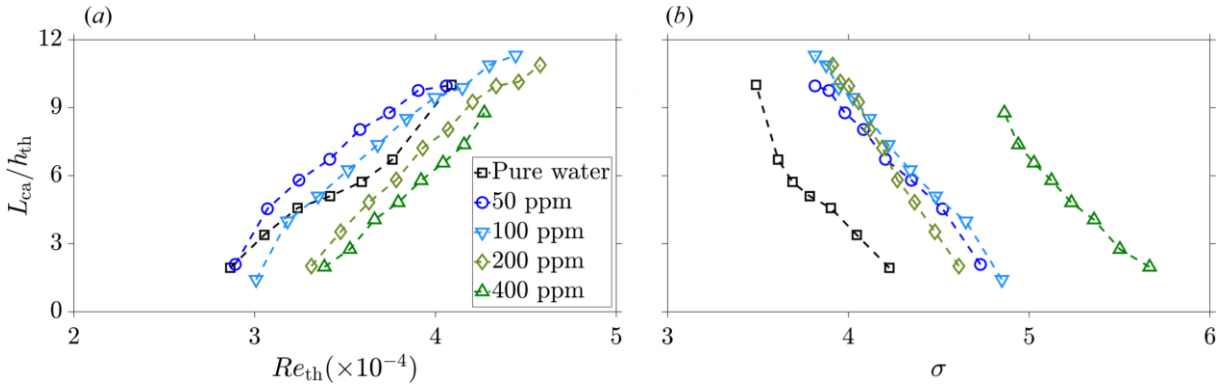

Figure 5-9 Variation of the normalized cavitation length with (*a*) throat Reynolds number Re_{th} and (*b*) cavitation number σ for pure water and four different concentrations of PAM solution in water.

5.6. Temporal variance of cavitation structures

In an instantaneous image captured from a cavitating flow, each square pixel can be fully or partially occupied by a vaporous phase, i.e., $0 \leq A_G \leq 1$. In an Eulerian reference frame, the time difference of A_G can provide local information on the growth or collapse of the cavities. In this study, the first-order time difference of A_G field is defined as:

$$\delta A_G(x, y, t_{k-1}) = A_G(x, y, t_k) - A_G(x, y, t_{k-1}), \tag{5-3}$$

where the index k shows the current instant; therefore, $\delta A_G > 0$ corresponds to the local growth of the cavitation structure, and correspondingly $\delta A_G < 0$ at a position in the flow field refers to the occurrence of a collapse. A value of $\delta A_G = 0$ means that a similar fluid phase is present at the same location at the instants $t_{k\text{-}1}$ and t_k; hence, it does not show any growth or collapse. Here, $\delta A_G > 0$ and $\delta A_G < 0$ are symbolized as δA_G+ and δA_G-, respectively. Figure 5-10(*a-b*) illustrate the spatiotemporal variations of δA_G, averaged in the y-direction at each instant, for only 5 % of the total recording time of $T = 0.895$ s. The process of obtaining $\overline{\delta A}_G(x, t)$ is commonly called the frame difference method (FDM) (Sato et al., 2013). The time difference of the fluctuations of A_G can be defined similarly as:

$$\delta a_G(x, y, t_{k-1}) = a_G(x, y, t_k) - a_G(x, y, t_{k-1}). \tag{5-4}$$

Visualization results given in Section 5.4 reveal that PAM additives suppress cloud cavitation under moderate conditions and alleviate the growth of cavity fronts in the supercavitation regime. It is well understood that the propagation of high-speed pressure waves induced by the collapse of cavitation bubbles in a pure water flow intensifies the pressure fluctuations in the flow field and enhances the cavitation process (Karathanassis et al., 2018; Wu et al., 2021; Zhang et al., 2019). Therefore, it can be hypothesized that polymer additives reduce cavitation intensity by affecting the local collapse and growth process in the flow field. To verify this hypothesis, r.m.s of the fluctuations of the time difference fields, i.e., $\delta a_{G,rms}$, were calculated separately for the collapse and growth regions in each solution flow. The resultant r.m.s fields were normalized by their associated time-averaged fields $\langle \delta A_G \rangle$. It is assumed here that the cavitation process is statistically symmetric relative to the centerline $y = 0$ and shows the most intense fluctuations in the streamwise direction and on the centerline. Here, $\delta a_{G^-,rms}/\langle \delta A_{G^-} \rangle$ is the defined to be the cavitation collapse level (CCL) and $\delta a_{G^+,rms}/\langle \delta A_{G^+} \rangle$ is the cavitation growth level (CGL).

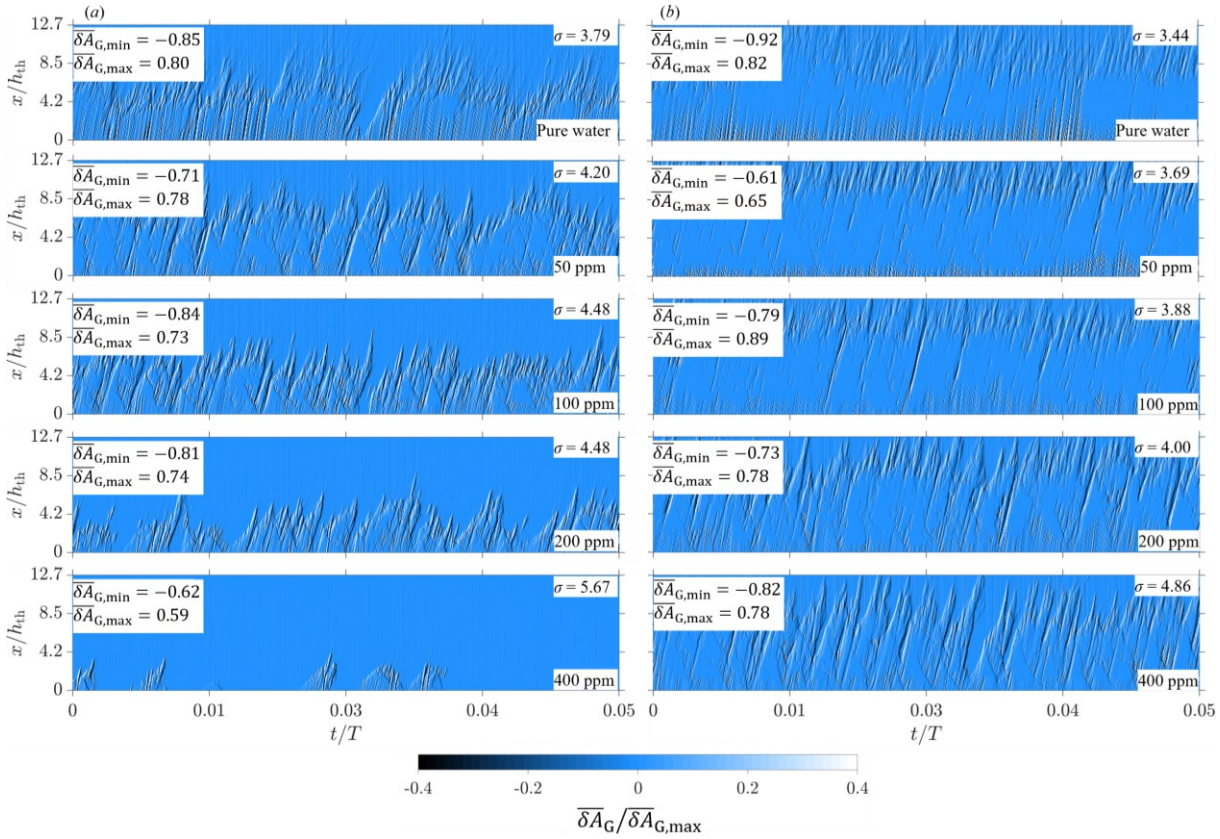

Figure 5-10 Spatiotemporal fields of y-averaged time difference of vapor ratio field $\overline{\delta A}_G$, normalized by its maximum value, for (*a*) $Re_{th} = 3.4 \times 10^4$ and (*b*) $Re_{th} = 4.4 \times 10^4$. Each row corresponds to a different concentration. From top to bottom, results for pure water, 50 p.p.m, 100 p.p.m, 200 p.p.m and 400 p.p.m. solutions are illustrated, respectively. From the total imaging period of $T = 0.895$ s, only 45 ms is illustrated. The color bar range is limited to ± 0.4 for better contrast.

Figure 5-11(*a-d*) show the variation of the normalized time variance fluctuations of collapse on $y = 0$, respectively, for water and 100, 200, and 400 p.p.m. solution flows. The maxima of the profiles are highlighted by cyan circles and connected via dashed black lines to demonstrate the trend of changes. Figure 5-11(*a*) illustrates that increasing the water flow rate elevates the CCL. For the highest tested throat Reynolds number, $Re_{th} = 4.5 \times 10^4$, the collapse fluctuations can be as high as ×10 the mean collapse time variance, revealing the extreme chaos associated with the supercavitation regime. Until $Re_{th} = 3.4 \times 10^4$, pure water flow experiences the highest collapse level at $x \approx 1.2\ h_{th}$. With a ≈ 10 % increase in the flow rate, the CCL shows a rapid increase, and the position of its peak shifts further downstream to $x \approx 1.8\ h_{th}$. After $Re_{th} = 3.4 \times 10^4$, maximum CCL continues to elevate almost linearly with an increase in the flow rate.

Figure 5-11(*b*) shows that the cavitation process in the 100 p.p.m. solution occurs with relatively lower CCLs than the cavitating pure water flow, where the maximum CCL shifts

downstream almost linearly for the entire range of the tested conditions. At the highest tested flow rate with $Re_{th} \sim 4.6 \times 10^4$, maximum CCL occurs at $x \approx 2.2\ h_{th}$ and $x \approx 3.1\ h_{th}$, respectively, for the pure water and the 100 p.p.m. solution flows, while the maximum CCL is relatively 15 % lower in the 100 p.p.m. solution. Also, compared to pure water, the PAM additives flatten the CCL profiles and relax the fluctuations globally. This result elucidates the CR effects of PAM additives. As Figure 5-11(*c*,*d*) illustrates, a further increase of the solution concentration to 200 p.p.m. and 400 p.p.m. alleviates the fluctuations significantly. For the maximum flow rate tested, CCL reduces by 52 % and 62 % for the 200 p.p.m. and 400 p.p.m. solutions.

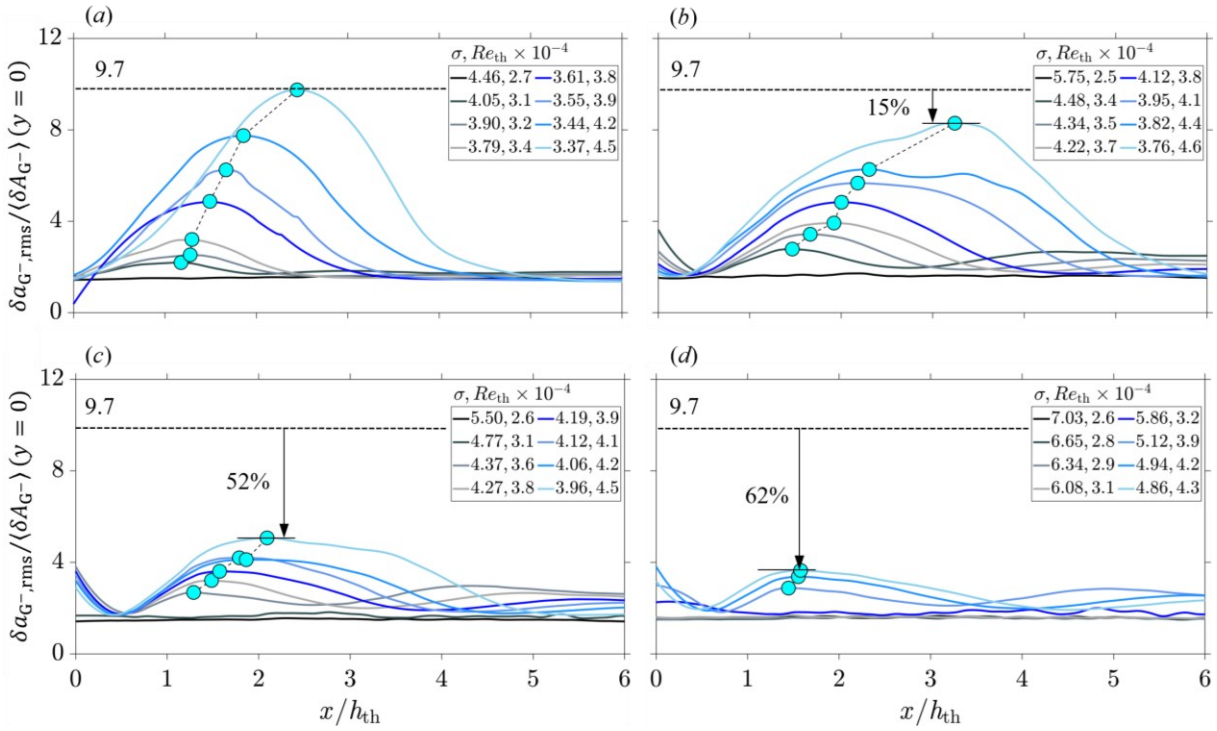

Figure 5-11 Streamwise variation of the normalized r.m.s of the time difference fluctuations of the collapsing vapor ratio field, CCL, on the centreline $y = 0$ for (*a*) pure water and (*b*) 100 p.p.m., (*c*) 200 p.p.m., and (*d*) 400 p.p.m. PAM solutions in water at different flow conditions. The maxima positions are highlighted by cyan circles and connected by a black dashed line on each figure to elucidate their variation. The reduction of the maximum CCL at the highest tested Re_{th} in each PAM solution relative to its counterpart in the pure water is also annotated.

The dependency of the maximum values of CCL and cavitation growth level (CGL) on Re_{th} and σ are depicted in Figure 5-12(*a*-*b*). Statistically, the absolute values of CCL and CGL should be identical. In the current study, the maximum relative difference between the absolute CCL and CGL is ≈ 0.1 %. Figure 5-12(*a*) shows that the cavitation collapse and growth fluctuations increase by increasing Re_{th} for pure water. As discussed in Section 5.4 and shown in Figure 5-12(*a*), PAM additives elevate the maximum CCL in the 50 p.p.m. solution relative to the

pure water flow. This behavior of the 50 p.p.m. solution escalates in the supercavitation regime. For solution concentrations of more than 50 p.p.m., PAM additives reveal a CR effect by relaxing the maximum CCL and CGL in the entire range of the tested Re_{th}.

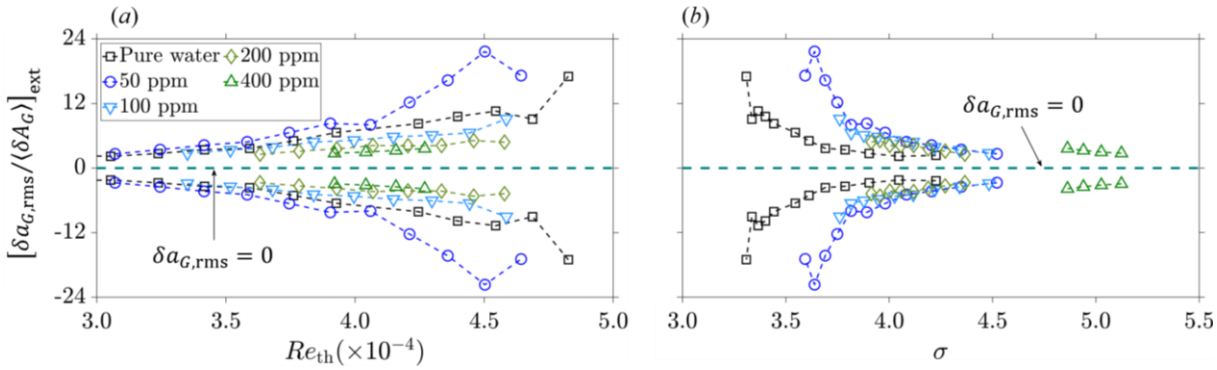

Figure 5-12 Variation of the extrema of the collapsing and growing $\delta a_{G,\mathrm{rms}}$, normalized by its corresponding extrema of $\langle \delta A \rangle_G$ versus (a) Re_{th}, and (b) σ, for pure water and different solutions of PAM in water. The subscript 'ext' stands for extrema, i.e., a maximum or a minimum.

Similarly, as Figure 5-12(*b*) shows, a reduction in σ exacerbates the cavitation process by increasing CCL. This increase is abrupt for water and the 50 p.p.m. solution and relaxes for higher concentrations. As discussed in Section 5.3, adding PAM additives increases the pressure drop over the nozzle compared to pure water for a similar Re_{th}. Hence, CCL and CGL profiles do not collapse on the same abscissa in Figure 5-12(*b*).

5.7. Shedding frequency

As was discussed in Section 5.4, one of the mechanisms through which the PAM additives relax the cavitation process is by significantly mitigating the collapse and growth fluctuations in the flow field. Tracking the temporal evolution of the cavitation structures in the PAM solutions (see Figure 5-7) reveals that additives also alter the shedding periodicity. A spectral analysis was performed on the high-speed pressure sensor data to quantify this behavior. Two approaches were applied to the time series of the pressure fluctuations $p_{\mathrm{d}}(t)$ to obtain the spectra of the dominant shedding frequencies: (1) fast Fourier transform (FFT) was utilized to obtain the power spectral density (PSD) of the data, i.e., $\mathcal{A}_{\mathrm{PSD}}(f)$, where f is the frequency, and (2) continuous wavelet transform (CWT) was used to obtain the time-dependent spectra of the shedding frequencies, i.e., $\mathcal{A}_{\mathrm{CWT}}(f)$. The probability of the instantaneous dominant frequencies $\mathcal{A}_{\mathrm{PDF}}(f)$ was obtained from the CWT results.

Figure 5-13(*a*,*b*) illustrates the spectral analysis results for two sample flow conditions with an intermediate and a high flow rate in pure water flow, and Figure 5-13(*c*,*d*) shows similar results for the 200 p.p.m. PAM solution. For each flow condition, left to right diagrams illustrate the temporal variation of the pressure fluctuations normalized by its maximum value, the PSD spectrum, the CWT spectrogram of the pressure signal, and the normalized PDF percentage of the maximum CWT-based signal frequency.

The maximum dominant frequencies obtained from the PSD-based and CWT-based spectral analysis were used to calculate the Strouhal number St, given in equation (5-2), for different solutions in the range of the tested flow conditions. Using the throat hydraulic diameter $D_{\mathrm{h,th}}$ as the characteristic length scale in equation (5-2), the resultant St (Re_{th}) and St (σ) profiles of different solutions are plotted, respectively, in Figure 5-14(*a*,*b*). The first and second rows are associated with the PSD and CWT spectral analysis. Comparing the PSD-based and CWT-based results for St (Re_{th}) and St (σ), the maximum relative difference was less than 1.5 % in the entire range of the tested solution concentrations and flow conditions. Therefore, the following discussion is attributed to both spectral analyses.

Figure 5-14(*a*) shows that St is almost constant before the cavitation onset in the pure water flow and is followed by a rapid increase in St as the flow begins to cavitate. After the onset, St reduces exponentially as the flow rate increases. PAM solutions with concentrations in the range

of 50-100 p.p.m. show a similar trend of changes in the St (Re_{th}) profile, with relatively smaller peaks of St. At a constant $Re_{th} > Re_{th,i}$, the 200 p.p.m. shows larger St relative to the pure water and other concentrations. In contrast, the 400 p.p.m. solution demonstrates lower St than the other dilute solutions until its inception at $Re_{th,i} = 3.7 \times 10^4$, after which St suddenly increases to values relatively higher than the other tested solutions.

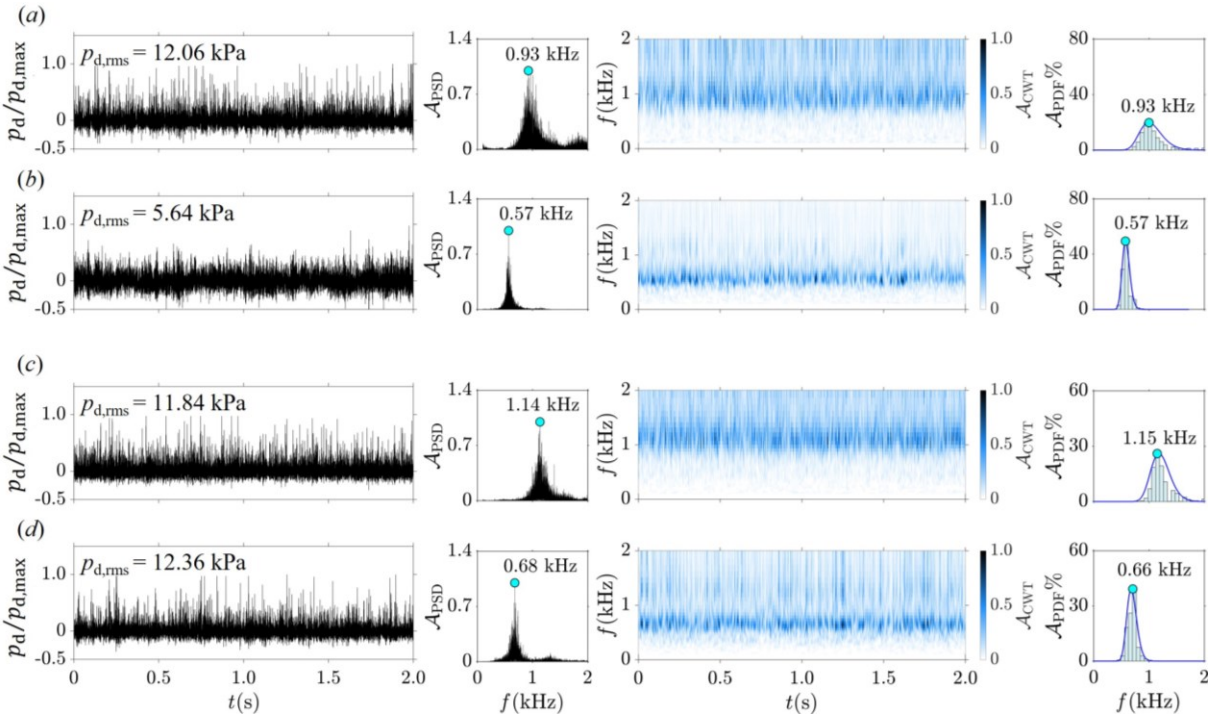

Figure 5-13 Spectral analysis results of the pressure fluctuation signal at the channel downstream, p_d, in pure water flow at (*a*) $Re_{th} = 3.6 \times 10^4$, $\sigma = 3.69$, and (*b*) $Re_{th} = 4.8 \times 10^4$, $\sigma = 3.31$, and in 200 p.p.m. solution flow at (*c*) $Re_{th} = 3.6 \times 10^4$, $\sigma = 4.48$ and (*d*) $Re_{th} = 4.8 \times 10^4$, $\sigma = 4.86$. Cavitation onset of pure water and 200 p.p.m. solution occur, respectively, at $Re_{th,i} = 2.5 \times 10^4$, $\sigma_i = 4.71$ and $Re_{th,i} = 3.3 \times 10^4$, $\sigma_i = 4.42$. In each of (*a-d*), from left to right, diagrams respectively represent the pressure fluctuation signal at the channel's downstream, p_d, normalized by its maximum value $p_{d,max}$, for a period of 2 s; the normalized PSD of p_d as a function of frequency, obtained using discrete FFT; the time-dependent behavior of the signal's frequency, colored by the normalized CWT amplitude; and the normalized PDF percentage of the maximum CWT-based signal frequency. Cyan circles on the PSD and PDF plots highlight the maximum dominant frequencies obtained using FFT and CWT.

Figure 5-14(*a*) illustrates that increasing the solution concentration reduces the dominant shedding frequency at the inception. Figure 5-14(*b*) shows that the St of the pure water abruptly increases as the cavitation process starts and gradually decreases as σ decreases. PAM solutions of 50 p.p.m. to 200 p.p.m. showed similar trends of changes in St (σ) profiles. As the flow rate increases and $\sigma \approx 6$ in the 400 p.p.m. solution, St increases slightly and maintains a value of St ≈ 0.1 until the inception point, where St suddenly increases to St ≈ 0.2, which is ≈ 70 %

smaller than the inception St of the pure water. These findings suggest that another mechanism by which the viscoelastic polymer molecules damp out cavitation is by reducing the inception dominant shedding frequency.

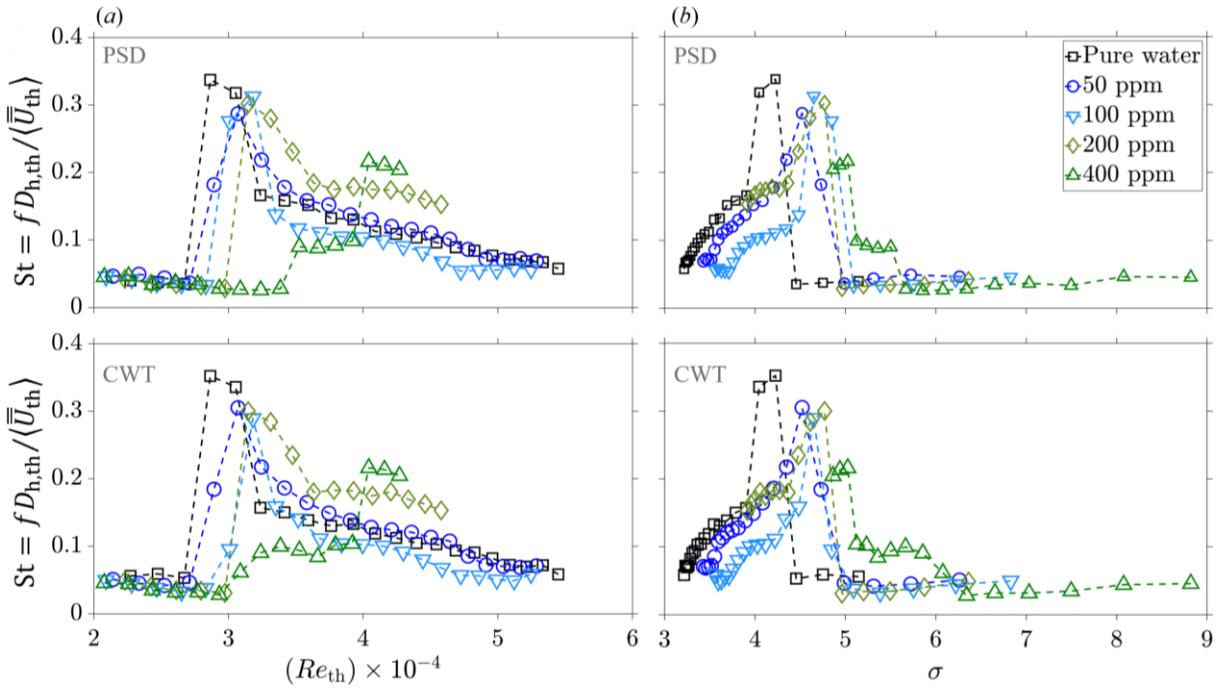

Figure 5-14 Throat hydraulic diameter $D_{h,th}$ based Strouhal number St (see equation (5-2)) as a function of (*a*) the throat's Reynolds number Re_{th}, and (*b*) cavitation number σ in pure water and different PAM solution flows. The first and second rows display the PSD and CWT spectral analysis results, respectively.

Strouhal numbers were also calculated based on the cavitation length L_{ca}. Figure 5-15(*a*,*b*) illustrates the resultant profiles. As shown in Figure 5-15(*a*), the St profile of pure water flow shows a local peak at the cavitation onset and, after a slight decrease, starts to increase almost linearly, in contrast to its counterpart in Figure 5-14(*a*). This behavior highlights that as Re_{th} increases, the increase in L_{ca} dominates the decrease in f. The St(Re_{th}) profiles of 50 p.p.m. and 100 p.p.m. solutions in Figure 5-14(*a*) show similar local peaks at the cavitation onset, with a reduced amplitude relative to the pure water. After the onset, St remains almost constant with an increase of Re_{th} for the 50 p.p.m. and 100 p.p.m. solutions. The St definition based on L_{ca} is ill-defined for non-cavitating flow. For instance, the 200 p.p.m. and 400 p.p.m. solutions have $L_{ca} = 0$ at $Re_{th} \lesssim 3.2 \times 10^4$, equivalent to St = 0 in this range. For higher Re_{th}, St grows linearly in both concentrations, with a smaller slope than pure water flow. As shown in Figure 5-14(*b*), as σ decreases, St(σ) profiles of the solutions display similar trends as of St(Re_{th}) for increasing Re_{th}.

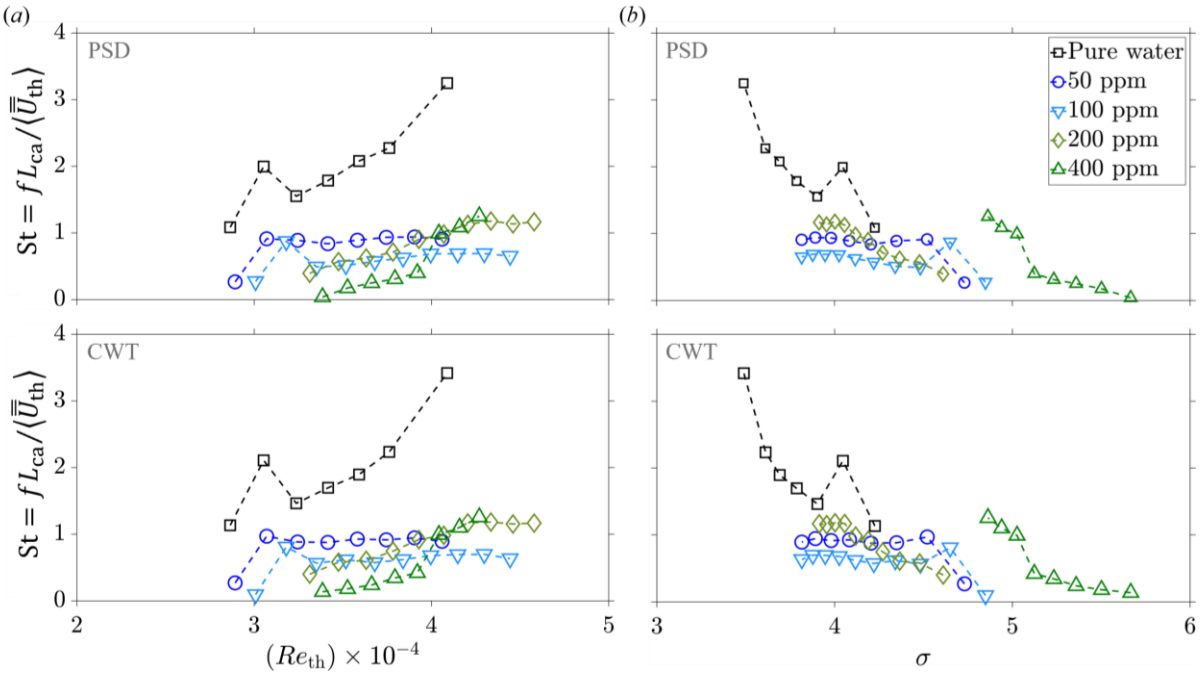

Figure 5-15 Cavitation length L_{ca} based Strouhal number St (see equation (5-2)) as a function of (*a*) the throat's Reynolds number Re_{th}, and (*b*) cavitation number σ in pure water and different PAM solution flows. The first and second rows display the PSD and CWT spectral analysis results, respectively.

5.8. Conclusion

An experimental study was conducted to elucidate the mechanisms of CR in viscoelastic dilute polymer solutions. For this aim, a mesoscale converging-diverging nozzle with a throat size of 2 mm was designed, and the temporal evolution and spatial variation of cavitation structures were captured using a high-speed imaging system. Instantaneous fluctuations of the downstream pressure were also recorded using high-speed pressure sensors. A wide range of flow conditions, $2 \times 10^4 < Re_{th} < 5 \times 10^4$ and $3 < \sigma < 9$, was tested for pure water flow and PAM concentrations of 50-400 p.p.m. Rheological measurements suggested that concentrations less than 100 p.p.m. had constant viscosities in the range of the tested shear rates, with viscosities of 5-20 % more than the pure water. Solutions with $C_s \geq 200$ p.p.m. indicated shear-thinning behavior with infinite shear viscosities relatively larger than the pure water flow. Numerical simulations showed that the wall shear stress at the throat could be as high as 1000 Pa, where the wall shear viscosity is very close to its infinite value. This result suggests that viscosity plays a minor role in the cavitation reduction mechanism of polymer additives. The PAM additives caused a high DR of 50 % for the maximum tested flow rate in the straight tube but increased the pressure drop over the nozzle relative to the pure water flow. Local increase of the shear viscosity at the nozzle inlet with relatively lower shear strain rates was the main reason for the pressure drop increase in PAM solutions.

Visualization of the temporal evolution of vapor ratio fields on the channel's midspan reveals that adding PAM additives delays the cavitation onset to higher flow rates. Micro collapsing bubbles densely populate the edge of cloud cavitation in the pure water flow. In contrast, in PAM solutions, wall cavities grow in the form of streaky structures in the direction of the core liquid flow, with relatively smoother interfaces, where dispersed micron size collapsing bubbles are scarce. The mean cavitation length L_{ca}, determined based on the position of the peak of $a_{G,rms}$, increased almost linearly with the throat's Reynolds number Re_{th} and decreased linearly with the cavitation number σ in all the tested solutions. At a similar Re_{th}, PAM concentrations of 50 p.p.m. and 100 p.p.m. showed an increase in L_{ca} relative to the pure water flow. As the solution concentration increased to more than 100 p.p.m., cavitation growth attenuated. In the 400 p.p.m. solution, at $Re_{th} = 4 \times 10^4$, L_{ca} is reduced by 30 % relative to the pure water.

Collapse and growth levels in cavitating water and solution flows were determined by calculating the fluctuations of the vapor-ratio time variance. The results indicated that the collapse

and growth process of cavitation bubbles in water occurs at relatively higher levels as the flow rate and the pressure drop over the nozzle increase. The tested PAM solutions showed a similar CCL and CGL increase trend by increasing the flow rate. For the entire range of tested flow conditions, the CCL of PAM solutions showed significant reductions relative to the water, with flattened variation profiles in the streamwise direction. As the PAM concentration increased in the solution, CCL reduced. The maximum level at which the cavitation bubbles collapse in the flow of the 400 p.p.m. solution is 60 % lower than the collapse level in the pure water at the highest tested Re_{th}. This result elucidates that the attenuation of the extreme collapse and growth fluctuations in a cavitating flow field is one of the main mechanisms polymer molecules reduce cavitation.

Spectral analysis of the measured downstream pressure fluctuations showed that the St of the water and the PAM solutions indicate a sudden peak at the cavitation inception and gradually reduces for higher Re_{th} and smaller σ. The inception St reduces significantly in the PAM solutions, which is ≈ 70 % relative to the water in the 400 p.p.m. solution. This result suggests that mitigation of the shedding frequency is another mechanism by which the PAM additives relax cavitation.

6. Newtonian developing turbulent flow

Chapter 5 discusses the detailed dynamics of hydrodynamic cavitation and elucidates the cavitation reduction mechanisms of the drag-reducing PAM agents in the flow. It is shown that the polymer additives shift the incipient cavitation index to higher values. In the bulk liquid flow, the local pressure fluctuations generated by the flow's turbulence initiate the cavitation process around the nuclei. At cavitation inception conditions, bulk flow is turbulent in most flow regions, and BLs are developing and non-equilibrium. It is not yet clearly understood how the boundary layers interact with the emerging cavitation bubbles and their main role in the initiation of the cavitation process. The first step in elucidating the details of this complex interaction is to understand the physics of the developing BLs in pure water and then polymeric solution flows.

As flow passes over the converging-diverging wall surfaces, it experiences a series of favorable and adverse pressure gradients of varying strength and is affected by the wall curvature. The impacts of these changes are significant on the developing BLs. Hence, the turbulence of non-equilibrium BLs developed over the wall surfaces of a one-sided converging-diverging flow channel, shown in Figure 3-2, was investigated at critical flow regions with ZPG, FPG, and APG. Each flow was studied at three different mass flow rates, close to the ones initiating cavitation in the CG test section.

This Chapter describes the obtained results for the pure water flow. Chapter 7 explains the findings associated with two concentrations of PAM solutions in water: 200 p.p.m. and 400 p.p.m. This Chapter starts with a review of the previous studies on the individual and combined effects of FPG, APG, and wall curvature on developing Newtonian turbulent BLs. Then, the results of the current study are presented in three main Sections for flows subjected to ZPG, FPG, and APG. The results of the fully developed ZPG flow were used as a baseline for comparison with other complex phenomena and to validate the utilized methodology. In each Section, a combination of statistical methods common in the study of turbulence flows was used to clearly explain the details of the mean flow statistics. It is important to note that flow fields subjected to pressure gradients were not homogeneous in the streamwise direction, which added to the complexity of the problem. Additionally, an analysis was performed to determine the measurement uncertainties of the main instantaneous and mean flow parameters and bulk BL variables.

6.1. Introduction

In most industrial applications, a turbulent flow passes over complex, non-flat surfaces, where the local flow velocity changes in the main flow direction due to a change in the curvature or inclination of wall surfaces in contact with the incoming turbulent flow. As a result, the flow may accelerate ($\partial U_e/\partial s > 0$) and cause a local FPG, i.e., $\partial P_e/\partial s < 0$, or it may decelerate locally ($\partial U_e/\partial s < 0$) and generate an APG, i.e., $\partial P_e/\partial s > 0$ flow region. The subscript 'e' denotes the BL edge (see Figure 2-1*b*). The non-zero pressure gradient results in non-equilibrium, developing BLs over the wall surface, where the mean turbulent statistics in all directions behave differently from the standard fully developed ZPG flows. Under FPG and APG, the flow usually generates two independent, decoupled layers, which are locally non-equilibrium (Balin and Jansen, 2021; Baskaran et al., 1987; Tsuji and Morikawa, 1976): (1) an inner layer mainly dominated by the pressure gradients where curvature effects are inconsequential, and (2) an outer layer that behaves as a free shear layer. In contrast to canonical ZPG flows on smooth flat surfaces, which have turbulent statistics invariant of the direction, statistics of flows subjected to pressure gradients locally change and are more complex to analyze.

Of particular interest are the turbulent flows alternately exposed to strong favorable and adverse pressure gradients, such as turbulent flow over airfoils, ship liners, or turbine blades. In such flows, BL statistics are affected by the accumulated turbulence history before that location, known as the "*history effect*" of the pressure gradient (Bobke et al., 2017; Vinuesa et al., 2017b). There is limited information on these pressure gradient turbulent BLs in the literature, and more experimental and numerical studies are required to elucidate the physics behind such flows.

Narasimha and Sreenivasan (1979) and later Sreenivasan (1982) described that any physical phenomenon that can eradicate or absorb turbulent energy, dissipate turbulent stresses, or cause strong streamwise acceleration can lead to *relaminarization* of the turbulent flow. The gradual process of relaminarization, depicted schematically in (Sreenivasan, 1982) for a one-sided converging tunnel, is replotted in Figure 6-1 based on the variables defined in this work and some modifications. In Zone I, BL statistics are almost invariant of the direction, and the standard logarithmic law of the wall is valid. As the flow accelerates, the local mean velocity profiles deviate from the standard law in Zone II, and when $\Delta_p \approx -5 \times 10^{-3}$ (Patel, 1965), *laminarescent* emerges.

Patel (1965) defined the non-dimensional FPG parameter, Δ_p, as:

$$\Delta_p(s) = \frac{\nu_w(s)}{\rho u_\tau^3(s)} \frac{dP_e(s)}{ds}, \tag{6-1}$$

where, P_e is the mean pressure at the edge of the BL. In Zone II, the modified turbulent flow statistics are at equilibrium.

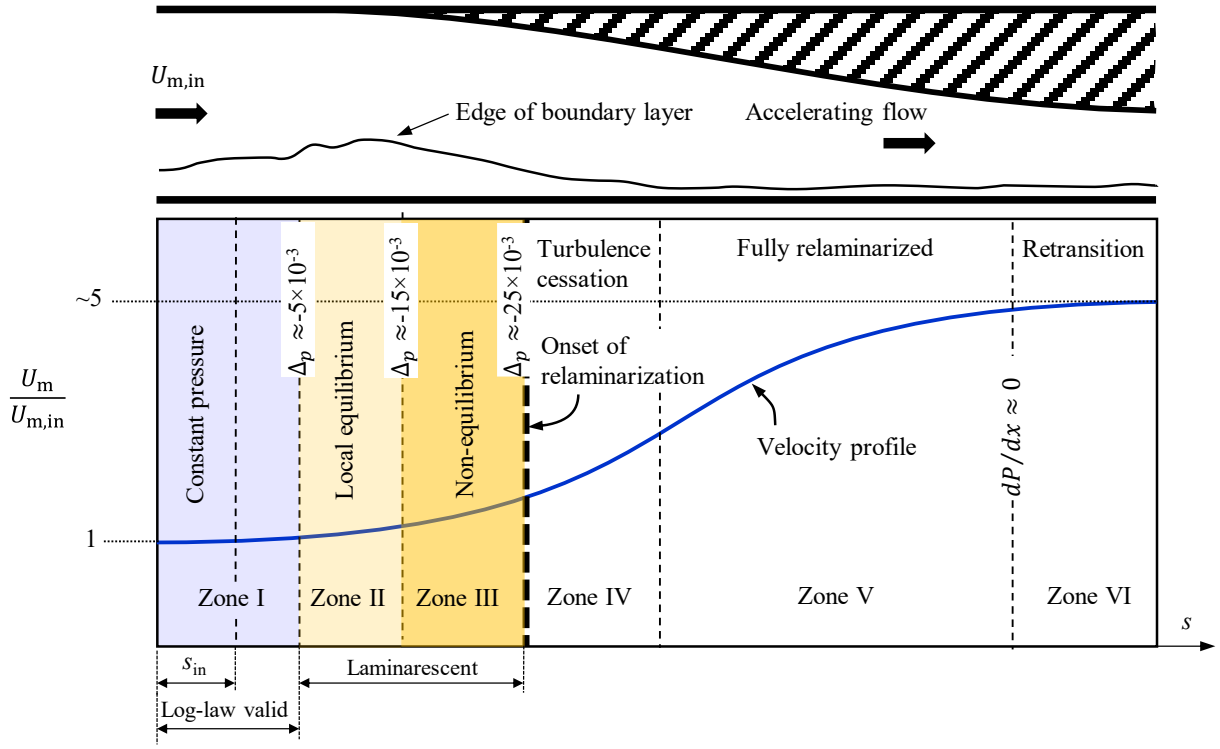

Figure 6-1 Qualitative classification of an accelerating turbulent flow under gradual FPG (not to scale). [*After* (Sreenivasan, 1982)]. Here, s_{in} denotes a wall-parallel inlet length with ZPG.

Further acceleration decreases the pressure gradient parameter, and when $\Delta_p \approx -15 \times 10^{-3}$, flow experiences non-equilibrium conditions, and BL thickness starts to reduce. A strong FPG significantly relaxes the velocity fluctuations and weakens the near-wall turbulence (Balin and Jansen, 2021). As Sreenivasan (1982) explained, the Laminarescent emerges at the start of Zone II and extends over Zone III. The endpoint of Zone III marks the onset of relaminarization, where flow ceases to be turbulent. Patel (1965) suggested that a value of $\Delta_p \approx -18 \times 10^{-3}$ marks the start of relaminarization. Narasimha and Sreenivasan (1979, 1973) and Sreenivasan (1982) proposed that $\Delta_p \approx -25 \times 10^{-3}$ and $K = 3 \times 10^{-6}$, and Moretti and Kays (1965) suggested that $K = 3.5 \times 10^{-6}$ indicate the initiation of the relaminarization process.

In a relaminarized flow, $K > 3 \times 10^{-6}$. The acceleration parameter is formulated as (Moretti and Kays, 1965):

$$K(s) = \frac{\nu_w(s)}{U_e^2}\frac{dU_e(s)}{ds}. \tag{6-2}$$

Non-dimensional shear stress gradient is defined as (Patel and Head, 1968):

$$\Delta_\tau(s) = \frac{\nu_w(s)}{\rho u_\tau^3}\frac{\Delta\tau}{n_{vs}}, \tag{6-3}$$

where $\Delta\tau = \tau_{vs}(s) - \tau_w(s)$. Here, $\tau_{vs}(s)$ is the mean total shear stress at the wall-normal position of the viscous sublayer edge, n_{vs}, at each wall-parallel position s. Patel and Head (1968) proposed a value of $\Delta_\tau \approx -9 \times 10^{-3}$ for the onset of relaminarization. Later, Bradshaw (1969) argued that $\Delta_\tau \approx -13 \times 10^{-3}$ marks the onset of logarithmic law overshoot and not exactly the onset of relaminarization. The onset of relaminarization is followed by turbulence cessation (Zone IV), where the logarithmic law region starts to disappear (Baskaran et al., 1987). As the flow acceleration continues, the flow becomes fully relaminarized (Zone V). In such a flow, the effect of the Reynolds stresses on the mean flow development is inconsequential (Sreenivasan, 1982).

Balin and Jansen (2021) performed a direct numerical simulation (DNS) study on the turbulent BL over a Gaussian-shaped smooth bump. They reported that the mean velocity profile deviated above the standard logarithmic law in the accelerated flow region. The reported deviation of the mean FPG velocity profile was in agreement with the experiments of Jones and Launder (1972), Pitot tube measurements of Jones et al. (2001), and numerical simulations of Spalart (1986) for an equilibrium sink flow. Jones et al. (2001) described the sink flow as a turbulent BL flow with a pressure gradient that follows the structure of a 2D potential flow, i.e., a flow with $U_e(s) = U_{in} / (1 - s / \mathcal{L})$ and constant acceleration parameter $K = \nu / (U_{in}\,\mathcal{L})$, from equation (6-2). Here, U_{in} is an upstream unperturbed wall-parallel velocity at the inlet of the sink flow region, and $\mathcal{L}$ is some characteristic length.

DNS of Balin and Jansen (2021) showed that under a stronger acceleration, some regions in the near-wall flow indicated spots of quiet flow (Zone IV in Figure 6-1). As the authors discussed, the relaminarization process (Zone V in Figure 6-1) did not complete, and only quasi-relaminarized regions were produced at the end of the FPG region. They reported significant

attenuation in the wall stress normalized Reynolds stresses and turbulent production rate in the quasi-relaminarized regions.

In contrast to FPG, an APG thickens the BL and may cause flow separation (Clauser, 1954). The wall friction is reduced in a decelerating flow, where the near-wall turbulence enhances compared to a ZPG flow. Sequential alteration of the pressure gradient sign makes the turbulent flow non-equilibrium (Tsuji and Morikawa, 1976). When a flow that was (partially-)relaminarized under FPG conditions experiences a downstream APG, it initiates a relatively quick process of reverting to turbulence (Baskaran et al., 1987). The reappearance of the logarithmic flow region and a significant increase in the turbulence statistics follows this reversion. Tsuji and Morikawa (1976) showed that when the logarithmic law breaks down by strong acceleration, a relatively large distance is necessary for the flow to regain its equilibrium turbulence state.

Volino (2020) studied the turbulence structures of a channel flow under changing pressure gradient conditions. Three ramp profiles were utilized on the channel's top wall to generate a sequence of mild to strong FPG to ZPG to APG on the incoming flow. The bottom surface of the test section was flat and parallel to the streamwise flow direction, where the flow was interrogated at different streamwise locations using PIV. The results show that under strong FPG, the wake was suppressed, and the mean streamwise velocity profile deviated above the standard logarithmic law when normalized using inner scales. The Reynolds stresses were significantly suppressed under strong FPG and were enhanced under APG conditions.

The DNS results of Balin and Jansen (2021), performed on the turbulent flow over a Gaussian bump, showed that a quasi-relaminarized flow (Zone IV in Figure 6-1) indicated a rapid retransition into turbulent flow under a sudden APG at the peak of the bump, downstream the FPG region. As a result, the flow's skin friction factor and turbulence increased significantly. This APG flow region marks the start of Zone VI in Figure 6-1. Performing DNS simulations on the suction side of a mildly convex airfoil, Pargal et al. (2022) showed that APG effects dominate the wall curvature effects except for the regions with a thick BL, where they are of comparable order.

Large-scale structures across the BL are more energized in an APG BL than in a ZPG BL. In an experimental study, Balantrapu et al. (2021) showed that energized large-scale motions in a decelerated flow increase turbulence activity in the outer region. These motions were associated with the second peak in streamwise Reynolds stresses. Their findings agreed with studies of Harun

et al. (2013) and Kitsios et al. (2017), which showed that stronger APG conditions intensified the second peak and shifted its position away from the wall.

There are relatively rare moments during which streamwise velocities of a turbulent flow reverse to the upstream direction in small, localized regions near the wall. These events are known as *reverse flow* (Bross et al., 2019; Willert et al., 2018) or *backflow* events in turbulent flows (Vinuesa et al., 2017a). The experimentally determined probability of the reverse flow events in a ZPG turbulent flow is 0.01 % - 0.018 % relative to the number of the measured streamwise velocity vectors (Willert et al., 2018). This probability was numerically obtained as ≈ 0.06 % (Lenaers et al., 2012). In a DNS, Vinuesa et al. (2017a) showed that APG could significantly increase the probability of reverse flow events to as high as ≈ 30 %.

In a detailed study, Maciel et al. (2018) showed that using u_τ as the scaling parameter is only valid for $H < 1.8$ and $\beta < 8$, where β is the Rotta-Clauser pressure gradient parameter (Clauser, 1954; Rotta, 1953) and is defined as:

$$\beta = \frac{\delta^*}{\tau_w}\frac{dP_e}{ds} = -\frac{\Delta}{u_\tau}\frac{dU_e}{ds}. \tag{6-4}$$

The defect displacement thickness Δ is given in equation (2-20). According to Maciel et al. (2018), the Zagarola-Smits velocity (Zagarola and Smits, 1998), $U_{zs} = U_e\,(\delta^* / \delta)$, and BL thickness δ, are the best scaling parameters to cover all ranges of defects, β, and H.

Patel and Sotiropoulos (1997) showed that strong convex curvature considerably reduces the Reynolds stresses and turbulent diffusion in the outer region, decreases skin friction and increases the wake of the mean velocity profile. Tulapurkara et al. (2001) examined a combination of APG and curvature effects on non-equilibrium turbulent flow for $\beta = 0.62$ and $\delta / R_w = 23 \times 10^{-3}$, where R_w is the curvature radius of the wall. Their results showed that the combined effect of APG and the convex or concave curvature intensified turbulence to levels higher than the superposition of individual effects. The wake asymmetry increased due to APG, the BL thickness was reduced, and turbulence was significantly suppressed on convex surfaces. In contrast, the concave surface increased the BL thickness and strengthened the turbulence intensities.

As discussed, a turbulent flow subjected to a streamwise pressure gradient establishes a developing BL on the wall surface with statistics that depend on the direction and does not necessarily follow the canonical turbulence of a fully developed ZPG. The complexity of the

interaction of the inner layer turbulence with large-scale motions in the outer layer of pressure gradient flows and their local and global effects on the turbulence statistics, coupled with non-trivial history effects, make the experimental and numerical study of such flows very challenging. The current study aims to shed more light on the turbulence behavior of developing BLs in a channel flow subjected to an alternative FPG to ZPG to APG to ZPG conditions with fully developed ZPG upstream conditions at moderate Reynolds numbers. Planar PIV was utilized to experimentally measure high-resolution velocity fields at the mid-span of a 2D channel and report the turbulent statistics of critical flow regions.

6.2. Zero-pressure gradient flow

Table 6-1 lists the main BL parameters of fully developed ZPG turbulent water flow at three conditions: $Re_\tau = 198$, $Re_\tau = 240$, and $Re_\tau = 282$. These results are attributed to the ZPG FOV highlighted in Figure 3-13. The estimated BL thicknesses are almost equal to the half-channel height of 4 mm, with 0.50 %, 2.00 %, and 0.25 % relative differences for $Re_\tau = 198$, $Re_\tau = 240$, and $Re_\tau = 282$. The negligible difference is due to the uncertainties associated with the velocity measurements. The ratio of the displacement thickness to the BL thickness, δ^* / δ, and the ratio of the momentum thickness to the BL thickness, θ / δ, remain almost constant at $\delta^* / \delta = 0.14$ and $\theta / \delta = 0.10$, as Re_τ increases. The shape factor H and Clauser (or defect) shape factor G show relative reductions of ≈ 5 % and ≈ 10 % as the mean velocity increases.

Dean (1978) showed that in a fully developed 2D turbulent channel flow with ZPG,

$$\left(\frac{U_e}{U_m}\right)_{Dean} = 1.28 Re_m^{-0.0116}, \tag{6-5}$$

$$c_{f,\,Dean} = 0.073 Re_m^{-0.25}, \tag{6-6}$$

where Re_m is given in equation (2-24). Clauser (1956) proposed a coefficient of 0.079 instead of 0.073 in equation (6-6). As listed in Table 6-1, the measured ratio U_e / U_m is identical to Dean's prediction of $U_e / U_m = 1.16$ for $Re_\tau = 198$, and $U_e / U_m = 1.15$ for $Re_\tau = 240$, and is only ≈ 1.7 % underpredicted for $Re_\tau = 282$. The calculated Reynolds numbers based on the bulk mean velocity U_m (see equation (2-24)) show that $6.3 \times 10^3 < Re_m < 9.6 \times 10^3$. The spatial resolution of the mean velocity measurements in wall units varied from $\Delta x^+ \times \Delta y^+ = 2.3 \times 2.3$ for $Re_\tau = 198$ to $\Delta x^+ \times \Delta y^+ = 3.3 \times 3.3$ for $Re_\tau = 282$.

The shear strain rates listed in Table 6-1 were obtained by fitting a straight line to the mean velocity profiles in the viscous sublayer based on the least square method. In all cases, the R coefficients of fits met the criterion of $R > 0.99$. As discussed in Section 4.1, the measured viscosity of the tap water used in the experiments was $\mu_w = 0.91 \pm 0.02$ mPa s. Using the estimated shear-strain values and measured μ_w, the mean wall shear stresses, τ_w were obtained using equation (2-18). The τ_w values were also determined using the empirical correlation of Dean (1978), given in equation (6-6), and are listed in Table 6-1. A comparison of the measured wall shear stresses and the ones estimated using equation (6-6) shows that the PIV results underpredicted the measured τ_w by ≈ 6-7 %.

Table 6-1 List of main bulk and near-wall BL parameters of the ZPG turbulent pure water flow.

Parameter	Unit	Case I	Case II	Case III
μ_w	mPa s	0.91	0.91	0.91
U_m	m s^{-1}	0.73	0.93	1.10
U_e	m s^{-1}	0.84	1.07	1.24
U_{zs}	m s^{-1}	0.12	0.15	0.16
U_e / U_m		1.16	1.15	1.13
$(U_e$ / $U_m)_{Dean}$		1.16	1.15	1.15
Re_m		6 366	8 029	9 628
Re_e		3 683	4 609	5 447
$Re_\tau = \delta^+$		198	240	282
δ	mm	3.98	3.92	3.99
δ^* / δ		0.14	0.14	0.13
θ / δ		0.10	0.10	0.09
H		1.44	1.42	1.36
G		5.70	5.66	5.12
$\dot{\gamma}_w \times 10^{-3}$	s^{-1}	2.25	3.41	4.56
τ_w	Pa	2.05	3.10	4.15
$\tau_{w,\,Dean}$	Pa	2.18	3.35	4.47
u_τ	mm s^{-1}	45.3	55.7	64.4
λ_v	µm	20.1	16.3	14.1
t_v	µs	443.9	293.5	219.3
$L_s^+ \times L_n^+$		178 × 262	219 × 322	253 × 373
$\Delta s^+ \times \Delta n^+$		2.3 × 2.3	2.9 × 2.9	3.3 × 3.3
U_m^+		16.1	16.7	17.1
U_e^+		18.6	19.2	19.3
$c_{f,e} \times 10^3$		7.73	7.15	6.87
$c_{f,m} \times 10^3$		8.17	7.71	7.37
$c_{f,Dean} \times 10^3$		5.77	5.43	5.37

Figure 6-2(*a*,*b*) depicts sample instantaneous wall-parallel and wall-normal velocity fluctuation fields of ZPG pure water flow at $Re_\tau = 282$, normalized by inner scales. The ranges of changes are adjusted to represent a visual contrast and do not necessarily denote the lower and upper bounds of the fluctuations. Velocity vectors are shown by black arrows on top of the plots and are scaled relative to the maximum velocity vector. High-speed and low-speed motions of fluid elements toward the wall or drifting away from it are evident in the fluctuating velocity fields.

Probability density functions (PDFs) of u_s^+ and u_n^+ in the ZPG pure water flow at $Re_\tau = 198$ are illustrated in Figure 6-3(*a*-*c*) for $n^+ = 14$, $n^+ = 49$, and $n^+ = 107$. Each PDF profile is compared to its corresponding Gaussian distribution fit, with a mean and standard deviation as of the measured distribution, shown with a dashed blue line. As Figure 6-3(*a*) shows, the distribution of u_s^+ at $n^+ = 14$ is not fully symmetric and shows a weak negative skewness. At the same near-wall position, the PDF of u_n^+ demonstrates a symmetric distribution with a large peak of ≈ 50 %,

slightly larger than the peak of its fitted Gaussian profile. This behavior indicates that almost one of each two instantaneous wall-normal velocity fluctuations is zero at this wall-normal position.

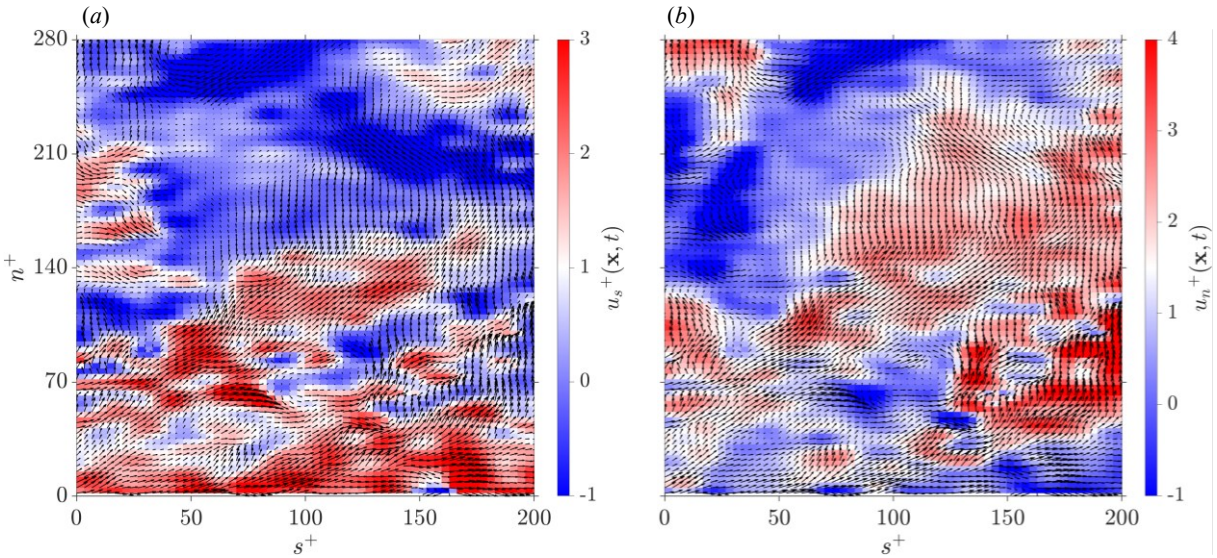

Figure 6-2 An instantaneous inner normalized (*a*) wall parallel and (*b*) wall-normal fluctuation velocity field at $Re_\tau = 282$ (see Table 6-1) for ZPG turbulent pure water flow (ZPG FOV in Figure 3-13). The fluctuating velocity vectors are shown by black arrows and are scaled for proper visualization.

Figure 6-3(*b*) demonstrates that at $n^+ = 49$, the distribution of wall-parallel velocity fluctuations is symmetric with a peak amplitude larger than the $n^+ = 14$ profile. The flatter tail of the u_s^+ profile at $n^+ = 14$ compared to its counterpart at $n^+ = 49$ indicates that the flow is more intermittent at this position in the buffer layer, with a relatively larger kurtosis. This region is adjacent to $n^+ \approx 12$, the location of the maximum turbulent production and the wall-parallel turbulence intensity peak in a fully developed ZPG channel flow (Kim et al., 1987).

The PDF of u_n^+ at $n^+ = 49$ is slightly negatively skewed, which shows a lower peak value and heavier tails (larger kurtosis) compared to its counterpart at $n^+ = 14$. As Figure 6-3(*c*) illustrates, the u_s^+ PDF distribution at $n^+ = 107$, has a weak positive skewness, indicating that the occurrence likelihood of weak positive u_s^+ is slightly more than negative u_s^+ fluctuations. Comparing the tail of the u_s^+ profile at $n^+ = 107$ with that at $n^+ = 49$, reveals a similar kurtosis level at both wall-normal positions in the outer layer and a marginally larger peak compared to the $n^+ = 49$ profile. The u_n^+ PDF profile at $n^+ = 107$ is symmetric and its peak value is relatively smaller than that at $n^+ = 49$.

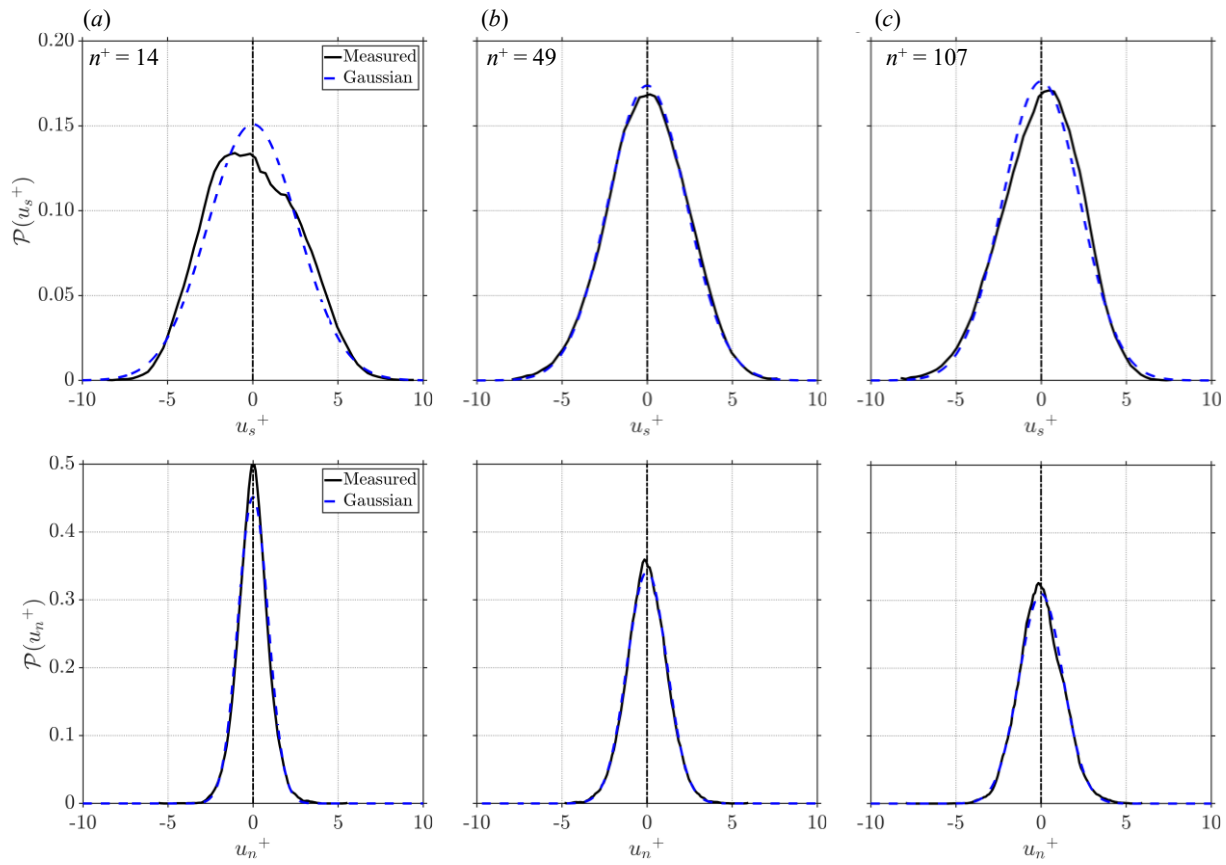

Figure 6-3 Probability density function (PDF) of the wall-parallel velocity fluctuations, u_s^+, and wall-normal velocity fluctuations, u_n^+, at (*a*) $n^+ = 13$, (*b*) $n^+ = 48$, and (*c*) $n^+ = 106$. The dashed blue profile on each figure shows a fitted normal distribution to the measured PDF. The results correspond to the ZPG pure water flow at $Re_\tau = 198$ (see Table 6-1).

6.2.1 Validation of the turbulence statistics

Figure 6-4 shows the statistical convergence of the ensemble-averaged wall-parallel velocity $\langle U_s \rangle$ at four different wall-normal positions for the ZPG pure water flow at $Re_\tau = 198$ (see Table 6-1). The long-time average, $\langle U_s \rangle_{N_t}$, normalizes the results at each wall position. Here, $N_t = 11\,000$ is the total number of the PIV velocity fields. The mean velocities converge into the reliability margin of $\pm 2\,\sigma_{u_s}/\langle U_s \rangle$ (Adrian and Westerweel, 2011), where $\sigma_{u_s}/\langle U_s \rangle$ denotes the normalized turbulence intensity and was assumed to have a representative value of $\sigma_{u_s} \approx 0.1$. Here, σ_{u_s} is the r.m.s. of the wall-parallel velocity fluctuations u_s, or the standard deviation of the instantaneous velocity U_s (see Appendix A).

The random noise of the mean velocity measurements was defined as the ratio of the maximum to the minimum difference of the last 20 % of $\langle U_s \rangle_N$ data to its associated long-time average $\langle U_s \rangle_{N_t}$,

i.e., $e_{\mathrm{R},\langle U_s\rangle}\% = \left[\left|\langle U_s\rangle_{N,\max} - \langle U_s\rangle_{N,\min}\right|/\langle U_s\rangle_{N_t}\right]_{0.8N_t\le N\le N_t}$. As listed in Table 6-2, the calculated random noises of the measured $\langle U_s\rangle$ were lower than 0.5 %, showing a good statistical convergence. In the tested flow conditions, random noises of the mean velocities were maximum near the wall and decreased for positions far from the wall.

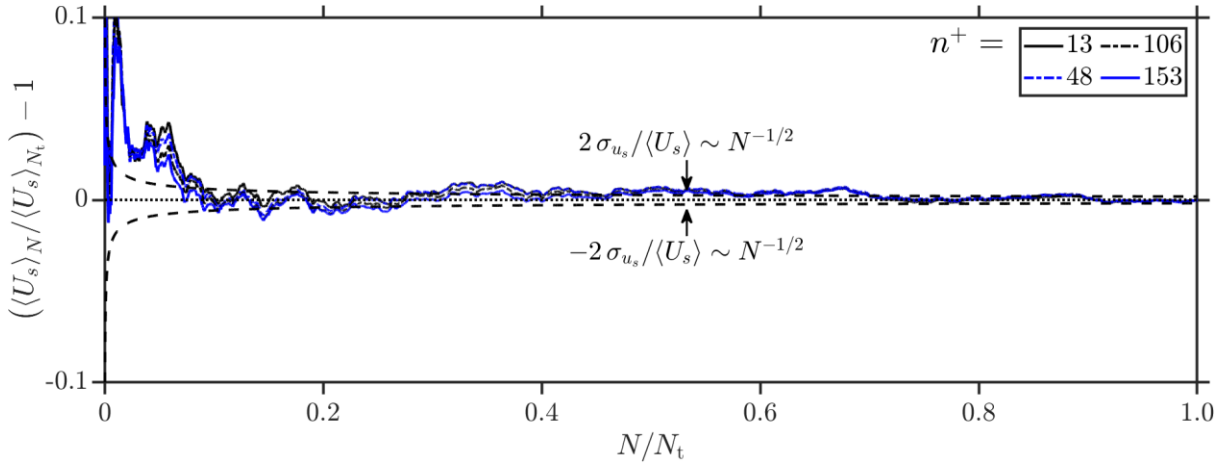

Figure 6-4 Variation of the ensemble-averaged streamwise velocity $\langle U_s\rangle$ at four different wall distances, as a function of the sample number N. The long-time average $\langle U_s\rangle_{N_t}$ normalizes the results, where N_t = 11 000, is the total number of velocity vector fields. The dashed black lines denote the reliability margins (Adrian and Westerweel, 2011). The results correspond to the ZPG pure water flow at Re_τ = 198 (see Table 6-1).

Table 6-2 Random noises of the mean wall-parallel velocity and Reynolds stresses at different wall-normal positions for the ZPG turbulent pure water flow at three different Re_τ (see Table 6-1).

	Re_τ = 198			Re_τ = 241			Re_τ = 282		
Parameter	n^+ = 14	n^+ = 49	n^+ = 119	n^+ = 17	n^+ = 60	n^+ = 146	n^+ = 19	n^+ = 69	n^+ = 169
$e_{\mathrm{R},\langle U_s\rangle}\%$	0.42	0.44	0.35	0.49	0.49	0.38	0.47	0.43	0.41
$e_{\mathrm{R},\langle u_s u_n\rangle}\%$	3.95	3.63	3.50	6.85	5.81	3.52	5.37	4.29	3.33
$e_{\mathrm{R},\langle u_s^2\rangle}\%$	1.17	2.56	3.44	1.68	3.51	3.91	2.67	2.82	4.57
$e_{\mathrm{R},\langle u_n^2\rangle}\%$	1.51	1.26	1.30	2.17	1.94	2.37	2.83	1.70	1.61

Figure 6-5(*a*) proves that the mean of the wall-parallel velocity fluctuations, $\langle u_s\rangle$, tends to zero by the long-time averaging used in the current study. Figure 6-5(*b-d*) illustrates the statistical convergence of the Reynolds stresses, each normalized by its long-time average. As seen, the N-sample averaged Reynolds shear stress $-\langle u_s u_n\rangle_N$ shows higher fluctuations compared to other Reynolds stresses. The random noises of measurements of the Reynolds stresses were calculated based on the same approach used for the mean velocity, using the last 20 % of the convergence data, and are listed in Table 6-2 for the tested Re_τ values. The random noises associated with $-\langle u_s u_n\rangle$ were overall higher than the wall-parallel and wall-normal Reynolds stresses at different wall-normal positions. With $e_{\mathrm{R}} < 7$ %, the measured Reynolds stresses show good statistical

convergence at different wall-normal positions. The random noise decreases systematically as the probed wall-normal positions move away from the wall.

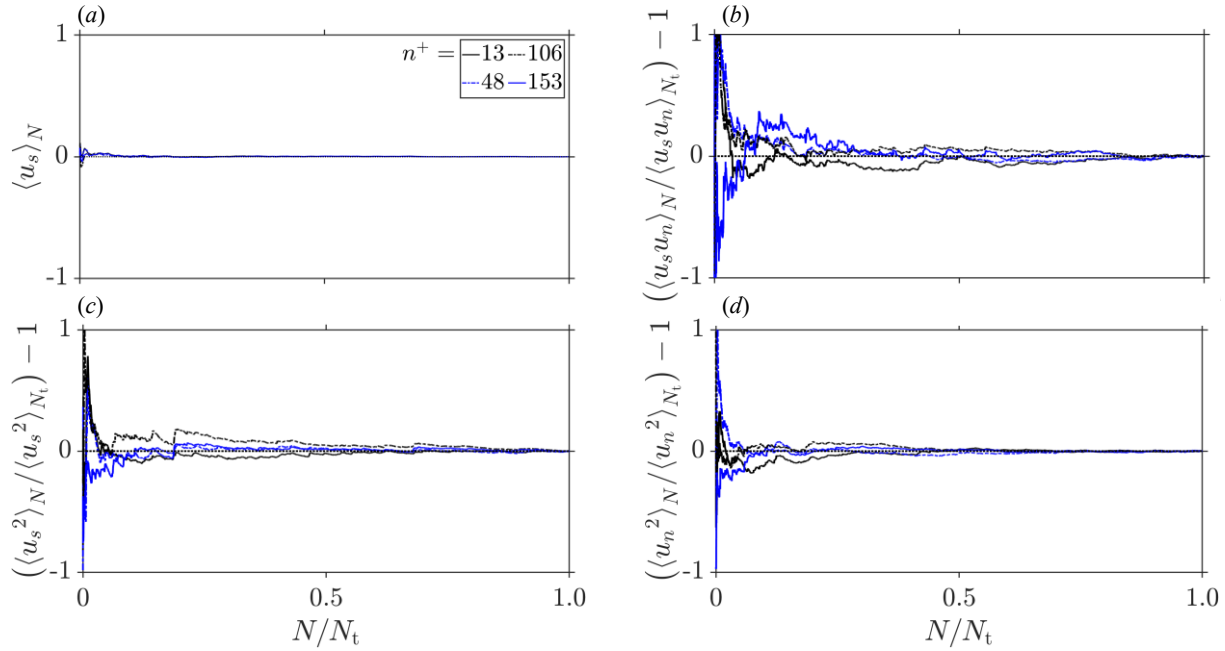

Figure 6-5 Statistical convergence of (*a*) $\langle u_s \rangle$, (*b*) $\langle u_s u_n \rangle$, (*c*) $\langle u_s^2 \rangle$, and (*d*) $\langle u_n^2 \rangle$ at four different wall distances. Here, N is the number of samples. Each profile is normalized by its corresponding long-time average. The results correspond to the ZPG pure water flow at $Re_\tau = 198$ (see Table 6-1).

Figure 6-6(*a-c*) illustrates the statistical convergence of the mean skewness, μ_3, and kurtosis, μ_4, (see Appendix A for formulations) at four different wall-normal positions for the ZPG pure water flow at $Re_\tau = 198$ (see Table 6-1). These higher-order statistics were calculated based on the wall-parallel component of the velocity fluctuation field, u_s.

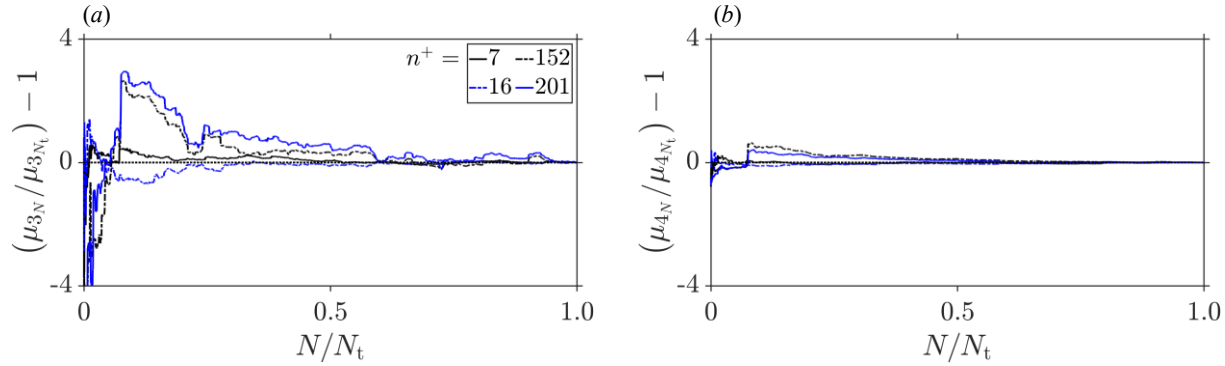

Figure 6-6 Statistical convergence of the (*a*) skewness, μ_3, and (*b*) kurtosis, μ_4, at four different wall distances. Here, N is the number of samples. Each profile is normalized by its corresponding long-time average. The results correspond to the ZPG pure water flow at $Re_\tau = 198$ (see Table 6-1).

The mean skewness values demonstrate higher fluctuations near the channel's centerline and start to converge when almost 90 % of the samples were used for averaging. The kurtosis converges faster than the skewness at the probed n^+ positions, where nearly 80 % of the samples were utilized for averaging. The convergence of the turbulence statistics was also quantified and confirmed for other tested flow conditions under the pressure gradients. The associated plots are not given here for brevity.

6.2.2 Uncertainty analysis

The uncertainties associated with the instantaneous PIV velocity fields and the resultant mean parameters, such as Reynolds stresses, were determined as an estimation of their corresponding measurement errors. For all the variables, the precision uncertainty, $\mathcal{U}_{\mathrm{P}}$, was estimated from the acquired data, and whenever applicable, the bias uncertainties, $\mathcal{U}_{\mathrm{B}}$, were also assessed using the manufacturers' specifications for the accuracy of the devices or from measurement calibrations.

As per the guidelines of the International Standards Organization, the precision uncertainty of a variable ϕ with a confidence interval of 95 % measured for $N_{\mathrm{t}} \geq 30$ observations is:

$$\mathcal{U}_{\mathrm{P},\phi} = 1.96\sigma_{\phi}/\sqrt{N_{\mathrm{t}}}, \tag{6-7}$$

where σ_{ϕ} is the standard deviation of the variable ϕ for N_{t} observations. For $N < 30$,

$$\mathcal{U}_{\mathrm{P},\phi} = 4.303\sigma_{\phi}/\sqrt{N_{\mathrm{t}}}. \tag{6-8}$$

The uncertainty of a variable F, a function of independent variables ϕ_i, i.e., $F = F(\phi_1, \phi_2, \ldots, \phi_M)$ can be approximated as:

$$\mathcal{U}_F^2 = \sum_{i=1}^{M} \left(\frac{\partial F}{\partial \phi_i}\right)^2 \mathcal{U}_{\phi_i}^2, \tag{6-9}$$

as long as the errors are small, random and independent.

1.1.1.1 Instantaneous velocity fields

An instantaneous wall-parallel PIV velocity component at a point in the flow field is defined as $U_s = \Delta s/\Delta t = \Delta S/(M\,\Delta t_{\mathrm{PIV}})$, where Δs and ΔS are the displacement magnitudes in the physical and image coordinates, M is the magnification factor and Δt_{PIV} is the timing between two PIV frames.

The bias uncertainty of U_s can be estimated by propagating the bias uncertainties of the independent variables using equation (6-9) as (Adrian and Westerweel, 2011):

$$\left(\frac{\mathcal{U}_{\mathrm{B},U_s}}{U_s}\right)^2 = \left(\frac{\mathcal{U}_{\mathrm{B},\Delta S}}{\Delta S}\right)^2 + \left(\frac{\mathcal{U}_{\mathrm{B},\Delta t_{\mathrm{PIV}}}}{\Delta t_{\mathrm{PIV}}}\right)^2 + \left(\frac{\mathcal{U}_{\mathrm{B},M}}{M}\right)^2, \tag{6-10}$$

where $\mathcal{U}_{\mathrm{B},\Delta S} \approx 0.1\ D_\mathrm{p}$. As given in Table 3-6, in this study, the mean particle image size is D_p = 2.86 pixels, M = 3.4 and Δt_{PIV} = 40-60 µs for the tested ZPG pure water flow measurements. The r.m.s. magnitude of the mapping fit function for image calibration was assumed to be the bias uncertainty of magnification, i.e., $\mathcal{U}_{\mathrm{B},M}$ = 0.13.

The bias uncertainty of the timing was assumed to equal the rise and fall times of the utilized LED, which was $\mathcal{U}_{\mathrm{B},\Delta t_{\mathrm{PIV}}}$ = 0.5 µs according to the manufacturer (iLA.LPS v3; ILA 5150 GmbH). The maximum bias uncertainty of the velocity measurements is of interest here, which, according to equation (6-9), occurs for the minimum Δt_{PIV} and ΔS. In the investigated flow fields, $(\Delta t_{\mathrm{PIV}})_{\mathrm{min}}$ = 40 µs and $(\Delta S)_{\mathrm{min}} \approx$ 5.1 pixels. The relative percentage of the contribution of each parameter on the maximum bias uncertainty of U_s is:

$$\left(\mathcal{U}_{\mathrm{B},\Delta S}/\Delta S\right)_{\mathrm{max}} \times 100\ \% \approx 5.6\ \%,$$
$$\left(\mathcal{U}_{\mathrm{B},\Delta t_{\mathrm{PIV}}}/\Delta t_{\mathrm{PIV}}\right)_{\mathrm{max}} \times 100\ \% \approx 1.3\ \%,$$
$$\left(\mathcal{U}_{\mathrm{B},M}/M\right)_{\mathrm{max}} \times 100\ \% \approx 3.8\ \%,$$

which results in $\left(\mathcal{U}_{\mathrm{B},U_s}/U_s\right)_{\mathrm{max}} \times 100\ \% \approx 6.9\ \%$. The results suggest that for the tested flow conditions, the timing, magnification (or calibration) and displacement uncertainties have the weakest to strongest effects on the maximum bias uncertainty of the instantaneous U_s velocities. As a result, the combined effect of the bias uncertainties can lead to an error of as high as ≈ 7 % of the measured wall-parallel velocity field.

The precision (or random) uncertainties of the instantaneous velocity fields were calculated using the correlation statistics method (Wieneke, 2015) in Commercial software (DaVis V8.4; LaVision GmbH). This method uses the variation of the intensity patterns between the two PIV frames to estimate the uncertainty of the instantaneous velocity fields (Wieneke, 2015). For each flow scenario, the instantaneous uncertainty fields of the wall parallel and wall-normal velocity fields, i.e., $\mathcal{U}_{U_s}(\boldsymbol{x},t)$ and $\mathcal{U}_{U_n}(\boldsymbol{x},t)$ were ensemble averaged using $N_\mathrm{t} \approx$ 11 000 samples, assuming a statistically stationary flow field. The resultant ensemble-averaged fields, $\langle\mathcal{U}_{U_s}\rangle(\boldsymbol{x})$ and

$\langle \mathcal{U}_{U_n} \rangle(\boldsymbol{x})$, were then spatially averaged in the wall-parallel direction, s, for the ZPG flows, assuming a homogeneous turbulent flow in this direction. The variation of the resultant mean uncertainty profiles of $\overline{\langle \mathcal{U}_{U_s} \rangle}(n)$ and $\overline{\langle \mathcal{U}_{U_n} \rangle}(n)$, normalized by their corresponding mean velocities U_m (see Table 6-1) are plotted in Figure 6-7(a,b) for the ZPG pure water flow.

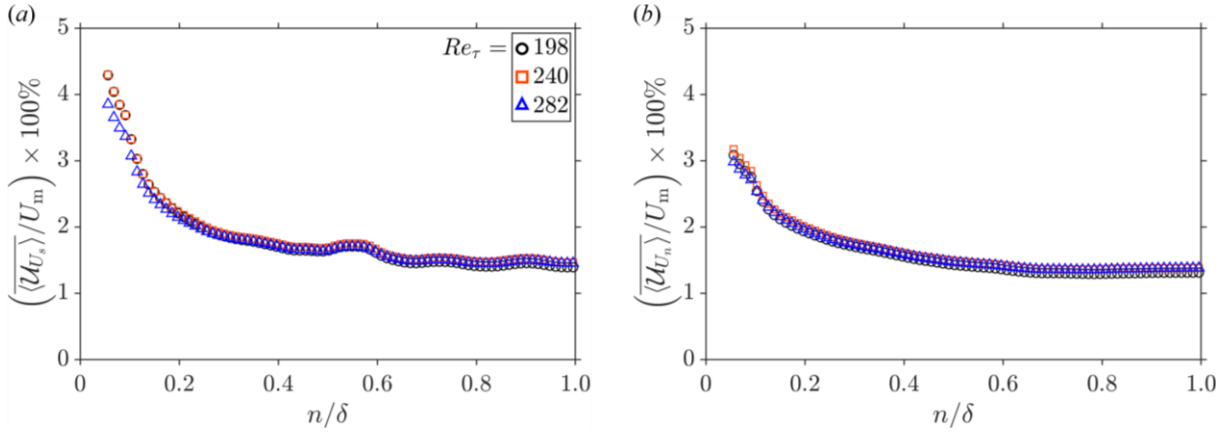

Figure 6-7 Wall-normal variations of the percentage of the ensemble and spatially averaged instantaneous uncertainties of the (a) wall-parallel and (b) wall-normal velocity fields relative to their corresponding mean velocities U_m (see Table 6-1). The instantaneous uncertainty fields were obtained using the correlation statistics method (Wieneke, 2015).

As Figure 6-7(a) illustrates, $\overline{\langle \mathcal{U}_{U_s} \rangle}$ is relatively higher in the near-wall region, where it can be as high as 4.5 % of the mean velocity. In the regions far away from the wall $\overline{\langle \mathcal{U}_{U_s} \rangle}$ shows a gradual reduction to smaller uncertainties in the order of 2 % of U_m. Wall-normal variation of $\overline{\langle \mathcal{U}_{U_n} \rangle}$, illustrated in Figure 6-7(b), indicates a similar trend as $\overline{\langle \mathcal{U}_{U_s} \rangle}$, but with relatively smaller uncertainties. The maximum of $\overline{\langle \mathcal{U}_{U_n} \rangle}$ happens close to the wall, where it is ≈ 3 % of U_m, and shows uncertainties in the order of 1.5 % of U_m away from the wall.

Figure 6-8(a,b) illustrates the temporal changes of the instantaneous wall-parallel and wall-normal uncertainties for ZPG pure water flow with $Re_\tau = 282$, spatially averaged over the area covered by the FOV and normalized by their corresponding mean wall-parallel velocities. Here, N shows the sample number, and $N_\mathrm{t} \approx 11\,000$ is the total number of the obtained PIV velocity fields. The wall-parallel uncertainty fluctuations show peak values of ≈ 0.030 U_m and minimum values of ≈ 0.015 U_m, with a mean of $\langle \bar{\bar{\mathcal{U}}}_{U_s} \rangle = 0.020\ U_\mathrm{m}$ and standard deviation of $\sigma_{\bar{\bar{\mathcal{U}}}_{U_s}} = 0.0023\ U_\mathrm{m}$, indicating a statistically stationary flow. The temporal changes of the mean wall-normal velocity

uncertainties, shown in Figure 6-8(*b*), show a similar trend of stable changes, with a mean of $\langle \bar{\bar{\mathcal{U}}}_{U_n} \rangle = 0.018\ U_\mathrm{m}$ and a standard deviation of $\sigma_{\bar{\bar{\mathcal{U}}}_{U_n}} = 0.0021\ U_\mathrm{m}$.

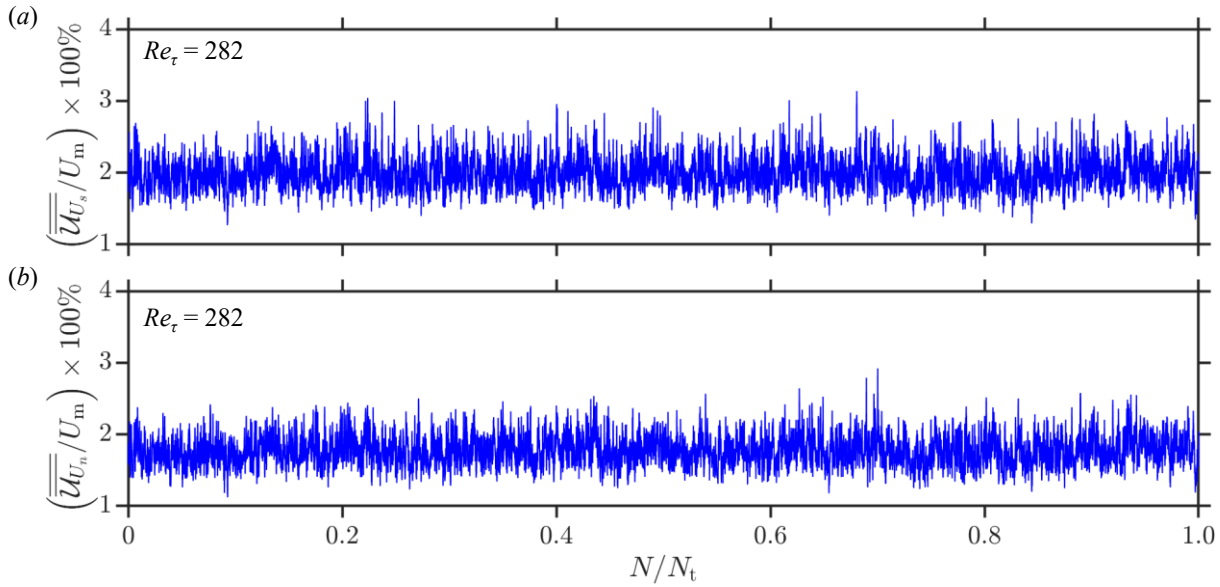

Figure 6-8 Percentage of the temporal changes of the instantaneous (*a*) wall-parallel and (*b*) wall-normal uncertainties for ZPG pure water flow with $Re_\tau = 282$ (see Table 6-1) relative to its mean velocity $U_\mathrm{m} = 1.1$ m s^{-1}, spatially averaged over the area covered by the FOV. Here, $N_\mathrm{t} \approx 11\ 000$.

1.1.1.2 Mean fields

The precision uncertainty of the mean wall-parallel flow field $\langle U_s \rangle$ is formulated as (Benedict and Gould, 1996; Sciacchitano and Wieneke, 2016):

$$\mathcal{U}_{\mathrm{P},\langle U_s \rangle} = \sigma_{u_s}/\sqrt{N_\mathrm{t}}, \tag{6-11}$$

where σ_{u_s} is the standard deviation of the instantaneous velocity fields U_s for N_t observations, as defined in Appendix A. The precision uncertainty of the mean Reynolds shear stress is (Sciacchitano and Wieneke, 2016):

$$\mathcal{U}_{\mathrm{P},\langle u_s u_n \rangle} = \sigma_{u_s}\sigma_{u_n}\sqrt{(1 + r_{sn}^2)/(N_\mathrm{t} - 1)}, \tag{6-12}$$

where r_{sn} is the autocorrelation coefficient of the fluctuating velocity fields u_s and u_n defined in equation (A-7) of Appendix A. Accordingly, with $i = s, n$,

$$\mathcal{U}_{\mathrm{P},\langle u_i^2 \rangle} = \langle u_i^2 \rangle \sqrt{2/N_\mathrm{t}}. \tag{6-13}$$

Figure 6-9(*a-d*) illustrates the percentage variations of the spatially averaged normalized uncertainties of the mean velocity and Reynolds stresses in the wall-normal direction. The

uncertainties in the measurement of the near-wall mean velocity $\langle U_s \rangle$ do not exceed 0.2 % of the mean velocity U_m, which decreases to lower values in regions far from the wall. This trend is almost similar for the three different tested ZPG water flows. Figure 6-9(b) shows that in the wall region and adjacent to the center of the channel, the uncertainties in the measurement of the Reynolds shear stresses can be as high as 7 % and 10 % of the local $-\overline{\langle u_s u_n \rangle}$. The relative uncertainties reduce to 2 - 3 % in the regions away from the wall and the centerline.

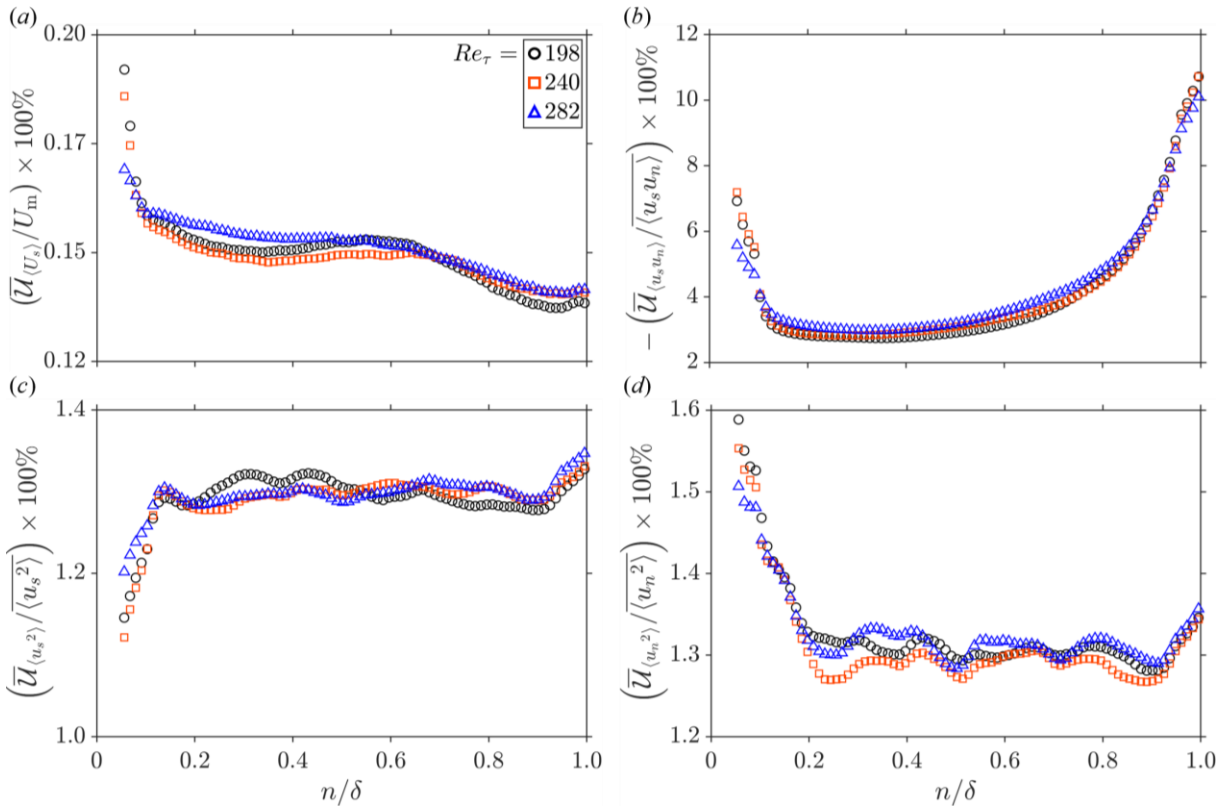

Figure 6-9 Wall-normal percentage variation of the spatially averaged normalized uncertainties of the mean (a) wall-parallel velocity, (b) Reynolds shear stress, (c) wall-parallel, and (d) wall-normal Reynolds stresses.

The estimated uncertainties of the mean wall-parallel Reynolds stress, shown in Figure 6-9(c), are relatively lower than the uncertainties of the Reynolds shear stress at different wall-normal positions. They have a minimum value of ≈ 1.1 % at the nearest detected position to the wall, which gradually increases to values of $\mathcal{O}$(1.3 %) of the local $\overline{\langle u_s^2 \rangle}$ in regions far away from the wall. Near the channel's center, the uncertainty marginally increases but does not exceed 1.3 %. Figure 6-9(d) demonstrates the wall-normal changes of the uncertainties of the wall-normal Reynolds stress. The peak uncertainty occurs close to the wall, where it is ≈ 1.6 % of the local $\overline{\langle u_n^2 \rangle}$. Away from the wall, the uncertainties reduce to $\mathcal{O}$(1.3 %) of the local $\overline{\langle u_n^2 \rangle}$.

1.1.1.3 Scaling parameters

The uncertainty of the mean wall shear stress $\mathcal{U}_{\tau_w}$ was estimated by propagating the uncertainty of the wall shear viscosity, $\mathcal{U}_{\mu_w}$, and uncertainty of the mean wall shear strain rate, $\mathcal{U}_{\dot{\gamma}_w}$, using equation (2-18) and equation (6-9):

$$\left(\frac{\mathcal{U}_{\tau_w}}{\tau_w}\right)^2 = \left(\frac{\mathcal{U}_{\mu_w}}{\mu_w}\right)^2 + \left(\frac{\mathcal{U}_{\dot{\gamma}_w}}{\dot{\gamma}_w}\right)^2. \tag{6-14}$$

No specific information was found from the resources provided by the manufacturer to estimate the bias uncertainty of the shear viscosity measurements. The precision uncertainty of the wall shear viscosity in each flow solution was estimated using equation (6-8) for $N_t = 3$ repetitions for all measurement points shown in Figure 4-1(*a*). In each solution flow, $\left(\mathcal{U}_{\mu_w}/\mu_w\right)$ was averaged for all measurement points and are listed in Table 6-3 as the estimated uncertainties of wall shear-viscosities in different solution flows.

The mean shear strain rate of the wall was determined by fitting a line to the mean velocity profile in the viscous sublayer. Investigation of the fitted lines showed that the maximum root mean square error (r.m.s.e.) of fit was ≈ 0.011 s^{-1}. This value is considered as the uncertainty in the determination of $\dot{\gamma}_w$, i.e., $\mathcal{U}_{\dot{\gamma}_w}$ = 0.011 s^{-1}. As given in Table 6-1, $\dot{\gamma}_w$ = 2 250 s^{-1} was the lowest measured strain rate, which results in a maximum uncertainty of the strain rate of $\left(\mathcal{U}_{\dot{\gamma}_w}/\dot{\gamma}_w\right)_{max} \times 100\ \% \approx 5 \times 10^{-4}$, which is inconsequential compared with the uncertainty of the μ_w measurements. As the results show, the uncertainties of the wall shear stress measurements are significantly affected by the uncertainties of the viscosity measurements, which are relatively higher for the 100 p.p.m. and 200 p.p.m. PAM solutions.

The uncertainty of the friction velocity u_τ can be estimated using the propagation uncertainty given in equation (6-9) as:

$$\left(\frac{\mathcal{U}_{u_\tau}}{u_\tau}\right)^2 = \frac{1}{4}\left[\left(\frac{\mathcal{U}_{\tau_w}}{\tau_w}\right)^2 + \left(\frac{\mathcal{U}_{\rho_L}}{\rho_L}\right)^2\right]. \tag{6-15}$$

Similarly, the uncertainty of the viscous length scale λ_v is:

$$\left(\frac{\mathcal{U}_{\lambda_v}}{\lambda_v}\right)^2 = \left(\frac{\mathcal{U}_{\mu_w}}{\mu_w}\right)^2 + \left(\frac{\mathcal{U}_{u_\tau}}{u_\tau}\right)^2. \tag{6-16}$$

The uncertainty of the wall-normal position n, normalized by λ_v and δ are:

$$\left(\frac{\mathcal{U}_{n/\lambda_v}}{n/\lambda_v}\right)^2 = \left(\frac{\mathcal{U}_n}{n}\right)^2 + \left(\frac{\mathcal{U}_{\lambda_v}}{\lambda_v}\right)^2. \tag{6-17}$$

$$\left(\frac{\mathcal{U}_{n/\delta}}{n/\delta}\right)^2 = \left(\frac{\mathcal{U}_n}{n}\right)^2 + \left(\frac{\mathcal{U}_\delta}{\delta}\right)^2. \tag{6-18}$$

Here, $\langle\rho_L\rangle$ = 1000 kg m^{-3}, $\mathcal{U}_{P,\rho_L}$ = 0.078 kg m^{-3}, with σ_{ρ_L} = 1.25 kg m^{-3} and N_t = 1000, from the flowmeter measurements discussed in Section 3.3. According to the manufacturer (Krohne Optimass 7000), the accuracy in the density measurements was ± 0.5 kg m^{-3} for on-site calibrations. This value is assumed to be the bias uncertainty of the density measurements, i.e., $\mathcal{U}_{B,\rho_L}$ = 0.5 kg m^{-3}, which results in $\left(\mathcal{U}_{\rho_L}/\rho_L\right) \times 100$ % = 5.06 × 10^{-4} %. As seen, this uncertainty value is insignificant compared with $\mathcal{U}_{\tau_w}$, which, as listed in Table 6-3, implies that the relative wall shear stress uncertainty is 2 × the relative uncertainty of the friction velocity.

Table 6-3 Estimated relative percentage of the mean uncertainties of the scaling parameters.

C_s (p.p.m.)	Pure water	100	200	400
$\left(\mathcal{U}_{\mu_w}/\mu_w\right) \times 100$ %	8.4	22.3	24.1	2.5
$\left(\mathcal{U}_{\tau_w}/\tau_w\right) \times 100$ %	8.4	22.3	24.1	2.5
$\left(\mathcal{U}_{u_\tau}/u_\tau\right) \times 100$ %	4.2	11.2	12.1	1.3
$\left(\mathcal{U}_{\lambda_v}/\lambda_v\right) \times 100$ %	9.4	25.0	27.0	2.8
$\left[\mathcal{U}_{n/\lambda_v}/(n/\lambda_v)\right]_{max} \times 100$ %	9.4	25.0	27.0	2.8

In this study, the uncertainty in estimating the wall-normal position was assumed to equal the image calibration error, which was ≈ 0.13 pixels. The smallest resolvable normal position above the wall equals the spatial resolution in the wall-normal direction, which was ≈ 8 pixels. Therefore, $(\mathcal{U}_n/n)_{max} \times 100$ % ≈ 1.63 %. The uncertainty in determining the boundary layer thickness was assumed to be a combination of the uncertainties of the mean edge velocity and the wall position. Here, $\left(\mathcal{U}_{U_e}/U_e\right) \times 100$ % = 0.13 % (see Figure 6-9*a*) and $\mathcal{U}_{n_w}$ ≈ 0.85 pixels (see Section 3.5.4) or $\left(\mathcal{U}_{n_w}/\Delta n\right) \times 100$ % = 10.65 %. As a result, $(\mathcal{U}_\delta/\delta) \times 100$ % ≈ 10.65 %, indicating that the error in the estimation of the wall position significantly affects the uncertainty of δ and errors in determining the edge velocity are relatively inconsequential.

6.2.3 Mean flow

The mean wall-parallel velocity profiles of the fully developed ZPG pure water flow, normalized by their corresponding inner scales, $\langle U_s\rangle^+$, are plotted in Figure 6-10(*a*) versus the

inner-normalized wall-normal position, n^+. The horizontal axis of n^+ has a logarithmic scale. The linear, $\langle U_s \rangle^+ = n^+$, and the standard logarithmic law of the wall, $\langle U_s \rangle^+ = 2.44 \ln(n^+) + 5.5$, were also plotted i Figure 6-10(a) and are shown by black dashed lines. As results demonstrate, the inner-normalized mean velocity profiles collapse on a similar profile and follow the law of the wall in the viscous sublayer ($n^+ < 5$) and log-law region ($n^+ > 30$). There is a marginal deviation of the profiles above the standard logarithmic law in $20 < n^+ < 30$, near the end of the buffer layer.

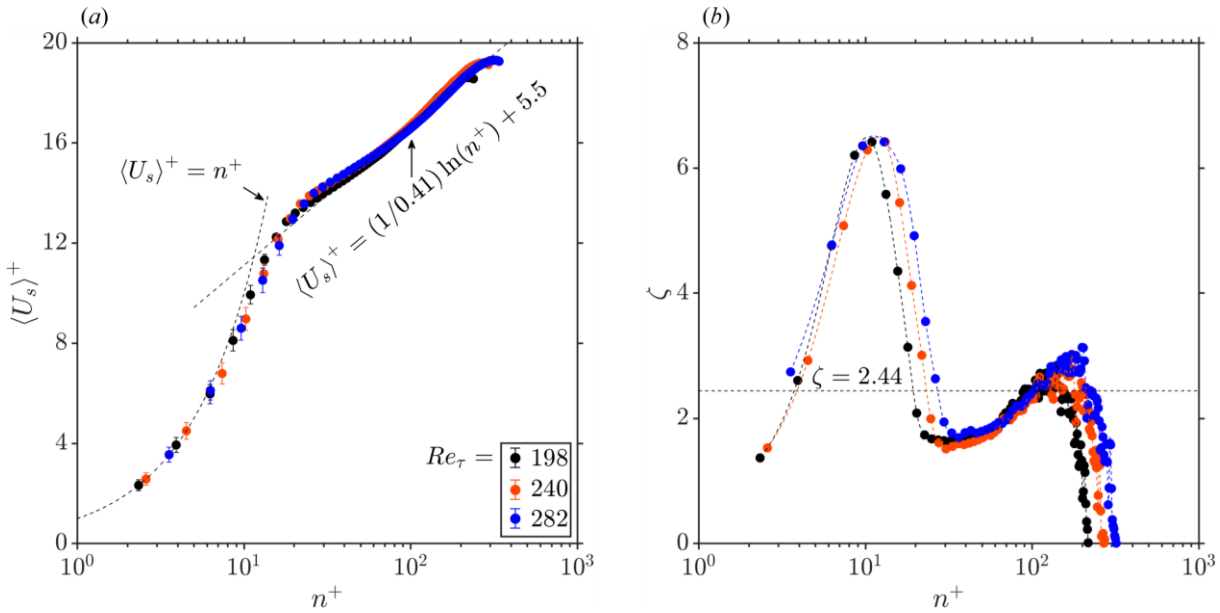

Figure 6-10 Inner normalized (a) mean wall-parallel velocity, $\langle U_s \rangle^+$, and (b) indicator function, ζ, variations with the inner normalized wall-normal position, n^+, for the ZPG turbulent pure water flow at three different Re_τ (see Table 6-1). Here, $\zeta = n^+ \, d\langle U_s \rangle^+ / dn^+$ and dashed lines plotted on (b) are only to clarify the trend of changes.

The log-indicator function, defined as $\zeta = n^+ \, d\langle U_s \rangle^+ / dn^+$, was calculated for each mean velocity profile of Figure 6-10(a), and the resultant profiles are illustrated in Figure 6-10(b). The log-indicator function equals the inverse Kármán constant for the standard logarithmic law, i.e., $\zeta = \kappa^{-1} \approx 2.44$. This line is plotted as a black dashed line in Figure 6-10(b). The ζ profiles almost collapse at $n^+ < 10$ and show their first peak at $n^+ \approx 12$, very close to the intersection point of the linear and logarithmic laws, which is $n^+ = 11.41$. As Re_τ increases, the log indicators show slightly wider profile shapes and exhibit their minimum to occur in the range of $30 < n^+ < 40$. The second peaks of the ζ profiles occur at the centerline of the channel, with peak values marginally larger than $\zeta = 2.44$.

Figure 6-11(a,b) illustrates the $\langle U_s \rangle$ profiles of Figure 6-10(a), normalized by two different outer scales. The mean profiles collapse in Figure 6-11(a) when normalized by U_e and δ. In

Figure 6-11(*b*), the Zagarola-Smits velocity (Zagarola and Smits, 1998), U_{zs}, normalizes the mean velocities, and as seen, profiles of $Re_\tau = 198$ and $Re_\tau = 240$ marginally collapse, but $Re_\tau = 282$ profile shows a positive upward offset from the other two, particularly out of the inner layer ($n/\delta > 0.1$).

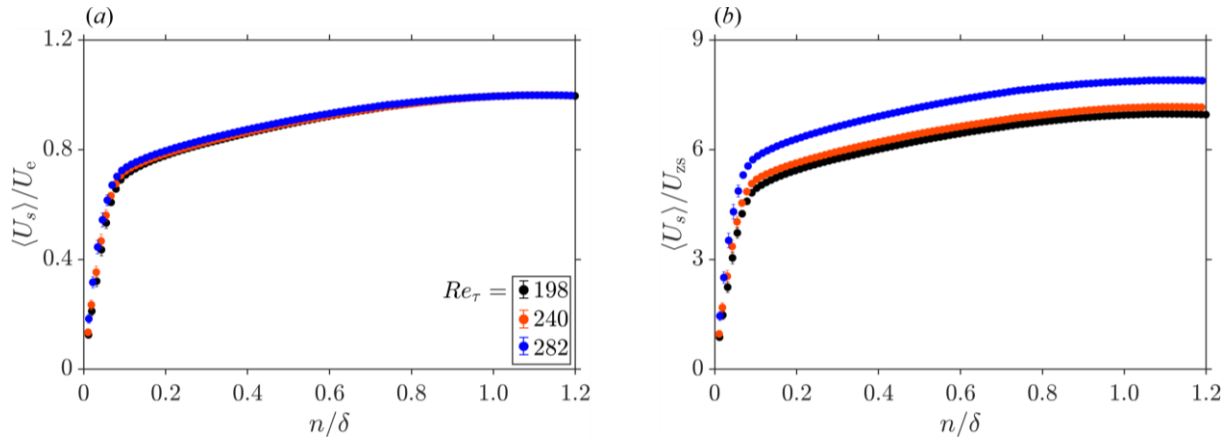

Figure 6-11 Variation of the mean wall-parallel velocity profiles, normalized by (*a*) boundary layer edge velocity, U_e, and (*b*) Zagarola-Smits velocity (Zagarola and Smits, 1998), U_{zs}, with the wall-normal position, normalized by the boundary layer thickness δ, for the ZPG turbulent pure water flow at three different Re_τ (see Table 6-1).

The variation of the inner-normalized mean Reynolds shear stress, $-\langle u_s u_n \rangle^+$, with n^+ is plotted in Figure 6-12(*a*) for three different Re_τ. The resultant profiles do not collapse onto a similar profile and show a peak value of $-\langle u_s u_n \rangle^+ \approx 1.0$ at $n^+ \approx 100$. For $Re_\tau = 282$, the peak of $-\langle u_s u_n \rangle^+$ shows a slight positive shift and occurs at $n^+ \approx 120$. When normalized by the outer scales, Figure 6-12(*b*) shows that mean Reynolds shear stresses almost collapse in the wall region, $n < 0.2\ \delta$, and near the centerline, $n > 0.8\ \delta$. In $0.2\ \delta < n < 0.8\ \delta$, $Re_\tau = 198$ shows a slightly higher peak value than the other two, which almost collapse and have an almost equal peak value.

Figure 6-12(*b*) and Figure 6-12(*e*) illustrate the variations of the mean wall-parallel Reynolds shear stress when normalized by the inner and outer scales. The peak occurs at $n^+ \approx 15$ for the tested flow conditions, and after a gradual decrease, demonstrates a plateau in $50 < n^+ < 90$. After $n^+ > 100$, the $\langle u_s^2 \rangle^+$ profiles decrease with a steeper slope relative to the near wall. As Figure 6-12(*b*) shows, increasing Re_τ shifts the $\langle u_s^2 \rangle^+$ profiles upward. As shown in Figure 6-12(*e*), $Re_\tau = 240$ profile collapses on the $Re_\tau = 198$ profile in $n < 0.6\ \delta$ and deviates from it and collapses on the $Re_\tau = 282$ profile in $n > 0.6\ \delta$. The variations of the wall-normal stresses at three different Re_τ are illustrated as normalized by inner scales in Figure 6-12(*c*) and by outer scales in Figure 6-12(*f*). The inner normalized profiles show a plateau at $n^+ \approx 100$, which indicates

a positive upward shift as Re_τ increases. The outer normalized profiles almost collapse onto a similar profile over the entire tested wall positions. The Re_τ = 198 profile slightly deviates from the other two wallward near the centerline in $n > 0.8\ \delta$ region.

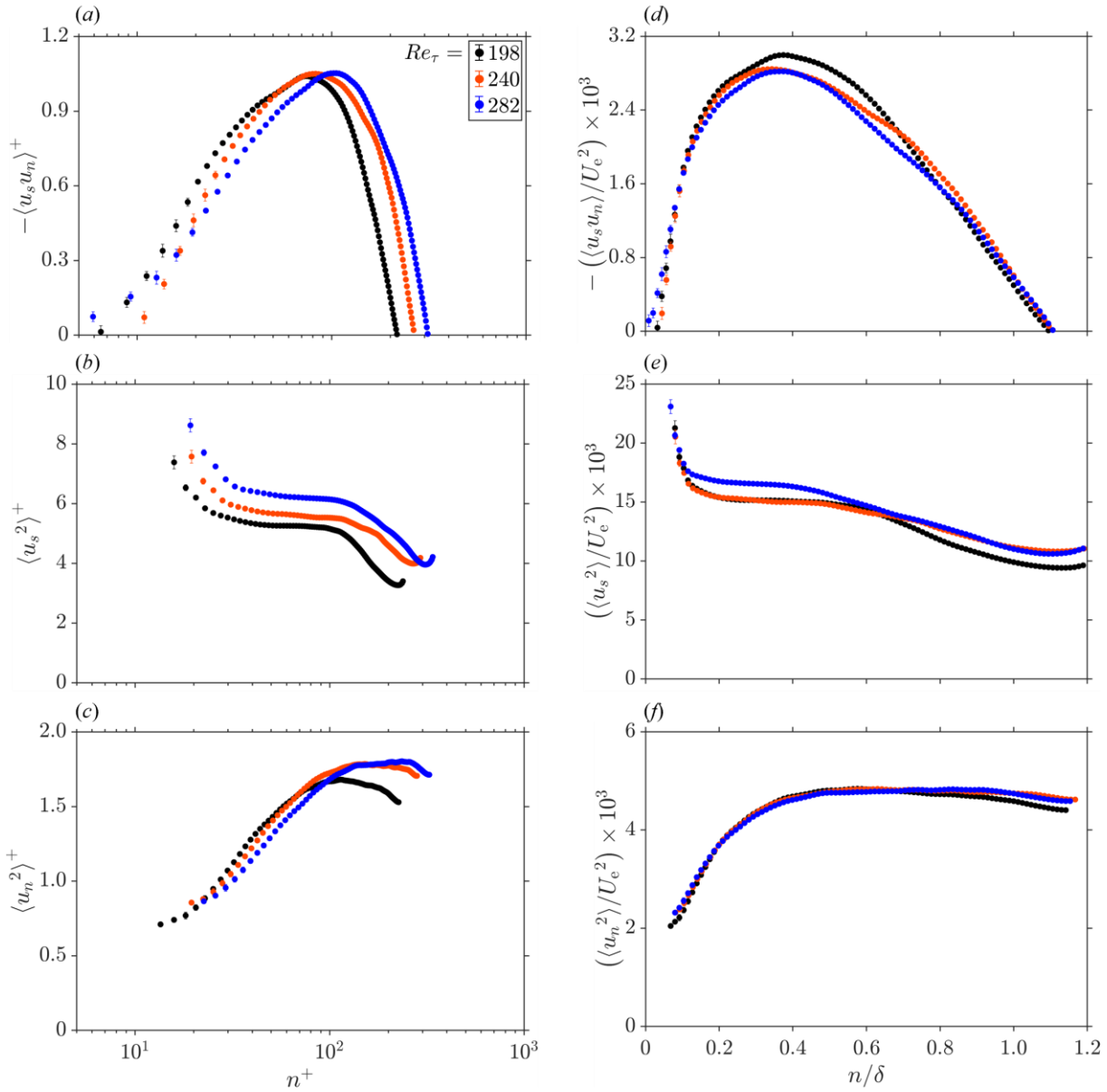

Figure 6-12 Inner normalized mean (*a*) Reynolds shear stress, $-\langle u_s u_n\rangle^+$, (*b*) wall-parallel Reynolds stress, $\langle u_s^2\rangle^+$, (*c*) wall-normal Reynolds stress, $\langle u_n^2\rangle^+$ with the inner normalized wall-normal position, n^+, and outer normalized mean (*d*) $-\langle u_s u_n\rangle/U_e^2$, (*e*) $\langle u_s^2\rangle/U_e^2$, and (*f*) $\langle u_n^2\rangle/U_e^2$, variations with the outer normalized wall-normal position, $n\ /\ \delta$, for the ZPG turbulent pure water flow at three different Re_τ (see Table 6-1).

Variations of the mean skewness, μ_3, and kurtosis, μ_4, with wall-normal positions normalized by the inner and outer length scales are given in Figure 6-13(*a-d*). For a normal Gaussian distribution, $\mu_3 = 0$ and $\mu_4 = 3$, which are denoted by black dashed lines on their corresponding

plots in Figure 6-13(*a-d*). The skewness profiles indicate elevated levels of uncertainty in the wall region and adjacent to the center of the channel. The skewness values oscillate in the range of $-0.4 < \mu_3 < 0.1$ and have their negative peaks in $100 < n^+ < 200$ (or $0.70 < n/\delta < 0.75$). The negative skewness values over the BL indicate that the low-speed ($u_s < 0$) fluid elements are more active than the high-speed ($u_s > 0$) elements and this activity is enhanced in the outer layer. The kurtosis of the tested mean velocity fields demonstrates high uncertainty levels, as illustrated in Figure 6-13(*c,d*). Their magnitudes vary between ≈ 2.7 and ≈ 4.0 and significantly deviate from the normal kurtosis adjacent to the center of the channel.

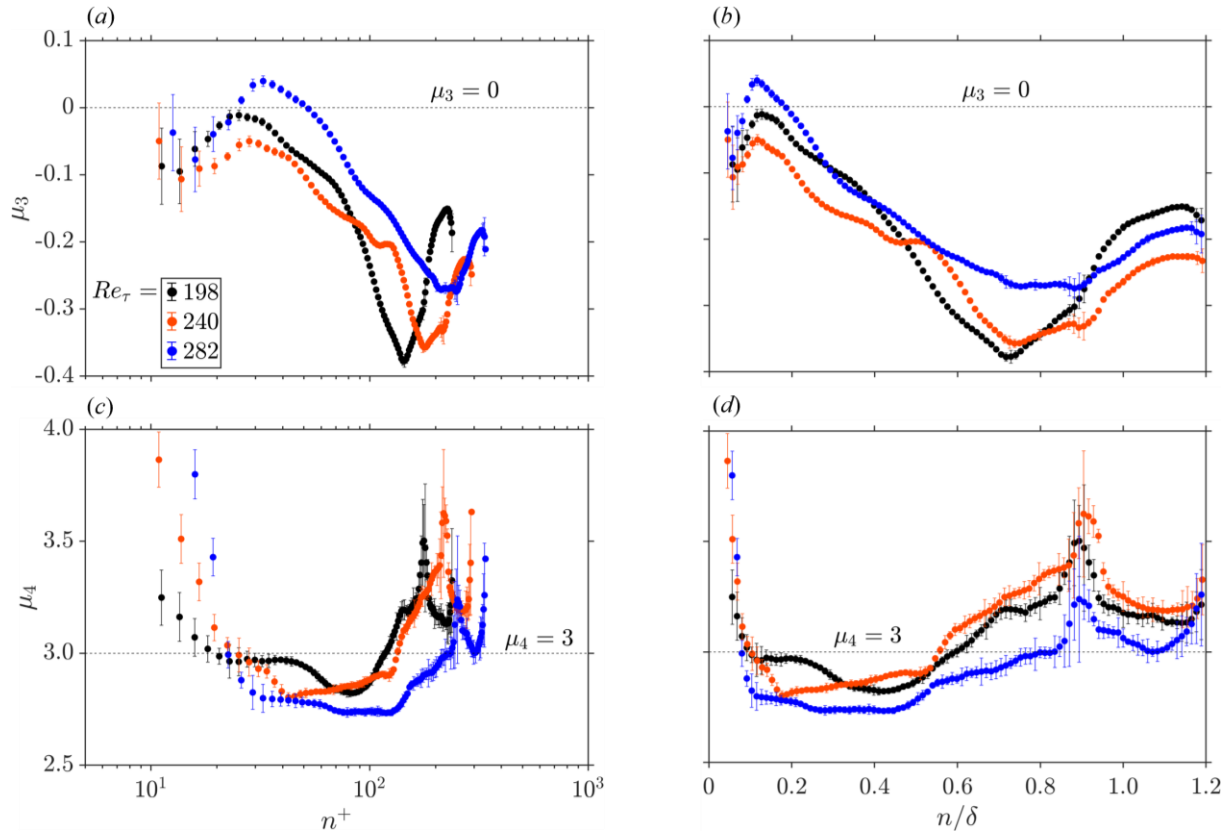

Figure 6-13 Variation of the mean skewness, μ_3, with the wall-normal positions, normalized by the (*a*) inner and (*b*) outer scales, and kurtosis, μ_4, with the wall-normal positions, normalized by the (*c*) inner and (*d*) outer scales, for the ZPG turbulent pure water flow at three different Re_τ (see Table 6-1).

6.2.4 Quadrant analysis

As explained by Wallace et al. (1972) and Willmarth and Lu (1972) and shown in Figure 6-14(*a-c*), the interaction of high-speed ($u_s > 0$) and low-speed ($u_s < 0$) fluid elements with the ones reflected outward from the wall ($u_n > 0$) or deflected towards the wall ($u_n < 0$) can be described on a 2D plot, with the horizontal and vertical axes representing the instantaneous

u_s ($\boldsymbol{x}_0$, t) and u_n ($\boldsymbol{x}_0$, t) at a known flow position $\boldsymbol{x}_0$. Based on the sign of the velocity fluctuations, such a plot can be divided into four quadrants: Q_1 to Q_4. Here, Q_1 represents the interaction of the high-speed fluid elements with the ones reflected outward from the wall. Similarly, Q_3 highlights the deflected motion of low-speed fluid elements toward the wall. The quadrant Q_2 demonstrate ejection events, where low-speed elements are ejected from the wall. In Q_4, high-speed fluids sweep the fluid elements moving toward the wall and generate sweep events. The Q_2 and Q_4 quadrants are associated with positive Reynolds stress-producing motions (Wallace et al., 1972).

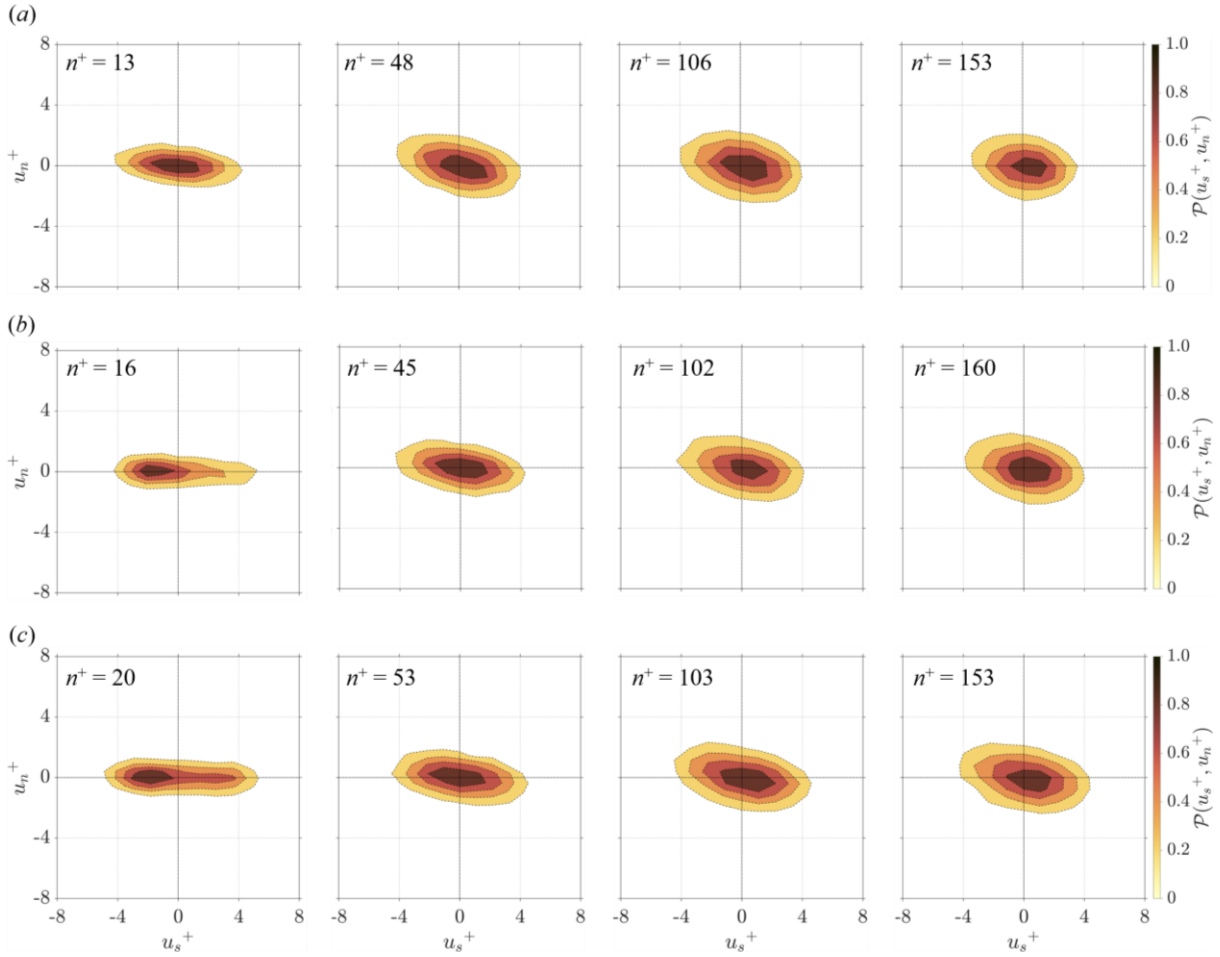

Figure 6-14 Joint probability density function (JPDF) of u_s^+ and u_n^+ at (*a*) Re_τ = 198, (*b*) Re_τ = 241, and (*c*) Re_τ = 282 of the ZPG turbulent pure water flow (see Table 6-1).

Figure 6-14(*a-c*) illustrates the joint probability density function (JPDF) of the instantaneous u_s and u_n velocity fluctuations, normalized by their associated friction velocities, at four different n^+ positions and for three different Re_τ listed in Table 6-1. At $n^+ \approx 13$, very close to the region of turbulence production peak, the JPDF of the ZPG water flow with Re_τ = 198 indicates that the ejection and sweep motions are relatively stronger than the interaction motions. This behavior is

also evident in Figure 6-15(*a*). As Figure 6-16(*a*,*b*) show, in this near-wall region, the sweep events dominate the ejection events, in agreement with the DNS of Kim et al. (1987).

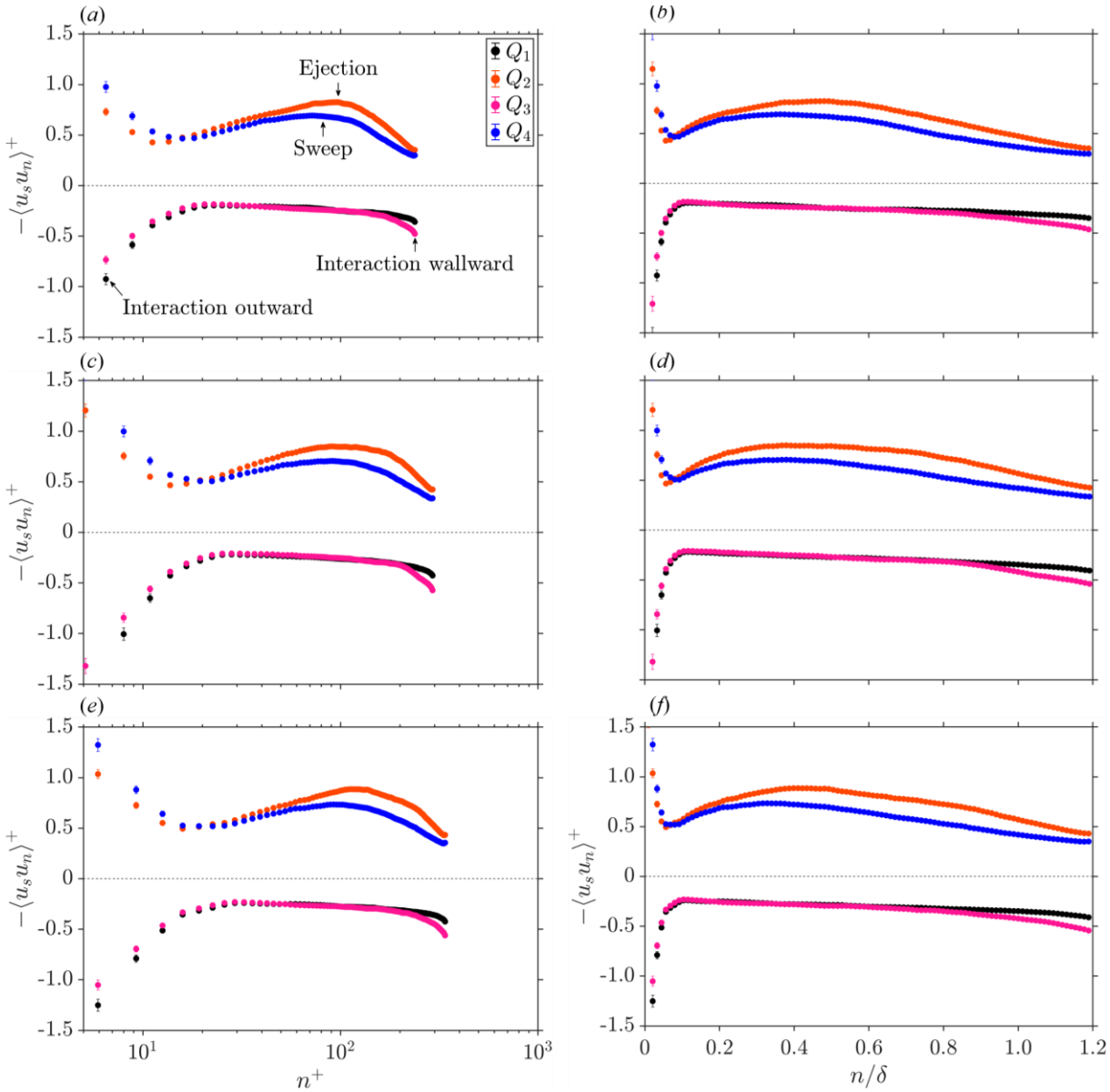

Figure 6-15 The variation of the inner-normalized mean interaction outward (Q_1), ejection (Q_2), interaction wallward (Q_3), and sweep (Q_4) events with the inner normalized wall-normal position, n^+, for (*a*) $Re_\tau = 198$, (*c*) $Re_\tau = 241$, and (*e*) $Re_\tau = 282$, and with the wall-normal position scaled by δ, for (*b*) $Re_\tau = 198$, (*s*) $Re_\tau = 241$, and (*f*) $Re_\tau = 282$, for the ZPG turbulent pure water flow (see Table 6-1).

At $n^+ \approx 48$, as shown in Figure 6-14(*a*), the turbulence-producing sweep and ejection events enhance compared to $n^+ \approx 13$ and continue to grow until almost $n^+ \approx 106$, after which the quadrant events balance out close to the channel centerline. Figure 6-14(*b*,*c*) illustrates similar behavior for flows with higher Re_τ in the outer layers. At $n^+ \approx 16$ of the $Re_\tau = 241$ flow, and

$n^+ \approx 20$ of the $Re_\tau = 282$ flows, shown in Figure 6-14(*b*,*c*), the enhancement of strong positive u_s relative to the negative u_s fluctuations is evident. Nevertheless, their probability is only 20 % compared to the high probability of the negative u_s fluctuations.

Figure 6-15(*a-f*) illustrates the variations of the conditionally averaged Reynolds shear stresses, normalized by the friction velocities of each flow condition versus the wall-normal positions, normalized by the inner viscous length scale, λ_v, and the outer length scale, δ. From the wall to $n^+ \approx 15$ ($n \approx 0.08\ \delta$), the activity of ejection and sweep events attenuate gradually, while the interaction motions outward from the wall or toward it escalate. After this wall position and until $n^+ \approx 100$ ($n \approx 0.5\ \delta$), the occurrence of low-speed fluid elements drifting away from the wall and high-speed elements moving wallward are amplified, while the interaction motions indicate a slow and marginal relaxation. Adjacent to the centerline, the quadrant events almost converge to equal magnitudes. This behavior is also evident in JPDF plots in Figure 6-14(*a-c*).

The variation of the ratio of the ejection to the sweep Reynolds shear stresses, $\langle u_{s\_} u_{n+} \rangle / \langle u_{s+} u_{n\_} \rangle$, with the normalized wall-normal positions are shown in Figure 6-16(*a*,*b*) for three different Re_τ values of the ZPG pure water flow. The sweep events (Q_4) for all three flows dominate the near-wall region's ejection events (Q_2). Both events balance out at $n^+ \approx 17$ for the $Re_\tau = 198$ flow, showing a marginal shift away from the wall for two other higher Re_τ and balance out at $n^+ \approx 20$. The ejection events dominate the sweep motions away from the wall, and their ascendancy continues to grow until the channel's centerline. The resultant profiles do not collapse when normalized by inner or outer scales.

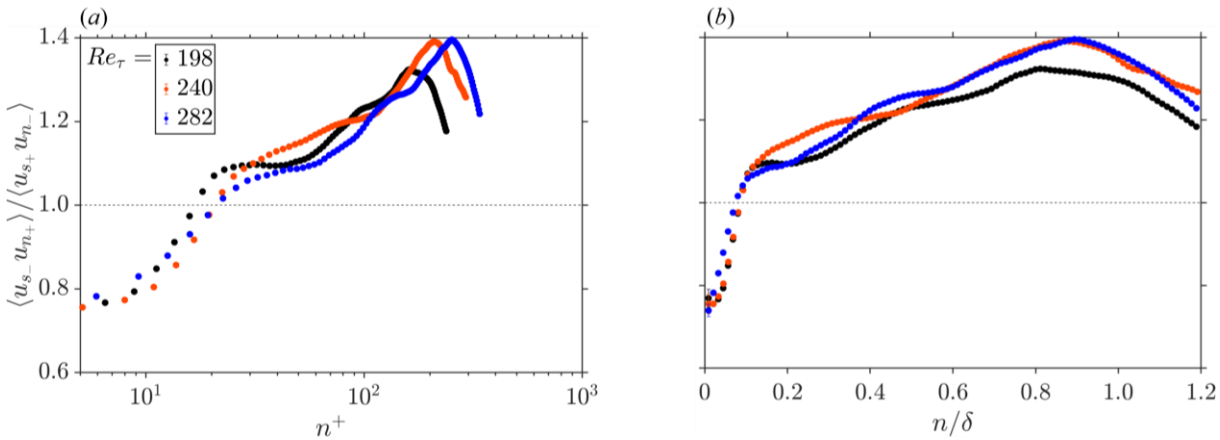

Figure 6-16 Variation of the ratio of the ejection (Q_2) to the sweep (Q_4) events with the (*a*) inner and (*b*) outer normalized wall-normal position for the ZPG turbulent pure water flow at three different Re_τ (see Table 6-1).

6.2.5 Energy spectra

Based on Kolmogorov's second similarity hypothesis (Kolmogorov, 1941), the transferred energy, E, to the Taylor eddies is proportional to the energy dissipation per unit mass, ε, and the wavenumber, k, as $E \propto \varepsilon^{2/3} k^{-5/3}$. Figure 6-17(*a-c*) illustrate the energy spectra $E(k)$, normalized by $n\,u_\tau^2$, as a function of the wavenumber, k, normalized by n, for three different Re_τ of ZPG pure water flow. The energy spectra were obtained by calculating the PSD of the time series of the wall-parallel and wall-normal fluctuating velocities located at different wall-normal positions.

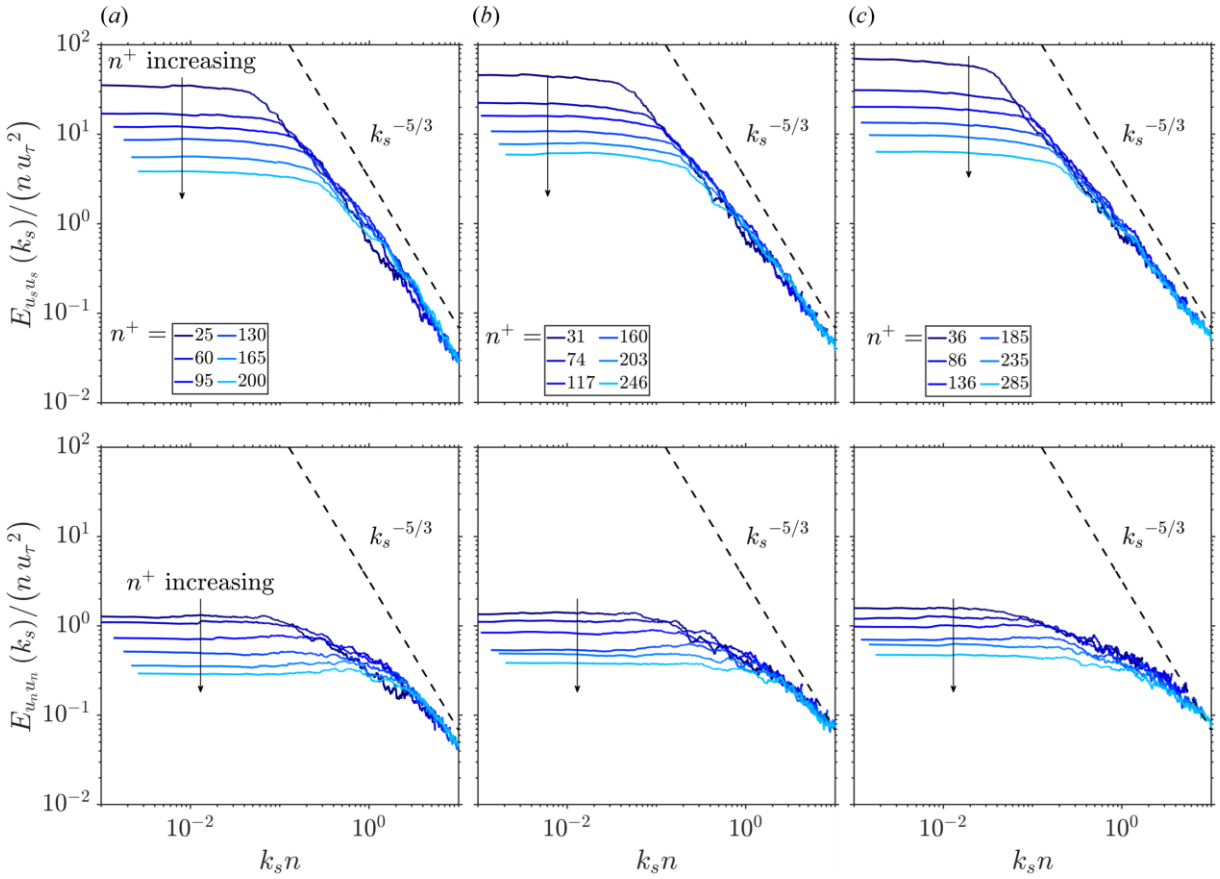

Figure 6-17 Variation of the inner normalized energy spectra with the normalized wall-parallel wavenumber $k_s n$ at different wall-normal positions n^+ for (*a*) $Re_\tau = 198$, (*b*) $Re_\tau = 241$, and (*c*) $Re_\tau = 282$ of the ZPG turbulent pure water flow (see Table 6-1). The first and second row shows the energy spectra results based on wall-parallel, u_s, and wall-normal, u_n, velocity fluctuations at the centerline of the ZPG FOV, at $x = 15\ h_{in}$, illustrated in Figure 3-13. The dashed line on each figure represents the theoretical variation of the energy spectra with the -5/3 slope of the Kolmogorov scale for a Newtonian flow (Kolmogorov, 1941).

The calculated PSD as a function of frequency, $\mathcal{A}_{\mathrm{PSD}}(f)$, was transformed into the energy spectrum as a function k as $E(k) = \mathcal{A}_{\mathrm{PSD}}(f)\langle U_s\rangle/2\pi$, where $k = 2\pi f/\langle U_s\rangle$, using Taylor's hypothesis of frozen turbulence (Fuchs et al., 2022; Taylor, 1938). As shown, in all tested flow

conditions, the amplitude of the flat segment of the profiles, representing the integral length scale, decreases for locations far away from the wall. The Taylor length scales, however, collapse for $E_{u_s u_s}$ with a slope almost in agreement with the $k_s^{-5/3}$ slope at all wall positions. As Re_τ increases, the slope marginally deviates from the Kolmogorov slope of $k_s^{-5/3}$. The $E_{u_n u_n}$ profiles also show a reduction in the size of the integral length scale for positions farther from the wall. The resultant profiles show a relatively smoother slope than $k_s^{-5/3}$ and do not follow this slope at intermediate scales. As explained in Section 3.5, the timing between the PIV velocity fields was 1 ms, equivalent to a frequency of 1 kHz; therefore, based on the Nyquist criterion, the upper limit of obtained energy frequencies was f_{max} = 500 Hz.

6.3. Accelerating flow

Developing turbulent boundary layers on the wall surfaces of the TG channel (see Figure 3-2) were undergone a series of mild to strong favorable and adverse pressure gradients occurring in succession when passing over the bump. The characteristics of the turbulent flow under continuous pressure gradient in regions on the flat surface upstream and downstream of the bump throat were investigated in this study. These regions are highlighted in Figure 3-13 and were interrogated using PIV. A zoomed-in detailed view of the converging and diverging regions of the channel is depicted in Figure 6-18, with the critical normalized streamwise locations in the global coordinates (x, y, z). These points mark the start and end points of the curved surface's concave, flat, and convex wall profiles upstream and flat wall surface downstream of the bump.

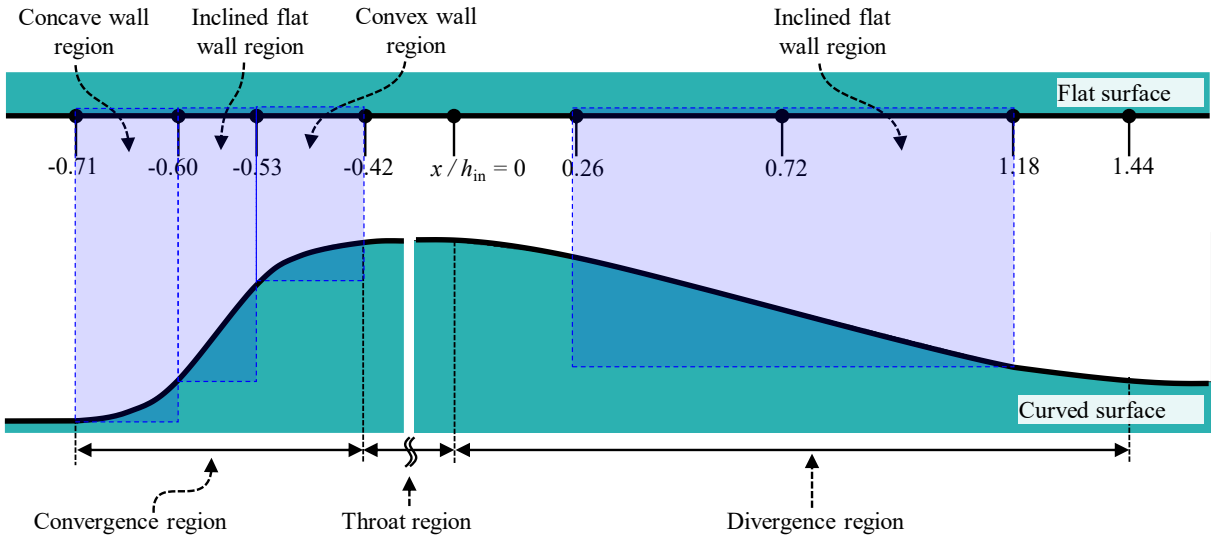

Figure 6-18 The streamwise coordinates of key locations and main flow regions in the interrogated pressure gradient regions of the TG geometry, normalized by the inlet height, h_{in} = 8 mm (not to scale).

This Section discusses the dynamics of developing turbulent boundary layers of pure water flow upstream of the bump on the flat surface, where the flow strongly accelerates. The mean velocity, Reynolds stress, skewness, and kurtosis fields obtained from PIV were spatially averaged in windows of $\pm \Delta s \approx \pm 47$ µm in the wall-parallel direction to reduce the noise of the data while preserving the field gradients. As a result of this process, the spatial resolution was reduced to $\approx 2\ \Delta s \approx \pm 94$ µm, and the number of streamwise data points was reduced from 71 to 35. The results discussed in this section are limited to $-0.71\ h_{in} \leq s \leq -0.57\ h_{in}$, where flow strongly accelerates. No averaging was performed in the wall-normal direction, and the resolution in this direction was intact: $\Delta n \approx \pm 47$ µm.

6.3.1 Boundary layer parameters

Figure 6-19(*a*) illustrates the wall-parallel variations of the local edge-to-mean velocity ratio, U_e/U_m, for three different flow conditions listed in Table 6-1 at the flat surface of the convergence region of the TG channel, calculated using the classical and generalized velocity approach discussed in Section 2.2. The results based on the generalized velocity approach are discerned using a tilde symbol over the related variables, i.e., $\widetilde{U}_e/\widetilde{U}_m$ in this case. At each wall-parallel position, s, the edge velocity, U_e (s), is where $\langle U_s \rangle$ is maximum and closest to the wall and mean velocity U_m is the average of $\langle U_s \rangle(s,n)$ in the wall-normal direction, from the wall to the edge of the boundary layer. A ninth-order polynomial curve was fitted to the resultant U_e profiles to accommodate the calculation of the spatial gradients of U_e over the domain.

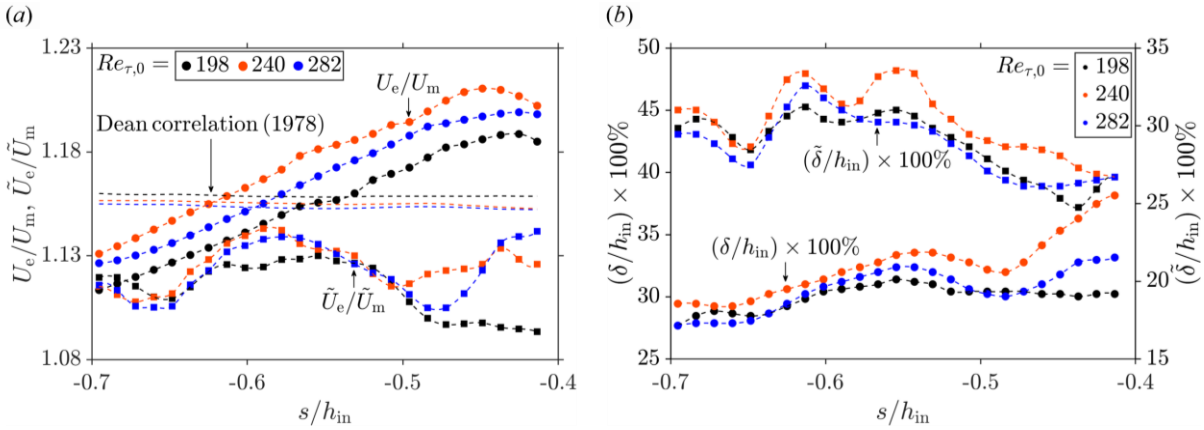

Figure 6-19 Wall-parallel variations of the (*a*) boundary layer edge velocity, U_e, ratio to the mean streamwise velocity, U_m, and (*b*) BL thickness, δ, normalized by h_{in}, for three different flow conditions of pure water flow at the flat surface of the convergence region of the TG channel (upstream of the throat). The correlation proposed by Dean (1978) for fully developed ZPG flow, given in equation (6-5), and the results based on the generalized velocity are also shown for reference. The legend shows the Re_τ values of the ZPG flow (see Table 6-1).

In all three flow conditions, U_e/U_m increases almost linearly with the streamwise position, showing that flow strongly accelerates in this region. The results show that as $Re_{\tau,0}$ increases, U_e/U_m increases at any streamwise location of the convergence region. The flow with $Re_{\tau,0} = 198$ has U_e/U_m values lower than the Dean's correlation (see equation (6-5)) for $s \leq -0.57\ h_{in}$, and increases to higher values for $s > -0.57\ h_{in}$. The U_e/U_m profile of the $Re_{\tau,0} = 198$ flow in Figure 6-19(*a*) shows a peak value of ≈ 1.19 at $s = -0.42\ h_{in}$, which corresponds to the end of the convergence region. The other two flow conditions with higher $Re_{\tau,0}$ show higher U_e/U_m values than the Dean's prediction over the inclined flat and convex flow regions. The flow with $Re_{\tau,0} = 240$ has a peak of $(U_e/U_m)_{max} \approx 1.22$ occurring at $s = -0.45\ h_{in}$, slightly upstream of the

throat's starting point. The flow with $Re_{\tau,0}$ = 282 indicates a peak value of ≈ 1.20, almost equal to that of $Re_{\tau,0}$ = 240, which occurs at s = - 0.42 h_{in}.

The velocity ratios, $\widetilde{U}_e/\widetilde{U}_m$, calculated based on the generalized velocity, show relatively lower values when compared to U_e/U_m, which indicates that the is not irrotational in the core region and is highly distorted. Nevertheless, as given in equations (2-9)-(2-11), generalized velocity is calculated based on the first derivates of the PIV velocity fields, and according to the analysis provided in Section 6.2.2, the uncertainty of the calculated vorticity fields can be as high as ≈ 6 % near the BL edge. The results show that in the three tested water flow scenarios, the calculated $\widetilde{U}_e/\widetilde{U}_m$ increase over the inclined flat surface and are relatively lower in other regions of the convergence region.

The profiles of the boundary layer thickness over the convergence region, normalized by h_{in}, are illustrated in Figure 6-19(*b*) for the three tested water flow conditions. The results show that the BL gradually thickens on the flat surface as it passes over the concave and inclined flat wall regions and peaks at $s \approx$ -0.57 h_{in}. As the flow enters the convex wall region, it marginally reduces until the mid-section of the convex region and starts to increase again in the second half of it. The normalized BL thickness profiles obtained from the general velocity, $\tilde{\delta}/h_{in}$, are also shown in Figure 6-19(*b*). These profiles show that in all three cases, the developing BL shrinks in size as it passes over the first half of the concave region, has its minimum at the middle of this section, and thickens in the next half of the concave region until its first peak at the starting point of the inclined flat region. Over the inclined flat wall region, BL thickness reduces until the middle of it and increases again in the second half until it reaches the second peak of the profile at the end of this region. This second peak was not observed for the $Re_{\tau,0}$ = 282 flow. After this point, the BL thickness gradually decreases over almost the entire convex region.

The profiles of the normalized integral parameters δ^* and θ are illustrated in Figure 6-20(*a*,*b*) for the three tested flow conditions subjected to FPG. Both parameters show similar trends, where they are minimum at the middle of the concave and convex regions and have a maximum plateau over the inclined flat wall region. The results indicate that increasing $Re_{\tau,0}$ increases the displacement and momentum thicknesses. The integral parameters estimated based on the general velocity show trends similar to the ones based on the classical definition but with values relatively larger than their classical counterparts.

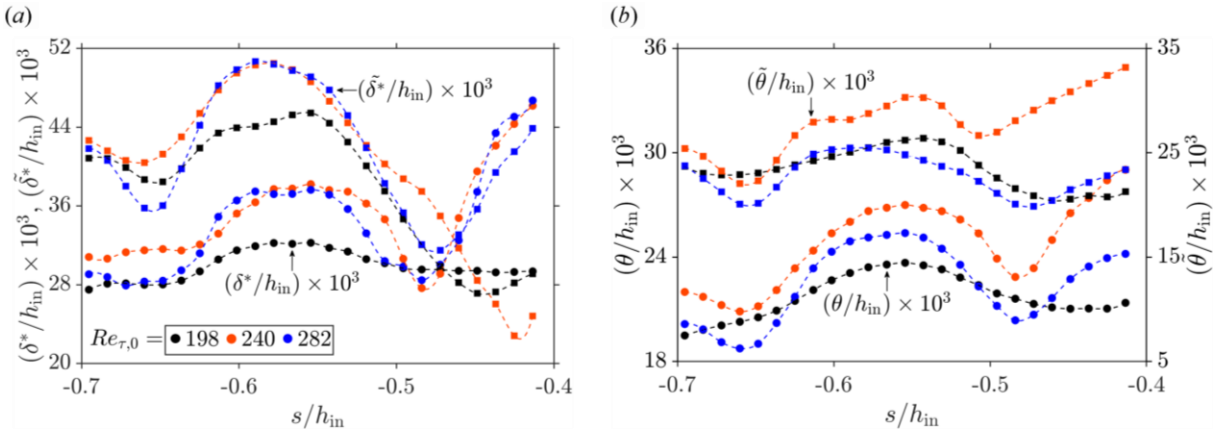

Figure 6-20 Wall-parallel variations of the (*a*) displacement thickness, δ^*, and (*b*) momentum thickness, θ, normalized by the inlet height, h_{in}, for three different flow conditions of pure water flow at the flat surface of the convergence region of the TG channel (upstream of the throat). The results based on the generalized velocity are also shown for reference. The legend shows the Re_τ values of the ZPG flow (see Table 6-1).

The streamwise variations of the pressure coefficient, c_p, and the streamwise edge pressure gradient, dP_e / ds, are illustrated in Figure 6-21(*a*) for three water flow conditions. The pressure coefficient is defined as

$$c_p = \frac{P_e - P_0}{\frac{1}{2}\rho_L U_{m,0}^2}, \tag{6-19}$$

where P_e is the pressure at the boundary layer edge, P_0 is a reference pressure and was assumed to be zero here. $U_{m,0}$ is the mean velocity of the ZPG flow at the same flow condition. The edge pressure was determined using equation (2-15) and based on local U_e values. All over the convergence region, $c_p < 0$ and $dP_e / ds < 0$, which indicates that the flow is subjected to continuous FPG in all three tested flow scenarios. The c_p profiles almost collapse in the first half of the convergence region and slightly deviate from each other in the second half, where acceleration intensifies due to a gradual reduction of the cross-sectional area.

The negative pressure gradient values are larger in magnitude for higher $Re_{\tau,0}$ at each s position. In all three flow conditions, the concave wall profile of the bump induces a strong FPG on the flow passing the flat surface. Over the inclined flat wall region, the FPG gets marginally milder until the middle of this region at $s \approx$ - 0.57 h_{in}, where FPG starts to get stronger again. The magnitudes of the negative pressure gradients continue to amplify over the first half of the convex region until $s \approx$ - 0.47 h_{in}, after which they start to get milder and tend towards relatively smaller negative pressure gradients as the flow approaches the throat region.

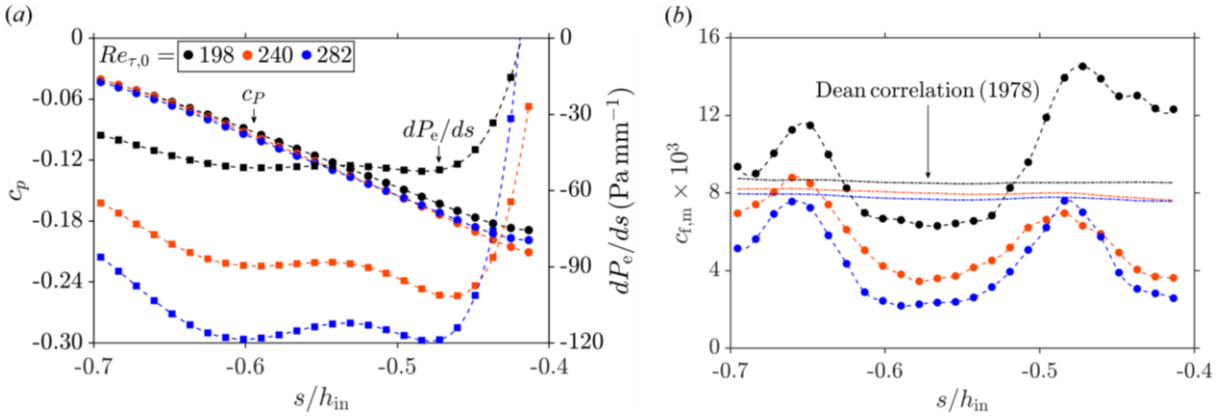

Figure 6-21 Wall-parallel variation of the (*a*) pressure coefficient, c_p, and streamwise edge pressure gradient, dP_e / ds, and (*b*) skin friction factor based on the mean velocity, $c_{f,m}$ (equation (2-26)), for three different flow conditions of pure water flow at the flat surface of the convergence region of the TG channel (upstream of the throat). The correlations proposed by Dean (1978) for fully developed ZPG flow, given in equation (6-6), are also shown in (*b*) for reference. The legend shows the Re_τ values of the ZPG flow (see Table 6-1).

As discussed, the c_p and pressure gradient profiles in Figure 6-21(*a*) show that flow is under continuous FPG in all three tested flow conditions. Nevertheless, the changes in the bump curvature due to the concave, flat, and convex profiles alter the strength of FPG in the convergence flow region over the flat surface. This trend is noticeable in the mean skin friction factor, $c_{f,m}$, profiles illustrated in Figure 6-21(*b*). The mean friction factors of all three flows start to increase as the flow enters the concave flow region at $s \approx$ - 0.71 h_{in}, and the increase continues until their first peak, which occurs at the middle of the concave region at $s \approx$ - 0.66 h_{in}. After the peak, the friction factors gradually reduce in the second half of the concave region until $s \approx$ - 0.60 h_{in}. The results show that the concave wall curvature of the bump, mounted to the bottom of the channel, exerted a relatively stronger FPG to the flow passing the flat surface in its first half, which was then weakened in the second half. The peak values of the flows with $Re_{\tau,0}$ = 198 and $Re_{\tau,0}$ = 240 at $s \approx$ - 0.66 h_{in} are higher than the prediction of Dean's correlation given in equation (6-6), while it is marginally lower for the flow with $Re_{\tau,0}$ = 282.

As Figure 6-21(*b*) shows, over the flat wall of the bump, inclined at 60 ° from $s \approx$ - 0.60 h_{in} to $s \approx$ - 0.53 h_{in}, the strength of the FPG is almost maintained in all three flow conditions, which generates an almost equilibrium FPG flow over this region. As the flow passes over the convex bump profile, the friction factor of the flow increases until its second peak at the middle of the concave wall, at $s \approx$ - 0.47 h_{in}, indicating that FPG improves in this region. Figure 6-21(*b*) shows that this behavior is common in all three tested flow scenarios. In the second half of the convex

region, the skin friction factor decreases, and FPG is weakened until $s \approx -0.42\ h_{in}$, where the convergence region meets the throat. The weakening of the FPG in the second half of the convex region is also evident in the pressure gradient profiles shown in Figure 6-21(*a*), where the negative dP_e / ds values decrease in magnitude. At each streamwise position, the local skin friction factor decreases as $Re_{\tau,0}$ increases.

Based on the DNS results performed for fully developed ZPG channel and pipe flows at high Reynolds numbers, Pirozzoli (2014) suggested that:

$$H = \frac{1}{1 - 6.907\sqrt{\frac{c_{f,\,Dean}}{2}}}, \tag{6-20}$$

where $c_{f,\,Dean}$ is given in equation (6-6). The DNS of Kim et al. (1987) for a fully developed channel flow with $Re_m = 5.6 \times 10^3$ resulted in $H = 1.62$. For the same Re_m, equation (6-20) gives $H \approx 1.80$, which overestimates the H value by ≈ 11 %. The variation of the shape factor, H, and the defect shape factor, G, with the normalized wall-parallel position, s / h_{in}, are shown in Figure 6-22(*a*,*b*) for three water flow scenarios in the accelerating flow region. H values predicted by equation (6-20), based on the local Re_m, are also shown in Figure 6-22(*a*) for reference.

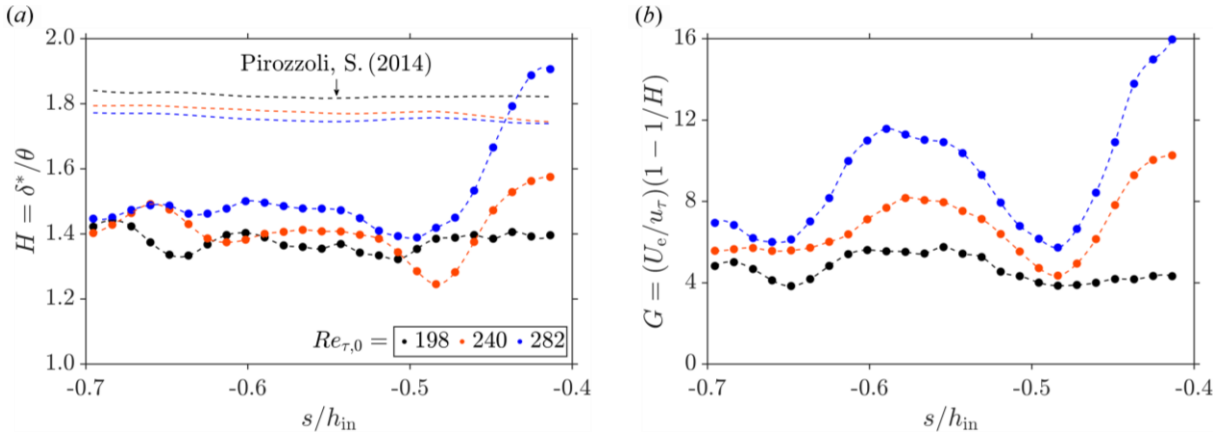

Figure 6-22 Streamwise variation of the (*a*) shape factor, H, and (*b*) deflect shape factor, G, for three different flow conditions of pure water flow over the flat surface of the convergence region of the TG channel (upstream of the throat). Predictions of the shape factor for fully developed ZPG channel flow based on equation (6-20) are also plotted in (*a*). The legend shows the Re_τ values of the ZPG flow (see Table 6-1).

H increases in all three tested flow conditions for stronger FPG conditions and higher $Re_{\tau,0}$. Kim et al. (1987) obtained a value of $G = 6.97$ for a fully developed ZPG channel flow with $Re_{\tau,0} = 180$. As the FPG weakens, i.e., as $Re_{\tau,0}$ decreases, the G values of the tested flow scenarios also decrease. They show two minima at the middle sections of the concave and convex regions

and a maximum plateau over the inclined flat wall region. Near the end of the convergence region, G increases to values as high as ≈ 16 for the flow with $Re_{\tau,0} = 282$.

The streamwise changes of Re_τ in the convergence region are illustrated in Figure 6-23(a). In all three flow scenarios, Re_τ increases in the first half of the concave region and, after its first peak, reduces almost linearly until the middle of the inclined flat wall region, where it shows a minimum. Over the second half of the inclined flat wall region, Re_τ increases again, which continues to the middle of the convex region. At the middle of the convex region, Re_τ experiences a second peak, after which it gradually reduces as it approaches the throat region. The Re_θ values shown in Figure 6-23(b) show larger values at each local position as the water flow rate increases. In the three illustrated profiles, Re_θ has two minima at the middle sections of the concave and convex regions and has a plateau maximum over the inclined wall region.

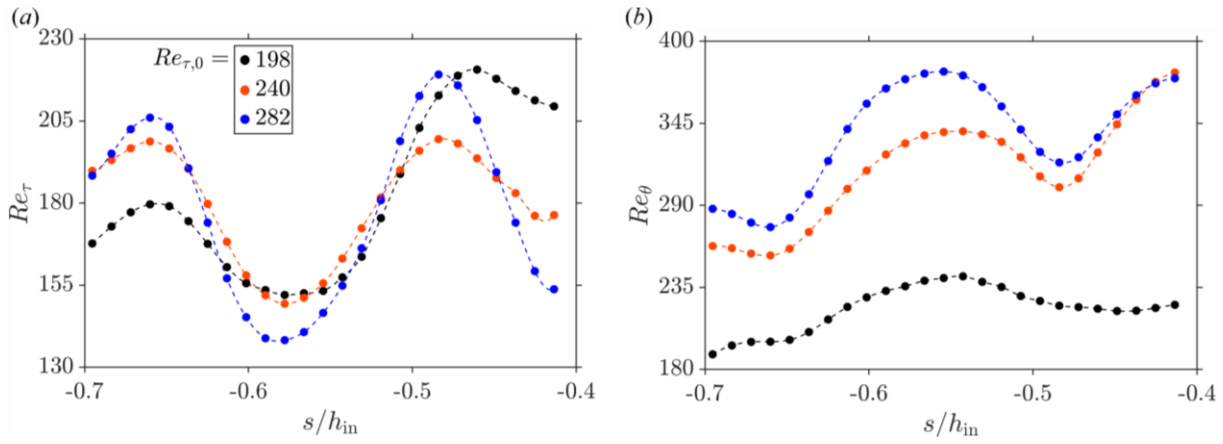

Figure 6-23 Streamwise variation of (a) Re_τ and (b) Re_θ, for three different flow conditions of pure water flow at the flat surface of the convergence region of the TG channel (upstream of the throat). The legend shows the Re_τ values of the ZPG flow (see Table 6-1).

Figure 6-24(a-c) demonstrate the local changes of the acceleration parameter, K, FPG parameter, Δ_p, and Rotta-Clauser pressure gradient parameter, β, introduced in Section 6.1, for three water flow conditions in the convergence region of the TG channel. All three tested flow conditions show that the evaluated K values are at least an order of magnitude larger than the critical $K = 3 \times 10^{-6}$ proposed by Sreenivasan (1982), marking the onset of relaminarization. Therefore, the strong acceleration forced the flows into a fully relaminarized state in the convergence region of the TG channel.

As shown in Figure 6-24(b), it is evident that the estimated Δ_p fall below the critical value of Δ_p = -0.025, proposed by Narasimha and Sreenivasan (1979, 1973) and Sreenivasan (1982), which

is another indication that flow is in the fully relaminarized regime in the accelerating region. Figure 6-24(*c*) illustrates that for all tested flows and over the entire convergence region, $\beta < 0$, and flow is under strong acceleration. The magnitudes of negative Δ_p and β values amplify over the entire convergence region as $Re_{\tau,0}$ increases.

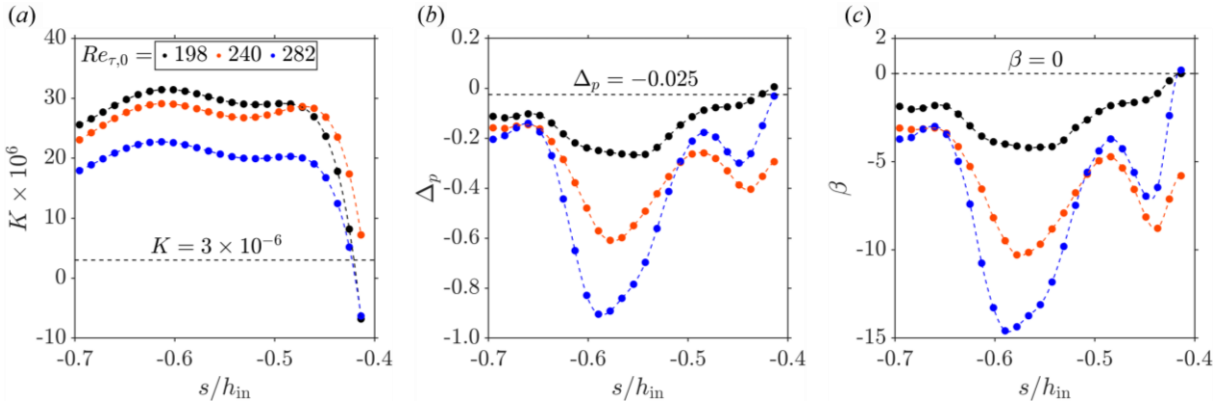

Figure 6-24 Streamwise variation of the (*a*) acceleration parameter, K (see equation (6-2)), (*b*) FPG parameter, Δ_p (see equation (6-1)), and (*c*) Rotta-Clauser pressure gradient parameter, β (see equation (6-4)), for three different flow conditions of pure water flow at the flat surface of the convergence region of the TG channel (upstream of the throat). The legend shows the Re_τ values of the ZPG flow (see Table 6-1).

6.3.2 Mean flow

Figure 6-25(*a-c*) shows the wall-normal variation of the mean wall-parallel velocity profiles, normalized by the local inner scales: $u_\tau\,(s)$ and $\lambda_v\,(s)$ and outer scales: $U_e\,(s)$ and $\delta\,(s)$, at eight different wall-parallel positions, and for three different water flow conditions. At each s position, inner scales were determined by fitting a line to the mean velocity data of the viscous sublayer. The local mean edge velocities and BL thicknesses were used to outer normalize the mean velocity and wall-normal positions, shown in the right column of Figure 6-25(*a-c*).

It is important to mention that using microscopic PIV, explained in Section 3.5, mean velocity vectors were obtained at 71 different wall positions in each interrogated FOV and were spatially averaged, which resulted in 35 velocity profiles with a spatial resolution of 94 µm. Nevertheless, only profiles at eight critical streamwise positions are illustrated: (1) the immediate upstream of the convergence region at s / h_{in} = -0.80, (2) the start point of the concave region at s / h_{in} = -0.71, (3) the middle point of the concave region at s / h_{in} = -0.65, (4) the end point of the concave region or start point of the inclined flat wall region at s / h_{in} = -0.60, (5) the middle point of the inclined flat wall region at s / h_{in} = -0.57, (6) the end point of the inclined flat wall region or start point of

the convex region at s / h_{in} = -0.53, (7) the middle point of the convex region at s / h_{in} = -0.48 and (8) the end point of the convex region or start point of the throat region at s / h_{in} = -0.42.

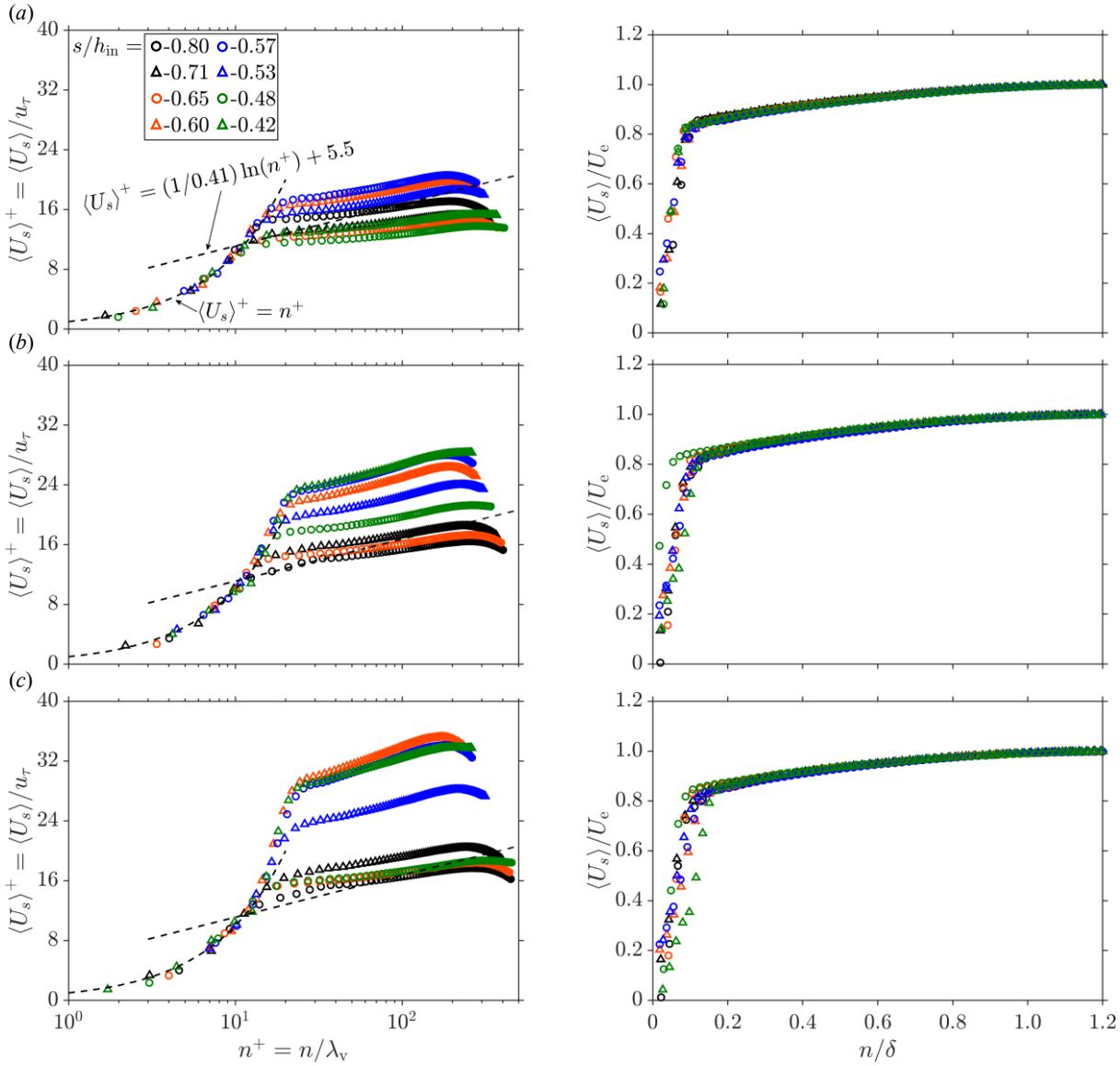

Figure 6-25 Wall-normal variation of the mean wall-parallel velocity profiles, normalized by the local inner scales (left) and by the outer scales (right), at eight selected wall-parallel positions for accelerating water flow over the flat surface of the TG channel's convergence region at (*a*) $Re_{\tau,0}$ = 198, (*b*) $Re_{\tau,0}$ = 240, and (*c*) $Re_{\tau,0}$ = 282.

As discussed before, flow is subjected to a continuous FPG in the convergence region and based on the behavior of the local pressure gradient parameters shown in Figure 6-24(*a-c*), flow relaminarizes in this region. However, due to the change of bump curvature, the magnitude of the exerted FPG varies along the region. At the immediate upstream of the concave region, the velocity profile partially deviates over the standard logarithmic law for all three tested low scenarios, which

indicates that flow is at non-equilibrium conditions. As the flow enters the concave region at $s / h_{in} = -0.71$, the velocity profile of the flow with $Re_{\tau,0} = 198$ falls below the log-law region. However, for higher $Re_{\tau,0}$ values shown in Figure 6-25(*b*,*c*), with a stronger entrance FPG, the velocity profile at $s / h_{in} = -0.71$ deviates above the log-law line, where it shows a logarithmic behavior, but with a slope smaller than $\kappa^{-1} \approx 2.44$.

Over the first half of the concave region, the curvature causes an increase in the skin friction factor (see Figure 6-21*b*), which pushes the velocity profile to an even lower level below the log-law line for the $Re_{\tau,0} = 198$. As $Re_{\tau,0}$ increases, a stronger FPG pushes the velocity profile over the buffer layer partially above the log line. The end of the concave region, which coincides with the start of the inclined flat wall region, located at $s / h_{in} = -0.60$, is where, as illustrated in Figure 6-21(*b*), the skin friction factor is minimum. At this position, as shown in Figure 6-21(*a*), the local negative pressure gradient is maximum, which implies that the local FPG is the strongest at this zone. As a result, the velocity profile is pushed far over the logarithmic line. As $Re_{\tau,0}$ increases, the deviation above the standard logarithmic law amplifies, the viscous sublayer thickens, and the velocity profile at $s / h_{in} = -0.60$ approaches the velocity profile of a laminar flow.

As shown in Figure 6-21(*a*,*b*), the strength of the FPG over the inclined flat wall region, from $s / h_{in} = -0.60$ to $s / h_{in} = -0.53$, is almost constant for the $Re_{\tau,0} = 198$. The FPG's strength marginally decreases over the first half and then gradually increases over the second half for the other two flow conditions with higher $Re_{\tau,0} = 240$. The velocity profiles over the inclined flat wall region lie above the logarithmic line and close to the velocity profile of the position with $s / h_{in} = -0.60$. As the flow passes over the convex region, the FPG strength reduces relatively over the first half of the region, which pushes the velocity profile down towards the logarithmic profile. For the $Re_{\tau,0} = 198$ flow, the profile of the middle section of the convex region falls below the log-law.

As Figure 6-25(*b*,*c*) shows, at the entrance of the throat region, at $s / h_{in} = -0.42$, the skin friction factor decreases to its second minimum for the $Re_{\tau,0} = 240$ and $Re_{\tau,0} = 282$, which shoots the velocity profile too far above the log-law close to the velocity profile at $s / h_{in} = -0.60$. For the lowest tested water flow rate with $Re_{\tau,0} = 198$, higher values of the skin friction factor at this position show that the strength of the FPG reduces, and the velocity profile falls mostly below the logarithmic profile and almost coincides with the entrance velocity profile. The outer-normalized velocity profiles of the accelerating water flow, illustrated in the right column of Figure 6-25(*b*,*c*),

collapse to a common profile in the regions away from the wall. Depending on the strength of the FPG, the velocity profiles marginally shrink or flatten near the wall and partially collapse.

The wall-normal variations of the normalized mean Reynolds shear stress over the convergence region of the TG channel are illustrated in Figure 6-26(*a-c*) for three different water flow rates. For the same flow conditions, the mean normalized wall-parallel and wall-normal Reynolds stress profiles are illustrated, respectively, in Figure 6-27(*a-c*) and Figure 6-28(*a-c*). The skewness and kurtosis profiles are illustrated in Figure 6-29(*a-c*). The results show that the wall-normal distributions of the $-\langle u_s u_n \rangle / u_\tau^2$ profiles at the entrance of the convergence region are almost similar to the ZPG flows (see Figure 6-12*a*), with peaks relatively lower than the ZPG flow. The damping of the Reynolds shear stresses under FPG is also evident in the outer-normalized profiles, shown in the right column of Figure 6-26(*a-c*). Increasing $Re_{\tau,0}$ does not show a significant change in the peak value of the damped Reynolds shear stresses.

The strong FPG relaxes the Reynolds shear stresses over the first half of the concave flow region, and at s / h_{in} = -0.65, flow experiences a relatively lower Reynolds shear stress compared to the entrance flow, where the skin friction factor is at its first peak. Over the second half of the concave region, the FPG gets milder, skin friction decreases gradually, and at s / h_{in} = -0.60, the starting point of the inclined flat wall region, the inner-normalized Reynolds shear stress significantly amplifies, and its peak elevates as $Re_{\tau,0}$ increases. This behavior is almost maintained until the middle of the inclined flat region at s / h_{in} = -0.57, over which the skin friction factor is nearly constant and minimum. Figure 6-26(*a-c*) illustrate that FPG regains its strength over the second half of the inclined flat wall region and damps turbulence production, which is revealed as a lower level of Reynolds shear stress at s / h_{in} = -0.53. The Reynolds shear stress damping continues over the first half of the convex region until s / h_{in} = -0.48. At the end of the convex region, where the incoming flow enters the throat, the FPG significantly weakens, and turbulence production is enhanced. As a result, the Reynolds shear stress profile shifts to a higher level.

The Reynolds shear stress profiles of the accelerating flow region, normalized by the outer scales, shown in the right column of Figure 6-26(*a-c*), show that as flow advances in the convergence region, the mean turbulence production activities in regions far from the wall gradually reduce, as the FPG continues to attenuate them. The attenuation of the Reynolds shear stresses intensifies as the water flow rate increases and FPG gets relatively stronger. Nevertheless,

the results show that near the wall, outer-normalized Reynolds shear stresses at the entrance of the throat region significantly enhance relative to the other positions over the convergence region. At this point, FPG weakens, and the turbulence production activities amplify.

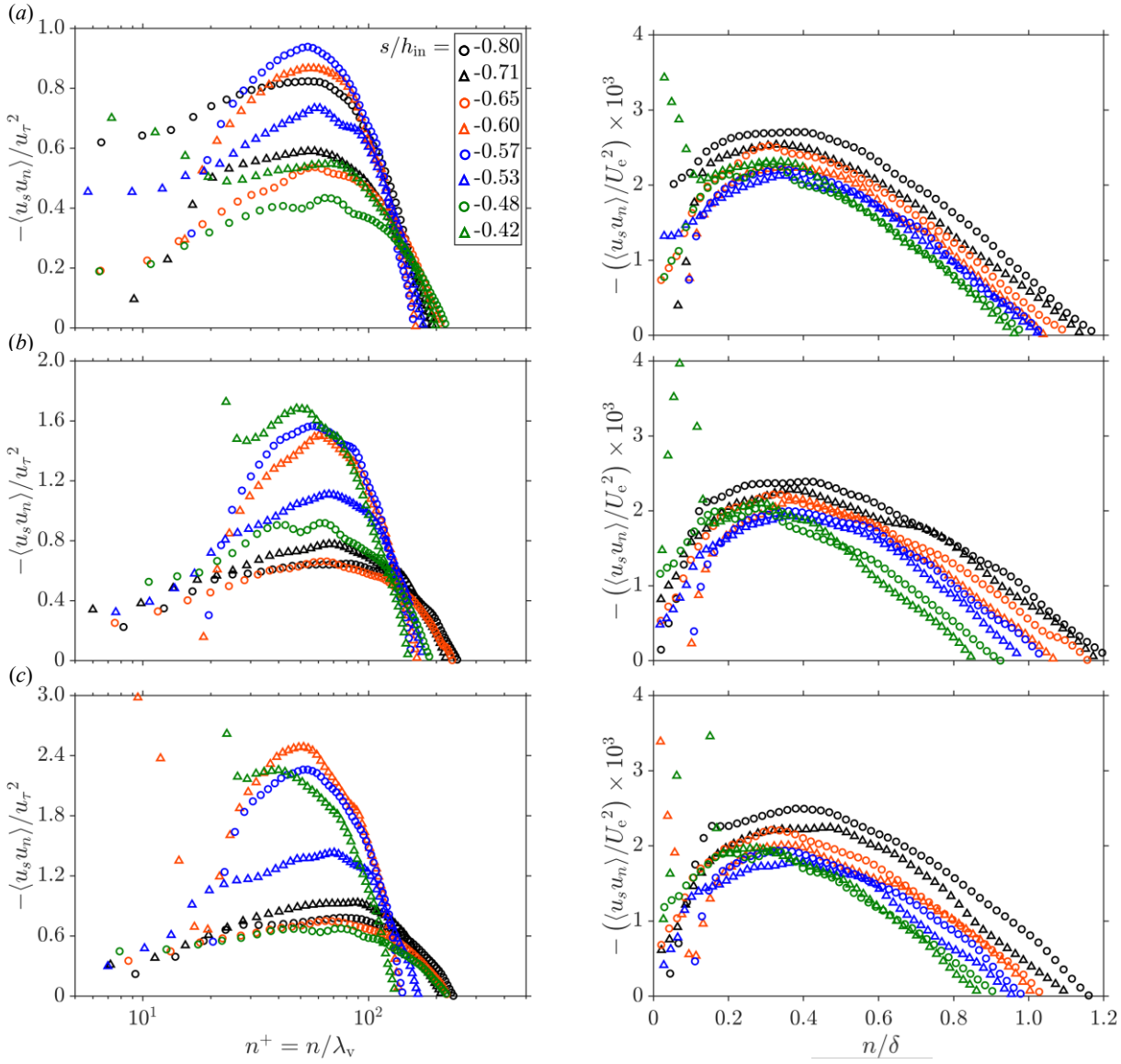

Figure 6-26 Wall-normal variation of the mean Reynolds shear-stress profiles, normalized by the local inner scales (left) and by the outer scales (right), at eight selected wall-parallel positions for accelerating water flow over the flat surface of the TG channel's convergence region at (*a*) $Re_{\tau,0}$ = 198, (*b*) $Re_{\tau,0}$ = 240, and (*c*) $Re_{\tau,0}$ = 282.

As Figure 6-27(*a-c*) illustrates, at the entrance of the convergence region, at s / h_{in} = -0.80, the inner-normalized wall-parallel Reynolds stresses almost resemble their counterparts in the ZPG flows. As the flow enters the concave region, $\langle u_s^2 \rangle^+$ enhances slightly for the two flow scenarios with higher flow rates. Then, it gradually attenuates over the first half of the region and coincides

with the entrance flow profile. At the end of the concave region, at s / h_{in} = -0.60, $\langle u_s^2 \rangle^+$ increases significantly due to a relative reduction in the skin friction factor.

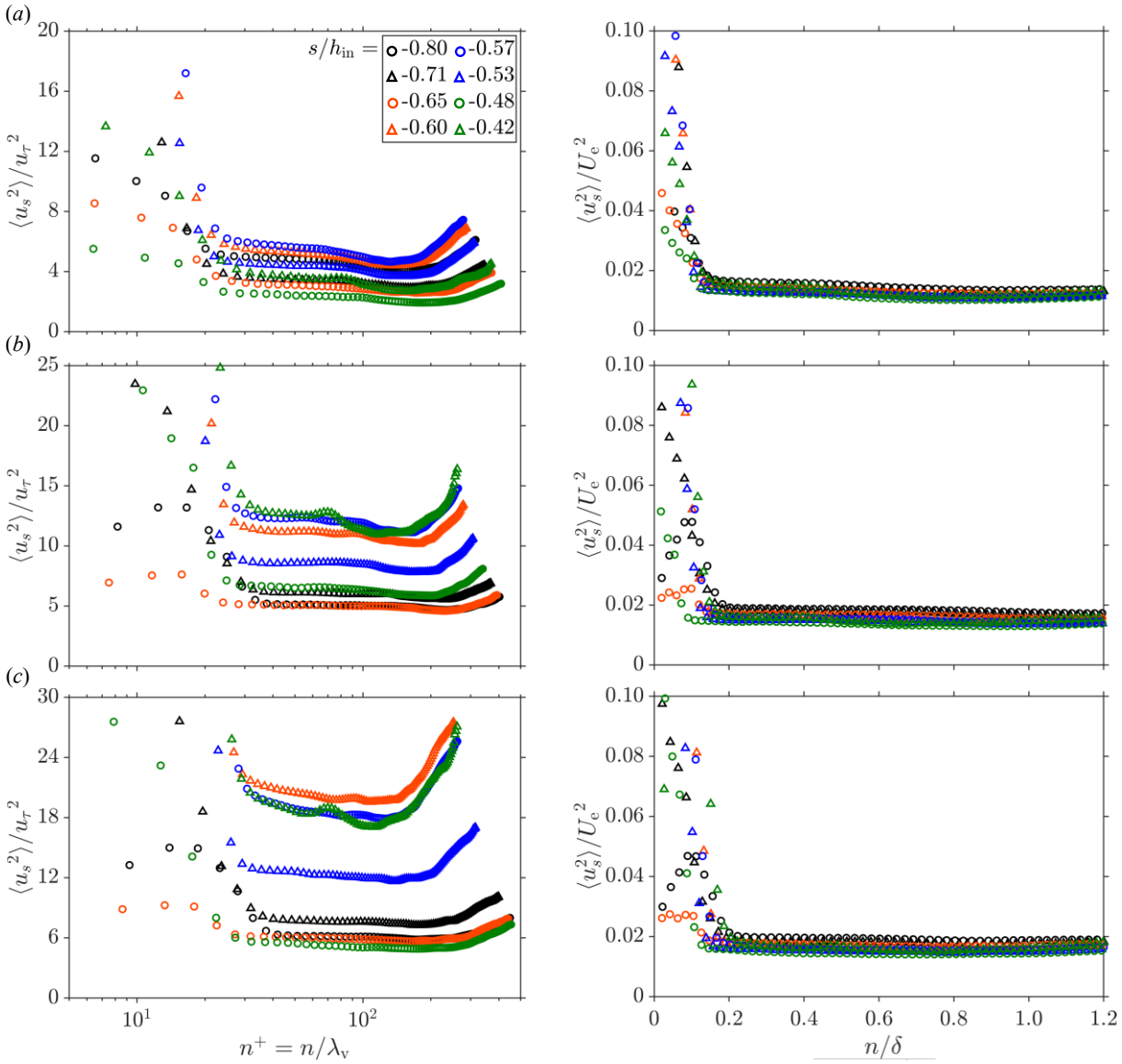

Figure 6-27 Wall-normal variation of the mean wall-parallel Reynolds stress profiles, normalized by the local inner scales (left) and by the outer scales (right), at eight selected wall-parallel positions for accelerating water flow over the flat surface of the TG channel's convergence region at (*a*) $Re_{\tau,0}$ = 198, (*b*) $Re_{\tau,0}$ = 240, and (*c*) $Re_{\tau,0}$ = 282.

Over the inclined flat wall region, the skin friction factor increases slightly, and as shown in Figure 6-27(*a-c*), $\langle u_s^2 \rangle^+$profile is pushed to a relatively lower level. Over the middle of the convex region at s / h_{in} = -0.48, where the skin friction factor is at its second peak, the intensity of $\langle u_s^2 \rangle^+$ is significantly attenuated. As the flow advances to the throat region, the skin friction factor decreases again, which amplifies the $\langle u_s^2 \rangle^+$ profiles. For the lowest tested flow rate, this

amplification is at a lower level compared to other positions in the convergence region, while for the two other higher flow rates, the amplification is significant. The results show that as $Re_{\tau,0}$ increases, $\langle u_s^2 \rangle^+$profiles elevate significantly. This behavior is consistent with the changes in the skin friction factor over the convergence region, shown in Figure 6-21(*b*).

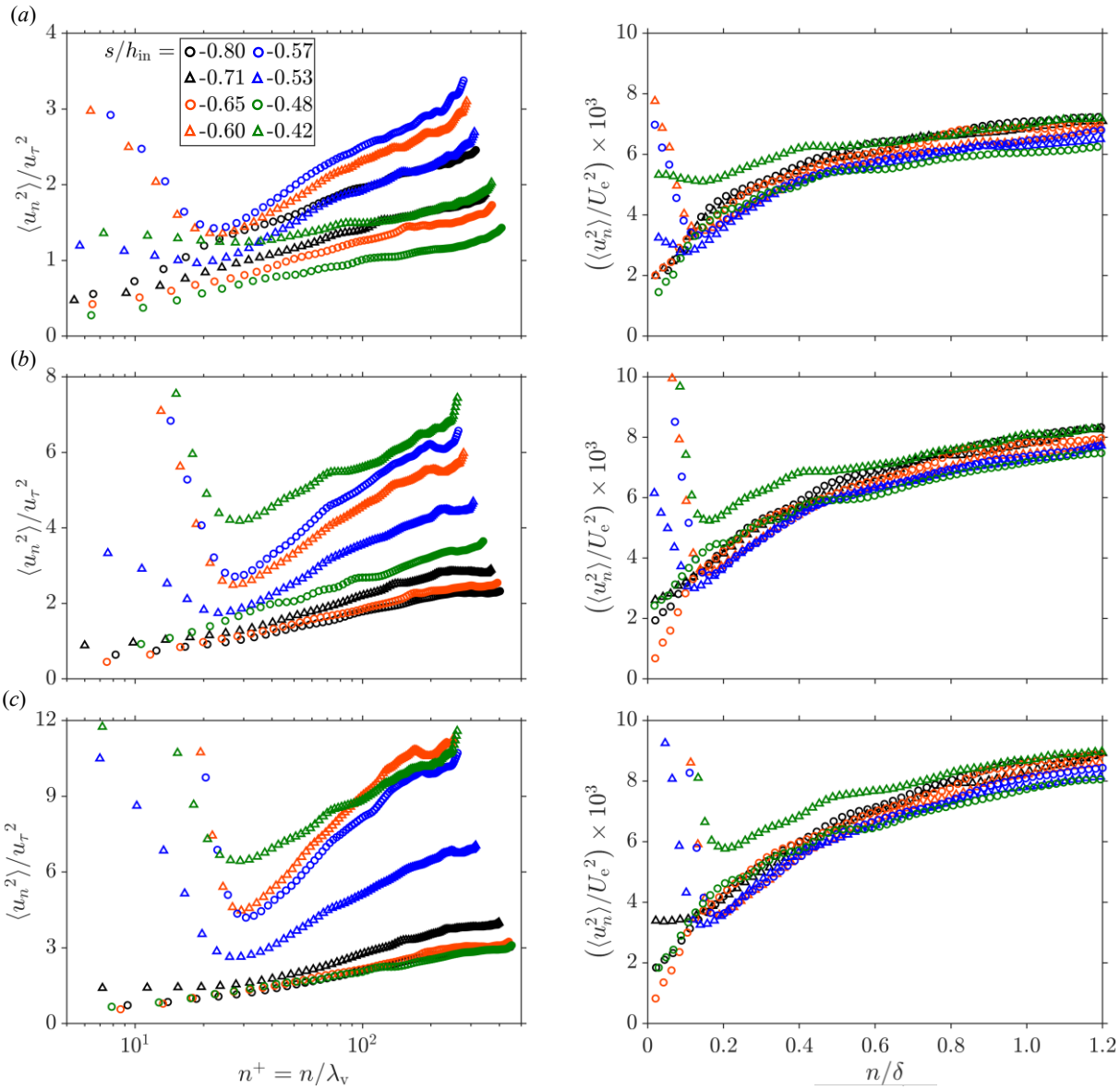

Figure 6-28 Wall-normal variation of the mean wall-normal Reynolds stress profiles, normalized by the local inner scales (left) and by the outer scales (right), at eight selected wall-parallel positions for accelerating water flow over the flat surface of the TG channel's convergence region at (*a*) $Re_{\tau,0}$ = 198, (*b*) $Re_{\tau,0}$ = 240, and (*c*) $Re_{\tau,0}$ = 282.

The outer-normalized wall-parallel Reynolds stress profiles, shown in the right column of Figure 6-27(*a-c*), indicate a gradual reduction in the intensity of the Reynolds stresses far from the wall as the flow advances in the convergence region. Near the wall, in agreement with $\langle u_s^2 \rangle^+$

profiles, the wall-parallel turbulence intensity amplifies significantly at positions where the skin friction factor is minimum. Compared to the ZPG flow profiles given in Figure 6-12(*a-c*), the wall-parallel turbulence intensities of the accelerated regions are significantly higher near the wall for the positions with minimum skin friction factor. Positions with larger c_f, such as the middle of the concave region, indicate peak values similar in magnitude to the ZPG flow profiles.

The normalized wall-normal Reynolds stress profiles over the accelerating water flow region are illustrated in Figure 6-28(*a-c*). Normalized by local u_τ^2, the intesntiy of the Reynolds stresses varies significantly over the convergence region and for different flow scenarios. For a lower flow rate, the local skin friction factors are larger than their counterparts for higher flow rates. As a result, when normalized by u_τ^2, the profiles of the flow with $Re_{\tau,0}$ = 198 settle at relatively lower levels. As the flow with $Re_{\tau,0}$ = 282 enters the acceleration region at s / h_{in} = -0.71, $\langle u_n^2 \rangle^+$ amplifies, and as it advances over the first half of the concave region, it attenuates until the middle of the region. Conversely, over the second half of the concave region, $\langle u_n^2 \rangle^+$ significantly elevates, where the profile shows a minimum at $n^+ \approx 30$. Remaining almost constant over the first half of the inclined flat wall region, $\langle u_n^2 \rangle^+$ relaxes over the second half of the domain. This reduction continues until the middle of the convex region. Over the second half of the convex flow region, $\langle u_n^2 \rangle^+$ amplifies again and at the entrance to the throat region, it shows a minimum at $n^+ \approx 30$, with a larger value relative to the profile at s / h_{in} = -0.60.

When normalized by the outer scales, the mean wall-normal Reynolds stress profiles, shown in the right column of Figure 6-28(*a-c*), indicate relatively similar trends over the outer layer. The results show that as the flow passes over different sections of the convergence region, depending on the strength of the FPG, the level of the wall-normal turbulence intensities mitigates marginally in the outer layer. Near the wall, from the start of the inclined flat wall region to the end of the concave region, the wall-normal Reynolds stress profiles reduce gradually from a larger value to a minimum at n / $\delta \approx 0.18$. After this point, it starts to increase again. It is evident from the results that the magnitude of the minimum value increases as the FPG gets milder. It is important to note that near the wall, the uncertainty of the obtained results is relatively larger than the outer layer. Hence, the real resultant near-wall profiles might differ from the illustrated ones.

The skewness and kurtosis profiles of the tested accelerating water flows are shown at different streamwise positions over the convergence region of the TG channel in Figure 6-29(*a-c*). In all

tested conditions, near-wall skewness significantly deviates from the zero skewness value of a Gaussian distribution and is left- or right-skewed depending on the wall-normal position. Away from the wall, $Re_{\tau,0} = 198$ profiles show that at all streamwise positions, the skewness values are negative. For the other two conditions with higher $Re_{\tau,0}$, skewness is almost zero over the outer layer and deviates from the standard value close to the BL edge. In all three flow scenarios, the flow at the entrance to the throat is highly skewed and has a large negative deviation from $\mu_3 = 0$.

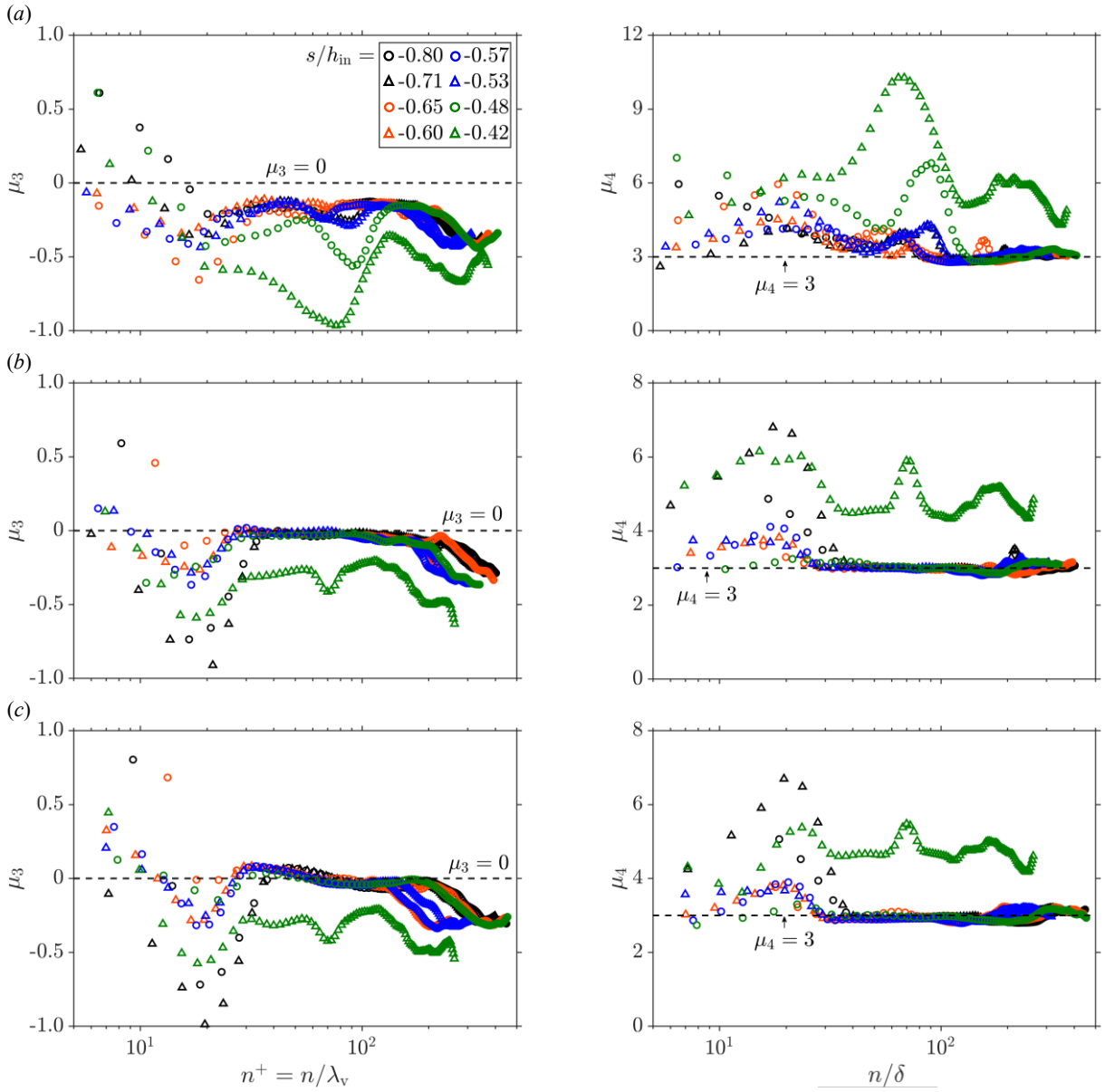

Figure 6-29 Wall-normal variation of the mean skewness, μ_3, profiles (left), and mean kurtosis, μ_4, profiles (right) at eight selected wall-parallel positions for accelerating water flow over the flat surface of the TG channel's convergence region at (*a*) $Re_{\tau,0} = 198$, (*b*) $Re_{\tau,0} = 240$, and (*c*) $Re_{\tau,0} = 282$.

Similar to the skewness profiles, the near-wall kurtosis profiles also deviate from the standard value for a Gaussian distribution, i.e., $\mu_4 = 3$. As the flow rate increases, the kurtosis values converge to the standard value at different positions in the convergence region for most of the outer layer. Nevertheless, the flow profile at the entrance of the throat region shows significant positive deviations from the standard value.

6.4. Decelerating flow

Developing turbulent BL undergoes deceleration over the divergence region, where the height of the TG channel increases gradually at a divergence angle of $\theta_d = 60°$ and finally reaches the inlet height of h_{in}= 8 mm. As shown in Figure 6-18, there is a convex curvature at the start of the diverging surface and a concave wall curvature at the end of it. As listed in Table 3-2, the radii of these curvatures are equal, i.e., r_d = 10 mm. As illustrated in Figure 3-13, the upper flat surface of the channel, centered at s / h_{in} = 0.72, was interrogated using PIV to investigate the turbulence of the developing BL subjected to an APG of varying strength. This section discusses the corresponding bulk boundary layer parameters and the mean flow.

6.4.1 Boundary layer parameters

As Figure 6-30(*a*) illustrates, the ratio of the edge to the mean wall-parallel velocity, U_e / U_m, decreases at a constant rate over the studied divergence region for the three tested water velocities. The measured ratios are smaller than Dean's correlation predictions (see equation (6-6)) for the ZPG flow. As the flow advances in the divergence region, the APG flattens the velocity profiles, where most of the measured velocities in the wall-normal direction have magnitudes close to edge velocity, resulting in U_e / U_m close to unity.

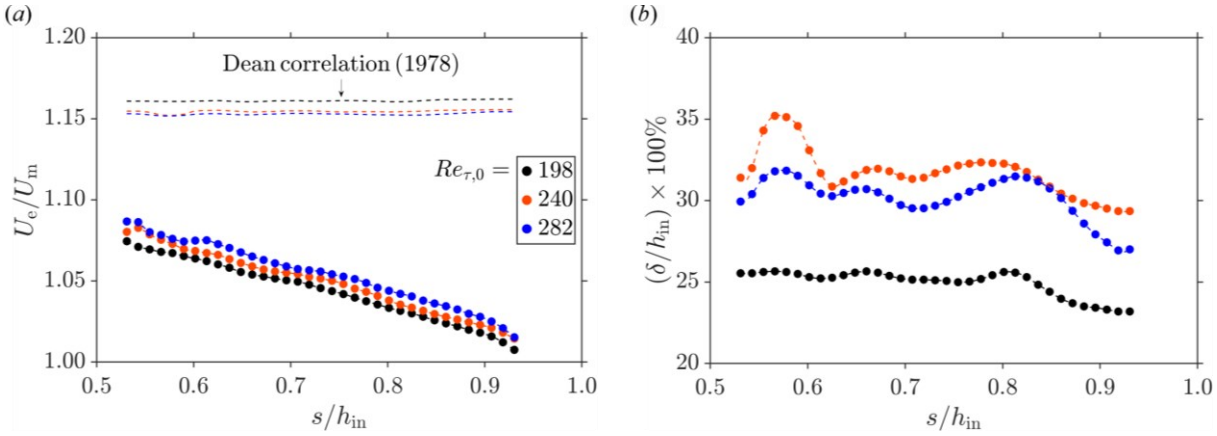

Figure 6-30 Wall-parallel variations of the (*a*) boundary layer edge velocity, U_e, ratio to the mean streamwise velocity, U_m, and (*b*) BL thickness, δ, normalized by h_{in}, for three different flow conditions of pure water flow at the flat surface of the divergence region of the TG channel (downstream of the throat). The correlation proposed by Dean (1978) for fully developed ZPG flow, given in equation (6-5), is also shown for reference. The legend shows the Re_τ values of the ZPG flow (see Table 6-1).

Figure 6-30(*b*) shows that as the $Re_{\tau,0}$ increases, the developing BL thickness increases in the divergence flow region, covering nearly 30 % of the channel's height. Here, the classical definition was utilized to calculate δ. The measured BL thicknesses indicate subtle variations over the region,

possibly due to the highly distorted core flow. The profiles of the integral parameters δ^* and θ, normalized by h_{in}, are illustrated in Figure 6-31(*a,b*). The profiles of the three tested flow conditions show a smooth peak at $s / h_{in} \approx 0.82$. This peak is particularly evident for the profile of the displacement thickness of the flow with $Re_{\tau,0} = 282$. As might be expected, increasing $Re_{\tau,0}$, amplifies the values of integral parameters over the entire deceleration region.

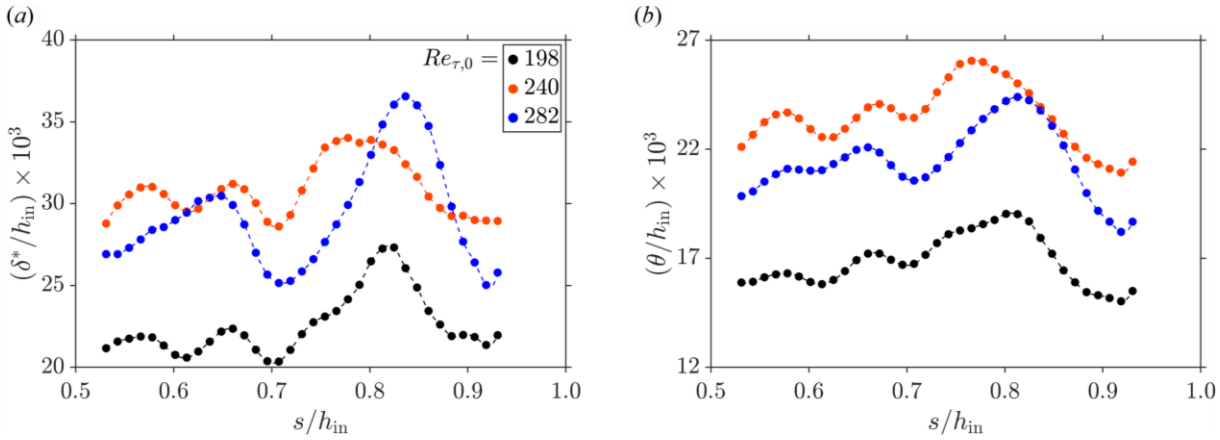

Figure 6-31 Wall-parallel variations of the (*a*) displacement thickness, δ^*, and (*b*) momentum thickness, θ, normalized by the inlet height, h_{in}, for three different flow conditions of pure water flow at the flat surface of the divergence region of the TG channel (downstream of the throat). The legend shows the Re_τ values of the ZPG flow (see Table 6-1).

The evaluated shape factor, H, and defect shape factor, G, profiles of the three different tested water flows are shown in Figure 6-32(*a,b*). The correlation of Pirozzoli (2014) for ZPG flows, given in equation (6-20), is also given in Figure 6-32(*a*) for reference. The H values remain almost constant over the divergence region, with subtle variations. Nevertheless, the highest tested flow indicates a smooth local peak at $s / h_{in} \approx 0.85$, possibly due to the highly distorted core region at this streamwise position.

The local variations of the defect shape factor profiles, illustrated in Figure 6-32(*b*), are substantial. At a known position, G increases as the shape factor or friction velocity decrease or edge velocity increases. As Figure 6-32(*a*) shows, at all positions, $1.2 < H < 1.5$; therefore, $0.16 < (1 - H^{-1}) < 0.33$. This result shows that the $(1 - H^{-1})$ term in G has a relaxing effect, but G profiles alternatively amplify and attenuate over the divergence region. Therefore, the impact of H on G is minimal. The edge velocity decreases gradually over the divergence region as the channel height increases linearly. Therefore, the effect of U_e on G should be a linear reduction in the streamwise direction, which contrasts with the G profiles' trends. This analysis shows that the

defect shape factor is a strong function of the friction velocity and local wall shear stress for these decelerating flows.

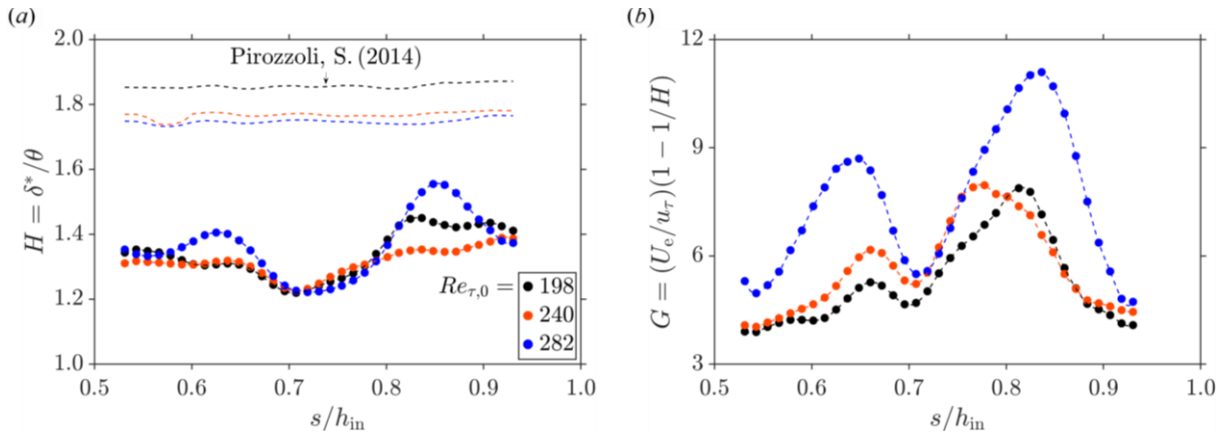

Figure 6-32 Streamwise variation of the (*a*) shape factor, *H*, and (*b*) deflect shape factor, *G*, for three different flow conditions of pure water flow over the flat surface of the divergence region of the TG channel (downstream of the throat). Predictions of the shape factor for fully developed ZPG channel flow based on equation (6-20) are also plotted in (*a*). The legend shows the Re_τ values of the ZPG flow (see Table 6-1).

Figure 6-33(*a*) demonstrates the pressure coefficient, c_p, profiles over the divergence region for three different water velocities. The c_p values are positive over the domain and gradually increase as the flow advances in the divergence region. The local edge pressure gradient profiles are also depicted in Figure 6-33(*a*), where the right axis shows their corresponding scale. As seen, the flow with the lowest tested velocity indicates almost a constant gradient over a wide range of the domain, which starts to increase close to the end of the domain. The pressure gradient profiles of the other two higher flow rates show similar behaviors with subtle variations.

Figure 6-33(*b*) demonstrates the skin friction factor profiles of the tested flows over the divergence region. The Dean's predictions of ZPG flows are also shown in the plot for reference. In all three tested scenarios, the friction factor decreases almost linearly under the strong APG until it reaches the vicinity of $s / h_{in} \approx 0.70$. At this point, the skin friction increases locally and generates a local peak, intensifying as the flow rate increases. As the flow advances further downstream, the friction factor decreases at a lower rate until $s / h_{in} \approx 0.78$. After this point, the friction factor increases again, mirroring almost the friction factor values before the minimum point. The location of the minimum friction factor in the divergence region is attributed to the point where flow tends to separate from the wall. Although no separation was observed in the current experiments, the subjected strong APG pushes the flow towards it. The flow gradually regains its

stability and uniformity as it advances toward the end of the divergence region, and hence friction factor approaches that of a ZPG flow.

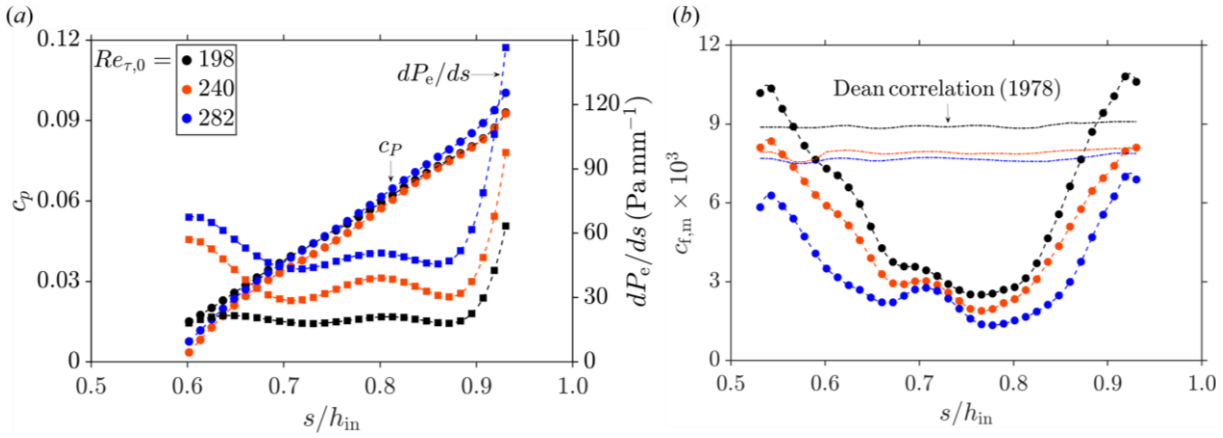

Figure 6-33 Wall-parallel variation of the (*a*) pressure coefficient, c_p, and streamwise edge pressure gradient, dP_e / ds, and (*b*) skin friction factor based on the mean velocity, $c_{f,m}$ (equation (2-26)), for three different flow conditions of pure water flow at the flat surface of the divergence region of the TG channel (downstream of the throat). The correlations proposed by Dean (1978) for fully developed ZPG flow, given in equation (6-6), are also shown in (*b*) for reference. The legend shows the Re_τ values of the ZPG flow (see Table 6-1).

Following the skin friction factor variations over the divergence region, the evaluated Re_τ profiles, shown in Figure 6-34(*a*), also indicate minimum points near $s / h_{in} \approx 0.78$. The Re_θ profiles are illustrated in Figure 6-34(*b*). The Re_θ values are almost constant over the divergence region with minor changes over the domain. However, as the water flow rate increases, the local variations in Re_θ amplify.

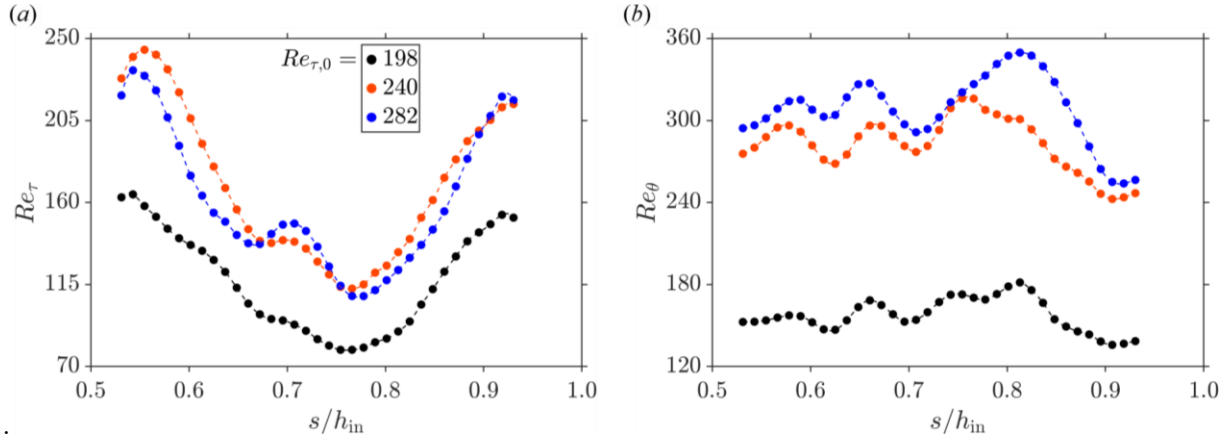

Figure 6-34 Streamwise variation of (*a*) Re_τ and (*b*) Re_θ, for three different flow conditions of pure water flow at the flat surface of the divergence region of the TG channel (downstream of the throat). The legend shows the Re_τ values of the ZPG flow (see Table 6-1).

As expected, the pressure gradient parameters, k, Δ_p and β, illustrated in Figure 6-35, indicate that flow is under strong APG over the divergence region. The K profiles obtained based on the local gradients of the BL edge velocities show that the exerted APG varies locally. There is an obvious first peak at $s / h_{in} \approx 0.65$, a minimum at $s / h_{in} \approx 0.70$, and a second peak at $s / h_{in} \approx 0.78$ in the Δ_p and β profiles of the tested water flows. The friction factor has its lowest value at $s / h_{in} \approx 0.78$, meaning that APG is relatively stronger at this point and flow is probable to separate. It is not obvious what causes the local minimum in the profiles, but they seem to be the result of the local interaction of the turbulence structures of the outer layer with the near-wall turbulence.

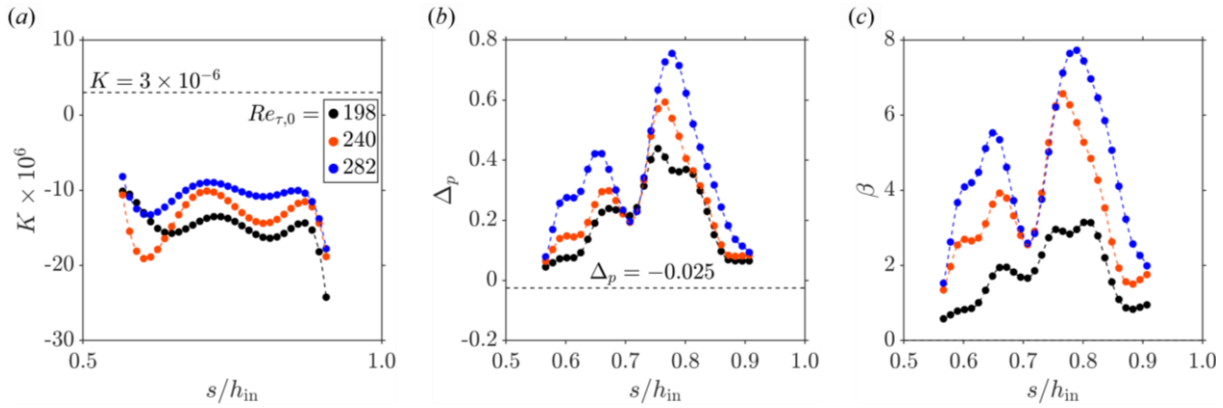

Figure 6-35 Streamwise variation of the (*a*) acceleration parameter, K (see equation (6-2)), (*b*) FPG parameter, Δ_p (see equation (6-1)), and (*c*) Rotta-Clauser pressure gradient parameter, β (see equation (6-4)), for three different flow conditions of pure water flow at the flat surface of the divergence region of the TG channel (downstream of the throat). The legend shows the Re_τ values of the ZPG flow (see Table 6-1).

6.4.2 Mean flow

The mean wall-parallel velocity profiles at different positions over the divergence region are illustrated in Figure 6-36(*a-c*) for three different flow conditions of water flow, normalized by the inner and outer scales. The standard linear viscous and logarithmic law profiles are also added to Figure 6-36(*a*) for reference. For the same flow conditions and positions, the normalized mean Reynolds shear stress and wall-parallel and wall-normal Reynolds stresses are depicted in Figure 6-37(*a-c*), Figure 6-38(*a-c*), and Figure 6-39(*a-c*), respectively.

Shown in Figure 6-36(*a*), as the decelerating flow with $Re_{\tau,0} = 198$ advances downstream, the normalized velocity profiles deviate above the standard logarithmic law, which continues until the vicinity of $s / h_{in} \approx 0.78$, where the skin friction factor is minimum and flow tends to separate. The deviated profiles are almost parallel to the logarithmic profile, and their offset is due to the strong APG they experience. All velocity profiles collapse on the viscous linear profile for $n^+ < 10$. The

wall shear stress gradually escalates toward the end of the divergence region while the flow is still under APG, which pushes the velocity profiles partially or entirely below the logarithmic profile.

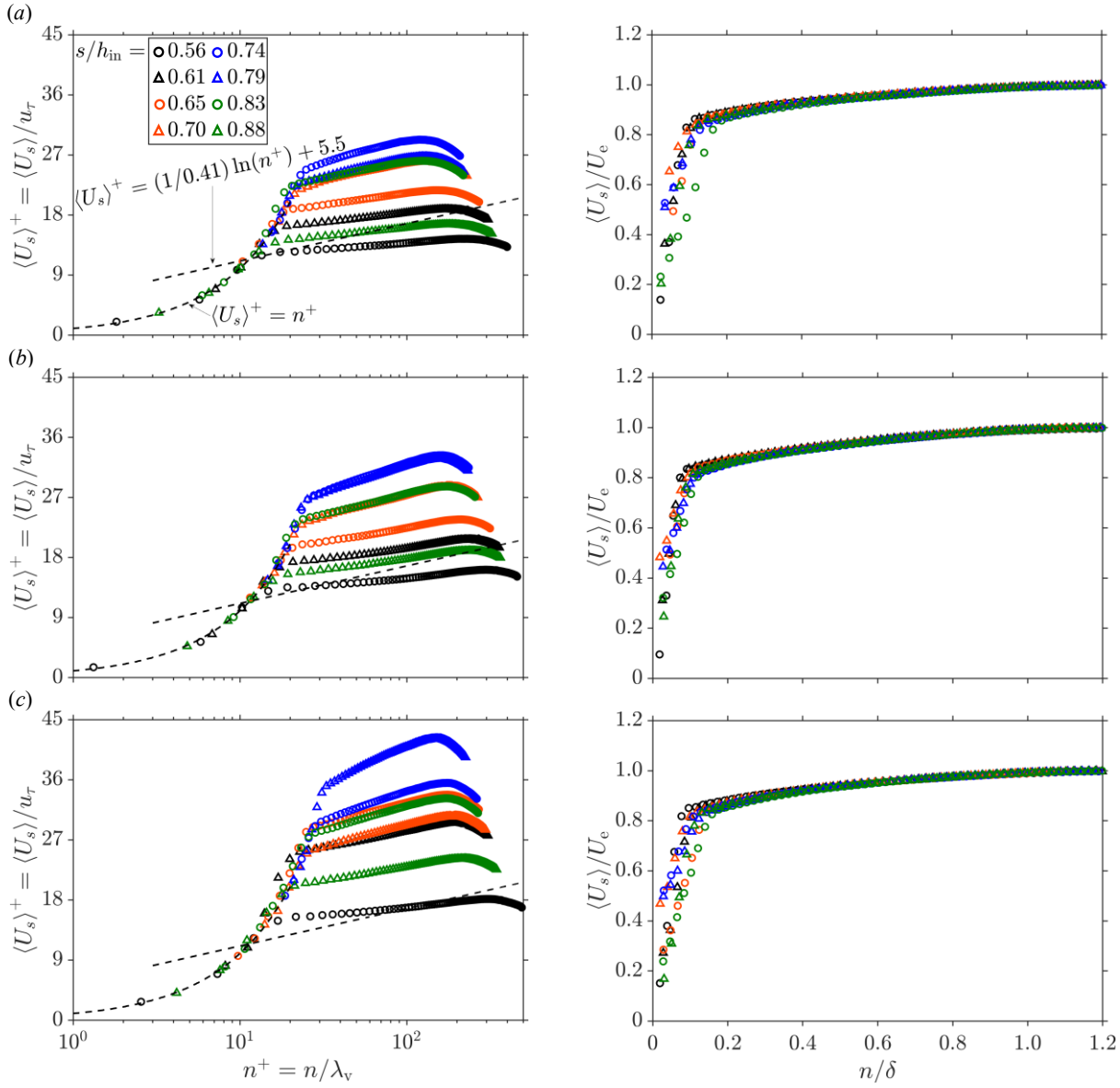

Figure 6-36 Wall-normal variation of the mean wall-parallel velocity profiles, normalized by the local inner scales (left) and by the outer scales (right), at eight selected wall-parallel positions for decelerating water flow over the flat surface of the TG channel's divergence region at (*a*) $Re_{\tau,0}$ = 198, (*b*) $Re_{\tau,0}$ = 240, and (*c*) $Re_{\tau,0}$ = 282.

The other two flow conditions with higher $Re_{\tau,0}$, shown in Figure 6-36(*b*,*c*), exhibit similar trends as the flow with $Re_{\tau,0}$ = 198, with profiles deviated to comparably higher levels due to an overall reduction of skin friction factor at these higher flow rates. The velocity profiles, normalized by the local edge velocity, illustrated in the right column of Figure 6-36(*a*-*c*), collapse on a similar profile in the outer layer and viscous sublayer for all three tested conditions. As the APG varies

the buffer layer thickness over the divergence region, the corresponding outer-normalized velocity profiles do not collapse and marginally differ.

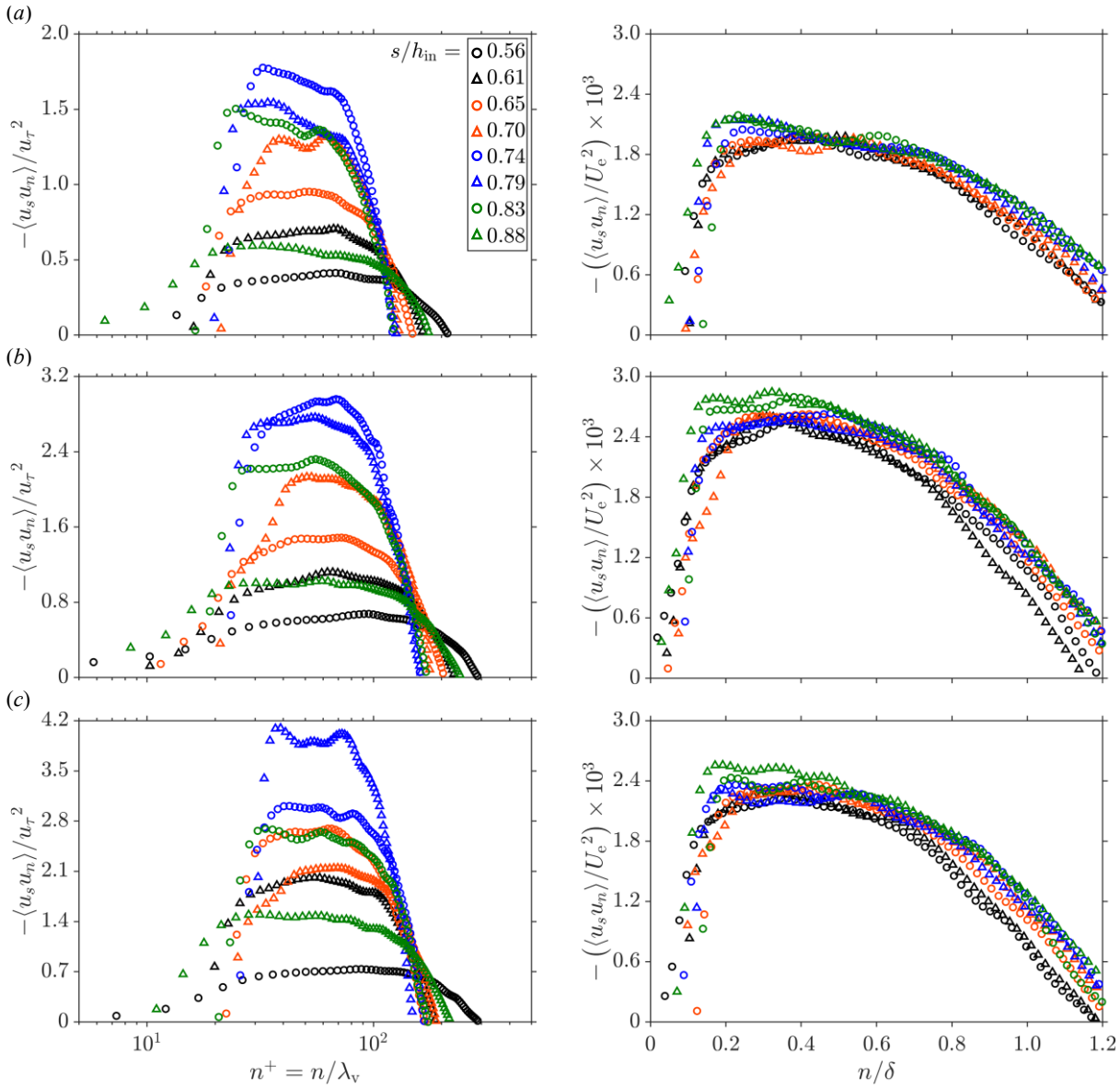

Figure 6-37 Wall-normal variation of the mean Reynolds shear-stress profiles, normalized by the local inner scales (left) and by the outer scales (right), at eight selected wall-parallel positions for decelerating water flow over the flat surface of the TG channel's divergence region at (*a*) $Re_{\tau,0} = 198$, (*b*) $Re_{\tau,0} = 240$, and (*c*) $Re_{\tau,0} = 282$.

As the APG strengthens over the divergence region, the mean inner-normalized Reynolds shear stress amplifies, and their profiles significantly elevate. For instance, the profile at $s / h_{\mathrm{in}} \approx 0.75$, shown in Figure 6-39(*a*), demonstrates this behavior. A smooth peak plateau is generated in the outer layer in $30 \lesssim n^+ \lesssim 100$, and the profile is relatively compressed compared to the profiles at the start of the interrogated region or close to the end of the divergence region, where APG is

weak. As $Re_{\tau,0}$ increases, the wall shear stress decreases over the domain, and the resultant Reynolds shear stress profiles elevate.

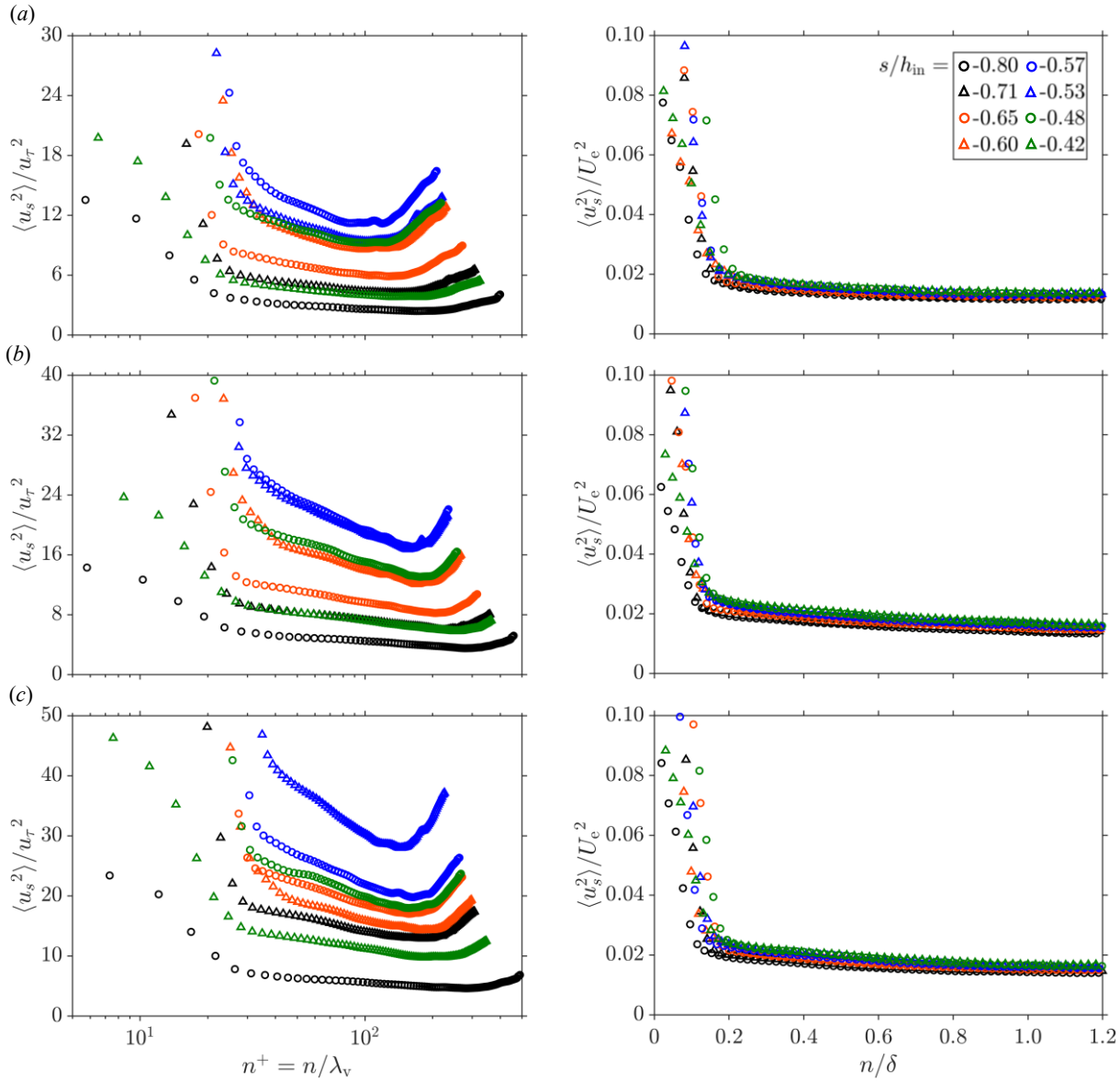

Figure 6-38 Wall-normal variation of the mean wall-parallel Reynolds stress profiles, normalized by the local inner scales (left) and by the outer scales (right), at eight selected wall-parallel positions for decelerating water flow over the flat surface of the TG channel's divergence region at (*a*) $Re_{\tau,0}$ = 198, (*b*) $Re_{\tau,0}$ = 240, and (*c*) $Re_{\tau,0}$ = 282.

Figure 6-39(*a-c*) shows that when normalized by the squared edge velocity, the Reynolds shear stress profiles do not exhibit extreme deviations. Nevertheless, in all tested flow conditions, in contrast to the inner-normalized profiles, where Reynold shear stresses were highly intensified at the point of minimum skin friction factor, they are slightly stronger at the regions close to the end of the divergence region. The main reason for this behavior is the smooth and relative reduction

of the edge velocity over the divergence region as flow advances downstream, which increases the Reynolds shear stresses when normalized by U_e^2.

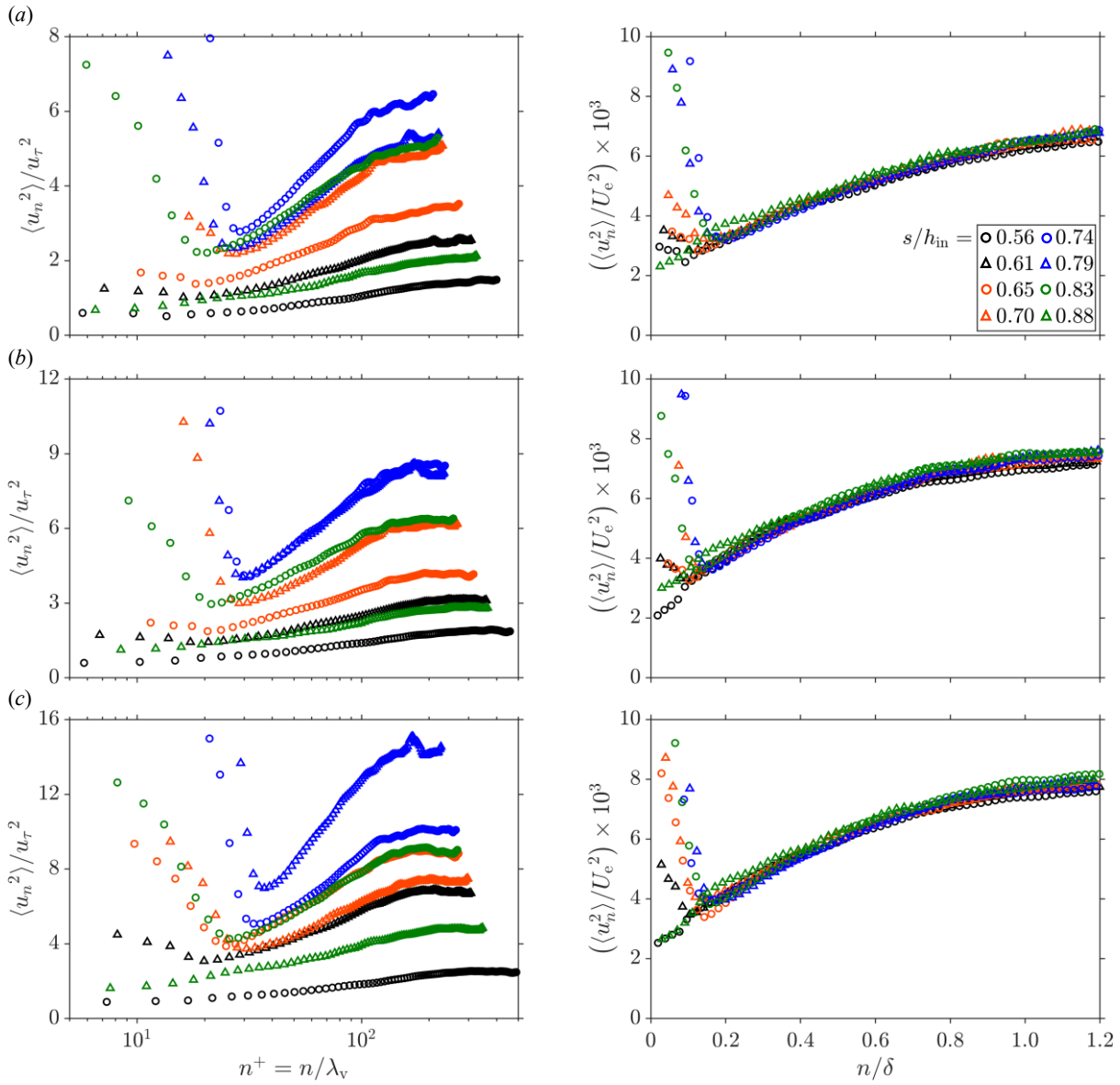

Figure 6-39 Wall-normal variation of the mean wall-normal Reynolds stress profiles, normalized by the local inner scales (left) and by the outer scales (right), at eight selected wall-parallel positions for decelerating water flow over the flat surface of the TG channel's divergence region at (*a*) $Re_{\tau,0}$ = 198, (*b*) $Re_{\tau,0}$ = 240, and (*c*) $Re_{\tau,0}$ = 282.

Similar to the Reynolds shear stress, the wall-parallel Reynolds stress profiles, illustrated in Figure 6-38(*a-c*), also show a wide range of changes over the deceleration region. As the flow approaches the point of minimum skin friction factor, the wall-parallel turbulence intensities amplify, and as flow advances downstream, wall shear stress increases, and wall-parallel turbulence intensity relaxes. All stress profiles indicate peaks in the buffer layer in $12 < n^+ < 15$,

but their magnitudes differ significantly based on the strength of the APG. The outer-normalized profiles almost collapse in the outer layer, and near the wall, they show peaks that are significantly higher than ZPG flows.

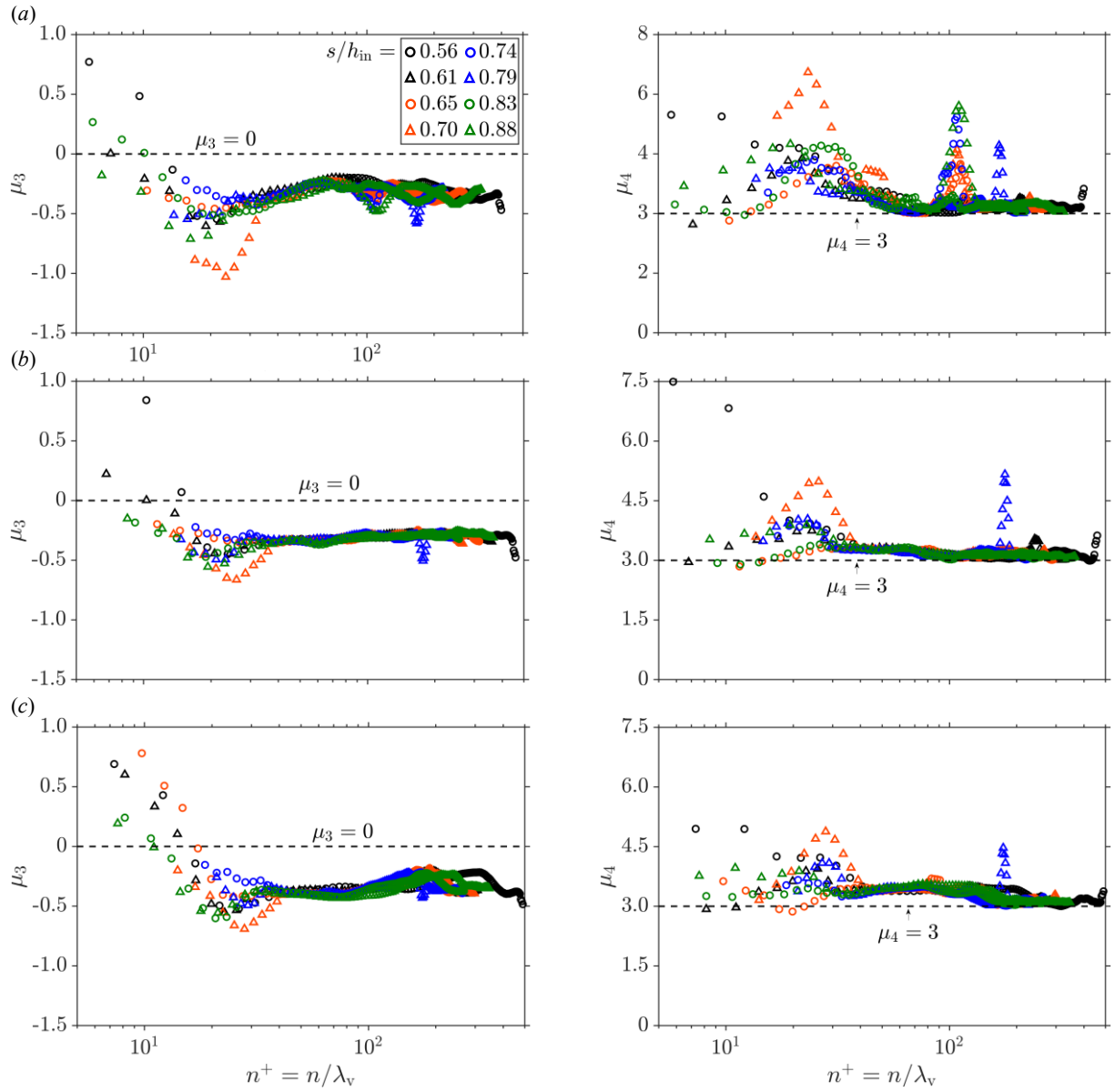

Figure 6-40 Wall-normal variation of the mean skewness, μ_3, profiles (left), and mean kurtosis, μ_4, profiles (right) at eight selected wall-parallel positions for decelerating water flow over the flat surface of the TG channel's divergence region at (*a*) $Re_{\tau,0} = 198$, (*b*) $Re_{\tau,0} = 240$, and (*c*) $Re_{\tau,0} = 282$.

Figure 6-39(*a-c*) illustrates the wall-normal variation of the mean wall-normal Reynolds stress profiles at different positions over the divergence region for three water flow rates. In regions of the flow where the skin friction factor decreases significantly due to a strong APG, the profiles are noticeably lifted to higher intensities. At these regions, for instance, at $s / h_{in} \approx 0.69$, the mean

profiles denote a minimum point somewhere in $30 < n^+ < 35$, where some studies called them 'knee-points' (Baskaran et al., 1987). A knee point is referred to the edge of an internal layer growing in the inner layer. In this work, such minimum points were only observed in the mean wall-normal Reynolds stress profiles, which might not be sufficient proof of internal BL development in the inner layer. Nevertheless, if there is any, the internal layer emerges at the first point with a strong APG and gradually drifts away from the wall. This behavior can be seen in Figure 6-39(*a-c*), as the knee points fade out downstream.

The outer normalized $\langle u_n^2 \rangle$ profiles, shown in the right column of Figure 6-39(*a-c*), almost collapse on a similar profile in the outer layer. Near the wall, the profiles show peaks in the vicinity of the streamwise positions with relatively lower friction factors, where the flow tends to separate. The level of the APG applied to the flow determines the magnitude of the peaks.

The skewness and kurtosis profiles of the decelerating flow at eight different streamwise positions over the divergence region are illustrated in Figure 6-40(*a-c*) for three flow scenarios. None of the skewness profiles collapse on the expected value of $\mu_3 = 0$ for a Gaussian distribution. In the outer layer, they have a negative offset of ≈ 0.4 and exhibit relatively larger positive values near the wall. The kurtosis profiles almost indicate values almost equal to that of a Gaussian distribution, i.e., $\mu_4 = 3$ in the outer layer along the divergence region. Nevertheless, they escalate in the near wall region, over the inner layer, and exhibit relatively large values.

6.5. Conclusion

Microscopic PIV was utilized to investigate developing turbulent BLs subjected to continuous pressure gradients of various signs and strengths over a converging-diverging bump in a rectangular channel flow. The flow was mainly studied in three different regions: (1) straight channel region, sufficiently far from the converging-diverging bump profile, with fully-developed ZPG flow, (2) convergence region, where the flow was subjected to a continuous effect of FPG of varying strength and wall curvature, and (3) divergence region with a decelerating flow, where APG of varying strength altered the flow turbulence locally. The mass flow rate was kept constant during each test, and flow fields were studied at three different inlet Reynolds numbers.

The results show that the flow statistics were fully converged. A detailed uncertainty analysis was performed on the main instantaneous and mean flow parameters. The bias uncertainty of the instantaneous wall-parallel velocity measurements was ≈ 7 %. The mean uncertainty of the instantaneous velocity fields, determined using the correlation statistics method of Wieneke (2015), showed that near-wall uncertainties could be as high as 4.5 %, and far from the wall, it reduces to values close to 2 % of the mean local wall-parallel velocity. The measurement uncertainties of the mean streamwise velocity field were at most 0.2 % of the local mean velocity.

The uncertainties of the mean normal Reynolds stress fields, i.e., uncertainties of $\langle u_s^2 \rangle(s,n)$ and $\langle u_n^2 \rangle(s,n)$ were less than 1.3 % and 1.6 % of their corresponding local mean values, where the peak values occurred mostly near the wall. The highest estimated uncertainties were associated with the mean Reynolds shear stress measurements. The results show that near the wall and centerline, they can be as high as 8 % and 10 % of their mean values, which drops to nearly 3 % in other wall positions.

The measured mean wall-parallel velocity profiles follow the linear profile in the viscous sublayer and collapse on the standard logarithmic profile in the outer layer. The applied velocimetry method resolved the mean velocity fields for wall positions with $n^+ > 2$. The $\langle u_s^2 \rangle^+$ profiles exhibited peaks at $n^+ \approx 13$, consistent with the previous reports of similar canonical 2D ZPG turbulent channel flows. A quadrant analysis was performed to elucidate the interaction of ejection, sweep, wallward and outward events over the turbulent BL. For the tested flow conditions, the sweep events dominate the ejection events in the near-wall region, and far from the wall, ejection motions dominate.

The evaluated skin friction factor profiles over the convergence and divergence regions show that overall, FPG increases and APG decreases the local friction factors. Nevertheless, it was found that the friction factor varies over the studied channel regions, even when the flow was fully under APG or FPG. Calculation of the non-dimensional pressure gradient parameters K, $\Delta_{p,}$ and β show that over the convergence region, flow experienced a continuous FPG but of varying strength. The K values were at least an order of magnitude larger than the critical value of $K = 3 \times 10^{-6}$, and Δ_p values significantly lower than $\Delta_p = -0.025$. These large magnitudes of pressure gradient parameters signify that the FPG flow might have transferred to a fully relaminarized regime in the convergence flow region. However, the mean statistics of the turbulent flow exhibit turbulent activities that were damped relative to a ZPG flow but possessed finite non-zero values. The parameter β was negative all over the convergence region, where it decreased to values as low as $\beta \approx -15$ for the flow with $Re_{\tau,0}$.

Conversely, the decelerating flow in the divergence region showed varying negative values of K, which were significantly lower than the critical value of $K = 3 \times 10^{-6}$ and locally reached values as low as $K = -20 \times 10^{-6}$ for the maximum tested flow rate. Negative K values with large magnitudes indicate that the flow in the divergence region experienced a strong APG of varying strength. Although no separation occurred over the APG region in the tested flow scenarios, over the entire domain, $\Delta_p \gg -0.025$ and its profile exhibited noticeable peaks at positions with strong APG, where flow tended to separate. At these positions, local β values reached values as high as $\beta \approx 8$ for flow with $Re_{\tau,0} = 282$.

All measured inner normalized mean velocity profiles of the pressure gradient flow regions collapse on the linear line of $\langle U_s \rangle^+ = n^+$ in the viscous sublayer and deviate from the standard logarithmic law in the outer layer. Depending on the local strength of the pressure gradient and wall shear stress, the profile may partially or fully deviate below or above the log law. At positions with a stronger FPG in the convergence region or with a weaker APG in the divergence region, the local friction factor increases; as a result, velocity profiles are pushed partially or fully below the logarithmic profile, and their slope becomes smaller than κ^{-1}. Conversely, for a position with a milder FPG or stronger APG, the local friction factor decreases, which causes the inner-normalized velocity profiles to deviate significantly above the logarithmic law profile. These profiles exhibit slopes similar to that of a ZPG, i.e., $\kappa^{-1} = 2.44$.

The inner normalized mean Reynolds shear stress profiles amplify as the skin friction factor decreases in the convergence region, even when the flow is fully subjected to a continuous FPG. Compared to a ZPG flow, the peak of the $-\langle u_s u_n \rangle^+$ profiles of the FPG flow are relatively larger at positions with smaller friction factors. Conversely, the outer normalized profiles show that FPG relaxes the Reynolds shear stresses compared to ZPG flows. This relaxation improves as the flow rate increases or FPG strengthens. Similar to Reynolds shear stress profiles, as FPG strength varies over the convergence region, the mean $\langle u_s^2 \rangle^+$ and $\langle u_n^2 \rangle^+$ profiles show different levels of intensity levels. The friction factor decreases at positions with a milder FPG, and the resultant normalized profiles escalate to higher levels. In contrast, when normalized by the outer scales, wall-parallel and wall-normal Reynolds stress profiles of the FPG flow indicate amplifications in their intensity relative to their corresponding ZPG flows.

One evident effect of APG is the significant amplification of the inner-normalized Reynolds shear stress, which escalates even more for higher flow rates. Nevertheless, when normalized by the local outer scales $U_e(s)$ and $\delta(s)$, the mean Reynolds shear stress profiles show similar intensity levels to that of a ZPG flow but with comparably flattened profiles over the outer layer. Similar to the Reynolds shear stress profiles, inner normalized profiles of $\langle u_s^2 \rangle$ and $\langle u_n^2 \rangle$ significantly amplify under strong APG. However, when normalized by outer scales, these stresses show relatively higher intensities than the ZPG flows, with peak values significantly higher than their counterparts in a ZPG flow at a similar mass flow rate. The $\langle u_n^2 \rangle$ profiles exhibit minimum points at positions subjected to APG in the divergence region, which might indicate the initiation of an internal layer in the inner layer. The minimum peak drifts away from the wall and finally disappears as the APG weakens and the skin friction factor increases.

7. Viscoelastic developing turbulent flow

Chapter 6 elucidated the main effects of favorable and adverse pressure gradients on the BL turbulence and explained the impact of wall curvature on local flow parameters in developing BLs. Consistent with previous studies, mean statistics of the water flows were invariant of the streamwise direction in the fully developed ZPG flows. In contrast, turbulent statistics of the flows subjected to pressure gradients varied with streamwise positions, and their values were functions of the strength of the applied pressure gradient. The question is how a non-Newtonian flow field, such as the ones tested in Chapter 5, behaves under a pressure gradient. The answer to this question is key to understanding the physics of cavitation reduction occurring in PAM solutions.

No information is available in the literature that explains the BL turbulence of polymer additives subjected to pressure gradient. In contrast, a wealth of previous, mostly experimental, studies examined the turbulence of dilute to concentrated polymeric solutions in fully developed ZPG channel and pipe flows. This Chapter starts with a review of the previous studies on the viscoelasticity effects of dilute polymer solutions on the turbulence of fully developed ZPG channel flows. Then, the results of the current study are presented in the form of three main Sections for two semi-dilute PAM solution flows with concentrations of 200 p.p.m. and 400 p.p.m., subjected to ZPG, FPG, and APG.

The results are provided in a structure similar to that of Chapter 6. The analysis results of the ZPG flow are provided to elucidate the individual effects of the PAM additives on the flow's turbulence and as a baseline for characterizing the impact of pressure gradients and wall curvature on such non-Newtonian flows. It is for the first time that the combined effect of continuous pressure gradient and wall curvature are studied in this detail on semi-dilute PAM solution flows.

7.1. Introduction

As discussed in Section 5.1, relative to a Newtonian fully developed turbulent flow, drag can be significantly reduced in a dilute solution flow of drag-reducing polymer additives. DR increases with the molecular weight of polymer agents, solution concentration, and flow rate (Sitaramaiah and Smith, 1969; Virk et al., 1970). Nevertheless, Virk et al. (1970) showed that a maximum DR (MDR) limit exists, and theoretically, a DR more than MDR is not feasible. Virk et al. (1970) showed that the ultimate wall profile for MDR is:

$$\langle U_s \rangle^+ = 11.7 \ln n^+ - 17.0\,, \tag{7-1}$$

for $n^+ > 11.6$, in a smooth pipe turbulent flow of polymer solutions. The tri-section point of the ultimate, Newtonian, and viscous profiles is at $\langle U_s \rangle^+$ = -17.08 and n_v^+ = 11.45. Virk et al. (1970) postulated three wall-normal zones in a polymer drag-reduced flow: viscous, *interactive,* and *Newtonian plug* zones, illustrated schematically in Figure 7-1. The velocity profile of a moderate drag-reduced flow, with $DR \leq 40\%$, falls into the Newtonian plug zone, where it has the slope of a Newtonian profile but shifts c_1^+ upwards. Virk et al. (1970) named c_1^+ the *effective slip*, which increases as the DR level increases. Therefore a velocity profile in the Newtonian plug zone has the form of:

$$\langle U_s \rangle^+ = (1/\kappa) \ln n^+ + c_0^+ + c_1^+, \qquad n^+ > n_N^+, \tag{7-2}$$

where n_N^+ is the wall-normal position where a Newtonian plug velocity profile intersects with the ultimate profile and can be calculated as:

$$n_N^+ = \exp\left(\frac{c_0^+ + c_1^+ + 17}{11.7 - \kappa^{-1}}\right). \tag{7-3}$$

As illustrated in Figure 7-1, the buffer layer is thicker in a drag-reduced flow than in a Newtonian flow, and its thickness increases as the DR level increases (Luchik and Tiederman, 1988; Min et al., 2003; Wei and Willmarth, 1992). After the critical $DR \approx 40$ %, the logarithmic layer is eradicated (White et al., 2012), and the slope and intercept values of the velocity profile do not follow equation (7-2) and approach Virk's ultimate profile given in equation (7-1).

Three main hypotheses have been developed so far to explain the onset of DR in dilute polymer solutions, which are based on: (1) time criterion (Berman, 1977; Hershey and Zakin, 1967; Lumley, 1969), (2) elongation-viscosity (Lumley, 1973), and (3) elastic theory (Sreenivasan and White, 2000; Tabor and Gennes, 1986). Based on the time criterion, the onset of DR occurs when the relaxation time of the polymers, λ, is larger than the viscous time scale, $t_v = \nu_w u_\tau^{-2}$, i.e., when $\lambda > t_v$. Based on the definition of the Weissenberg number, $We_i = \lambda / t_v$, the time criterion for the DR to initiate in polymer solution is $We_i > 1$. Here, the subscript 'i' empathizes that the inner time scale t_v was used in the definition of the Weissenberg number. As Berman (1977) discussed, the onset We_i can vary between 1 and 8, depending on the properties of the polymer additives and the bulk solvent. The DNS of Min et al. (2003) showed that onset occurred at $We_i \approx 6$.

The elongation viscosity hypothesis explains that the stretch of randomly coiled polymer molecules, known as the 'coil-stretch' transition, in strong deformation regions, such as in the buffer layer, increases the extensional (or effective) viscosity in these regions and is responsible for the DR (Lumley, 1973, 1969). The condition of $\lambda > t_v$ significantly enhances the elongation viscosity, which thickens the buffer layer and damps small eddies (Min et al., 2003; Ptasinski et al., 2003). However, this hypothesis was critiqued for being incapable of describing the existence of stress deficit and explaining the onset of DR (Sreenivasan and White, 2000).

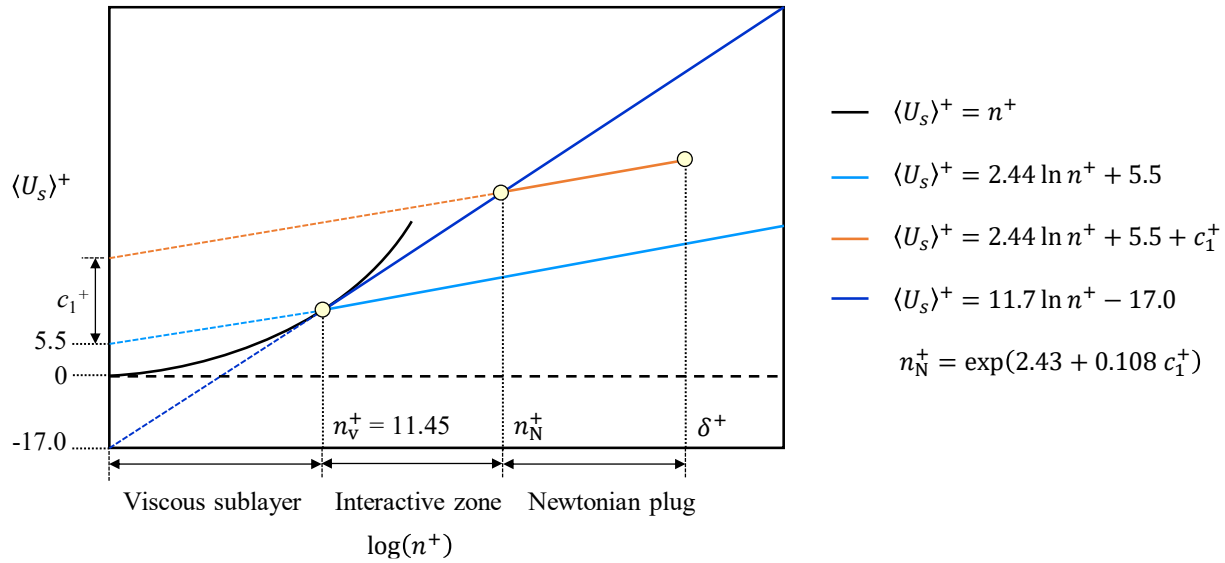

Figure 7-1 Schematic illustration of the near-wall mean velocity profiles and corresponding zones in a polymer drag-reduced flow. The schematic is replotted based on Figure 4 of Virk et al. (1970), with some modifications.

Based on the elastic theory (Tabor and Gennes, 1986), elongated polymer molecules extract energy from the viscous sublayer and store it as elastic energy (Min et al., 2003). When the relaxation time is sufficiently long, i.e., $\lambda \gg t_v$, the stored energy is transported and released into the buffer and log-law layers (Min et al., 2003). Stretch of long-chain polymers with $\lambda > t_v$ thickens the buffer layer and modifies the mean velocity profile, resulting in a different distribution of wall shear stresses (White and Mungal, 2008). The released energy enhances the streamwise turbulence intensity and attenuates the fluctuations of the wall-normal and spanwise velocities, which results in a reduction in the wall shear stress and accordingly causes DR (Arosemena et al., 2020; Dubief et al., 2004; Min et al., 2003; Ptasinski et al., 2003).

Warholic et al. (2001) obtained high DR of 41 % and 55 % using 1.25 p.p.m. and 50 p.p.m. solutions of a copolymer of PAM and sodium acrylate in a fully developed turbulent channel flow. Their PIV measurements showed that velocity fluctuations normal to the wall, small-scale

turbulent structures, swirling motions, and ejection events were significantly damped in the viscoelastic polymer solutions. The mean wall-parallel Reynolds stresses, $\langle u_s^2 \rangle$, were almost equal to that of pure water in the near wall region, but when normalized by the square of the friction velocity, i.e., $\langle u_s^2 \rangle^+ = \langle u_s^2 \rangle / u_\tau^2$, the peak values were significantly higher than the pure water flow. This behavior is expected since, for instance, in the 50 p.p.m. polymer solution of Warholic et al. (2001) with $DR = 55$ %, $(\tau_w)_{PAM} \approx 0.54\ (\tau_w)_{wat}$, which implies $(u_\tau^2)_{PAM} \approx 0.54\ (u_\tau^2)_{wat}$. Therefore, $\langle u_s^2 \rangle^+_{PAM} \approx 1.85\ \langle u_s^2 \rangle^+_{wat}$ for almost equal values of $\langle u_s^2 \rangle$. For the 50 p.p.m. solution, the peak of the normalized streamwise Reynolds stress was $\langle u_s^2 \rangle^+_{max} \approx 14.5$. A remedy for this is to normalize the turbulence intensities and the wall-normal positions by the friction velocity of the Newtonian turbulent flow, $u_{\tau,0}$. In contrast to mean streamwise intensities, the dimensional and normalized wall-normal Reynolds stress $\langle u_n^2 \rangle$ and Reynolds shear stress $-\langle u_s u_n \rangle$ were significantly attenuated in the polymer solutions, with the Reynolds shear stresses approaching a zero value for wall normal positions above a quarter of the channel's height.

Min et al. (2003) used the Oldroyd-B model as the constitutive equation of polymer stresses in their DNS to model the elasticity of the polymer molecules as linear Hookean dumbbells. They simulated fully developed ZPG dilute polymer solutions with shear viscosities of ≈× 1.11 of the Newtonian flow for different Weisenberg (We_i) numbers at a low and a high Reynolds number. They showed that increasing We_i attenuates r.m.s of the streamwise velocity fluctuations, normalized by the Newtonian friction velocity adjacent to the wall, but enhances them away from the wall. Min et al. (2003) reported that the r.m.s of the wall-normal and spanwise velocity fluctuations, normalized by $u_{\tau,0}$, decreased in the entire channel as We_i increased. Experimental results of Luchik and Tiederman (1988) and Warholic et al. (2001, 1999) also reported similar turbulent dynamics in ZPG flows of dilute polymer solutions.

The DNS of Ptasinski et al. (2003) showed that the streamwise turbulent intensity increases for higher levels of DR but decreases at MDR. They used the finitely extensible nonlinear elastic (FENE) spring model, with the Peterlin approximation (FENE-P), to simulate the forces applied by the polymers to the flow and generate a constitutive equation for the polymer stress tensor. The authors showed that the Reynolds shear stress is strongly reduced near the wall but remains at a finite non-zero value. Their results show that the polymer's stress contains ≈ 40% of the total shear

stress at MDR, which highlights that under this condition, a considerable part of the energy produced by the mean flow is transferred to polymers as elastic energy.

Mitishita et al. (2021) studied a fully developed turbulent yield stress flow using laser doppler anemometry. They utilized concentrated Carbopol solutions in water and confirmed that the solution was fully yielded in all their tests. In agreement with the shear-thinning polymer solutions, their results for the simple viscoplastic flow also showed a streamwise enhancement and a wall-normal decrease in the velocity fluctuations. The authors showed that adding Carbopol additives energized the large-scale turbulent structures and attenuated the energy of smaller turbulence scales. This result was illustrated by the energy spectra of the viscoplastic flows relative to the pure water flow, where the energy decayed with a slope of -7/2 in the inertial range, different from the -5/3 slope of the Kolmogorov scale for a Newtonian flow (Kolmogorov, 1941).

Many studies discuss the turbulence of viscoelastic dilute solution flows in fully developed ZPG channels. While the details of the exact mechanism by which polymer molecules cause DR is still under debate. DNS and PIV measurements confirm that drag-reducing additives thicken the buffer layer, enhance the streamwise, and attenuate the wall-normal and spanwise turbulence intensities. However, it is not known how the polymer additives modify the turbulence of flows under mild to strong pressure gradients. In Chapter 6, it was shown that, in agreement with previous studies, a strong FPG reduces the turbulence intensities, relaminarizes the flow, and makes the BL thinner. A strong APG enhances the turbulent activity, thickens the BL, and might cause separation. This Chapter aims to elucidate the dynamics of developing turbulent BLs when the viscoelasticity and pressure gradient effects are combined. To the author's knowledge, there is no available literature on this interesting phenomenon.

7.2. Validation of turbulence statistics

The statistical convergence of the mean wall-parallel velocity in tested PAM solutions was investigated by monitoring the variation of the N-sample averages, $\langle U_s \rangle_N$, at different wall distances and three different flow conditions. Figure 7-2(a,b) illustrates the convergence of $\langle U_s \rangle$ at four wall-distances from the buffer layer to the outer layer, near the channel's centerline, for 200 p.p.m. and 400 p.p.m. PAM solutions with ZPG and at $Re_\tau = 141$.

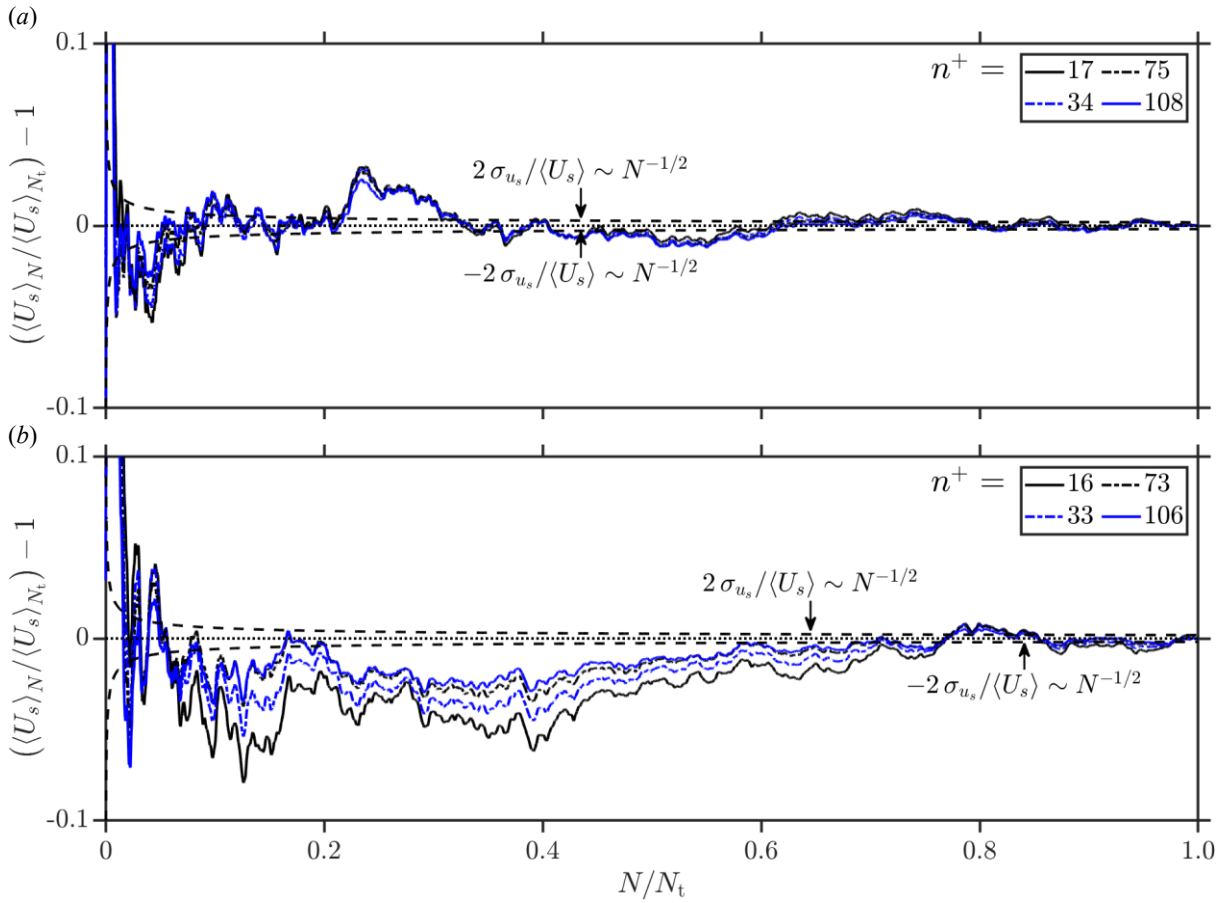

Figure 7-2 Variation of the ensemble-averaged streamwise velocity $\langle U_s \rangle$ at four different wall distances, as a function of the sample number N for (a) 200 p.p.m. and (b) 400 p.p.m. ZPG PAM solution flows at $Re_\tau = 141$ (see Table 7-3 and Table 7-4). The long-time average $\langle U_s \rangle_{N_t}$ normalizes the results, where $N_t = 11\,000$, is the total number of the velocity fields. The dashed black lines denote the reliability margins (Adrian and Westerweel, 2011).

As Figure 7-2(a,b) shows, the convergence of the mean velocities is achieved, and the long-time averages $\langle U_s \rangle_{N_t}$ fall into the reliability margin of $\pm 2\,\sigma_{u_s}/\langle U_s \rangle$ (Adrian and Westerweel, 2011). Here, a representative value of $\sigma_{u_s} = 0.1$ was used in plots of Figure 7-2(a,b). Even though, compared to the convergence profiles of the pure water flow, shown in Figure 6-4, the oscillations of the PAM profiles are more significant, even in the last 20 % of the data. As will be discussed

later in this Chapter, this might be because of the interaction of polymer molecules with the turbulent water flow in PAM solutions, which enhances the wall-parallel velocity fluctuations.

The fast convergence of the first-order averages of velocity fluctuations $\langle u_s \rangle_{N_t} \to 0$ and $\langle u_n \rangle_{N_t} \to 0$ at the different probed locations from the buffer to the outer layer at the vicinity of the centerline for both 200 p.p.m. and 400 p.p.m. ZPG PAM solutions at $Re_\tau = 141$ are illustrated in the two top rows of Figure 7-3(*a*,*b*). Similar fast convergences were observed for other tested flow conditions but are not presented here for the brevity of the discussion. The mean wall-parallel and wall-normal Reynolds stresses demonstrate excellent convergence with ≈ 80 % of samples ($N \approx 9\,000$) used for averaging in both tested PAM solutions. However, these Reynolds stresses converge faster in the 200 p.p.m. solution than in the 400 p.p.m. solution.

Compared to pure water, PAM solutions demonstrate a slower convergence for a similar number of samples. As Figure 7-3(*a*,*b*) illustrates, the amplitude of the mean Reynolds shear stresses greatly oscillate in the first 20-30 % of the data, and they hardly converge until ≈ 90 % of the samples were used for averaging. This behavior is evident for both tested PAM solutions, and the oscillations are more violent than their counterpart for the water flow, shown in Figure 6-5(*b*).

Random noises of the mean velocity measurements, calculated based on the procedure explained in Section 6.2.1, are listed in Table 7-1 and Table 7-2 for 200 p.p.m. and 400 p.p.m. ZPG PAM solution flows. The maximum calculated $e_{R,\langle U_s \rangle}$ for the 200 p.p.m. flow is ≈ 1.66 % for $n^+ \approx 19$ at $Re_\tau = 154$ and it is ≈ 1.37 % for $n^+ \approx 16$ at $Re_\tau = 141$ for the 400 p.p.m. flow. The results show that the random noises reduce for wall position farther from the wall and tend to $e_{R,\langle U_s \rangle} < 1$ %. As discussed before, compared to the ZPG pure water flow, the random noises of mean velocities are an order of magnitude larger in the tested PAM solutions due to the enhancement of longitudinal velocity fluctuations in these viscoelastic solutions.

Table 7-1 Random noises of the mean wall-parallel velocity and Reynolds stresses at different wall-normal positions for the ZPG 200 p.p.m. PAM solution flow at three different Re_τ.

	$Re_\tau = 117$			$Re_\tau = 141$			$Re_\tau = 154$		
Parameter	$n^+ = 14$	$n^+ = 50$	$n^+ = 100$	$n^+ = 17$	$n^+ = 50$	$n^+ = 100$	$n^+ = 19$	$n^+ = 55$	$n^+ = 100$
$e_{R,\langle U_s \rangle}$%	1.07	0.60	0.40	0.63	0.51	0.30	1.66	1.24	0.87
$e_{R,\langle u_s u_n \rangle}$%	6.81	9.47	7.52	10.09	6.83	10.07	7.67	10.41	10.89
$e_{R,\langle u_s^2 \rangle}$%	3.43	3.77	6.23	2.95	2.34	2.03	1.92	2.75	2.47
$e_{R,\langle u_n^2 \rangle}$%	2.53	1.82	1.96	2.16	3.46	1.61	4.96	2.92	1.71

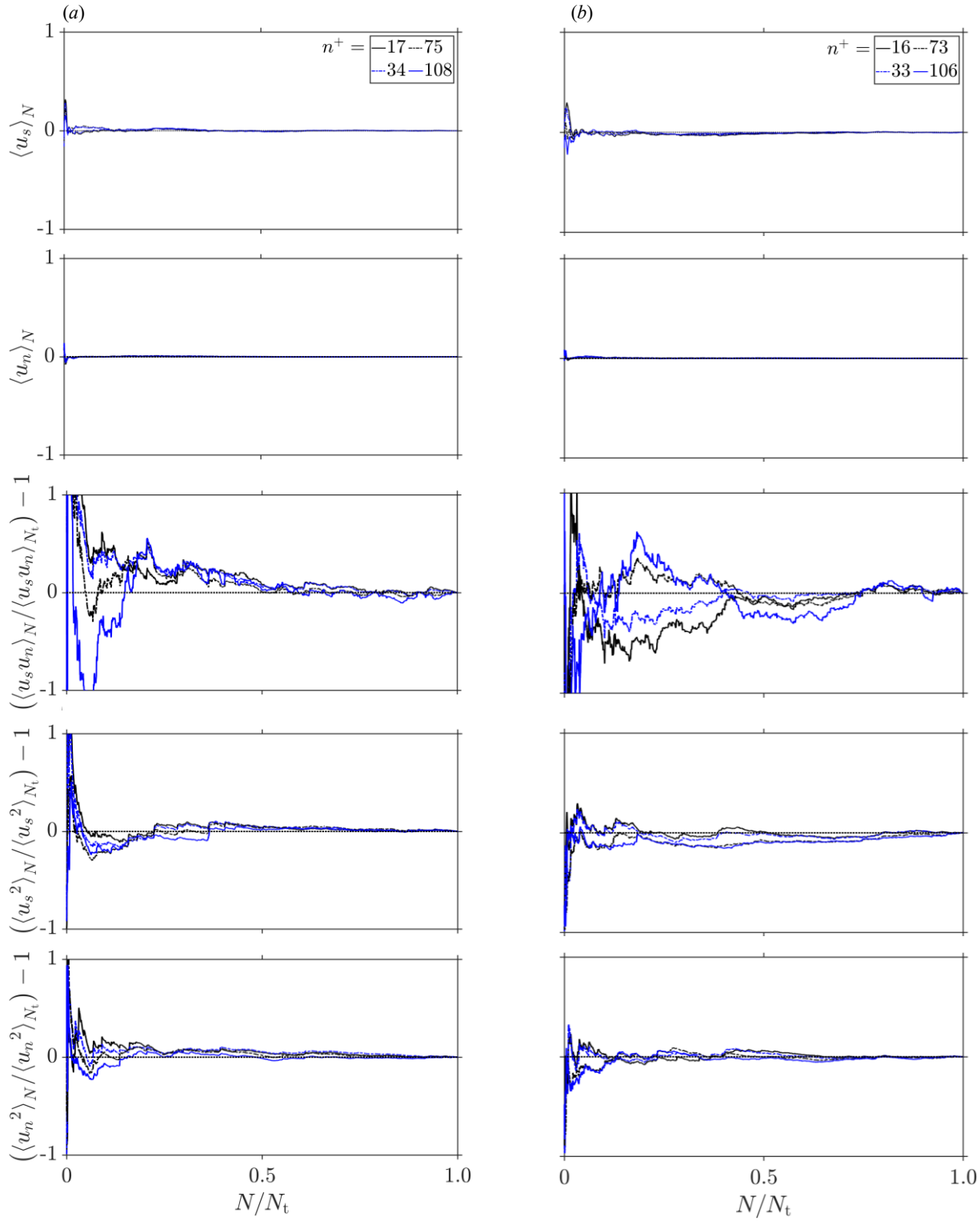

Figure 7-3 Statistical convergence of $\langle u_s \rangle$, $\langle u_n \rangle$, $\langle u_s u_n \rangle$, $\langle u_s^2 \rangle$ and $\langle u_n^2 \rangle$ at four different wall distances for (*a*) 200 p.p.m. and (*b*) 400 p.p.m. ZPG PAM solution flows at $Re_\tau = 141$ (see Table 7-3 and Table 7-4). Here, $N_t = 11\,000$ is the total number of samples. Each profile is normalized by its corresponding long-time average.

The calculated random noises of $\langle u_s^2 \rangle$ and $\langle u_n^2 \rangle$ are listed in Table 7-1 and Table 7-2 for 200 p.p.m. and 400 p.p.m. ZPG PAM solution flows. Overall, the wall-parallel Reynolds stresses show a maximum random noise lower than ≈ 6.5 % in the 200 p.p.m. and ≈ 4.5 % in the 400 p.p.m. ZPG solutions. The random noise of $\langle u_n^2 \rangle$ Reynolds stress measurements does not exceed ≈ 5.0 % in the 200 p.p.m. and ≈ 3.5 % in the 400 p.p.m. ZPG solutions.

Table 7-2 Random noises of the mean wall-parallel velocity and Reynolds stresses at different wall-normal positions for the ZPG 400 p.p.m. PAM solution flow at three different Re_τ.

	Re_τ = 107			Re_τ = 126			Re_τ = 141		
Parameter	n^+ = 12	n^+ = 43	n^+ = 79	n^+ = 16	n^+ = 52	n^+ = 96	n^+ = 16	n^+ = 57	n^+ = 89
$e_{R,\langle U_S \rangle}$%	1.27	0.90	1.06	1.91	1.13	0.55	1.37	0.83	0.82
$e_{R,\langle u_s u_n \rangle}$%	6.93	9.34	12.58	19.34	9.07	6.99	11.93	7.42	12.48
$e_{R,\langle u_S^2 \rangle}$%	4.21	4.11	3.11	3.76	2.12	2.70	2.85	2.46	4.44
$e_{R,\langle u_n^2 \rangle}$%	2.59	2.06	3.53	1.83	1.48	1.70	2.01	3.31	2.65

As Figure 7-3(*a*,*b*) demonstrates, the random noises of $\langle u_s u_n \rangle$ measurement, listed in Table 7-1 and Table 7-2, are relatively higher compared to the mean wall-parallel and -normal Reynolds stresses in the polymer solutions. Overall, $e_{R,\langle u_s u_n \rangle}$ is lower than ≈ 11 % in the monitored wall-normal positions in the 200 p.p.m. solution and smaller than ≈ 20 % in the 400 p.p.m. solution. This relatively large random noise is associated with high amplitude fluctuations near the wall region. Overall, the random noises of mean Reynolds shear stress measurements in the tested polymer solutions are × 2-3 more intense than the ZPG pure water flow.

Statistical convergence of the skewness and kurtosis of the tested PAM solutions were also investigated by probing the variation of their ensemble averages with the number of samples at four different wall-normal positions, spanning the near wall to the outer layer. Figure 7-4(*a*,*b*) illustrates these variations for the 200 p.p.m. and 400 p.p.m. ZPG solution flows. The oscillations of the kurtosis damp after ≈ 50 % of the samples were used for averaging and converged faster than the skewness to their final ensemble averages at different wall distances. In contrast, as the top row of Figure 7-4(*a*,*b*) demonstrates, the skewness profiles hardly converged to a final value, even with the total number of the samples, N_t = 11 000, used for averaging. The results show that the oscillations of the skewness are more intense in the near-wall region.

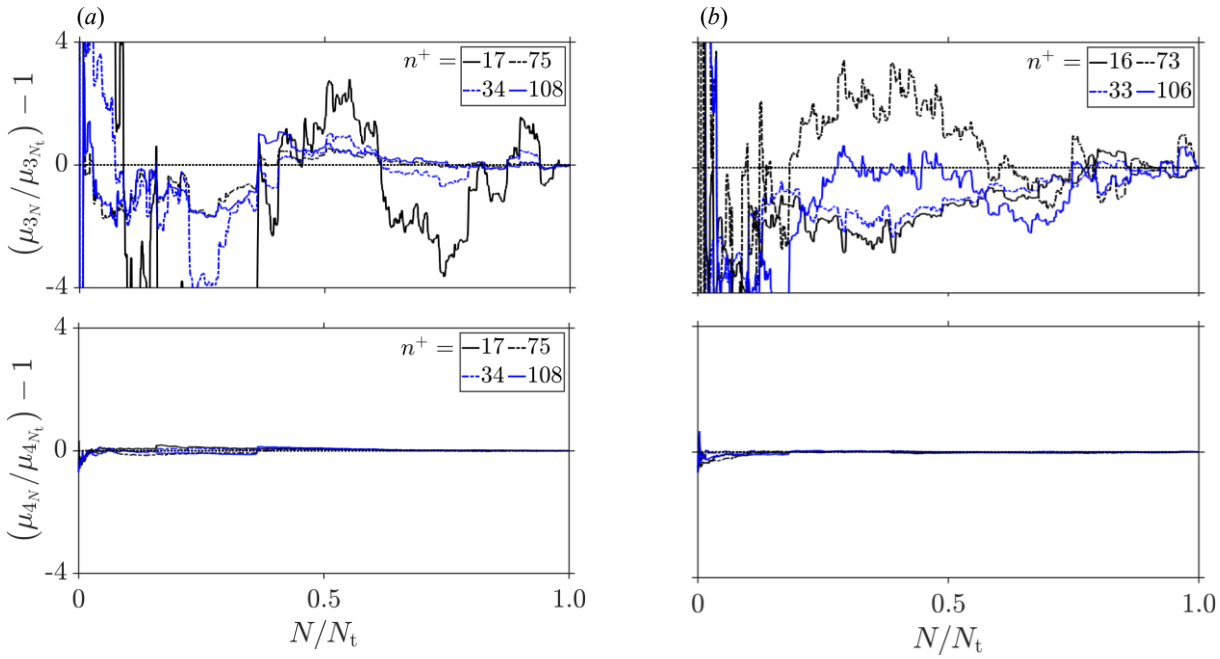

Figure 7-4 Statistical convergence of the skewness, μ_3 and kurtosis, μ_4, for (*a*) 200 p.p.m. and (b) 400 p.p.m. ZPG PAM solution flows at $Re_\tau = 141$. Here, $N_t = 11\,000$. Each profile is normalized by its long-time average.

7.3. Zero pressure gradient flow

Table 7-3 and Table 7-4 list the main BL parameters of fully developed ZPG 200 p.p.m. and 400 p.p.m. PAM solutions at three conditions: $Re_\tau = 117$, $Re_\tau = 141$, and $Re_\tau = 154$ for the 200 p.p.m. and $Re_\tau = 107$, $Re_\tau = 126$, and $Re_\tau = 141$ for the 400 p.p.m. solution. These conditions are equivalent to $3.6 \times 10^3 < Re_m < 6.2 \times 10^3$ and $3.6 \times 10^3 < Re_m < 6.0 \times 10^3$ for, respectively, the 200 p.p.m. and 400 p.p.m. solution flows. The measurements are attributed to the ZPG FOV highlighted in Figure 3-13. The determined U_e / U_m values in the PAM solutions are overall larger than the ones obtained from equation (6-5), developed by (Dean, 1978) for ZPG fully turbulent Newtonian flow, denoting that the polymer additives alter the structure of the mean velocity.

Table 7-3 List of main bulk and near-wall BL parameters of the ZPG turbulent 200 p.p.m. solution flow.

Parameter	Unit	Case I	Case II	Case III
μ_w	mPa s	1.61	1.58	1.57
U_m	m s^{-1}	0.77	0.99	1.20
U_e	m s^{-1}	0.93	1.22	1.49
U_{zs}	m s^{-1}	0.17	0.25	0.31
U_e / U_m		1.21	1.23	1.24
$(U_e / U_m)_{Dean}$		1.16	1.16	1.16
Re_m		3 684	5 044	6 164
Re_e		2 227	3 101	3 833
$Re_\tau = \delta^+$		117	141	154
δ_{99}	mm	3.86	4.02	4.03
δ^* / δ		0.19	0.20	0.21
θ / δ		0.11	0.12	0.13
H		1.70	1.68	1.66
G		7.88	8.89	9.87
$\dot{\gamma}_w \times 10^{-3}$	s^{-1}	1.47	1.95	2.30
τ_w	Pa	2.36	3.09	3.61
DR %		0.1	17.1	30.4
u_τ	mm s^{-1}	48.6	55.6	60.1
λ_v	μm	33.1	28.5	26.1
t_v	μs	680.3	511.8	434.6
$L_x^+ \times L_y^+$		108 × 160	126 × 186	137 × 202
$\Delta x^+ \times \Delta y^+$		1.4 × 1.4	1.7 × 1.7	1.8 × 1.8
U_m^+		15.8	17.9	20.0
U_e^+		19.1	22.0	24.8
$c_{f,e} \times 10^3$		8.05	6.26	5.02
$c_{f,m} \times 10^3$		9.37	8.66	8.24
$c_{f,Dean} \times 10^3$		5.51	4.14	3.24

In each case, the least square method was used to fit a line to the mean velocity profile in the viscous sublayer and determine the mean shear strain rate, $\dot{\gamma}_w$. The shear strain rate values were introduced into the CY models, explained in Section 4.1, to obtain the wall shear viscosity, μ_w.

The μ_w of the 200 p.p.m. solution at $Re_\tau = 117$ is × 1.77 the water viscosity, and it is × 1.86 the water viscosity at $Re_\tau = 107$ in the 400 p.p.m. solution. The PAM solutions are shear-thinning and as Re_τ and equivalently $\dot{\gamma}_w$ increases, the wall shear viscosity decreases. The mean wall shear stress was calculated using the determined μ_w and $\dot{\gamma}_w$ values, i.e., $\tau_w = \mu_w \dot{\gamma}_w$. The equivalent Newtonian $\tau_{w,0}$ was calculated using equation (6-6) for each case with Re_m of the PAM solution, and it was used to evaluate the *DR* % in the polymer solutions. Here, *DR* % = 1 - $(\tau_w/\tau_{w,0})$.

Table 7-4 List of main bulk and near-wall BL parameters of the ZPG turbulent 400 p.p.m. solution flow.

Parameter	Unit	Case I	Case II	Case III
μ_w	mPa s	1.69	1.62	1.59
U_m	m s^{-1}	0.75	0.97	1.16
U_e	m s^{-1}	0.96	1.23	1.48
U_{zs}	m s^{-1}	0.23	0.28	0.34
U_e / U_m		1.28	1.27	1.27
$(U_e / U_m)_{Dean}$		1.16	1.16	1.16
Re_m		3 693	4 819	5 980
Re_e		2 369	3 054	3 805
$Re_\tau = \delta^+$		107	126	141
δ_{99}	mm	4.15	4.02	4.09
δ^* / δ		0.24	0.22	0.23
θ / δ		0.13	0.13	0.13
H		1.80	1.74	1.77
G		9.90	10.33	11.70
$\dot{\gamma}_w \times 10^{-3}$	s^{-1}	1.12	1.58	1.89
τ_w	Pa	1.89	2.56	3.00
DR %		17.6	28.3	38.6
u_τ	mm s^{-1}	43.4	50.6	54.8
λ_v	μm	38.9	32.0	29.0
t_v	μs	895.3	631.9	528.5
$L_x^+ \times L_y^+$		92 × 135	112 × 165	123 × 182
$\Delta x^+ \times \Delta y^+$		1.2 × 1.2	1.5 × 1.5	1.6 × 1.6
U_m^+		17.3	19.2	21.2
U_e^+		22.2	24.3	26.9
$c_{f,e} \times 10^3$		6.68	5.45	4.46
$c_{f,m} \times 10^3$		9.36	8.76	8.30
$c_{f,Dean} \times 10^3$		4.06	3.39	2.76

The boundary layer thickness, δ, is 3.50 % smaller than the half channel width at $Re_\tau = 117$ in the ZPG 200 p.p.m. solution. For $Re_\tau = 141$ and $Re_\tau = 154$, δ is 0.50 % and 0.75 % larger than 0.5 h_{in}. These negligible discrepancies are mainly associated with the uncertainties in the PIV measurements and determination of the wall position. The estimated displacement thicknesses are ≈ 43 % and ≈ 64 % larger than the δ^*/δ of the pure water. As Re_τ increases, H reduces to 1.66

and 1.77 in the 200 p.p.m. and 400 p.p.m. solutions. The increase of Re_τ reduced the G values. Compared to the pure water flow, H and G parameters are larger in the polymer solution flows. The spatial resolution of the measured mean velocity was $\Delta x^+ \times \Delta y^+ = 1.8 \times 1.8$ at $Re_\tau = 154$ in the 200 p.p.m. sand it was $\Delta x^+ \times \Delta y^+ = 1.6 \times 1.6$ at $Re_\tau = 141$ in the 400 p.p.m. solution.

Figure 7-5(*a*,*b*) demonstrates sample instantaneous fluctuating velocity fields in the wall-parallel and wall-normal directions for the ZPG 200 p.p.m. and 400 p.p.m. PAM solutions at $Re_\tau = 141$. The ranges of changes were adjusted to represent visually interpretable plots, and they do not necessarily denote the actual ranges of fluctuations. Velocity vectors, scaled by the maximum velocity, are also inserted on the top of the plots and are shown by black arrows.

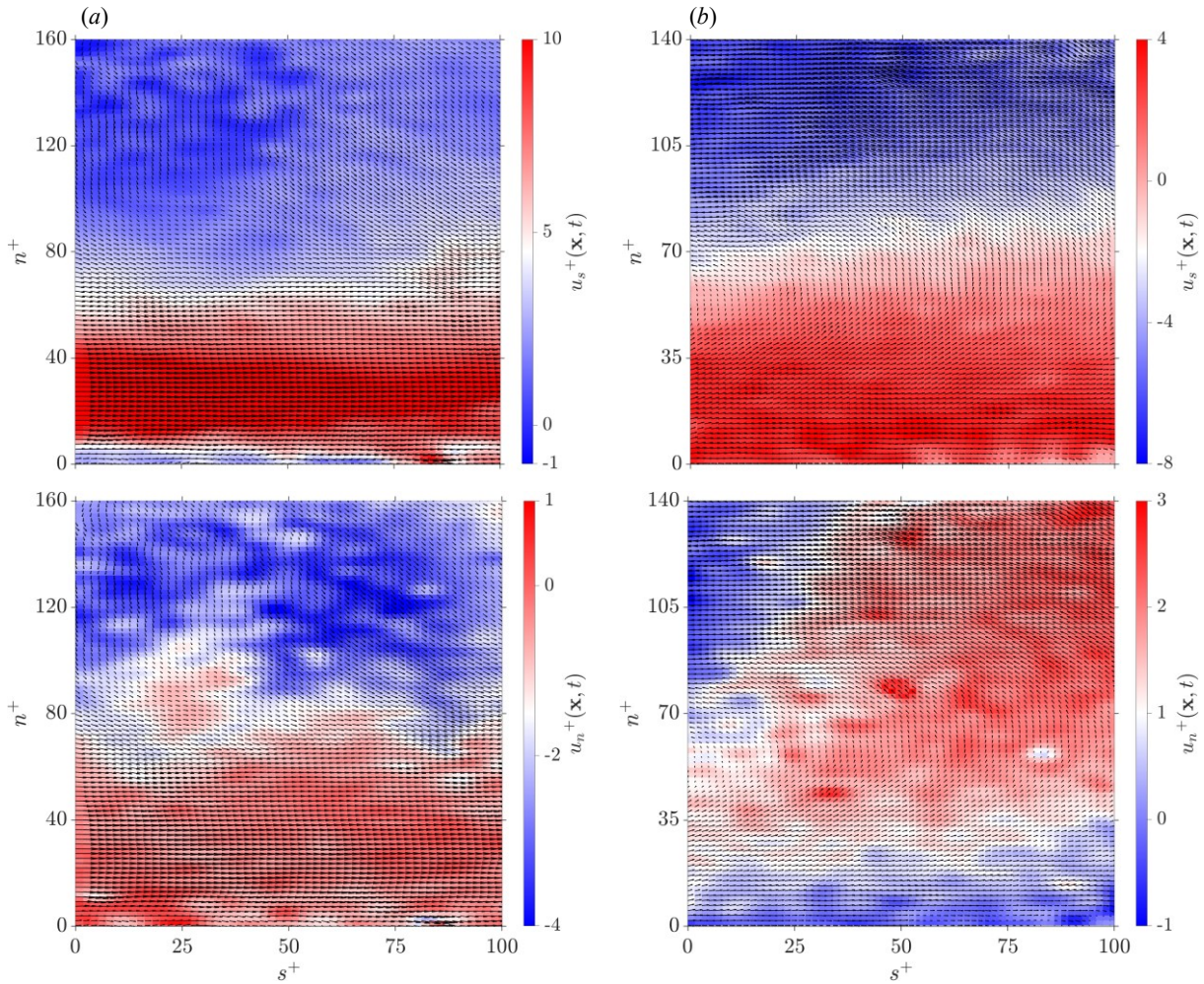

Figure 7-5 An instantaneous inner normalized wall-parallel, $u_s^+(\boldsymbol{x}, t)$, and wall-normal, $u_n^+(\boldsymbol{x}, t)$, fluctuating velocity field for (*a*) 200 p.p.m. and (*b*) 400 p.p.m. ZPG PAM solution flow (ZPG FOV in Figure 3-13) at $Re_\tau = 141$ (see Table 7-3 and Table 7-4). The fluctuating velocity vectors are shown by black arrows and are scaled by the magnitude of the maximum velocity vector.

Comparing the fluctuation fields of the PAM solutions with the ones of the water flow, shown in Figure 6-2(*a*,*b*), it is evident that the polymer additives enhance the wall-parallel velocity fluctuations and make their distributions more uniform. Near the wall, high-speed fluid elements drifting away from the wall are more recognizable than the ones moving toward the wall. Also, low-speed fluid elements are rare in the near-wall region in both solution concentrations.

The PDFs of the instantaneous inner normalized u_s^+ and u_n^+ are presented in Figure 7-6(*a-c*) for ZPG PAM 200 p.p.m. solution at $Re_\tau = 141$, and at three wall positions of $n^+ = 17$, $n^+ = 34$, and $n^+ = 108$. The measured probability distribution of u_s^+ at $n^+ = 17$ collpases well onto the fitted Gaussian profile, indicating a symmetric distribution with a lower peak amplitude than the fitted profile's peak. The heavy tail of the distribution and its wider shape compared to the pure water profile, shown in Figure 6-3(*a*), demonstrates a larger kurtosis value and activation of stronger u_s fluctuations in the buffer layer of the ZPG 200 p.p.m. polymer solution.

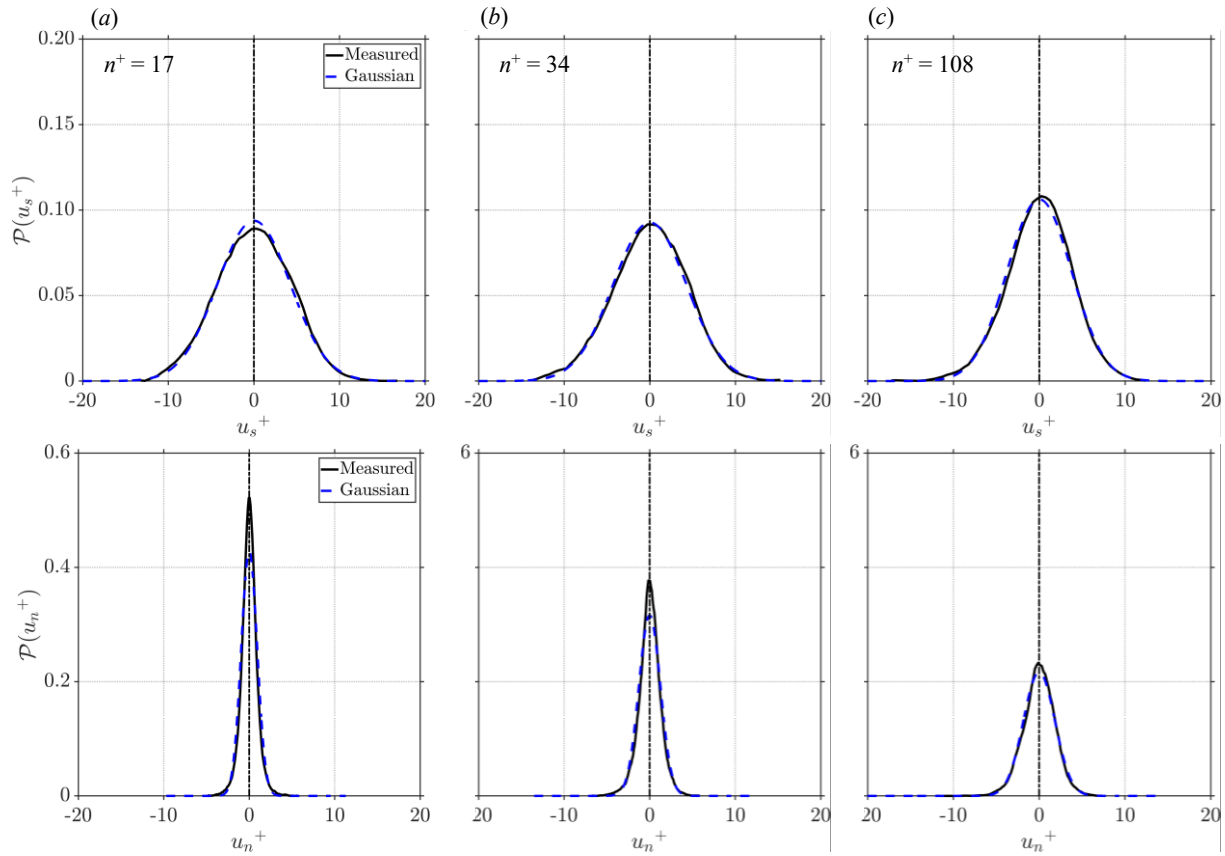

Figure 7-6 Probability density function (PDF) of the wall-parallel velocity fluctuations, u_s^+, and wall-normal velocity fluctuations, u_n^+, at (*a*) $n^+ = 9$, (*b*) $n^+ = 34$, and (*c*) $n^+ = 108$. The dashed blue profile on each figure shows a fitted normal distribution to the measured PDF. The results correspond to the ZPG PAM 200 p.p.m. solution flow at $Re_\tau = 141$ (see Table 7-3).

PDF distribution of u_n^+ at $n^+ = 17$, shown in Figure 7-6(a), demonstrates a symmetric distribution with a measured peak slightly higher than the Gaussian fit's peak. The narrow profile shape with light tails indicates a relatively small kurtosis and a peak value of $\mathcal{P}(u_n^+) \approx 0.55$ reveals that it is ≈ 55 % probable that velocity fluctuations normal to the wall are zero at $n^+ = 17$. A comparison of the $\mathcal{P}(u_n^+)$ profile at $n^+ = 17$ with that of pure water flow at $n^+ = 14$, illsutrated in Figure 6-3(a), denotes the significant suppression of strong u_n^+ fluctuations in the 200 p.p.m. solution. A similar behavior was observed in the buffer layer of the 400 p.p.m. solution (not shown here), with even a narrower distribution and stronger suppression of fluctuations.

As Figure 7-6(b) illustrates, the profile at $n^+ = 34$ is symmetric with a peak amplitude of ≈ 0.09. With a lower peak and heavier tails compared to the $\mathcal{P}(u_s^+)$ of pure water flow at $n^+ = 49$, shown in Figure 6-3(b), it is evident that the polymer additives increased the wall-parallel intermittency of the outer layer and intensified the stronger u_s^+ fluctuations. The $\mathcal{P}(u_n^+)$ profile of the 200 p.p.m. solution at $n^+ = 34$ shows a lower peak and a wider profile compared to its counterpart at $n^+ = 17$, which indicates the intensification of stronger u_n fluctuations at this position. As Figure 7-6(c) shows, the $\mathcal{P}(u_s^+)$ profile s symmetric, with a marginal positive skewness, and almost a similar kurtosis to that at $n^+ = 34$, and a relatively higher peak.

Compared to $n^+ = 34$ profile, the strong u_n^+ fluctuations are intensified at $n^+ = 108$, where the peak is relatively smaller and the kurtosis larger. Comparing the $\mathcal{P}(u_s^+)$ and $\mathcal{P}(u_n^+)$ profiles in the outer layer of the PAM solutions with those in the water, shown in Figure 6-3(b,c), shows that strong u_s^+ and u_n^+ fluctuations are, respectively, enhanced and suppressed in the PAM solutions. The 400 p.p.m. solution (not shown here) indicated similar behavior as the 200 p.p.m. solution, with more intense suppression of u_n^+ and enhancement of u_s^+ fluctuations.

7.3.1 Mean flow

Figure 7-7(a,b) illustrates the distribution of the mean wall-parallel velocity of the ZPG 200 p.p.m. and 400 p.p.m. PAM solution flows, normalized by their associated inner scales. The linear, $\langle U_s \rangle^+ = n^+$, and logarithmic, $\langle U_s \rangle^+ = 2.44 \ln n^+ + 5.5$, laws of the wall and Virk's asymptote profile, $\langle U_s \rangle^+ = 11.7 \ln n^+ - 17$, are also plotted as dashed black lines on the figures. As Figure 7-7(a,b) shows, the profiles collapse in the viscous sublayer and follow the linear law of the wall. Nevertheless, the velocity profiles deviate from the standard logarithmic law away from the wall, where the buffer layer thickens and almost disappears for higher concentrations and

velocities. In both tested solutions, with $DR < 39$ %, none of the profiles converge to the ultimate profile, and as the Re_τ increases, and accordingly DR enhances, the slope of the velocity profiles in the outer layer becomes steeper and approaches the ultimate profile.

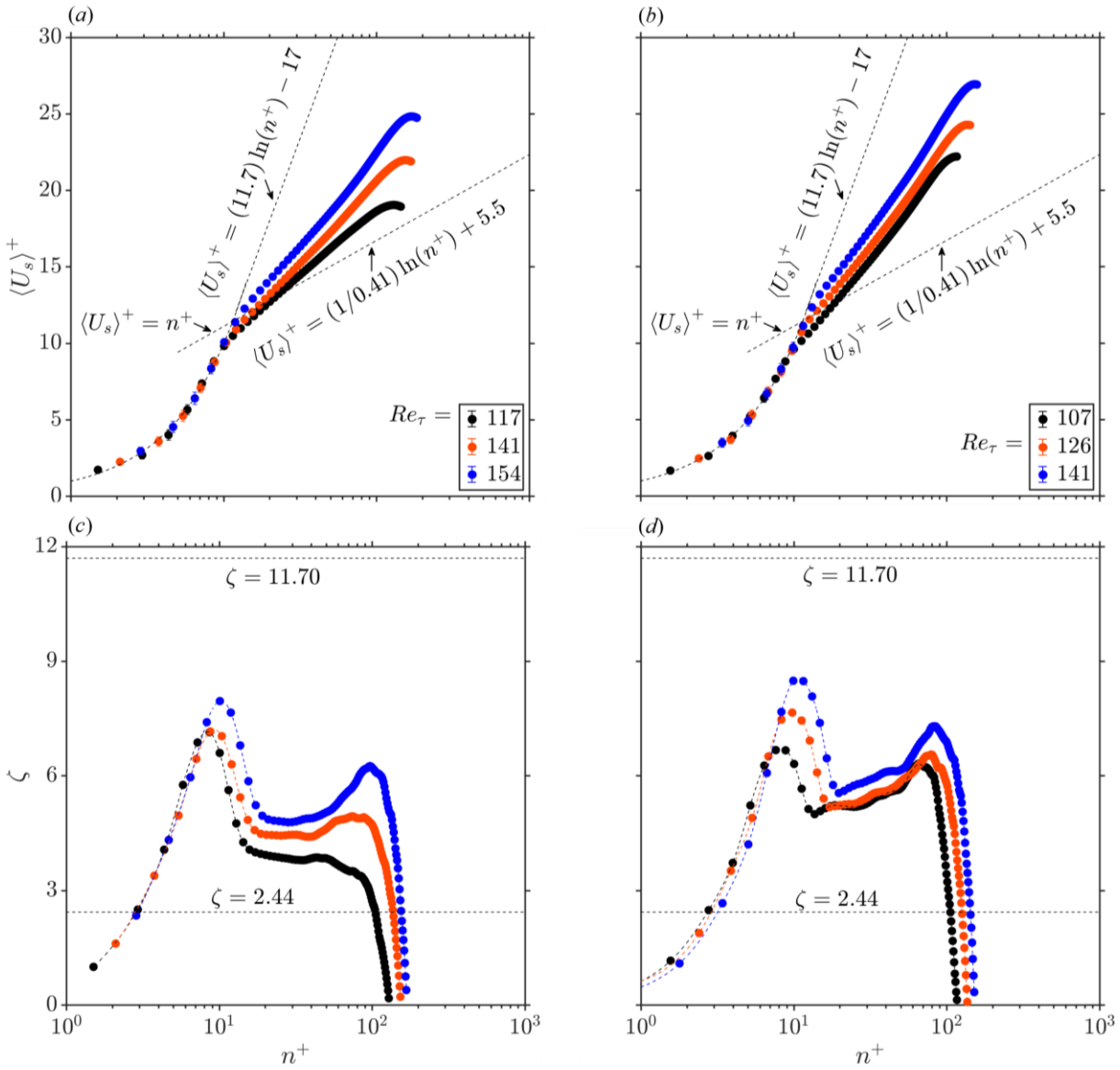

Figure 7-7 Mean inner normalized wall-parallel velocity, $\langle U_s \rangle^+$, and log-indicator function, ζ, variations with the inner normalized wall-normal position, n^+, for (*a*) 200 p.p.m. and (*b*) 400 p.p.m. ZPG PAM solution flows at three different Re_τ (see Table 7-3 and Table 7-4). The standard linear and logarithmic laws of the wall and Virk's ultimate velocity profile (Virk et al., 1970) are shown as dashed black lines on the plots in (*a*) and (*b*). The values of the log-indicator function of the logarithmic and Virk's ultimate laws are shown by the black horizontal dashed lines on (*c*) and (*d*). The colored dashed splines shown on ζ profiles in (*c*) and (*d*) are only to demonstrate the trends and are not obtained experimentally.

The log-indicator function was calculated for the obtained mean wall-parallel velocity profiles of the PAM solutions and are illustrated in Figure 7-7(*c*,*d*). As is evident from the plots, none of

the no-Newtonian velocity profiles demonstrate a logarithmic behavior nor converge to the ultimate profile with $\zeta = 11.7$. In both solution concentrations, the ζ profiles show a first peak at $n^+ \approx 10$ for the lowest Re_τ and slightly shifts away from the wall, where the highest tested Re_τ indicate first peaks occurring at $n^+ \approx 12$. In the 200 p.p.m. solution, the log-indicator profiles of $Re_\tau = 141$ and $Re_\tau = 154$ show a second peak occurring at the centerline of the channel, which is also repeated for the tested Re_τ of the 400 p.p.m. solution.

The mean velocity profiles of the non-Newtonian ZPG profiles were also normalized by U_e, and Zagarola-Smits velocity, U_{zs}, (Zagarola and Smits, 1998), and their corresponding wall-normal positions were normalized by δ, and the results are illustrated in Figure 7-8(*a-d*). The velocity profiles normalized by U_e, almost collapse for the 200 p.p.m. solution and collapse well for the 400 p.p.m. solution. In contrast, the velocity profiles of the 200 p.p.m. solution, normalized by U_{zs}, deviate toward lower values as Re_τ increases and only collapse in the inner near wall region. As shown in Figure 7-8(*d*), the velocity profiles of the 400 p.p.m. PAM solution show smaller deviations when normalized by U_{zs}, but do not collapse on a similar profile.

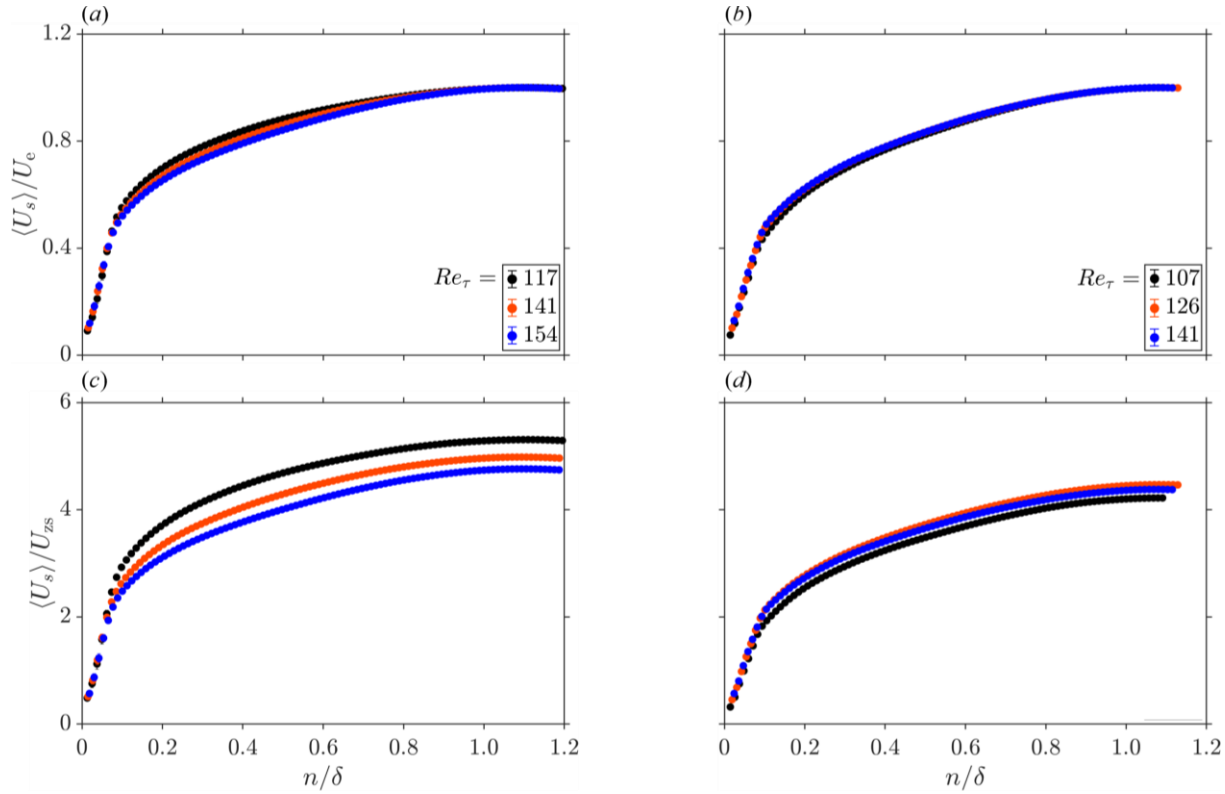

Figure 7-8 Variation of the mean wall-parallel velocity profiles of the ZPG 200 p.p.m. solution flow normalized by the (*a*) U_e, and (*b*) U_{zs}, and ZPG 400 p.p.m. solution flow normalized by (*c*) U_e, and (*d*) U_{zs}, with n / δ, at three different Re_τ (see Table 7-3 and Table 7-4).

The distribution of the mean Reynolds shear stress in the boundary layer of the ZPG 200 p.p.m. and 400 p.p.m. PAM solutions, normalized by the inner and outer scales, are shown for three different Re_τ in Figure 7-9(*a-d*). When normalized by the inner scales, the peak of the 200 p.p.m. solution increases as Re_τ increases and its location moves from $n^+ \approx 60$ for $Re_\tau = 117$ to slightly farther from the wall to $n^+ \approx 80$ for the flow with $Re_\tau = 154$. The $-\langle u_s u_n \rangle^+$ profiles of the 400 p.p.m. solution show almost an equal peak value for the $Re_\tau = 107$ and $Re_\tau = 126$ flows, which increases for the $Re_\tau = 141$ flow. The peak locations of the 400 p.p.m. solution profiles shift from $n^+ \approx 60$ for the $Re_\tau = 107$ flow to $n^+ \approx 70$ for the other two flow conditions with higher Re_τ. The mean Reynolds shear stress profiles of non-Newtonian flows, normalized by the outer scales, illustrated in Figure 7-9(*c*,*d*), indicate that the profiles partially collapse near the wall region and adjacent to the centerline and show evident deviations from each other in the outer layer region, which are more significant for the 400 p.p.m. solution.

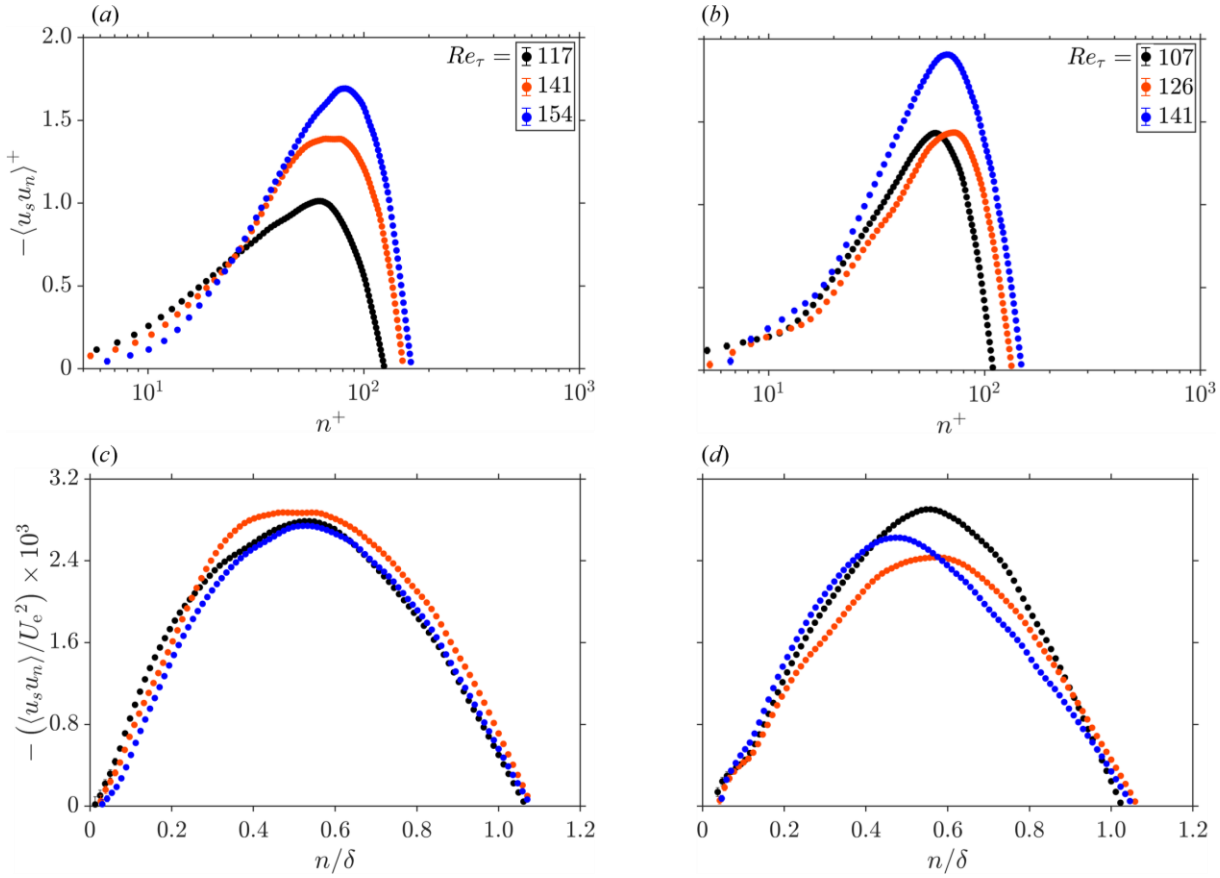

Figure 7-9 Variation of the mean Reynolds shear stress with the wall-normal position, normalized by the inner scales for the ZPG (*a*) 200 p.p.m. and (*b*) 400 p.p.m. solutions, and normalized by the outer scales for ZPG (*c*) 200 p.p.m. and (*d*) 400 p.p.m. solution flows at three different Re_τ (see Table 7-3 and Table 7-4).

Figure 7-10(*a-d*) demonstrates the changes of the mean wall-parallel Reynolds stress profiles with the wall-normal position, normalized by the inner and outer scales, at three different Re_τ for ZPG 200 p.p.m. and 400 p.p.m. solution flows. Compared to the pure water flow results given in Figure 6-12(*c,d*), the location of the peak $\langle u_s^2 \rangle$ profiles of the 200 p.p.m. solution is shifted farther from the wall to $n^+ \approx 30$, where the profiles indicate more of a plateau rather than a peak. This plateau is shifted further away from the wall for the 400 p.p.m. and its starting point varies for different Re_τ. The profiles normalized by the outer scales, do not collapse in any of the tested PAM solutions. Compared to the $\langle u_s^2 \rangle / U_e^2$ profiles of the pure water flow, Figure 7-10(*c,d*) demonstrates that the addition of polymer additives significantly increased the wall parallel turbulence intensity, where the peak $\langle u_s^2 \rangle / U_e^2$ values show an overall ≈ 58 % and ≈ 87 % increase in the 200 p.p.m. and 400 p.p.m. solutions.

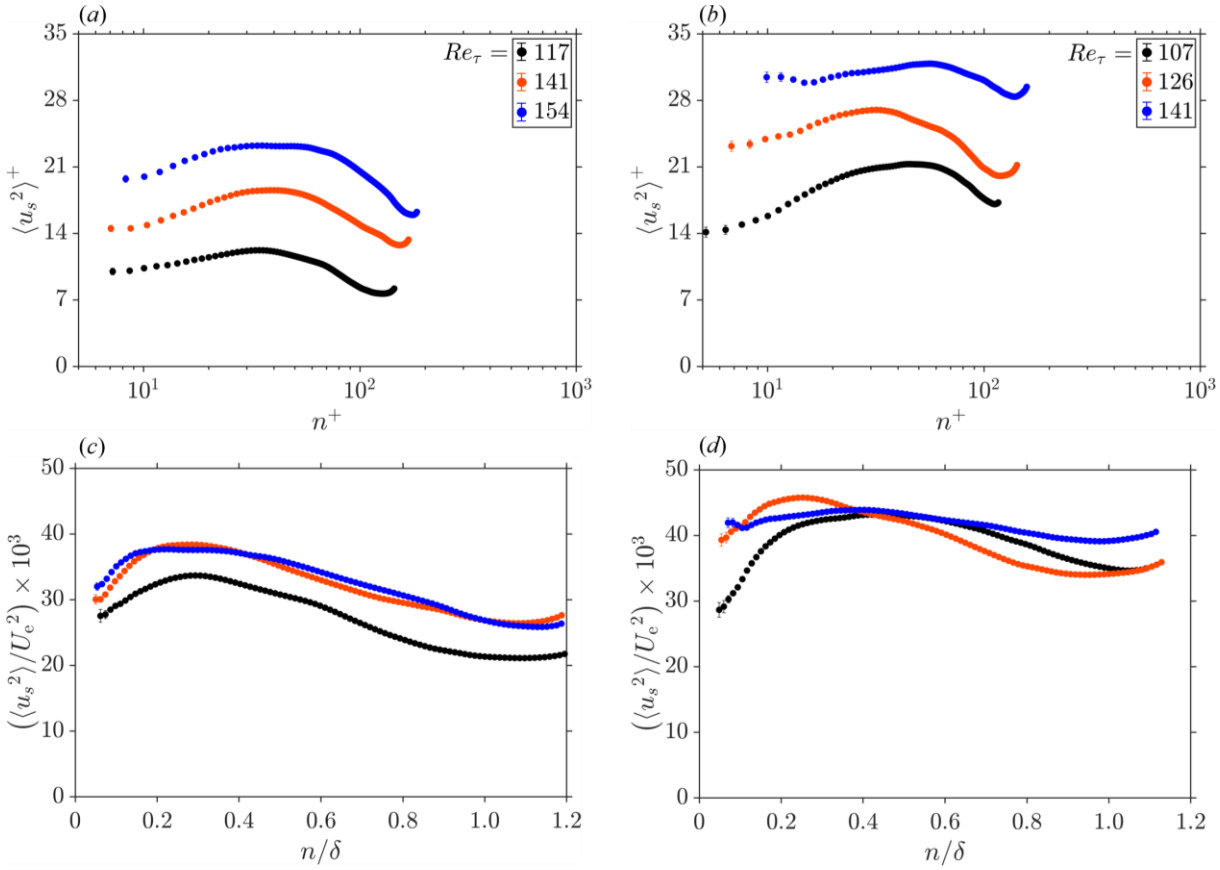

Figure 7-10 Variation of the mean wall-parallel Reynolds stress with the wall-normal position, normalized by the inner scales for the ZPG (*a*) 200 p.p.m. and (*b*) 400 p.p.m. solutions, and normalized by the outer scales for ZPG (*c*) 200 p.p.m. and (*d*) 400 p.p.m. solution flows at three different Re_τ (see Table 7-3 and Table 7-4).

Figure 7-11(*a-d*) illustrates that the mean wall-normal Reynolds stress profiles collapse in the near-wall region when normalized by the inner or outer scales and start to deviate from each other

in the outer layer. The $\langle u_n^2 \rangle$ values gradually increase until a quarter of the channel and, after this point, show a plateau with a smoother slope until the middle of the channel. Comparison of the outer normalized profiles of the ZPG non-Newtonian profiles with the pure water profiles given in Figure 6-12(*f*), the non-Newtonian $\langle u_n^2 \rangle / U_e^2$ values are larger.

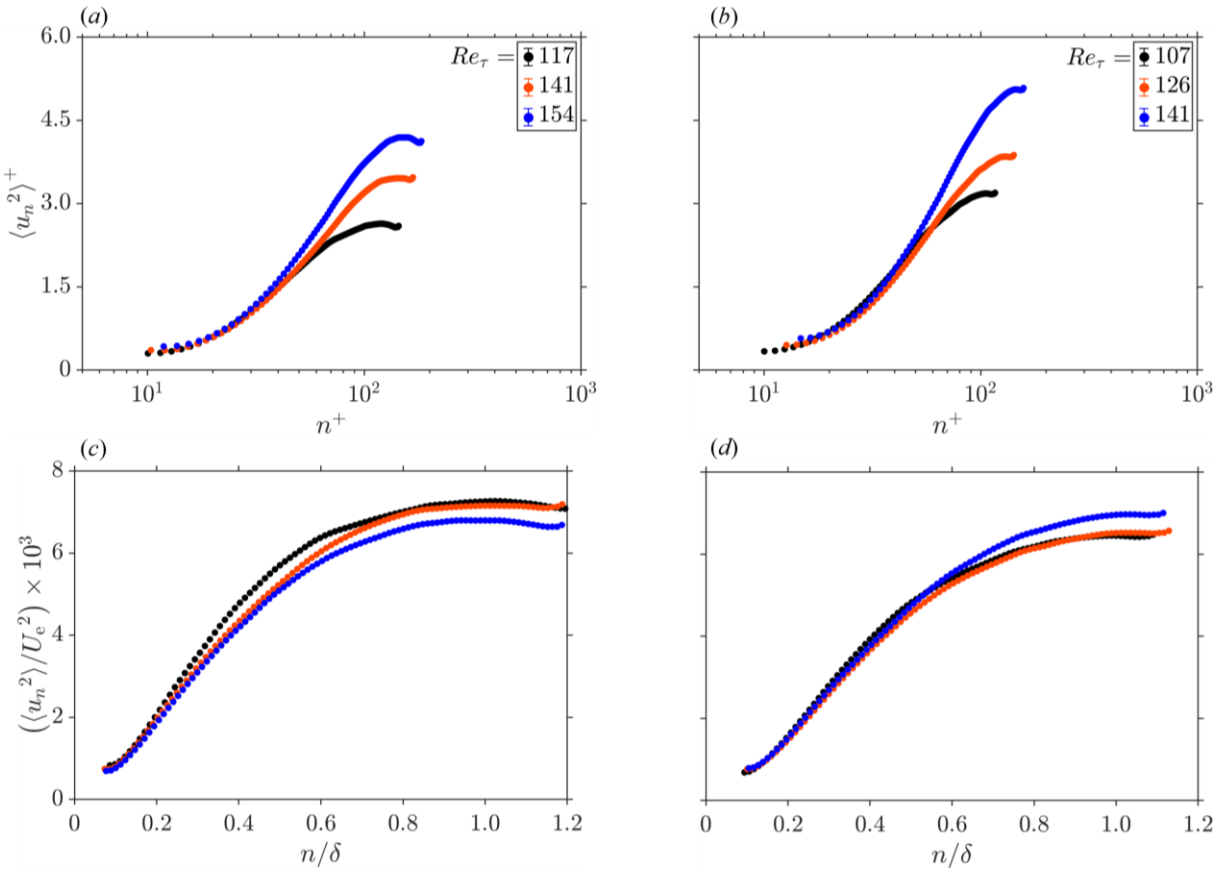

Figure 7-11 Variation of the mean wall-normal Reynolds stress with the wall-normal position, normalized by the inner scales for the ZPG (*a*) 200 p.p.m. and (*b*) 400 p.p.m. solutions, and normalized by the outer scales for ZPG (*c*) 200 p.p.m. and (*d*) 400 p.p.m. solution flows at three different Re_τ (see Table 7-3 and Table 7-4).

The distribution of the skewness and kurtosis of the ZPG 200 p.p.m. and 400 p.p.m. solutions over the boundary layer thickness are illustrated in Figure 7-12(*a-d*). The results show high kurtosis uncertainties in the wall region for the 200 p.p.m. solution near the center of the channel. Compared to the skewness of a normal distribution, i.e., $\mu_3 = 0$, the skewness of the non-Newtonian flows show oscillations around this value in a range of $-0.3 < \mu_3 < 0.6$, with the higher values occurring in the wall region. The kurtosis profiles indicate oscillations from 2.5 to less than 4.0 in both solutions, where their maxima happen at the center of the channel. The results show

that in both solution flows, as Re_τ increases the kurtosis values of the outer layer tend to values smaller than the standard $\mu_4 = 3$ value.

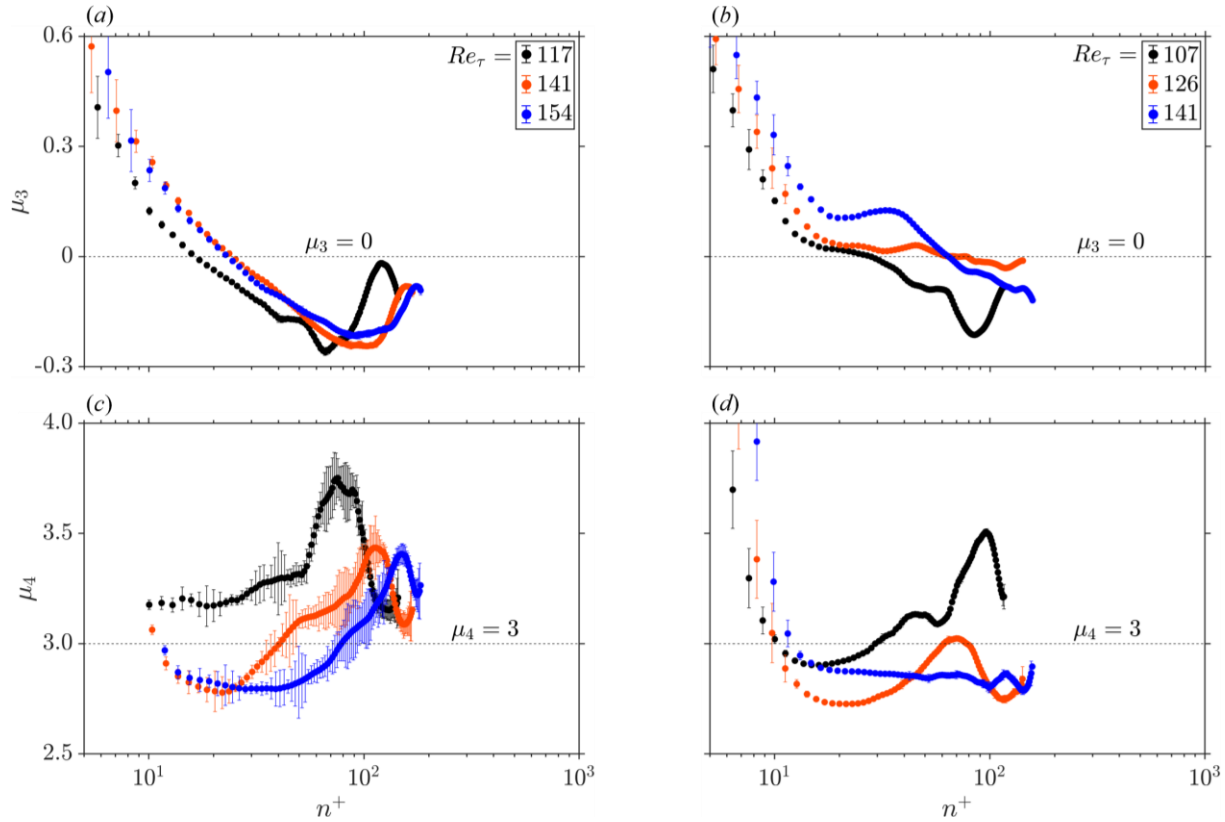

Figure 7-12 Variation of the mean skewness, μ_3, with the inner-normalized wall-normal position for the ZPG (*a*) 200 p.p.m. and (*b*) 400 p.p.m. solutions, and variation of the mean kurtosis, μ_4, with n^+ for the ZPG (*c*) 200 p.p.m. and (*d*) 400 p.p.m. solution flows at three different Re_τ (see Table 7-3 and Table 7-4). The error bars indicate the standard deviation of the streamwise averaging.

7.3.2 A note on scaling

The selection of the proper scaling parameters for the turbulent flow parameters is open to debate and discussion in the research field. The inner scales u_τ and λ_ν properly normalize the mean velocity profiles of a ZPG Newtonian flow, where the profiles of a wide range of Reynolds numbers show a self-similarity and collapse on each other. This self-similarity is also evident in the ZPG pure water flow results discussed in this study, as shown in Figure 6-10(*a*). However, as shown in Figure 7-7(*a*,*b*), the inner normalized mean velocity profiles of the shear-thinning non-Newtonian flows, such as the semi-dilute PAM solutions tested in this study, only collapse in the viscous sublayer and deviate from the standard logarithmic law in the outer layer. This deviation usually escalates for higher DR levels, as was observed here.

When normalized by the outer scales U_e and δ, the mean velocity profiles usually show self-similarity in the outer layer region, where the profiles collapse. Also, as discussed in Section 6.1, Maciel et al. (2018) showed that the Zagarola-Smits velocity (Zagarola and Smits, 1998), $U_{zs} = U_e\ (\delta^* / \delta)$, was a proper choice for scaling all ranges of defects, β, and H. The effect of inner and outer normalization on the mean velocity and Reynolds stresses are investigated in this Section for the tested ZPG pure water, 200 p.p.m. and 400 p.p.m. solution flows.

Figure 7-13(*a*,*b*) show the variation of the mean wall-parallel velocity profiles of the tested Newtonian and non-Newtonian ZPG flows, normalized by their corresponding U_e and U_{zs} velocities versus the wall-normal positions, normalized by δ. As shown, $\langle U_s \rangle / U_e$ profiles of different Re_τ of the water and 400 p.p.m. solution collapse into an almost similar profile and slightly deviate in the outer layer for the 200 p.p.m. solution. In contrast, when normalized by U_{zs}, the profiles do not collapse, and all tested flows show noticeable deviations from each other.

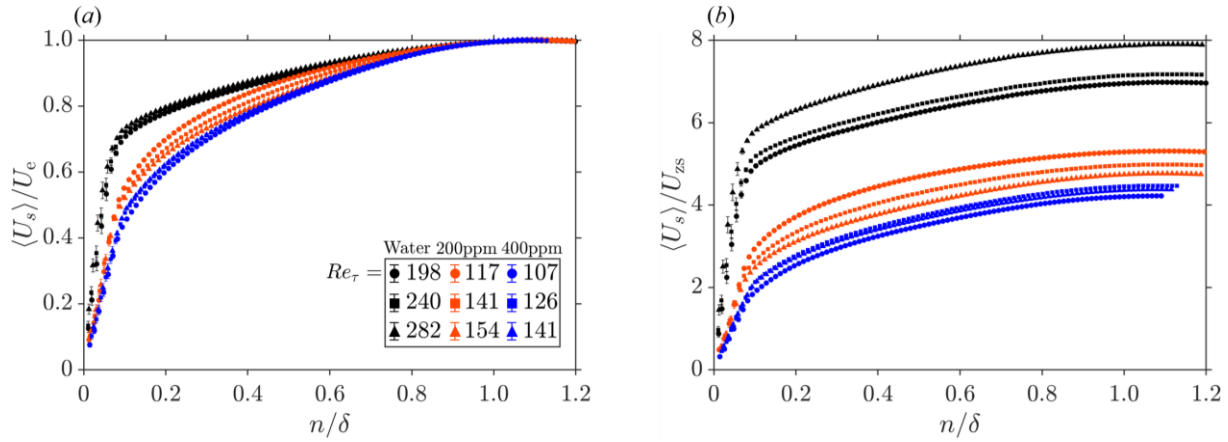

Figure 7-13 Variation of the mean wall-parallel velocity, $\langle U_s \rangle$, normalized by the (*a*) edge velocity, U_e, and (*b*) Zagarola-Smits velocity, U_{zs}, with n, normalized by the boundary layer thickness, δ, for the ZPG pure water, 200 p.p.m. and 400 p.p.m. PAM solution flows, each at three different Re_τ (see Table 6-1, Table 7-3, and Table 7-4).

Figure 7-14(*a-c*) illustrates the mean Reynolds stress profiles of all tested Newtonian and non-Newtonian shear-thinning PAM solution flows with ZPG, normalized by the Newtonian inner scales $u_{\tau,0}$ and $\lambda_{v,0}$, and outer scales of U_e and δ, and U_{zs} and δ. The $u_{\tau,0}$ and $\lambda_{v,0}$ were obtained by calculating the corresponding wall shear stress, $\tau_{w,0}$, using Dean's correlation (Dean, 1978) given in equation (6-6) and water's wall viscosity μ_w = 0.91 mPa s. Overall, The inner normalized Reynolds shear stresses of different tested flows do not collapse for the range of Re_τ examined. The peak values of $-\langle u_s u_n \rangle / u_{\tau,0}^2$ increase by $\approx$ 20 % for the polymer solutions and remains almost constant in 200 p.p.m. and 400 p.p.m. solutions, at the highest examined Re_τ. Normalized

by U_e^2, overall, the PAM solutions show relatively lower levels of Reynolds shear stress compared to the pure water flow. Normalization of the mean Reynolds shear stresses by the squared Zagarola-Smits velocity, U_{zs}^2, indicates that the addition of PAM solutions significantly attenuates the Reynolds shear stress in the entire boundary layer, and this attenuation is further amplified for the more concentrated 400 p.p.m. solution. The peak value of the highest examined Re_τ of pure water reduces by ≈ 67 % and ≈ 72 % in the 200 p.p.m. and 400 p.p.m. solution flows.

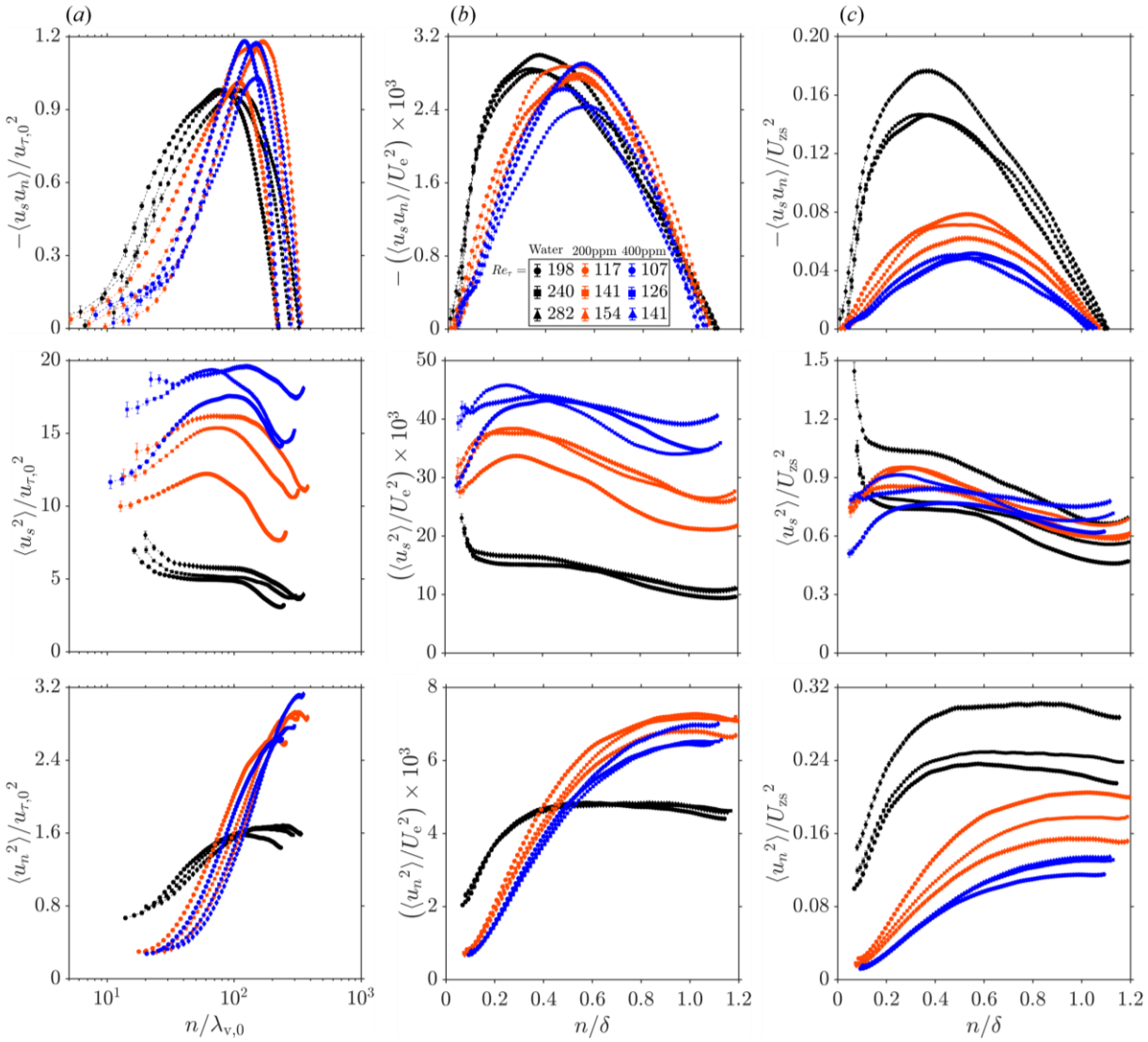

Figure 7-14 Variation of the Reynolds shear stress, $-\langle u_s u_n\rangle$ (top row), wall-parallel Reynolds stress, $\langle u_s^2\rangle$ (middle row), and wall-normal Reynolds stress, $\langle u_n^2\rangle$ (bottom row), with the wall-normal postion, n, (*a*) normalized by the Newtonian squared friction velocity $u_{\tau,0}^2$, and viscous length scale, $\lambda_{v,0}$, (*b*) normalized by the outer scales U_e^2 and δ, and (c) normalized by the outer scales U_{zs}^2 and δ, for the ZPG pure water, 200 p.p.m., and 400 p.p.m. PAM solution flows, each at three different Re_τ (see Table 6-1, Table 7-3, and Table 7-4).

As is illustrated in the middle row of Figure 7-14(*a-c*), the mean wall-parallel Reynolds shear stresses are significantly enhanced in the PAM solutions relative to the pure water flow when normalized by the inner scales or the outer scale of U_e^2 and grow as the polymer concentration increases. When normalized by U_{zs}^2, the trend of changes becomes random, and overall, the PAM solution profiles fall lower than the results of the Re_τ = 282 and above the Re_τ = 198 of the pure water flow, far from the wall and below the centerline.

7.3.3 Quadrant analysis

The Reynold shear stress of the ZPG 200 p.p.m. and 400 p.p.m. PAM solution flows were conditionally averaged based on the signs of the fluctuating instantaneous u_s and u_n velocities over the boundary layer thickness and the inner normalized results are illustrated in Figure 7-15(*a*)-(*c*) for three different Re_τ. Also, the ratio of the ejection (Q_2) to the sweep (Q_4) motions of the conditional averaged Reynolds shear stresses for different Re_τ and the two examined solution concentrations are illustrated in Figure 7-16(*a*,*b*).

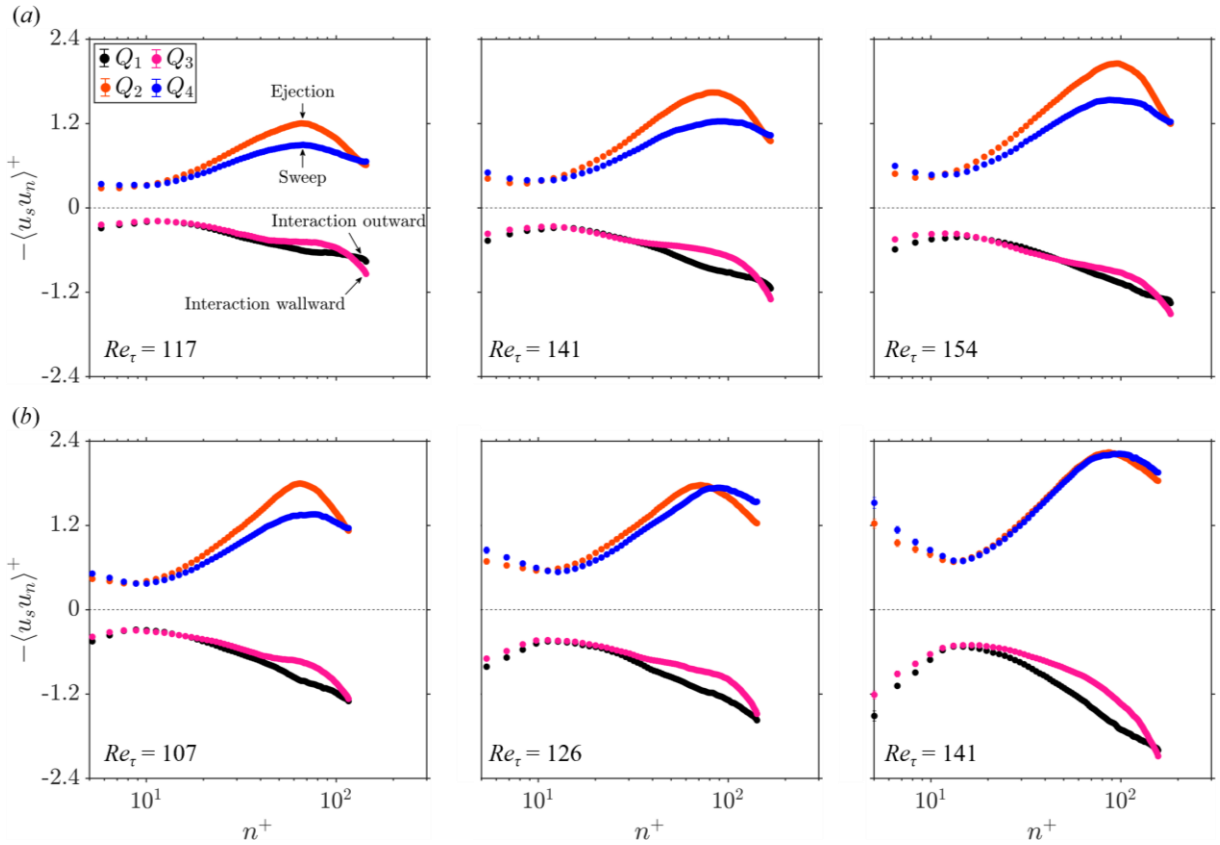

Figure 7-15 Variation of the mean interaction outward (Q_1), ejection (Q_2), interaction wallward (Q_3), and sweep (Q_4) events with the inner normalized wall-normal position, n^+, for (*a*) 200 p.p.m. and (*b*) 400 p.p.m. ZPG PAM solution flows at three different Re_τ (see Table 7-3 and Table 7-4), labeled on each plot.

For all tested 200 p.p.m. solution flows, the near wall region is dominated by the sweep events, and ejection events dominate far away from the wall. The sweep and ejection motions balance out at almost $n^+ \approx 12$ for the three tested Re_τ. As shown in Figure 7-16(a), both events gradually increase to a peak at $n^+ \approx 70$ for $Re_\tau = 117$ and $Re_\tau = 141$ and at $n^+ \approx 100$ for $Re_\tau = 154$, with the sweep events indicating more of a plateau at these positions. In the near-wall region, the wallward interaction motions marginally dominate the outward interaction motions, and this domination enhances in the wall region as Re_τ increases in the 200 p.p.m. solution. At $n^+ \approx 12$, both events balance out, which continues farther from the wall to $n^+ \approx 50$, after which the wallward motions dominate the outward interactions.

As Figure 7-16(b) illustrates, for the three tested Re_τ in the 400 p.p.m. PAM solution, sweep events dominate at the near wall region, which balances out with the ejection events at $n^+ \approx 8$ for the $Re_\tau = 107$, at $n^+ \approx 12$ for the $Re_\tau = 126$, and at $n^+ \approx 16$ for the $Re_\tau = 141$. In all three tested Re_τ, the ejection events dominate far away from the wall, but their strengths significantly attenuate as the Re_τ increases, a phenomenon that was not apparent in the 200 p.p.m. solution.

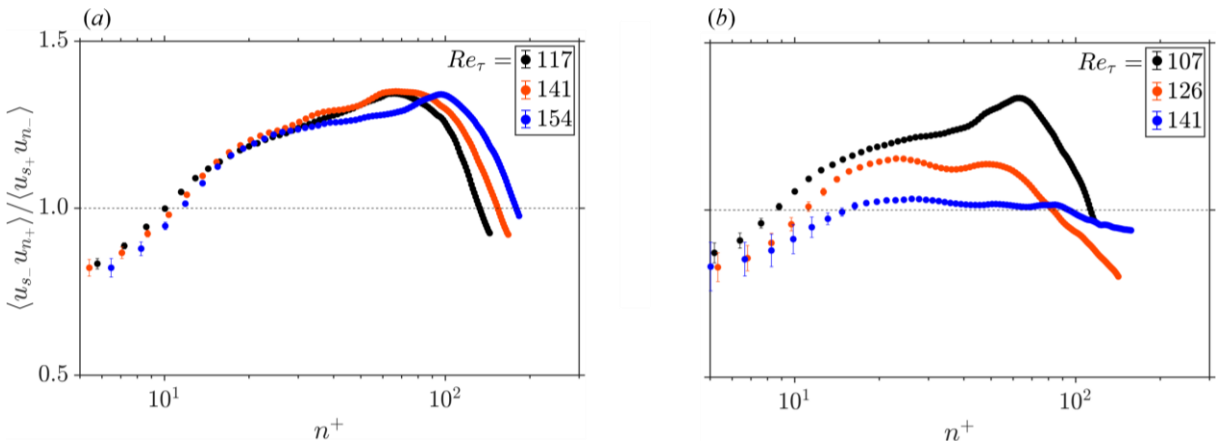

Figure 7-16 Variation of the ratio of the ejection (Q_2) to the sweep (Q_4) events with the inner normalized wall-normal position, n^+, for (a) 200 p.p.m. and (b) 400 p.p.m. ZPG PAM solution flows at three different Re_τ (see Table 7-3 and Table 7-4).

The JPDF contours of the u_s^+ and u_n^+ velocity fluctuations at four different wall-normal positions and for three different Re_τ are illustrated in Figure 7-17(a-c) for the ZPG 200 p.p.m. solution flow. Per the results shown in Figure 7-15(a,b) and Figure 7-16(a,b), near the wall, the likelihood of the sweep and interaction wallward motions is slightly larger than the ejection and interaction outward motions. For positions far away from the wall, for instance, at $n^+ = 64$ in the $Re_\tau = 117$ flow of the 200 p.p.m. solution, the ejection events are relatively stronger than the

sweep events. At the same position, the wallward interaction motions are marginally stronger than the outward motions. Adjacent to the center of the channel, the Q_1 and Q_3, and Q_2 and Q_4 quadrant motions almost converge and show similar magnitudes.

Near the wall in the 200 p.p.m. solution flow, the probability of the occurrence of strong wall-parallel velocity fluctuations is several orders of magnitude larger than the likelihood of strong wall-normal fluctuations, and this difference increases as the Re_τ increases. The JPDF contours of the 400 p.p.m. solution flow showed probabilities similar to that of the 200 p.p.m. solution, with only different scales of quadrant events. They are not shown here for the brevity of the discussion.

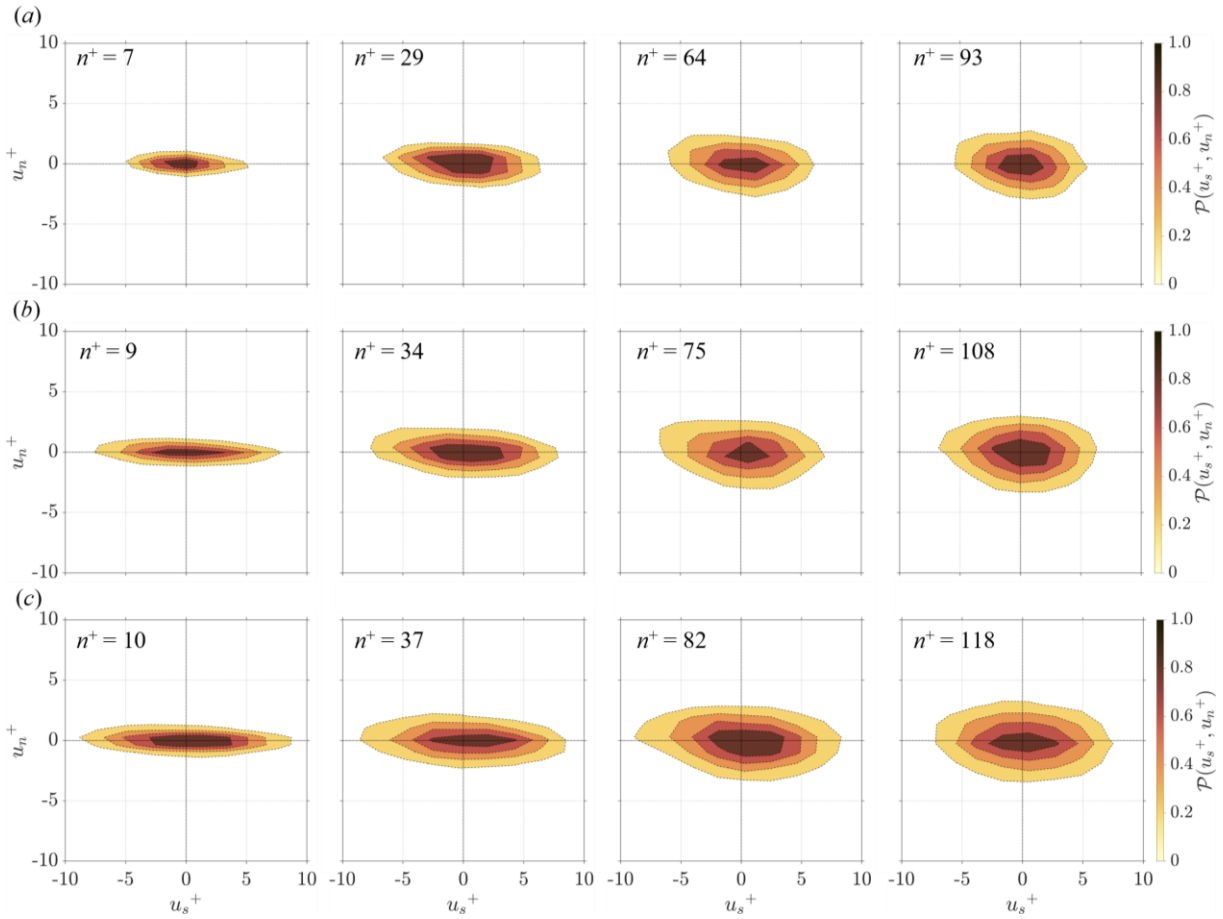

Figure 7-17 Joint probability density function (JPDF) of u_s^+ and u_n^+ at (*a*) Re_τ = 117, (*b*) Re_τ = 141, and (*c*) Re_τ = 154 of the ZPG 200 p.p.m. PAM solution flow (see Table 7-3).

7.3.4 Energy cascade

Figure 7-18(*a-c*) illustrates the variation of the inner normalized energy spectra based on the wall-parallel velocity fluctuations at different wall-normal positions as a function of the dimensionless wavenumber k_s, at three different Re_τ in the ZPG 400 p.p.m. PAM solution. As

seen, except for the profiles very close to the wall, the other $E_{u_s u_s}(k_s)$ profiles almost collapse in the inertial length scale range and follow the Kolmogorov scaling of $k_s^{-5/3}$.

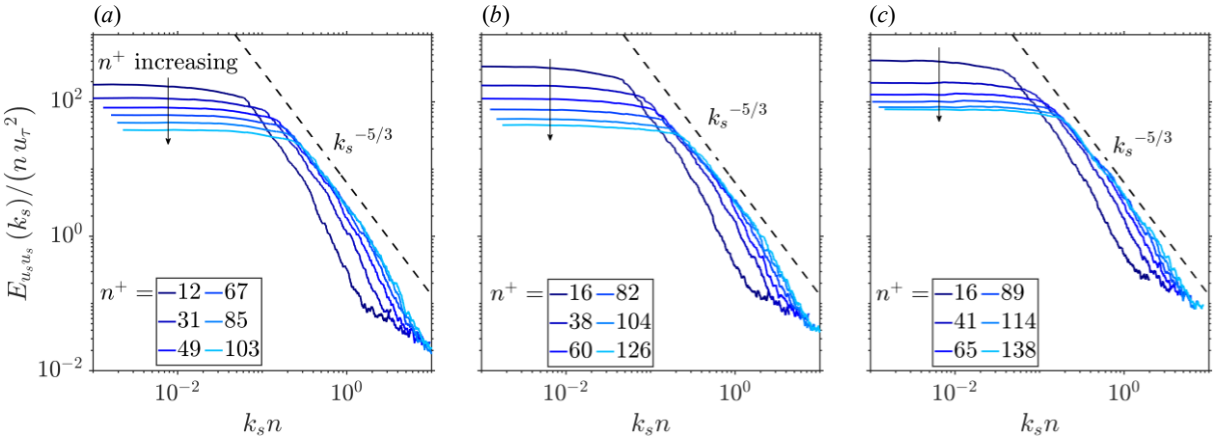

Figure 7-18 Variation of the inner normalized energy spectra with the normalized wall-parallel wavenumber $k_s n$ at different wall-normal positions n^+ for (*a*) $Re_\tau = 117$, (*b*) $Re_\tau = 141$, and (*c*) $Re_\tau = 154$ of the ZPG 400 p.p.m. PAM solution flow (see Table 7-3). The energy spectra are based on wall-parallel, u_s, velocity fluctuations at the centerline of the ZPG FOV, at $x = 15\ h_{in}$, illustrated in Figure 3-13. The dashed line on each figure represents the theoretical variation of the energy spectra with the -5/3 slope of the Kolmogorov scale for a Newtonian flow (Kolmogorov, 1941).

7.4. Accelerating flow

As discussed in Section 7.3, adding minute amounts of PAM to the pure water flow with ZPG significantly alters the BL turbulence, where inner-normalized velocity profiles deviate above the standard logarithmic law. Consistent with the previous studies, as concentration or Re_τ increases, the drag reduction increases, and the corresponding velocity profile tends toward Virk's ultimate profile. When normalized by the edge velocity, mean Reynolds shear stress attenuates in the polymeric solution flow compared with the water flow, and its peak shifts farther from the wall.

It was discussed in detail in Section 6.3 that the turbulence of the BL developing over the walls of the convergence region was noticeably modified by the strong FPG and wall curvature effects. The skin friction factor, integral parameters such as the shape factor, and mean flow statistics were not spatially invariant and varied in the streamwise direction. Their deviation from their counterparts for the canonical ZPG flow depended on the strength of the FPG and wall curvature at that streamwise position.

This section investigates the combined effects of the strong FPG, wall curvature, and PAM on the BL turbulence over the convergence region of the TG channel and aims to elucidate the dynamics behind this complex phenomenon. The section describes the streamwise variation of the main BL parameters for the 200 p.pm. and 400 p.p.m solution flows at three different mass flow rates subjected to continuous FPG of varying strength. It is then followed by a detailed representation and discussion of the mean flow statistics for each solution flow.

7.4.1 Boundary layer parameters

Figure 7-19(*a*,*b*) illustrates that U_e / U_m varies with the streamwise position in the convergence region. The U_e / U_m profiles are not linear; in both solutions, from the vicinity of the middle of the inclined flat region at s / h_{in} = -0.53, toward the end of the convergence region, the slope of changes increases slightly. It continues until the flow leaves the convergence region. In the 200 p.p.m. solution, as $Re_{\tau,0}$ increases from 117 to 141, U_e / U_m is almost equal to that of the flow with $Re_{\tau,0}$ = 117 until the middle of the inclined wall region at s / h_{in} = -0.57. Passing this point, U_e / U_m increases relative to that of the flow with $Re_{\tau,0}$ = 117. Nevertheless, as $Re_{\tau,0}$ increases to 154, U_e / U_m values drop below those of the other two flow rates over the entire convergence region.

In contrast to the 200 p.p.m. flow, increasing $Re_{\tau,0}$ from 107 to 121 in the 400 p.p.m. solution flow decreases the local U_e / U_m until the end of the inclined flat wall region. Over the convex part,

local U_e / U_m of flows with $Re_{\tau,0}$ = 107 and $Re_{\tau,0}$ = 121 are almost equal. When $Re_{\tau,0}$ increases to 141, the U_e / U_m profile jumps above the profile of the flow with $Re_{\tau,0}$ = 141 but remains lower than that of the flow with $Re_{\tau,0}$ = 107 until the start of the convex region. After this point, over the convex wall zone, local U_e / U_m of the flow with $Re_{\tau,0}$ = 141 dominates the other two. As discussed in Section 6.2.2, the uncertainties in determining the exact location of the wall and the BL edge, distortion of the core region, and the nonlinear behavior of the non-Newtonian PAM solutions might have impacted the absolute values of the evaluated U_e / U_m.

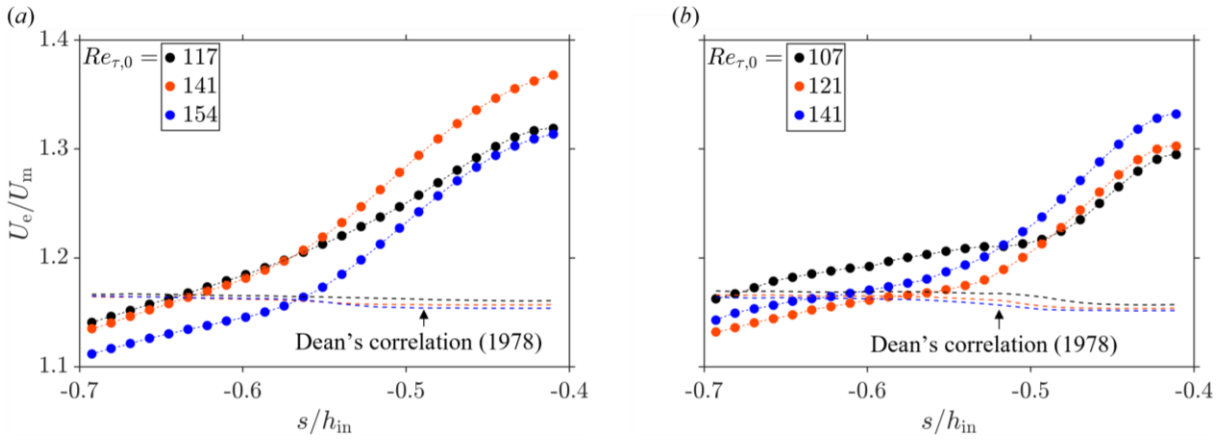

Figure 7-19 Wall-parallel variations of the boundary layer edge velocity, U_e, ratio to the mean streamwise velocity, U_m, for three different flow conditions of (*a*) 200 p.p.m. and (*b*) 400 p.p.m. PAM solution flows at the flat surface of the convergence region of the TG channel (upstream of the throat). The correlations proposed by Dean (1978) for fully developed ZPG flow, given in equation (6-5), are also shown for reference. The legend shows the Re_τ values of the ZPG flow (see Table 7-3 and Table 7-4).

Figure 7-20(*a*,*b*) illustrates that the pressure coefficient, c_p, and the pressure gradient, dP_e / ds, vary over the convergence region in both PAM solutions. Figure 7-20(*a*) shows that local dP_e / ds remains almost intact until the end of the concave part in all three tested flow rates. As flow advances over the inclined flat wall, the local pressure gradient gradually decreases (increases in magnitude) until the vicinity of the start of the convex region, where it shows a minimum peak. At this point, the FPG's strength is maximum. Over the concave part, it increases toward zero values, where FPG effects weaken gradually. Results show that as the flow rate increases, the strength of the FPG also increases, which is evident in the local growth of the negative pressure gradient values. Equivalently, $c_p < 0$ and gradually decrease over the convergence region.

The pressure coefficient and gradient profiles of the 400 p.p.m. flow, illustrated in Figure 7-20(*b*), indicate similar behaviors as the profiles of the 200 p.p.m. flow. Nevertheless, the dP_e / ds profiles show almost no variations until the end of the concave region. After this point,

they gradually decrease downstream. These profiles exhibit peaks at the center of the convex region, where the FPG is the strongest, and are comparably larger in magnitude than those in the 200 p.p.m. flow. After the peak point, the FPG is gradually quenched until s / h_{in}, at the entrance of the throat region, where it almost vanishes, i.e., dP_e / $ds \rightarrow 0$.

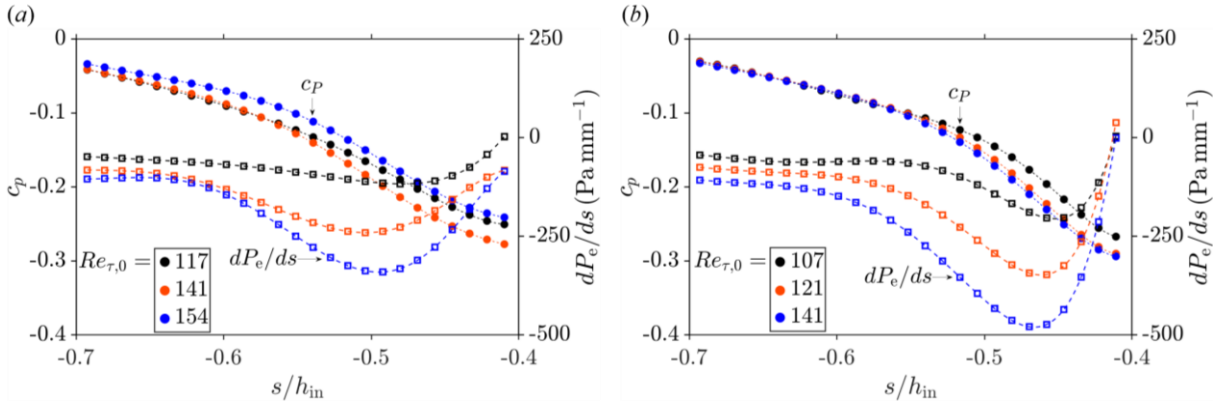

Figure 7-20 Wall-parallel variation of the pressure coefficient, c_p, and streamwise edge pressure gradient, dP_e / ds, for three different flow conditions of (*a*) 200 p.p.m. and (*b*) 400 p.p.m. PAM solution flows at the flat surface of the convergence region of the TG channel (upstream of the throat). The legend shows the Re_τ values of the ZPG flow (see Table 7-3 and Table 7-4).

Figure 7-21(*a*,*b*) shows the skin friction factor profiles of the 200 p.p.m. and 400 p.pm. PAM solutions over the convergence region for three different mass flow rates. The first obvious result from both plots is that increasing the flow rate attenuates the local friction relatively in both concentrations. The profiles of the 200 p.p.m. solution flow, shown in Figure 7-21(*a*), denote that the friction factor gradually drops over the first half of the concave region. Slightly downstream of the middle of this region, at s / $h_{in} \approx$ -0.62, the profiles show a weak peak, after which c_f drops again until s / $h_{in} \approx$ -0.57, the mid-section of the inclined wall region, where profiles have a negative peak. After this point, c_f gradually increases under the strong FPG until its peak point at the mid-section of the convex region. After the peak, c_f slowly drops to smaller values and tends to the Dean ZPG values (see equation (6-6)). This trend of changes is almost similar in other tested flow rates in both concentrations but with amplified extrema for higher flow rates.

The weak peaks occurring over the concave region of the 200 p.p.m. flow are less pronounced in the profiles of the 400 p.p.m. flow, given in Figure 7-21(*b*). The friction factor profiles of the 400 p.p.m. flow also show a minimum adjacent to the mid-section of the inclined wall region at s / $h_{in} \approx$ -0.57. The c_f values gradually increase after this point until they reach their peak almost at the end of the convex part of the channel.

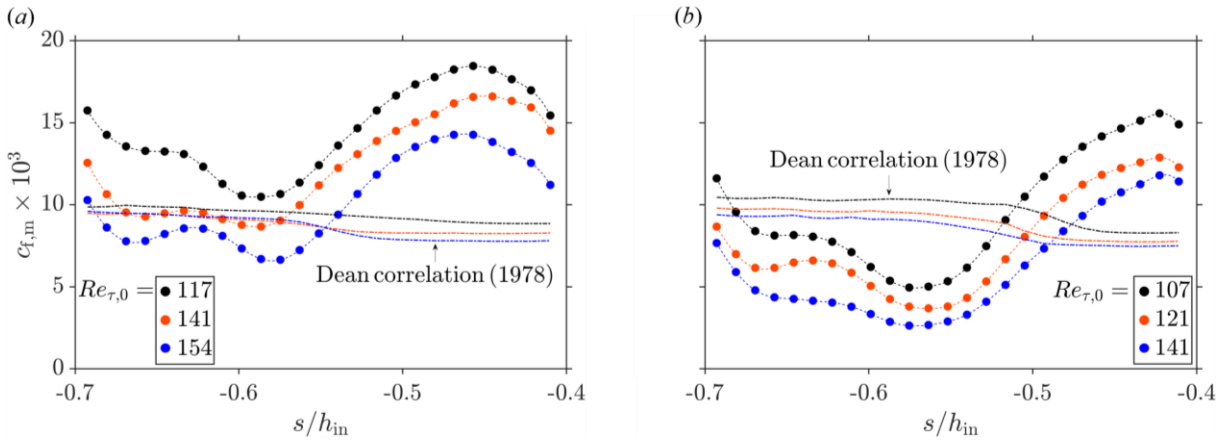

Figure 7-21 Wall-parallel variation of the skin friction factor based on the mean velocity, $c_{f,m}$ (see equation (2-26)), for three different flow conditions of (*a*) 200 p.p.m. and (*b*) 400 p.p.m. PAM solution flows at the flat surface of the convergence region of the TG channel (upstream of the throat). The legend shows the Re_τ values of the ZPG flow (see Table 7-3 and Table 7-4).

Figure 7-22(*a*,*b*) illustrates the streamwise variations of the shape factor, H, for the 200 p.p.m. and 400 p.p.m. solution flows. The predictions from the correlation suggested by Pirozzoli (2014) and given in equation (6-20), valid for high Reynolds number fully developed channel flows, are also illustrated in the plots. There is a weak dependency of H on the streamwise position, and it almost remains at an average of $H \approx 1.33$ for the 200 p.p.m. and $H \approx 1.36$ for the 400 p.p.m. solution flows at the tested flow rates. Nevertheless, local H values are marginally higher in both solutions over the concave region from $s / h_{in} \approx -0.71$ to $s / h_{in} \approx -0.60$. Compared to the predicted values, the shape factors of the PAM solutions are noticeably lower at a similar flow rate.

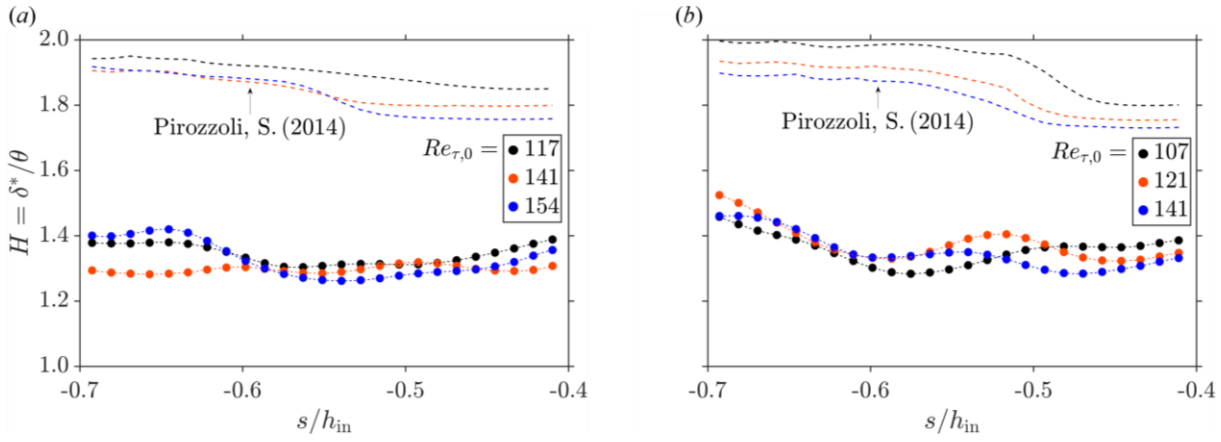

Figure 7-22 Wall-parallel variation of the shape factor, H, for three different flow conditions of (*a*) 200 p.p.m. and (*b*) 400 p.p.m. PAM solution flows at the flat surface of the convergence region of the TG channel (upstream of the throat). The legend shows the Re_τ values of the ZPG flow (see Table 7-3 and Table 7-4).

Figure 7-23(*a*,*b*) shows that Re_τ varies locally with the streamwise position in both accelerating PAM solution flows. Over the concave region, Re_τ remains almost constant. As the flow advances over the inclined flat wall region, Re_τ gradually increases until the mid-section of the convex part, where it shows a peak. The results show that as the flow rate increases, the peak Re_τ also increases. Figure 7-23(*b*) illustrates a similar trend of changes for the 400 p.p.m. solution. However, peak Re_τ values of the 400 p.p.m. solution are slightly higher than the 200 p.p.m. solution.

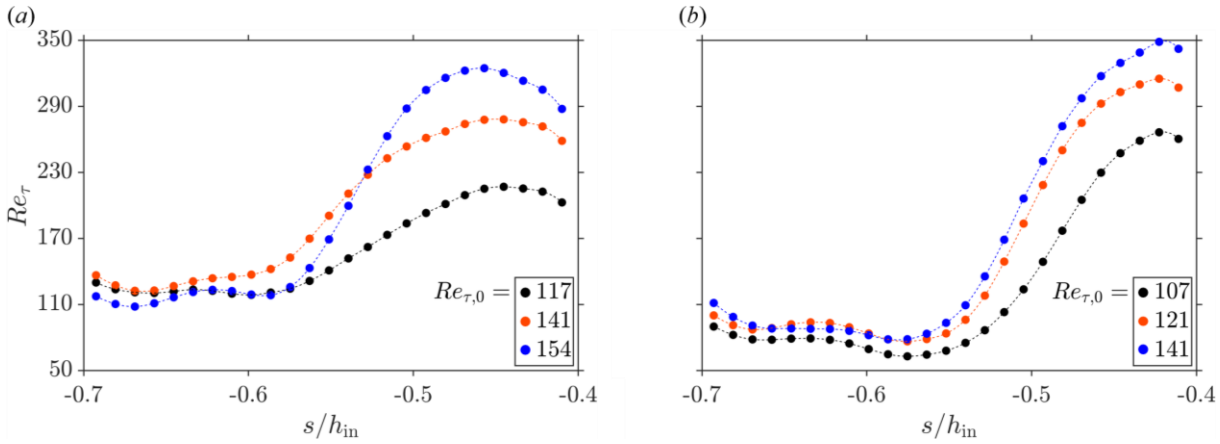

Figure 7-23 Wall-parallel variation of Re_τ for three different flow conditions of (*a*) 200 p.p.m. and (*b*) 400 p.p.m. PAM solution flows at the flat surface of the convergence region of the TG channel (upstream of the throat). The legend shows the Re_τ values of the ZPG flow (see Table 7-3 and Table 7-4).

The Re_θ profiles of the 200 p.p.m. and 400 p.p.m. flows are depicted in Figure 7-24(*a*,*b*). All profiles show a general increase over the convergence region, where the slope of the changes increases after the flow passes the concave flow region. The $Re_\theta\,(s)$ of the 400 p.p.m. solution shown in Figure 7-24(*b*) indicates that increasing the flow rate amplifies the local Re_θ.

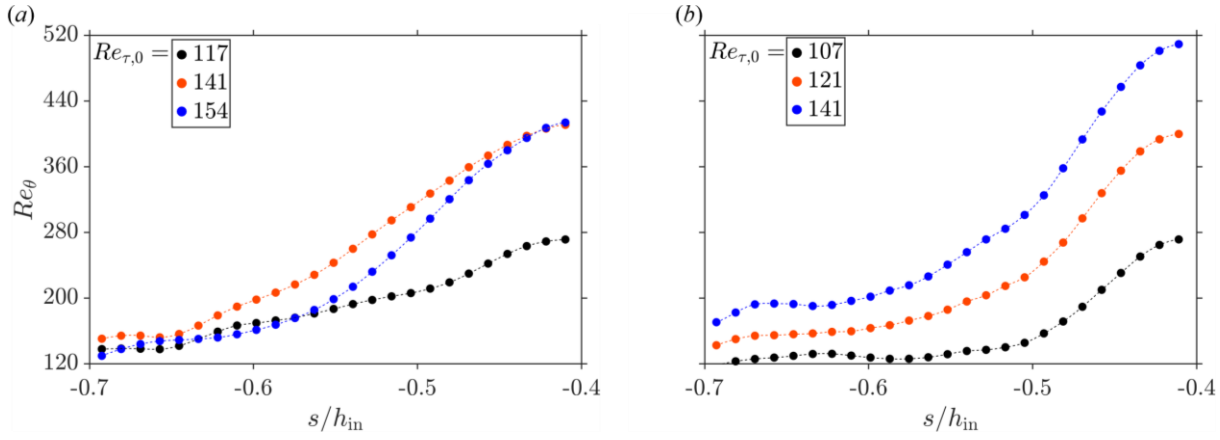

Figure 7-24 Wall-parallel variation of Re_θ for three different flow conditions of (*a*) 200 p.p.m. and (*b*) 400 p.p.m. PAM solution flows at the flat surface of the convergence region of the TG channel (upstream of the throat). The legend shows the Re_τ values of the ZPG flow (see Table 7-3 and Table 7-4).

However, the 200 p.p.m. flow with $Re_{\tau,0} = 154$, illustrated in Figure 7-24(*a*), show relatively lower values than that of the flow with $Re_{\tau,0} = 141$. This unexpected behavior might be due to the relatively high uncertainties of the wall shear viscosity measurements of the 200 p.p.m. flow, which, as discussed in Section 6.2.2, can be as high as ≈ 24 % of the measured μ_w. This uncertainty and errors in estimating the boundary layer edge velocity, U_e, and momentum thickness, θ, propagate into the evaluated Re_θ values and may result in deviated absolute values.

The non-dimensional pressure gradient parameters K, Δ_p, and β are plotted as a function of the wall-parallel position in Figure 7-25(*a-c*). The plots associated with the 200 p.p.m. flow are given in the top row, and profiles of the 400 p.p.m. flow are illustrated in the bottom row. The K values are at least two orders of magnitude larger than the critical $K = 3 \times 10^{-6}$. Therefore, both PAM solution flows are expected to be fully relaminarized under the strong FPG. The K values also vary with the streamwise position and show peaks in the vicinity of the starting point of the convex region at $s / h_{in} \approx -0.48$.

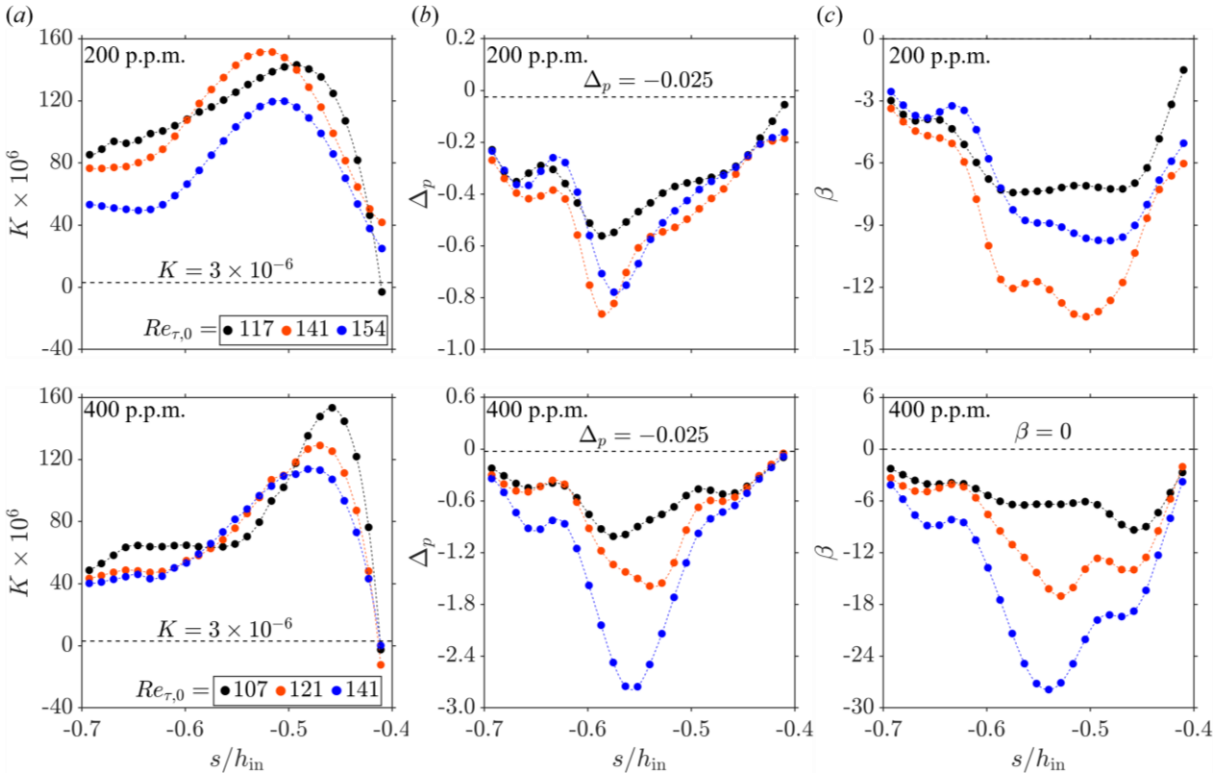

Figure 7-25 Streamwise variation of the (*a*) acceleration parameter, K (see equation (6-2)), (*b*) FPG parameter, Δ_p (see equation (6-1)), and (*c*) Rotta-Clauser pressure gradient parameter, β (see equation (6-4)), for three different flow conditions of 200 p.p.m. (top row) and 400 p.p.m. (bottom row) at the flat surface of the convergence region of the TG channel (upstream of the throat). The legend shows the Re_τ values of the ZPG flow (see Table 7-3 and Table 7-4).

The Δ_p profiles shown in Figure 7-25(*b*) fall well below the critical value of Δ_p = -0.025, which marks the onset of relaminarization. Almost all the profiles in both solutions show negative peaks in the range of -0.60 < s / h_{in} < -0.57, which coincides with the first half of the inclined wall region. The results show that increasing Re_τ amplifies the negative peak values. The β profiles, shown in Figure 7-25(*c*), indicate variations almost similar to those of the Δ_p profiles. At any streamwise position, $\beta < 0$, which means strong FPG. In the highest tested flow rate, $|\beta|_{max} \approx 14$ in the 200 p.p.m. and $|\beta|_{max} \approx 28$ in the 400 p.p.m. solution.

7.4.2 Mean flow of the 200 p.p.m PAM solution

The mean normalized streamwise velocity profiles of the 200 p.p.m. PAM solution flow over the convergence region are plotted in Figure 7-26(*a-c*) for three different inlet conditions. The left column demonstrates the inner-normalized, and the right column shows the outer-normalized profiles. At all streamwise positions and in all flow conditions, velocity profiles collapse on $\langle U_s \rangle^+ = n^+$ profile in the near-wall region.

As the flow enters the concave region, the inner-normalized velocity profile is squeezed well below the logarithmic law in all three tested flow conditions. Over the second half of the concave part, the strength of the FPG is attenuated. As a result, c_f slightly increases, and the inner-normalized velocity profiles escalate toward the logarithmic law. A higher flow rate decreases the local c_f and pushes the velocity profile significantly above the standard logarithmic profile. This behavior is evident in Figure 7-26(*c*) at s / h_{in} = -0.60.

As flow approaches the throat region, FPG weakens significantly, and despite the stabilizing effect of the convex curvature, the friction factor increases considerably over the convex region. Thus, the corresponding velocity profiles are partially or fully pushed below the logarithmic law. The results show that even at the highest tested flow rate, the profiles that deviate above the log-law have slopes almost equal to κ^{-1} and do not indicate any inclination toward the ultimate profile.

The right column of Figure 7-26(*a-c*) denotes that when the mean velocity profiles are normalized by their local edge velocities, they almost collapse into a similar profile in the outer layer. Nevertheless, a close look at the resultant profiles indicates that as flow advances in the convergence region, the applied FPG marginally reduces the normalized velocity value and pushes it toward a laminar velocity profile.

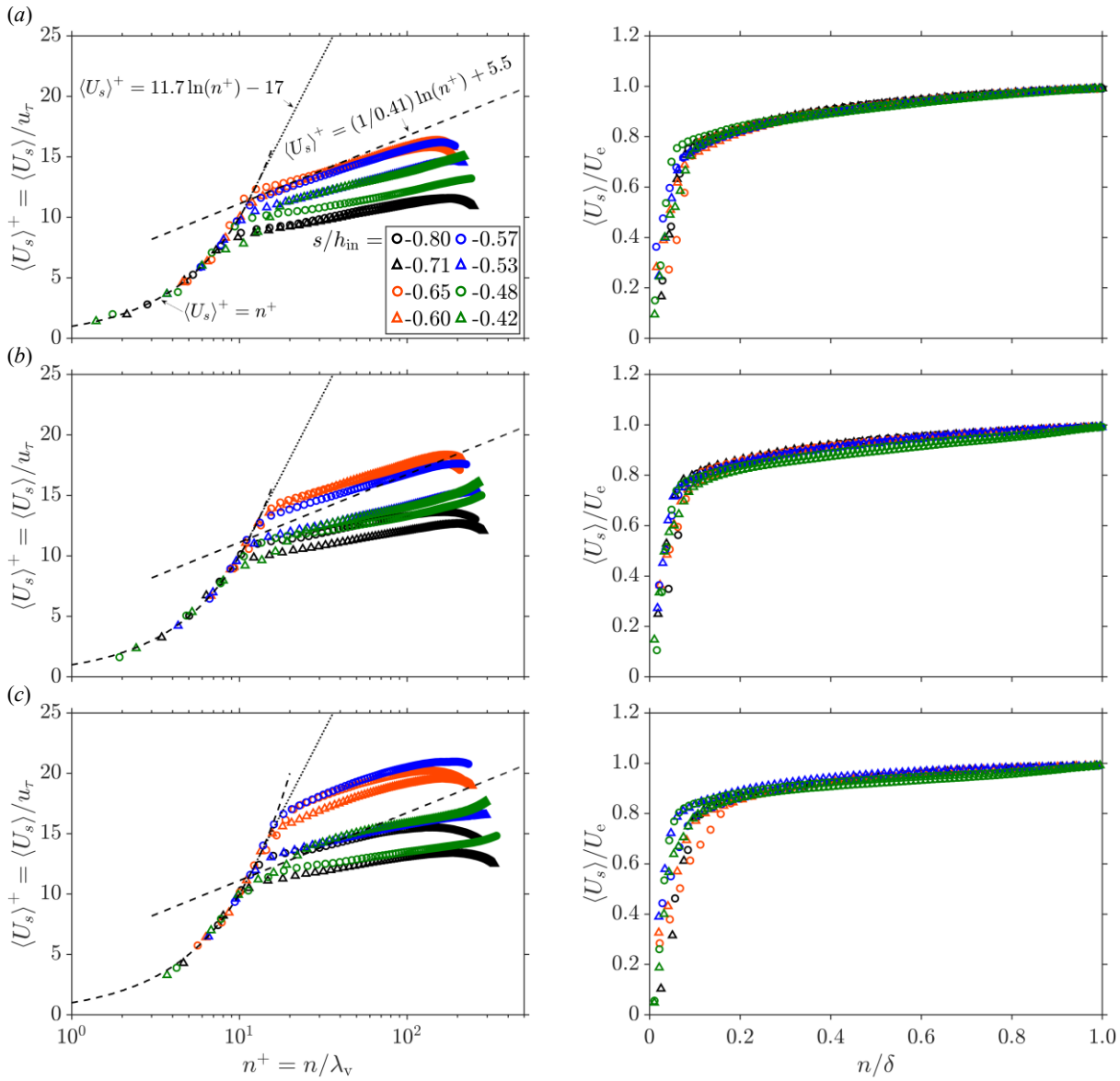

Figure 7-26 Wall-normal variation of the mean wall-parallel velocity profiles, normalized by the inner (left) and outer scales (right), at eight selected wall-parallel positions for accelerating 200 p.p.m. PAM solution flow over the flat surface of the TG channel's convergence region at (*a*) $Re_{\tau,0}$ = 117, (*b*) $Re_{\tau,0}$ = 141, and (*c*) $Re_{\tau,0}$ = 154.

Figure 7-27(*a-c*) shows the mean normalized Reynolds shear stress profiles of the accelerating 200 p.p.m. solution flow. For the same flow conditions, Figure 7-28(*a-c*) and Figure 7-29(*a-c*) illustrate the mean normalized wall-parallel and wall-normal Reynolds stresses. The inner-normalized results show that as the flow with $Re_{\tau,0}$ = 117 advances into the second half of the concave region, the turbulent production significantly increases near the wall due to FPG weakening and destabilizing effect of the concave wall structure. Flowing over the inclined wall

region, FPG regains its strength. As the $-\langle u_s u_n \rangle^+$ profile at s / h_{in} = -0.53 in Figure 7-27(a) shows, the mean Reynolds shear stress is noticeably damped compared to that at s / h_{in} = -0.65.

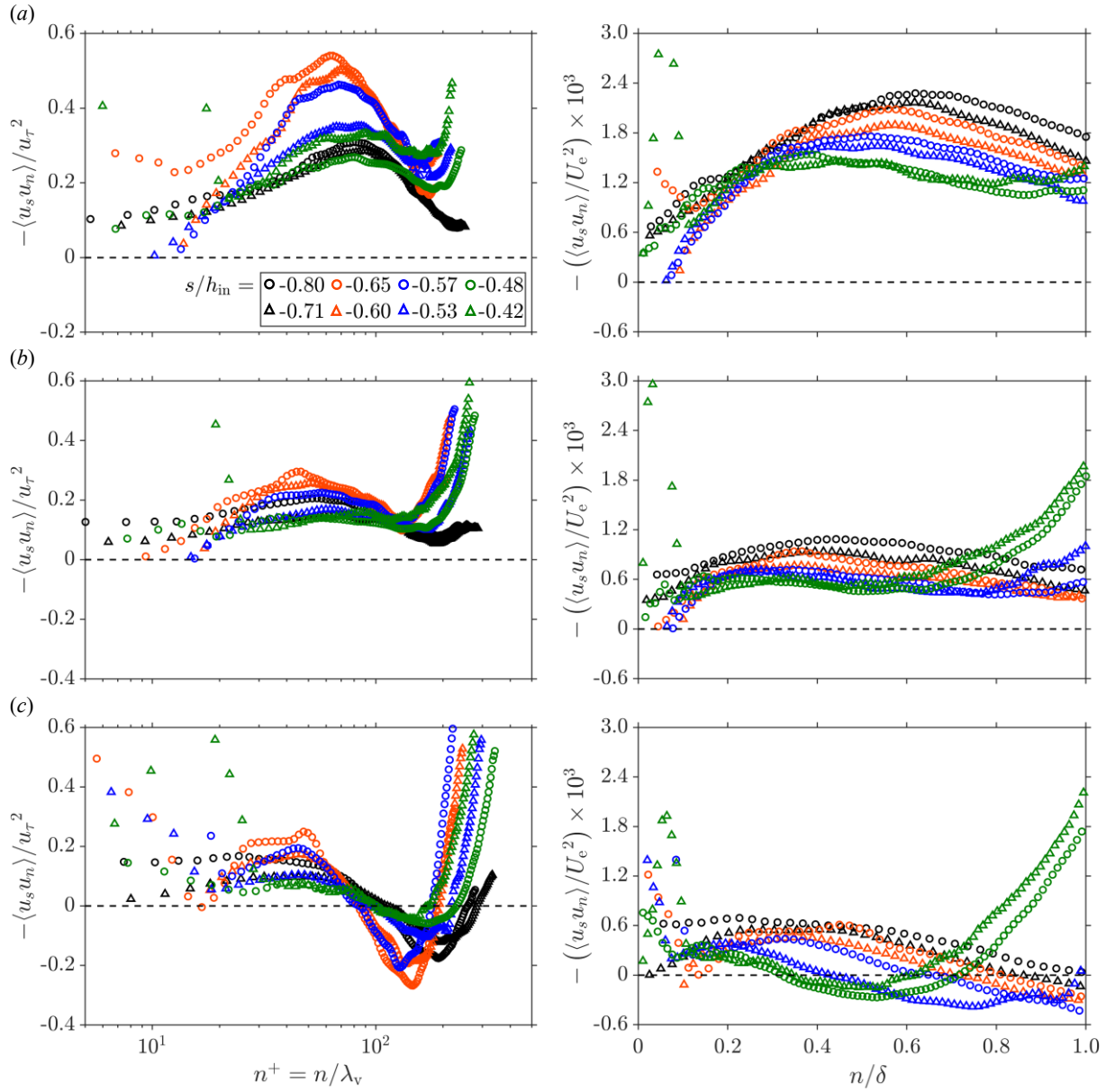

Figure 7-27 Wall-normal variation of the mean Reynolds shear-stress profiles, normalized by the inner (left) and outer scales (right), at eight selected wall-parallel positions for accelerating 200 p.p.m. PAM solution flow over the flat surface of the TG channel's convergence region at (a) $Re_{\tau,0}$ = 117, (b) $Re_{\tau,0}$ = 141, and (c) $Re_{\tau,0}$ = 154.

As flow passes over the convex region, FPG weakens, and the turbulence production intensity should naturally enhance, but convex curvature stabilizes the flow. The combination of these effects results in a $-\langle u_s u_n \rangle^+$ profile that is less intense than the entrance flow. Adjacent to the throat region, FPG and curvature effects almost disappear, and turbulence production intensifies

again, as is seen in the $-\langle u_s u_n \rangle^+$ profile at s / h_{in} = -0.42. The other two flow conditions with higher flow rates show similar trends of changes when their relative profiles are compared in the streamwise direction. Nevertheless, when compared with each other, it is clear that as the flow rate increases, the combined effects of polymer additives, FPG, and local wall curvature, significantly damp the mean Reynolds shear stress.

Maximum $-\langle u_s u_n \rangle^+$ occurs in the middle of the concave region at s / h_{in} = -0.65. As $Re_{\tau,0}$ increases from 117 to 154, $-\langle u_s u_n \rangle^+_{max}$ decreases from ≈ 0.55 to ≈ 0.25, a reduction of ≈ 54 %. This reduction occurs while at a higher flow rate, wall shear stress reduces relatively, which should, in turn, escalate the $-\langle u_s u_n \rangle^+$ profile. Mean Reynolds shear stress profiles, normalized by the local U_e^2 values and shown in the right column of Figure 7-27(*a-c*), can better reveal the effect of polymers on reducing turbulence production. The profiles of the flow with $Re_{\tau,0}$ = 117 show that as flow advances in the convergence region, the peak $-\langle u_s u_n \rangle / U_e^2$ gradually drops until flow leaves the region. Other flows with higher flow rates show similar behavior. However, the peak of ≈ 2.3 × 10^{-3} in the outer layer of the flow with $Re_{\tau,0}$ = 117 reduces to ≈ 0.6 × 10^{-3} in the flow with $Re_{\tau,0}$ = 154, which is a ≈ 74 % reduction in the mean Reynolds shear stress and turbulent production rate.

Figure 7-9(*c*) shows that the peak value of the mean Reynolds shear stress in the ZPG flow of the 200 p.p.m. solution is $[-\langle u_s u_n \rangle / U_e^2]_{max}$ ≈ 2.8 × 10^{-3} for almost all three tested flow rates. Compared to the ZPG flow, Figure 7-27(*a-c*) denotes that FPG significantly attenuates the mean Reynolds shear stress for higher flow rates. Also, the $-\langle u_s u_n \rangle / U_e^2$ profiles of the accelerating pure water flow, shown in Figure 6-26(*a-c*), indicate that $[-\langle u_s u_n \rangle / U_e^2]_{max}$ reduces from ≈ 2.8 × 10^{-3} in the lowest tested flow rate to ≈ 2.5 × 10^{-3} in the highest tested flow rate. Compared to the peak of $[-\langle u_s u_n \rangle / U_e^2]_{max}$ ≈ 2.8 × 10^{-3} in the ZPG water flow profiles, shown in Figure 6-12(*b*), it can be found that FPG causes only a reduction of ≈ 14 % in the highest tested flow rate. As discussed, $[-\langle u_s u_n \rangle / U_e^2]_{max}$ reduces to ≈ 0.6 × 10^{-3} in the FPG flow of the 200 p.p.m. solution with $Re_{\tau,0}$ = 154, which indicates a significant reduction of ≈ 78 % when compared with its ZPG counterpart. Therefore, it can be concluded that nearly 14 % of this reduction is due to FPG and ≈ 64 % due to polymer additives.

While a significant attenuation of the mean Reynolds shear stress occurs over the outer layer of the BL, the results show that as the flow enters the throat region, a significant peak appears in

$-\langle u_s u_n \rangle$ profiles near the wall. However, due to the high measurement uncertainties of $-\langle u_s u_n \rangle$ (see Section 6.2.2) in the wall region, it was not easy to locate the exact position of the peak. Results show that the peak occurs somewhere in $10 < n^+ < 20$ or $0 < n/\delta < 0.2$.

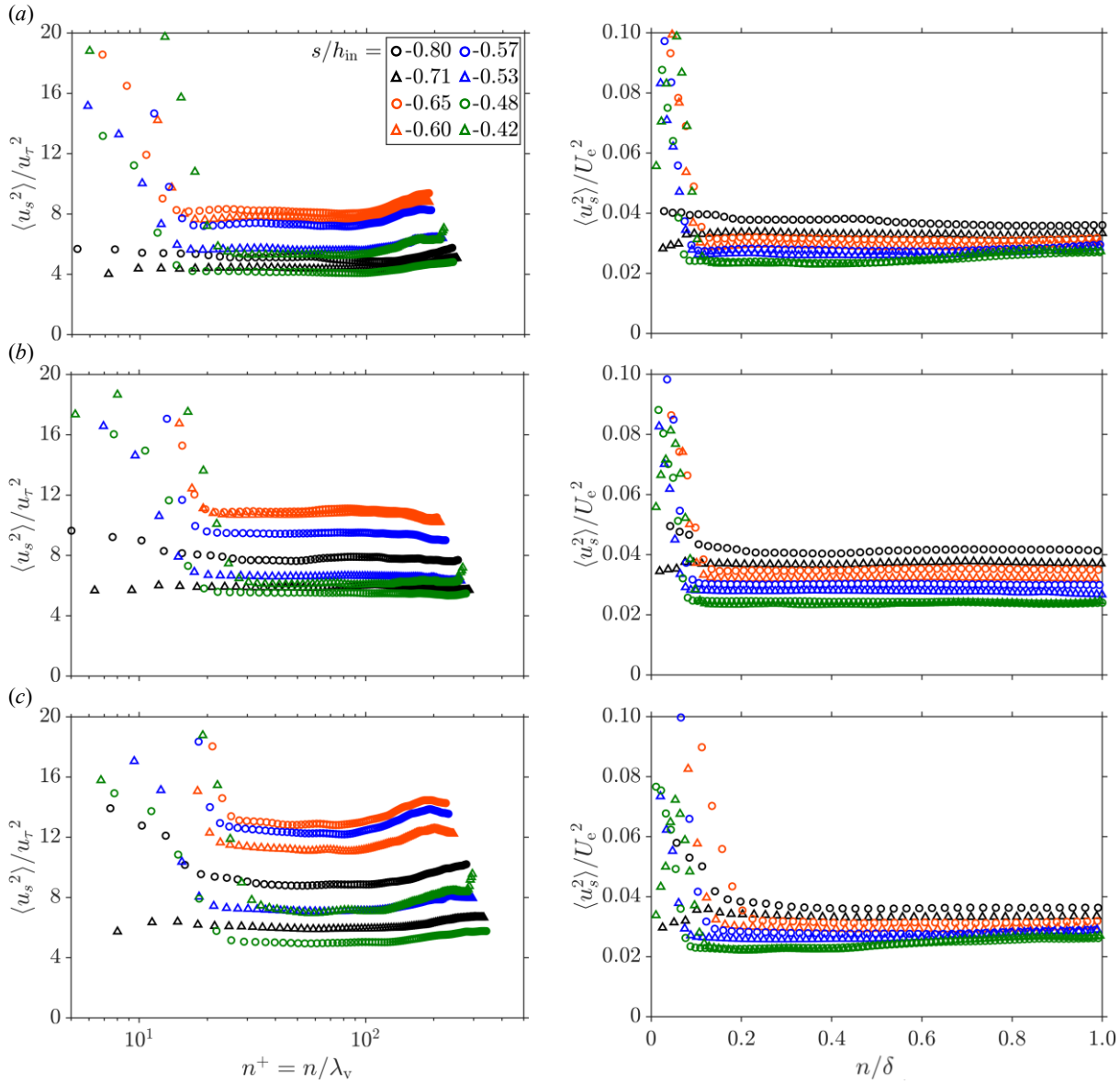

Figure 7-28 Wall-normal variation of the mean wall-parallel Reynolds stress profiles, normalized by the local inner scales (left) and outer scales (right), at eight selected wall-parallel positions for accelerating 200 p.p.m. PAM solution flow over the flat surface of the TG channel's convergence region at (*a*) $Re_{\tau,0} = 117$, (*b*) $Re_{\tau,0} = 141$, and (*c*) $Re_{\tau,0} = 154$.

Another critical phenomenon that occurs locally in the accelerating flow of the 200 p.p.m. solution with $Re_{\tau,0} = 154$ is the emergence of negative mean Reynolds shear stress zones in the outer layer of some profiles. Durbin (1993) referred to these as 'counter-gradient' Reynolds shear

stresses. Similar negative Reynolds shear stresses were also reported in the DNS study of Pandey et al.(2020) on a channel flow subjected to non-uniform body force. The FPG and primarily the addition of the polymer additives relaminarizes the flow and quenches the turbulence production.

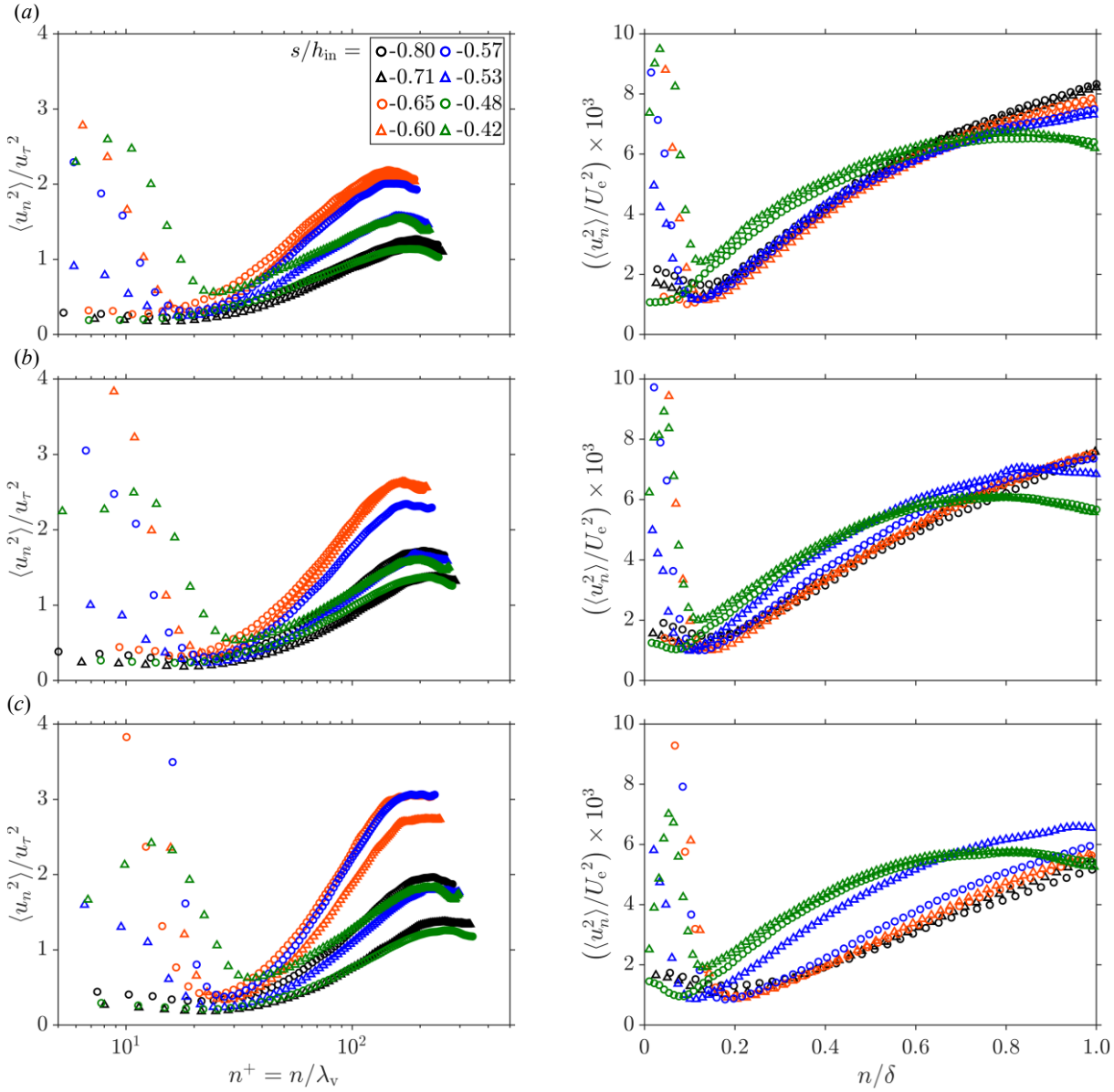

Figure 7-29 Wall-normal variation of the mean wall-normal Reynolds stress profiles, normalized by the inner (left) and outer scales (right), at eight selected wall-parallel positions for accelerating 200 p.p.m. PAM solution flow over the flat surface of the TG channel's convergence region at (*a*) $Re_{\tau,0}$ = 117, (*b*) $Re_{\tau,0}$ = 141, and (*c*) $Re_{\tau,0}$ = 154.

As shown in Figure 7-28(*a-c*), all $\langle u_s^2\rangle^+$ profiles indicate significant peaks near the wall. Over the outer layer, $\langle u_s^2\rangle^+$ values are almost constant for each position. As the solution flows downstream, $\langle u_s^2\rangle^+$ profile at s / h_{in} =-0.65, at the middle of the concave region, escalates and lies above other profiles in all tested flow rates. As flow advances downstream toward the throat, FPG

weakens, friction factor increases and $\langle u_s^2 \rangle^+$ profiles relax to levels comparable with the profiles of the entrance flow. In contrast to the inner-normalized profiles, the outer-normalized profiles, depicted in the right column of Figure 7-28(*a-c*), indicate that $\langle u_s^2 \rangle / U_e^2$ values gradually mitigate as flow advances in the convergence region. Near the wall, profiles show significant peak values. A comparison of the $\langle u_s^2 \rangle / U_e^2$ profiles of the 200 p.p.m. flow subjected to FPG with those of the ZPG flow reveals that the streamwise turbulence intensities in the outer layer are almost of a similar order. Also, FPG profiles show relatively larger peaks near the wall than the ZPG flows.

Similarly, mean wall-normal Reynolds stresses, normalized by the inner scales and shown in Figure 7-29(*a-c*), indicate higher turbulent intensity levels over the second half of the concave region. In contrast, when normalized by the outer scales, the wall-normal intensities gradually enhance as the flow advances in the convergence region. From the middle of the inclined flat wall region towards the throat, wall-normal turbulent activities intensify, and the resultant $\langle u_n^2 \rangle / U_e^2$ profiles are shifted to higher levels.

One noticeable behavior that the $\langle u_n^2 \rangle / U_e^2$ profiles of the accelerating 200 p.p.m. flow show is the local minima at positions after the concave region. The results show that as the flow enters the inclined wall region, $\langle u_n^2 \rangle$ abruptly drops from a larger value to a minimum somewhere in $20 < n^+ < 25$ and then gradually increases. Other positions past the concave surface exhibit similar behavior, while the profiles over the concave region lack a minimum.

The wall-normal variation of the mean skewness and kurtosis at selected streamwise positions are shown in Figure 7-30(*a-c*) for three flow conditions of the accelerating 200 p.p.m. solution flow. The skewness profiles almost collapse into a similar profile for all three tested flow rates in the outer layer. Near the wall, the skewness profiles show noticeable deviations from each other. As $Re_{\tau,0}$ increases, the departure of the skewness values above the normal $\mu_3 = 0$ line amplifies. Near the throat entrance, skewness shows large negative skewness in the wall region.

The kurtosis profiles of the flow with $Re_{\tau,0} = 117$ do not collapse on a similar profile nor on the normal $\mu_4 = 3$ line of a Gaussian distribution. As the flow rate increases, μ_4 profiles collapse but remain larger than $\mu_4 = 3$. Nevertheless, the profile at $s / h_{in} = -0.42$, at the entrance of the throat region, shows a significant deviation from other profiles and shifts to larger μ_4 values (≈ 4.5) in all three tested flow rates.

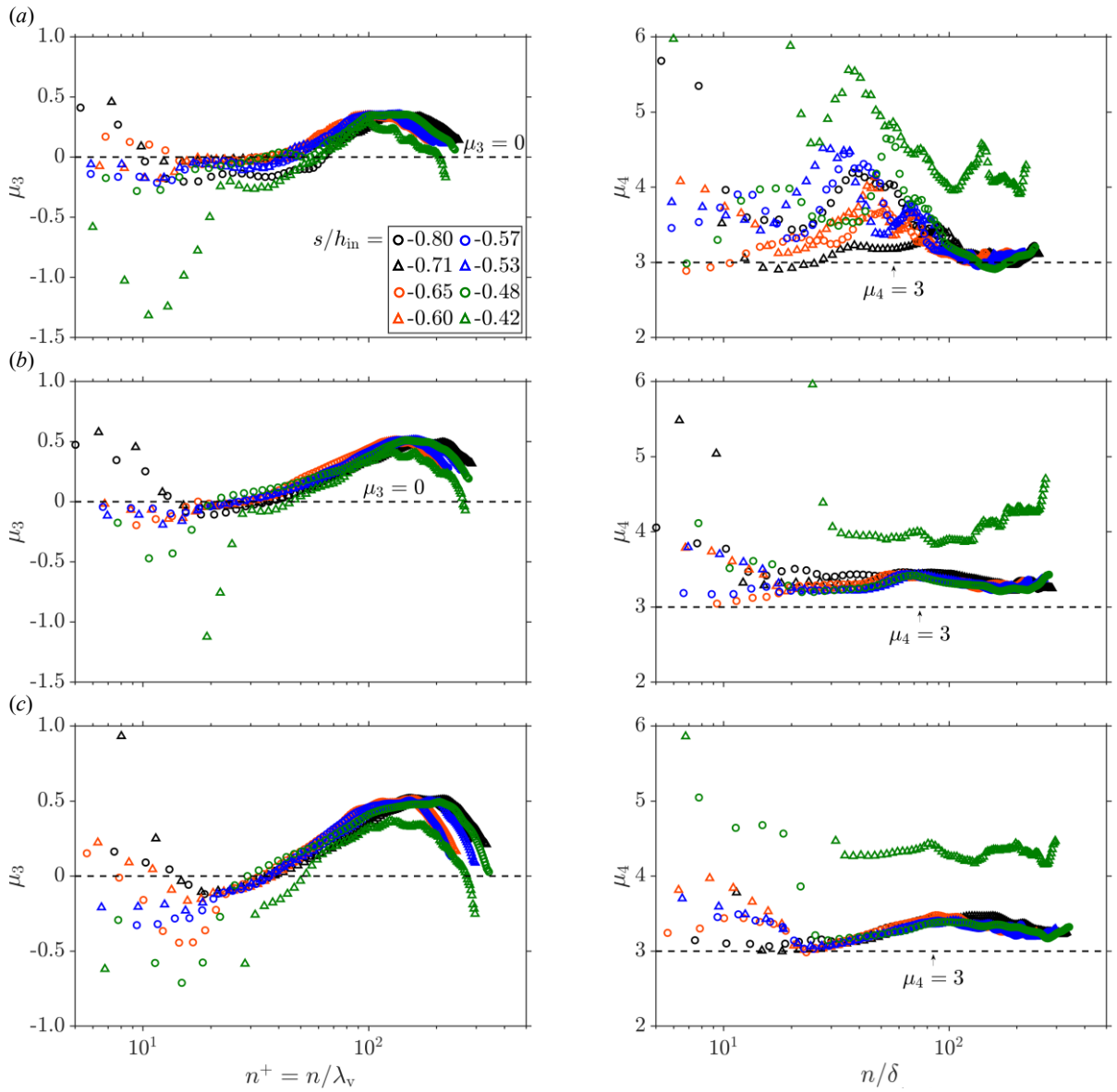

Figure 7-30 Wall-normal variation of the mean skewness, μ_3, profiles (left), and mean kurtosis, μ_4, profiles (right) at eight selected wall-parallel positions for accelerating 200 p.p.m. PAM solution flow over the flat surface of the TG channel's convergence region at (*a*) $Re_{\tau,0} = 117$, (*b*) $Re_{\tau,0} = 141$, and (*c*) $Re_{\tau,0} = 154$.

7.4.3 Mean flow of the 400 p.p.m. PAM solution

Figure 7-31(*a-c*) illustrates the wall-normal mean streamwise velocity profiles of the 400 p.p.m. flow under acceleration for three different flow rates. On the left column, velocity and wall-normal positions are normalized by the inner viscous scales; on the right column, they are normalized by outer scales. The ultimate profile of Virk et al. (1970) for Newtonian fully-developed ZPG flows is also inserted in figures for reference. It is evident from the inner-normalized profiles that all of them collapse on the linear law in the viscous sublayer.

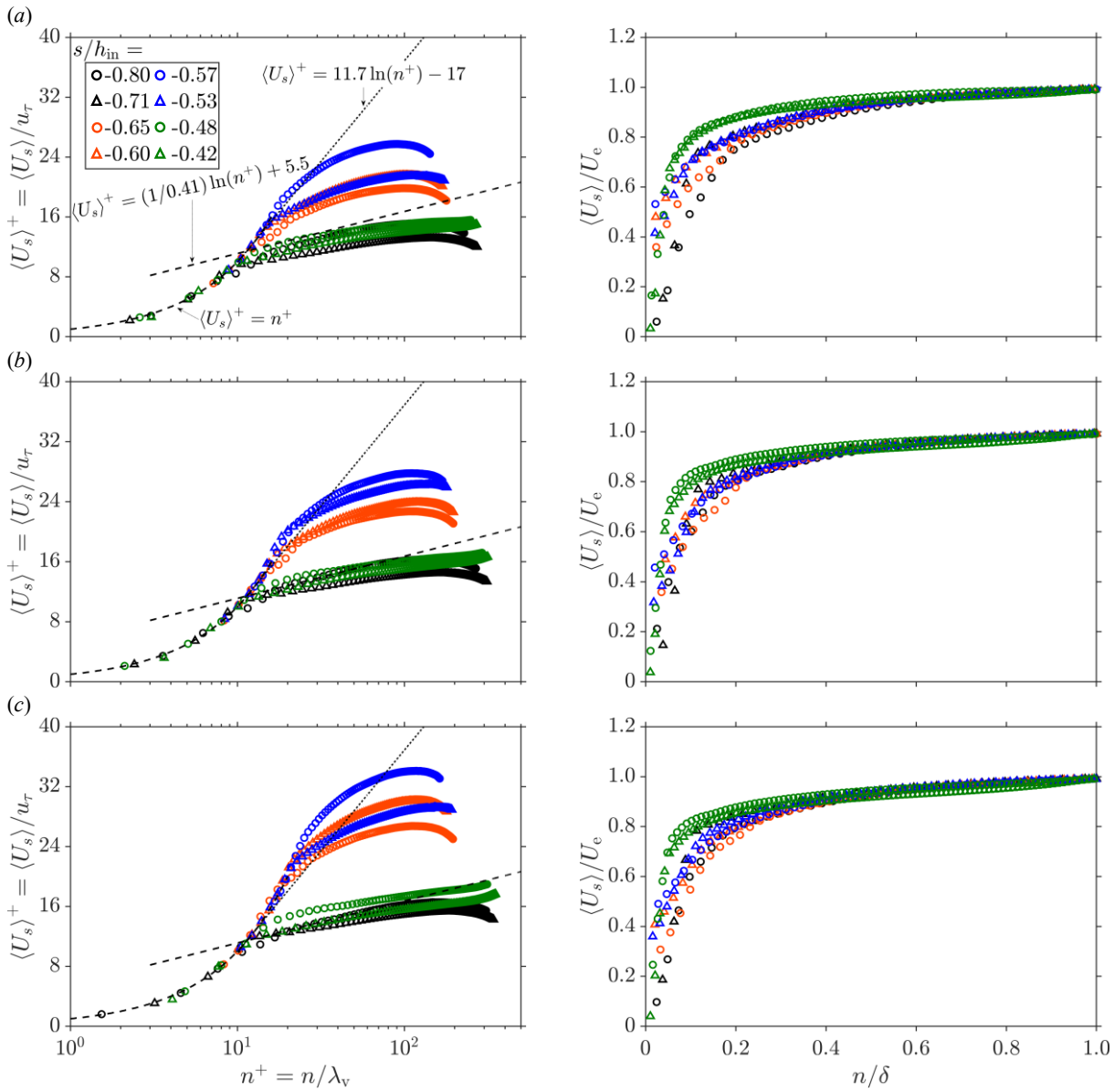

Figure 7-31 Wall-normal variation of the mean wall-parallel velocity profiles, normalized by the local inner (left) and outer scales (right), at eight selected wall-parallel positions for accelerating 400 p.p.m. PAM solution flow over the flat surface of the TG channel's convergence region at (*a*) $Re_{\tau,0}$ = 107, (*b*) $Re_{\tau,0}$ = 126, and (*c*) $Re_{\tau,0}$ = 141.

Figure 7-31(*a*) shows that $\langle U_s\rangle^+$ profile elevates as the flow passes over the second half of the concave region. The elevation continues until the middle of the inclined flat wall region, where it slightly passes over the ultimate profile. The velocity profiles that deviate above the standard logarithmic law do not exhibit a log shape, which escalates as the profile rises even higher toward the ultimate profile. White et al. (2012) also identified a similar behavior for drag-reduced polymer solutions at MDR in ZPG experiments.

The 400 p.p.m. solution with $Re_{\tau,0}$ = 107 flowing toward the convex region stabilizes, and the corresponding velocity profiles fall almost below the standard log law. A similar behavior is repeated for the 400 p.p.m. flow with $Re_{\tau,0}$ = 126, with profiles more elevated over the second half of the concave region, compared to the flow with $Re_{\tau,0}$ = 107. At $Re_{\tau,0}$ = 126, the flow over the second half of the inclined flat region partially passes above the ultimate profile in the buffer layer and falls close but below it in the outer layer. A similar trend is repeated for the higher flow rate with $Re_{\tau,0}$ = 141. A large portion of the $\langle U_s \rangle^+$ profile at s / h_{in} = -0.57, at the middle of the inclined wall region, rises above the ultimate profile and does not exhibit a logarithmic behavior. At s / h_{in} = - 0.57, the combination of the FPG and the polymer additives attenuates the skin friction factor noticeably and causes the velocity profile to deviate even above the ultimate profile.

The outer normalized velocity profiles, shown in the right column of Figure 7-31(*a-c*), denote that the profiles collapse over the outer layer and vary in form near the wall. For instance, in the flow with $Re_{\tau,0}$ = 107, as flow advances in the convergence region, the $\langle U_s \rangle / U_{\text{e}}$ profiles widen and, near the throat region's entrance, almost reform to the shape of a canonical ZPG turbulent flow.

Figure 7-32(*a-c*) demonstrates the wall-normal variations of the mean Reynolds shear stress over the convergence region for the 400 p.p.m. PAM solution flow at three different flow rates. For the same flow conditions, Figure 7-33(*a-c*) and Figure 7-34(*a-c*) illustrate the mean wall-parallel and wall-normal Reynolds stress profiles. Figure 7-32(*a*) shows that $-\langle u_s u_n \rangle^+$ profiles of the accelerating 400 p.p.m. flow with $Re_{\tau,0}$ = 107 at various streamwise positions have values in the order of $\mathcal{O}(0.1)$ in the outer layer. Near the wall, $-\langle u_s u_n \rangle^+$ indicate negative values at s / h_{in} = - 0.65, at the middle of the concave region, and at s / h_{in} = -0.53, at the start of the convex part. The higher flow rates resemble the same behavior and the order of $-\langle u_s u_n \rangle^+$ only changes slightly compared to those of the flow with $Re_{\tau,0}$ = 107.

One noticeable characteristic of the Reynolds shear stress profiles is the emergence of a local peak at $n^+ \approx 50$, at the middle of the concave region, at s / h_{in} = -0.65, which amplifies as the flow rate increases. It is not clear what causes this peak. Still, its persistent appearance in all three tested flow rates and a magnitude larger than the average, and the measurement uncertainties confirm that it is not an experimental artifact.

The outer-normalized mean Reynolds shear stress profiles, illustrated in the right column of Figure 7-32(*a-c*), indicate that as the flow passes over the inclined wall region, turbulence

production is slightly mitigated relative to the entrance flow. The profiles at the middle of the convex part, at $s / h_{in} = -0.48$, show that Reynolds shear stress becomes negative over a noticeable portion of the outer layer in the flow with $Re_{\tau,0} = 126$. The counter-gradient negative zones almost vanish as $Re_{\tau,0}$ increases to 141.

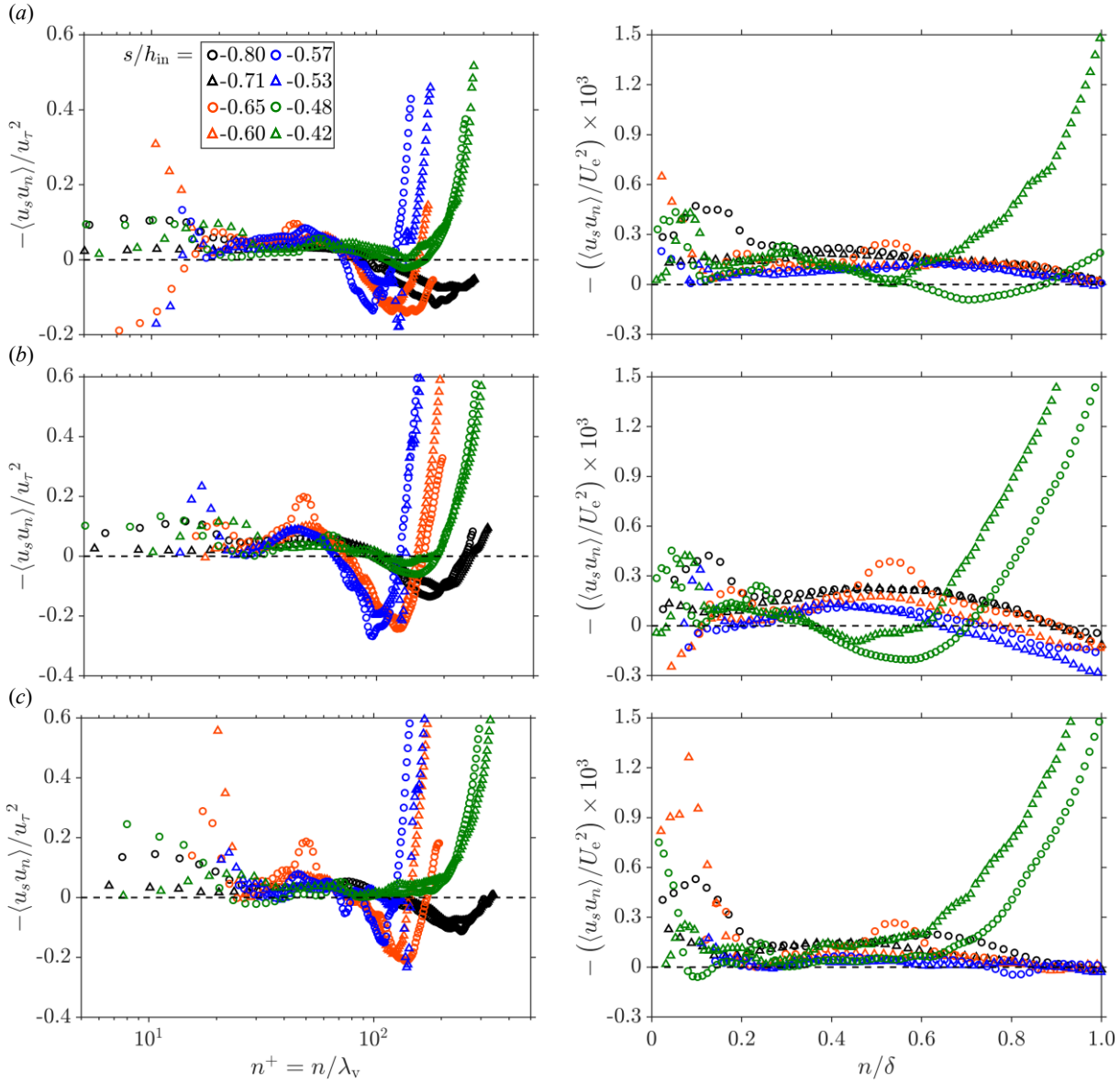

Figure 7-32 Wall-normal variation of the mean Reynolds shear-stress profiles, normalized by the inner (left) and outer scales (right), at eight selected wall-parallel positions for accelerating 400 p.p.m. PAM solution flow over the flat surface of the TG channel's convergence region at (*a*) $Re_{\tau,0} = 107$, (*b*) $Re_{\tau,0} = 126$, and (*c*) $Re_{\tau,0} = 141$.

The $-\langle u_s u_n \rangle / U_e^2$ profiles over the second half of the convex region behave almost differently from the profiles of other streamwise positions. One common characteristic of different tested flow rates is that in the normal positions with $n / \delta > 0.6$, they suddenly increase to large values until

they meet the edge of the BL. One reason for this can be the highly distorted core region over those positions and that the core flow is partially rotational due to the complex interaction of the weak FPG with the semidilute polymer solution.

The mean Reynolds shear stresses of the outer layer remain almost at $\mathcal{O}(0.2 \times 10^{-3})$, independent of the flow rate. The $-\langle u_s u_n \rangle / U_e^2$ profiles of the accelerating 200 p.p.m. flow, shown in Figure 7-27(*a-c*), indicate that the maximum outer layer values change from $\approx 2.4 \times 10^{-3}$ in the flow with $Re_{\tau,0} = 117$ to a maximum of $\approx 0.6 \times 10^{-3}$ in the flow with $Re_{\tau,0} = 141$. Comparing the two solutions at the highest flow rates shows a reduction of ≈ 67 %, and comparison at equal $Re_{\tau,0} = 141$, shows a maximum decrease of ≈ 76 % in the turbulence production. Also, compared to the $-\langle u_s u_n \rangle / U_e^2$ profiles of the accelerating water flow, shown in Figure 6-26(*a-c*), the 400 p.p.m. solution reduces the Reynolds shear stress by a maximum of ≈ 92 % under FPG.

Figure 7-33(*a-c*) shows that similar to the 200 p.p.m. flow, variation of the FPG's strength over the convergence region and corresponding changes in the local skin friction factor results in the $\langle u_s^2 \rangle^+$ profiles of varying intensities over the region. In all tested flow conditions, flow at the middle of the inclined flat wall region, at $s / h_{in} = -0.57$, shows the most amplified profile. As flow advances to the convex part, the strong curvature effects stabilize the flow and the resultant $\langle u_s^2 \rangle^+$ profiles coincide with the entrance flow in the outer layer.

Both inner- and outer-normalized profiles indicate that as the flow passes over the convergence region, $\langle u_s^2 \rangle^+$ exhibit strong peaks at $n^+ \approx 12$, with varying intensity in the streamwise direction. The $\langle u_s^2 \rangle / U_e^2$ profiles denote that FPG marginally attenuates the wall-parallel fluctuations as flow advances in the acceleration region. Compared to the $\langle u_s^2 \rangle / U_e^2$ profiles of the 200 p.p.m. flow, shown in Figure 7-28(*a-c*), wall-parallel turbulence is damped over the outer layer.

The $\langle u_n^2 \rangle^+$ profiles, shown in Figure 7-34(*a-c*), denote that the combination of the FPG and the viscoelastic effects significantly attenuates the wall-normal fluctuations in the range of $20 < n^+ < 30$, in the buffer layer, for all tested flow conditions. Nevertheless, $\langle u_n^2 \rangle^+$ slightly larger in the outer layer at the entrance of the convergence region. As the flow enters the second half of the concave part at $s / h_{in} = -0.65$, a knee point emerges in the profiles. The mean wall-normal Reynolds stress decreases almost linearly from a relatively large value to nearly zero at the knee point and increases after it, with a smoother slope in the outer layer. The knee point persists in the profiles of other streamwise positions until the start of the convex region. As the flow enters this

region, the near-wall $\langle u_n^2 \rangle^+$ values relax. The profiles of higher flow rates follow a similar trend of changes. However, as the flow rate increases, the profiles with detectable knee points get squeezed in the wall-normal direction. As a result, the successive decrease and increase before and after the minimum occur with relatively steeper slopes.

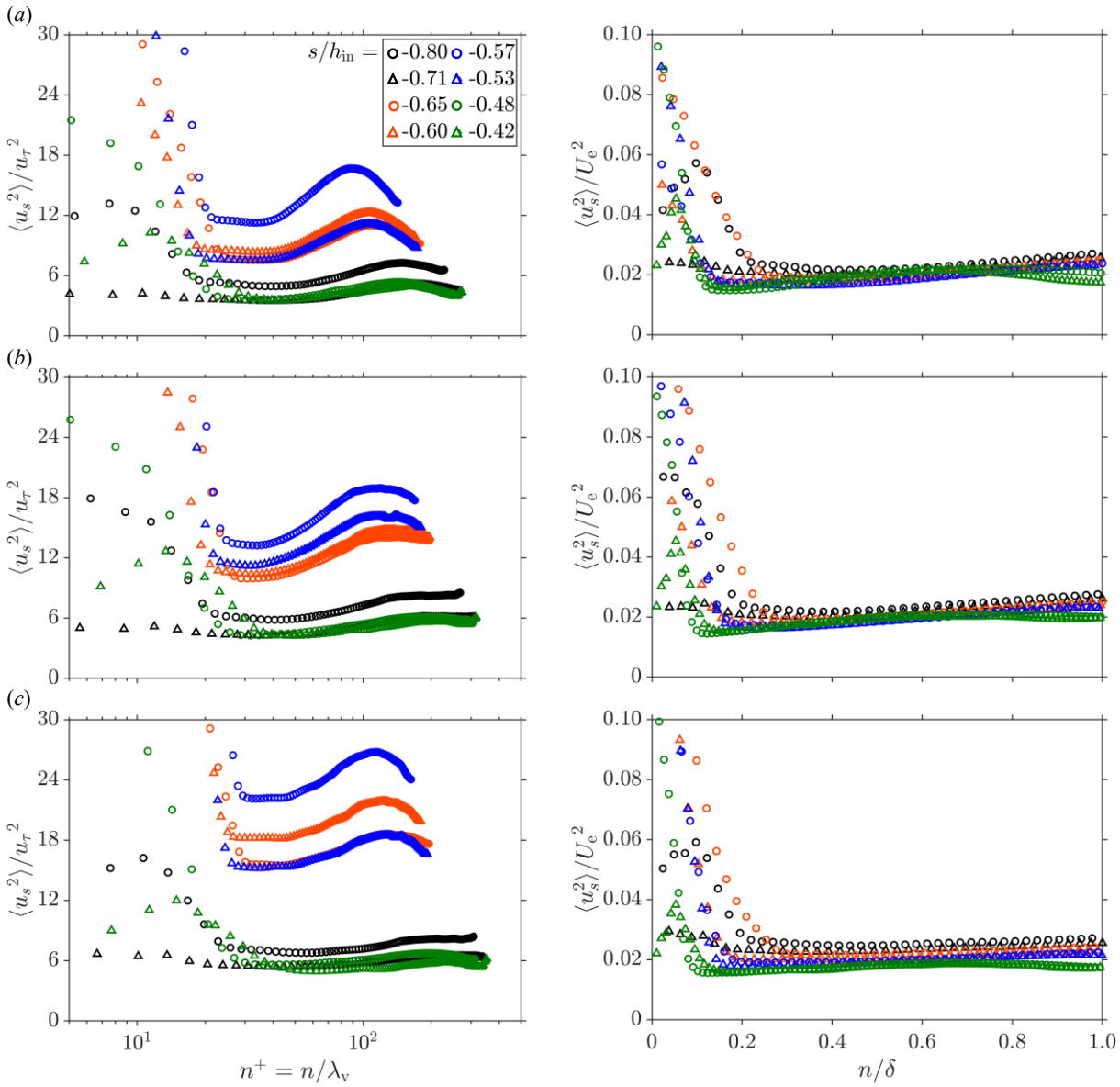

Figure 7-33 Wall-normal variation of the mean wall-parallel Reynolds stress profiles, normalized by the inner (left) and outer scales (right), at eight selected wall-parallel positions for accelerating 400 p.p.m. PAM solution flow over the flat surface of the TG channel's convergence region at (*a*) $Re_{\tau,0}$ = 107, (*b*) $Re_{\tau,0}$ = 126, and (*c*) $Re_{\tau,0}$ = 141.

The $\langle u_n^2 \rangle / U_\mathrm{e}^2$ profiles almost collapse in the outer layer for all tested flow rates, except the profiles over the convex region, which deviate noticeably to higher levels relative to the other profiles. Results show that increasing the flow rate affects only the intensity of the near-wall

profiles and does not have a significant effect on the $\langle u_n^2 \rangle / U_e^2$ values over the outer layer. Also, compared to the accelerating 200 p.p.m. profiles, given in Figure 7-29(*a-c*), the outer layer values of $\langle u_n^2 \rangle / U_e^2$ are damped even more in the accelerating 400 p.p.m. flow.

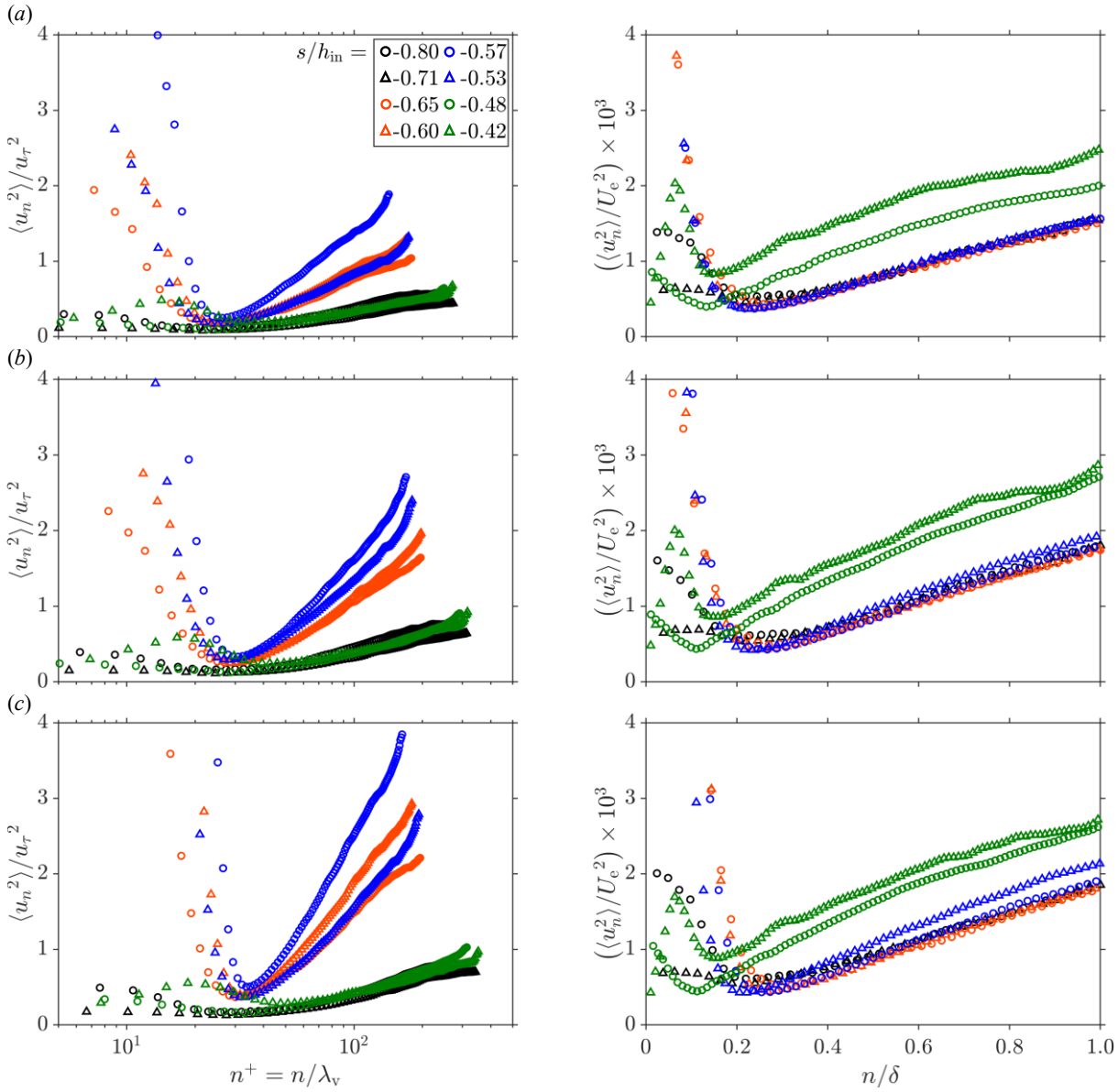

Figure 7-34 Wall-normal variation of the mean wall-normal Reynolds stress profiles, normalized by the inner (left) and outer scales (right), at eight selected wall-parallel positions for accelerating 400 p.p.m. PAM solution flow over the flat surface of the TG channel's convergence region at (*a*) $Re_{\tau,0}$ = 107, (*b*) $Re_{\tau,0}$ = 126, and (*c*) $Re_{\tau,0}$ = 141.

Figure 7-35(*a-c*) demonstrates the wall-normal variation of the skewness and kurtosis of the 400 p.p.m. flow under acceleration. None of the skewness profiles fully collapse on $\mu_3 = 0$ of a Gaussian distribution. In the outer layer, the profiles are positively skewed, and near the wall, they show both highly skewed negative and positive values. The kurtosis profiles partially collapse on

$\mu_4 = 3$ line over the buffer layer but indicate relatively higher values near the wall and lower values in the outer layer relative to the normal value. Also, the kurtosis values of the fluctuations over the second half of the convex region show a significant deviation relative to the other profiles.

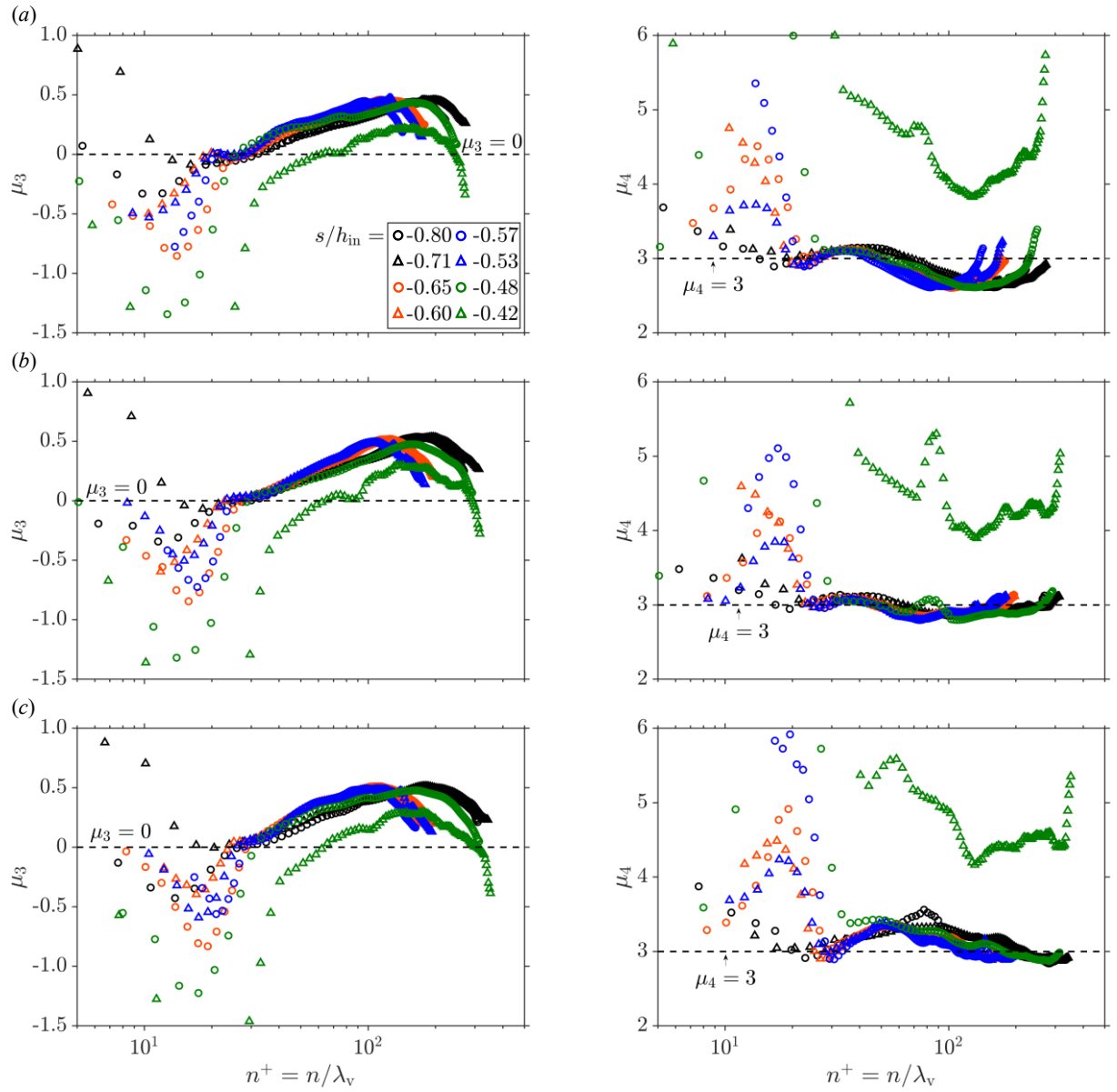

Figure 7-35 Wall-normal variation of the mean skewness, μ_3, profiles (left), and mean kurtosis, μ_4, profiles (right) at eight selected wall-parallel positions for accelerating 400 p.p.m. PAM solution flow over the flat surface of the TG channel's convergence region at (*a*) $Re_{\tau,0} = 107$, (*b*) $Re_{\tau,0} = 126$, and (*c*) $Re_{\tau,0} = 141$.

7.5. Decelerating flow

In Section 6.4, it was discussed that the combination of APG and local curvature effects alters the BL turbulence in a pure water flow, resulting in noticeable local deviations of the mean flow statistics from the canonical ZPG Newtonian flows. It was also discussed in detail in Section 7.3 that how adding minute amounts of PAM to water reduced the drag, mitigated the production of turbulence, and enhanced the streamwise velocity fluctuations, consistent with previous related studies. Section 7.5 investigated the effects of strong FPG of varying strength on polymeric solution flows. It was shown that the polymer additives significantly attenuate the Reynolds shear stress in the tested decelerating non-Newtonian flows to the extent that at some streamwise positions in the convergence region of the channel, counter-gradient negative Reynolds shear stresses emerge due to the full relaminarization of the flow.

This Section investigates the combined effects of the polymer addition, APG of varying strength, and local wall curvatures on the dynamics of the solutions with concentrations of 200 p.p.m. and 400 p.p.m. in the divergence part of the TG channel. The aim is to elucidate the local physics of the developing BLs subjected to APG, explore the mean flow statistics variations due to these effects, and explain the emergence of possible relaminarized zones in such flows. The section presents the streamwise variations of the bulk BL parameters, such as the skin friction factor. Then, the mean flow statistics of the decelerating 200 p.p.m. and 400 p.p.m. flows are provided and discussed in detail.

7.5.1 Boundary layer parameters

Figure 7-36(*a*,*b*) illustrates the velocity ratio profiles of U_e / U_m for the decelerating flows of the 200 p.p.m. and 400 p.p.m. solutions. U_e / U_m decreases almost linearly over the interrogated flow region in both flows. In the 200 p.p.m. flow, increasing the $Re_{\tau,0}$ to 141 enhances the local U_e / U_m. However, as Figure 7-36(*a*) shows, the U_e / U_m profile of the flow at $Re_{\tau,0} = 154$ drops below the $Re_{\tau,0} = 141$ profile and above the profile of $Re_{\tau,0} = 117$. The U_e / U_m profiles of the 400 p.p.m. flow, shown in Figure 7-36(*b*), denote that increasing the $Re_{\tau,0}$ mitigates the local U_e / U_m values. The velocity ratios of this flow fall below the predictions of Dean's correlation for the fully developed ZPG flow.

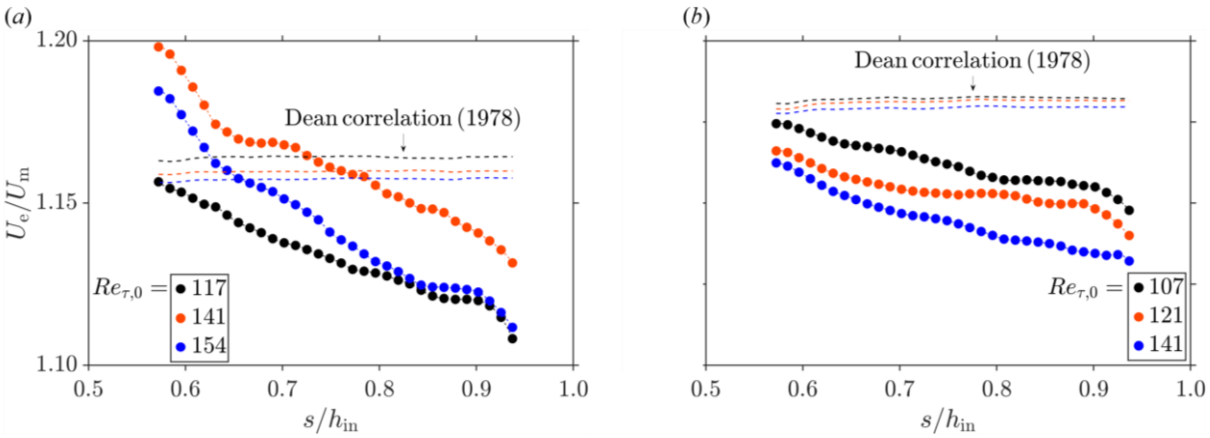

Figure 7-36 Wall-parallel variations of the boundary layer edge velocity, U_e, ratio to the mean streamwise velocity, U_m, for three different flow conditions of (*a*) 200 p.p.m. and (*b*) 400 p.p.m. PAM solution flows at the flat surface of the divergence region of the TG channel (downstream of the throat). The correlations proposed by Dean (1978) for fully developed ZPG flow, given in equation (6-5), are also shown for reference. The legend shows the Re_τ values of the ZPG flow (see Table 7-3 and Table 7-4).

The streamwise dependency of the pressure coefficient, c_p, is illustrated in Figure 7-37(*a*,*b*) for the two tested PAM solution flows at three different flow rates. The local streamwise gradients of the BL edge pressure are also plotted in Figure 7-37(*a*,*b*). In the decelerating flow region, c_p (*s*) > 0, and its profile denotes a gradual increase over the examined region. Results show that, generally, c_p enhances locally for higher flow rates. In both flows, dP_e / *ds* (*s*) > 0, which grows as $Re_{\tau,0}$ increases. Although changes in the local pressure gradient with the streamwise position are relatively small, they exhibit a weak peak at $s / h_{in} \approx 0.78$, which amplifies for higher flow rates.

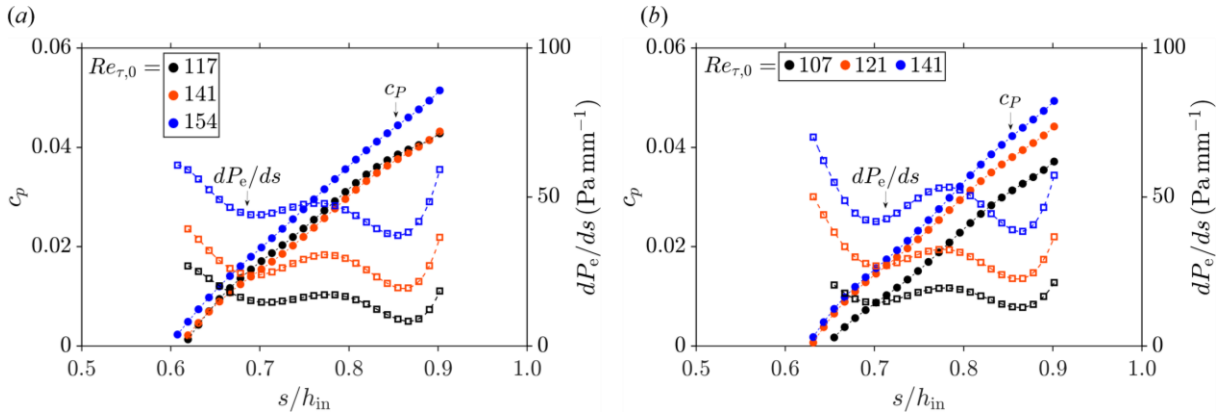

Figure 7-37 Wall-parallel variation of the pressure coefficient, c_p, and streamwise edge pressure gradient, dP_e / *ds*, for three different flow conditions of (*a*) 200 p.p.m. and (*b*) 400 p.p.m. PAM solution flows at the flat surface of the divergence region of the TG channel (downstream of the throat). The legend shows the Re_τ values of the ZPG flow (see Table 7-3 and Table 7-4).

Figure 7-38(*a*,*b*) illustrates the changes in the skin friction factor over the divergence region for the decelerating flows of the 200 p.p.m. and 400 p.p.m. solutions. Figure 7-38(*a*) depicts that

the flow with $Re_{\tau,0} = 117$ enters the studied domain with a friction factor relatively larger than its counterpart in the ZPG flow, which is predicted using Dean's correlation (see equation (6-6)). As flow advances in the divergence region, the friction factor gradually decreases until it reaches a minimum value of $c_{f,m} \approx 4 \times 10^{-3}$ at $s / h_{in} \approx 0.78$. After this point, the friction factor slowly enhances until it leaves the examined domain.

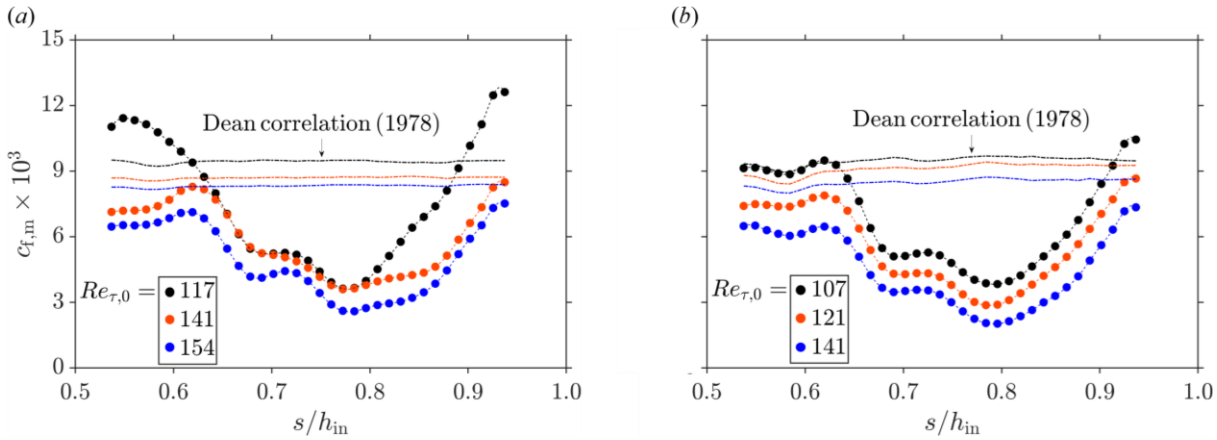

Figure 7-38 Wall-parallel variation of the skin friction factor based on the mean velocity, $c_{f,m}$ (see equation (2-26)), for three different flow conditions of (*a*) 200 p.p.m. and (*b*) 400 p.p.m. PAM solution flows at the flat surface of the divergence region of the TG channel (downstream of the throat). The legend shows the Re_τ values of the ZPG flow (see Table 7-3 and Table 7-4).

The $c_{f,m}$ profiles of the other two higher flow rates exhibit an almost similar trend of changes. Increasing $Re_{\tau,0}$ decreases the local friction factor over the tested decelerating domain. The 400 p.p.m. profiles, illustrated in Figure 7-38(*b*), behave similar to the 200 p.p.m. profiles. The two higher ones show nearly equal friction factors over the domain when compared at an equal flow rate. However, when the two flow concentrations are compared at an equal $Re_{\tau,0} = 141$, friction profiles of the 400 p.p.m. flow falls below that of the 200 p.p.m. flow, which indicates the stronger friction-reducing effect of the higher concentration.

Figure 7-39(*a*,*b*) shows the variation of the shape factor, H, in the 200 p.p.m. and 400 p.p.m. flows. The correlation of Pirozzoli (2014), given in equation (6-20), is used to predict the H values for fully developed ZPG flows at the local Re_m of the solutions and are plotted as dashed black lines. The obtained shape factors in both concentrations and flow conditions fall below the ZPG profiles. The 200 p.p.m. profiles oscillate in the range of $1.60 < H < 1.81$, and those of the 400 p.p.m. flow in $1.55 < H < 1.78$. The H profiles exhibit streamwise variations that might be due to the core region distortion. Since the classical definitions were utilized to determine displacement and momentum thickness, the rotationality was not accounted for in the evaluation of H.

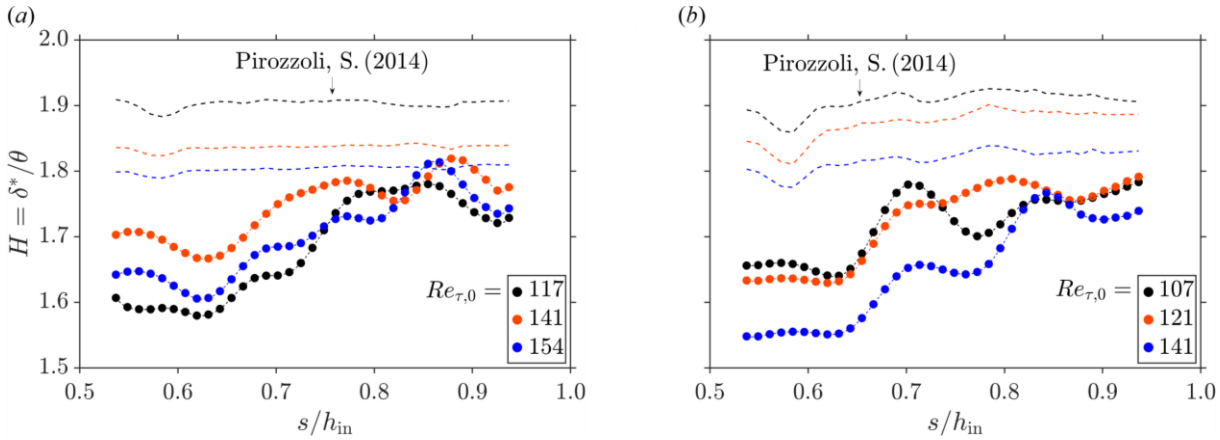

Figure 7-39 Wall-parallel variation of the shape factor, H, for three different flow conditions of (*a*) 200 p.p.m. and (*b*) 400 p.p.m. PAM solution flows at the flat surface of the divergence region of the TG channel (downstream of the throat). The legend shows the Re_τ values of the ZPG flow (see Table 7-3 and Table 7-4).

Re_τ profiles shown in Figure 7-40(*a*,*b*) vary with the streamwise position and indicate significant changes in this direction. They respond to the applied APG similar to the skin friction factor, shown in Figure 7-38(*a*,*b*). The results show that Re_τ also increases locally in both flows as the flow rate increases.

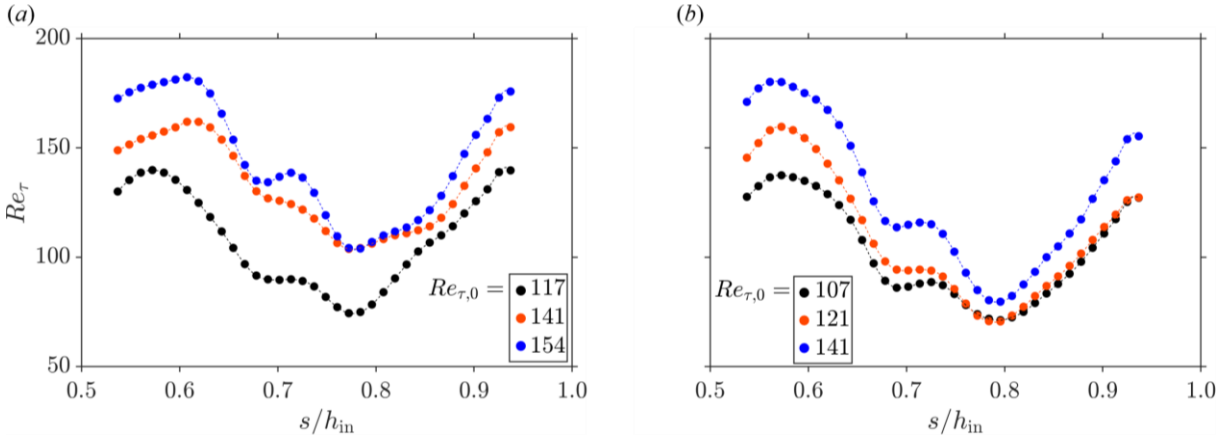

Figure 7-40 Wall-parallel variation of Re_τ for three different flow conditions of (*a*) 200 p.p.m. and (*b*) 400 p.p.m. PAM solution flows at the flat surface of the divergence region of the TG channel (downstream of the throat). The legend shows the Re_τ values of the ZPG flow (see Table 7-3 and Table 7-4).

Figure 7-41(*a*,*b*) illustrates the Re_θ profiles of the 200 p.p.m. and 400 p.p.m. solutions, each at three different flow rates. In contrast to Re_τ, Re_θ exhibits a weak dependency on the streamwise position. It increases from ≈ 200 in the flow with $Re_{\tau,0}$ = 117 to ≈ 380 in the flow with $Re_{\tau,0}$ = 154. In the 400 p.p.m. flow, Re_θ enhances from ≈ 200 to ≈ 280 as Re_τ increases from 107 to 141. At $Re_{\tau,0}$ = 141, Re_θ in the 200 p.p.m. flow is ≈ 14 % larger than in the 400 p.p.m. flow.

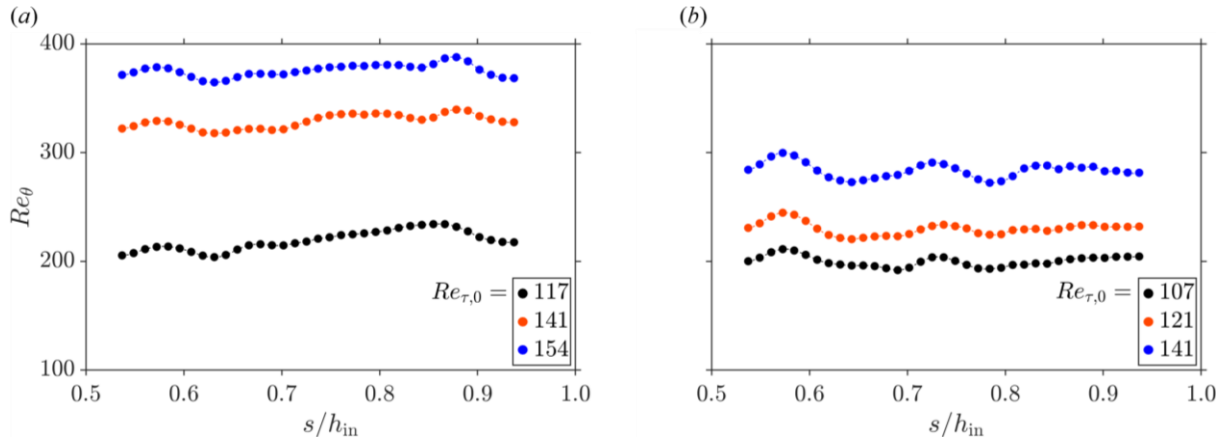

Figure 7-41 Wall-parallel variation of Re_θ for three different flow conditions of (*a*) 200 p.p.m. and (*b*) 400 p.p.m. PAM solution flows at the flat surface of the divergence region of the TG channel (downstream of the throat). The legend shows the Re_τ values of the ZPG flow (see Table 7-3 and Table 7-4).

Figure 7-42(*a*,*b*) illustrates the non-dimensional pressure gradient parameters K, Δ_p, and β for the decelerating 200 p.p.m. (top row) and 400 p.p.m. (bottom row) flows. All K profiles of the 200 p.p.m. flow fall below the critical value of $K = 3 \times 10^{-6}$, which, as proposed by Sreenivasan (1982), marks the onset of relaminarization. The largely negative values of K over the divergence region denote that flow is under strong APG. The K profiles of the 400 p.p.m. flow are also way below the critical K and show relatively larger negative values than the 200 p.p.m. flow.

The Δ_p profiles, shown in Figure 7-42(*b*), show that over the entire examined divergence region, $\Delta_p > -0.025$ in both solutions. The Δ_p values exhibit a prominent peak at $s / h_{in} \approx 0.78$, where the skin friction factor is minimum, and flow can separate. Although no separation was observed under the tested flow conditions, the peak values of Δ_p are indications of relatively large APG at this critical position. Results show that as the flow rate increases, the peak Δ_p amplifies. Also, the peak value of the highest flow rate in the 400 p.p.m. flow is ≈ 20 % larger than that in the 200 p.p.m. flow.

The β profiles show similar streamwise dependency as the Δ_p profiles. In both solutions flows, increasing the flow rate enhances the β values, exhibiting peaks where the friction factor is minimum. The results show that $\beta > 0$ for all flow conditions in both concentrations and increases to values as high as $\beta \approx 12$ at the peak of the highest tested flow rate.

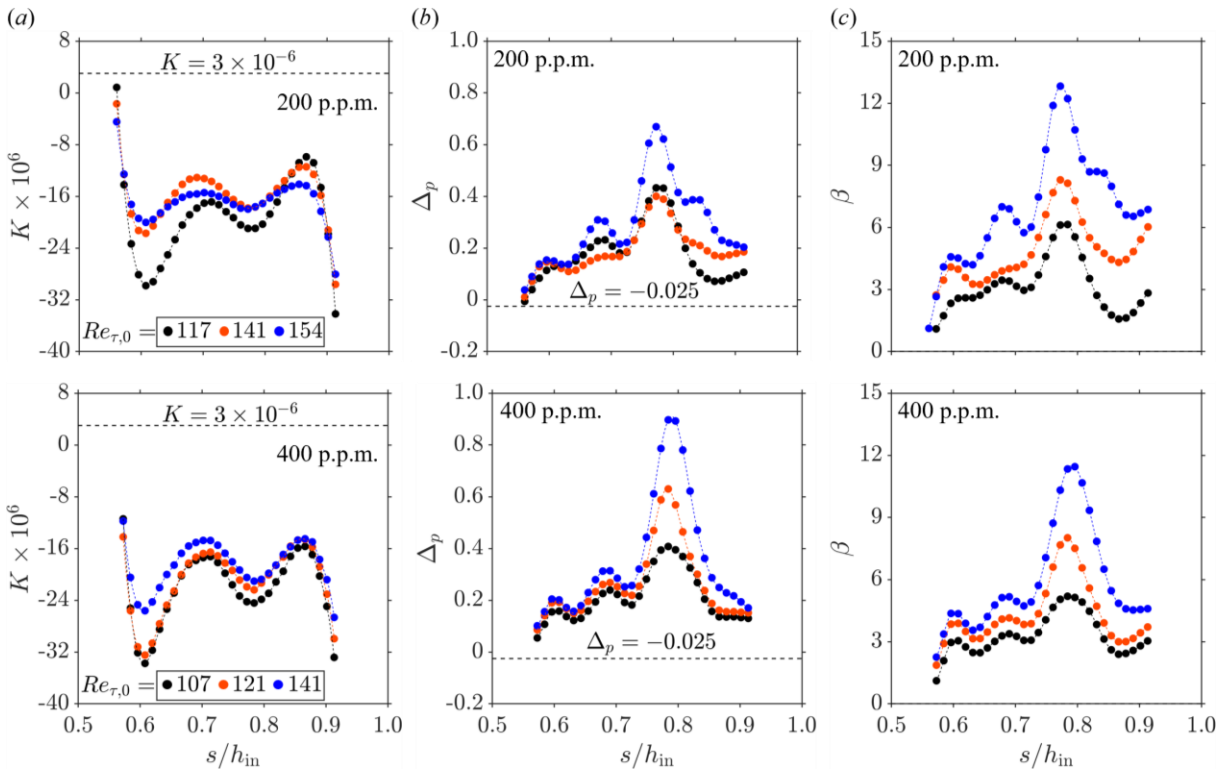

Figure 7-42 Streamwise variation of the (a) acceleration parameter, K (see equation (6-2)), (b) FPG parameter, Δ_p (see equation (6-1)), and (c) Rotta-Clauser pressure gradient parameter, β (see equation (6-4)), for three different flow conditions of 200 p.p.m. (top row) and 400 p.p.m. (bottom row) at the flat surface of the divergence region of the TG channel (downstream of the throat). The legend shows the Re_τ values of the ZPG flow (see Table 7-3 and Table 7-4).

7.5.2 Mean flow of the 200 p.p.m. PAM solution

Figure 7-43(a-c) illustrates the mean normalized streamwise velocity profiles of the 200 p.p.m. PAM solution flow under strong deceleration of varying strength. The inner- and outer-normalized results are presented in the left and right columns, respectively. The standard linear and logarithmic laws and the ultimate profile of Virk et al. (1970) for fully developed ZPG flows are also plotted on the figures for reference. Results are shown at eight streamwise positions on the top surface of the TG channel, with equal distancing over the examined flow field in the divergence region.

As Figure 7-43(a) shows, the 200 p.p.m. flow with $Re_{\tau,0} = 117$ enters the examined flow field with $\langle U_s \rangle^+(s)$ deviated below the log-law. As flow advances downstream, due to deceleration, the friction factor gradually decreases, and as a result, the velocity profiles diverge above the log profile and tend towards the ultimate profile. At $s / h_{\text{in}} = 0.79$, the position that was identified as the location of the minimum friction factor (see Figure 7-38b), $\langle U_s \rangle^+$ collapses on the ultimate profile over the outer layer of the BL.

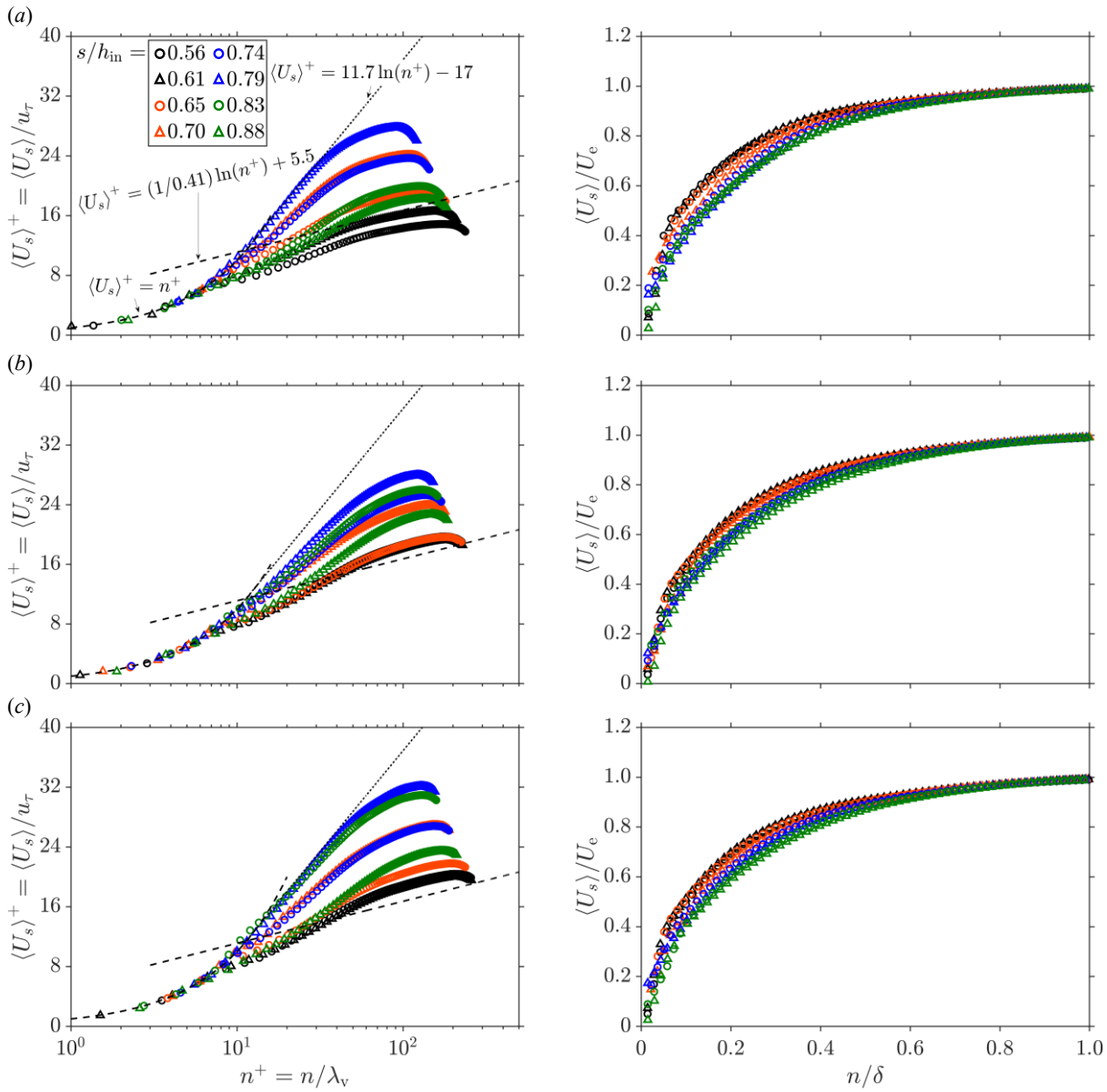

Figure 7-43 Wall-normal variation of the mean wall-parallel velocity profiles, normalized by the inner (left) and outer scales (right), at eight selected wall-parallel positions for decelerating 200 p.p.m. PAM solution flow over the flat surface of the TG channel's divergence region at (*a*) $Re_{\tau,0}$ = 117, (*b*) $Re_{\tau,0}$ = 141, and (*c*) $Re_{\tau,0}$ = 154.

As the solution flows downstream, the friction factor enhances slowly, which pushes the $\langle U_s\rangle^+$ profile down toward the log-law. For instance, at s / h_{in} = 0.83, the profile partially deviates below the logarithmic profile in the buffer layer and shifts above it in the outer layer, with a profile that does not indicate a logarithmic behavior. The flows with $Re_{\tau,0}$ = 141 and $Re_{\tau,0}$ = 154 show a similar trend of changes. At these higher flow rates, all $\langle U_s\rangle^+$ profiles deviate partially or fully above the standard log law and lie below or on the ultimate profile. Also, all the velocity profiles collapse in the viscous sublayer. The outer-normalized mean velocity profiles, shown in the right

column of Figure 7-43(*a-c*), indicate that all profiles almost collapse near the BL edge. From the wall to the middle of the BL, profiles differ in intensity depending on the APG's strength.

The mean normalized Reynolds shear stress profiles are illustrated in Figure 7-44(*a-c*). Figure 7-45(*a-c*) and Figure 7-46(*a-c*) represent the mean normalized wall-parallel, and wall-normal Reynolds stresses for the same flow conditions.

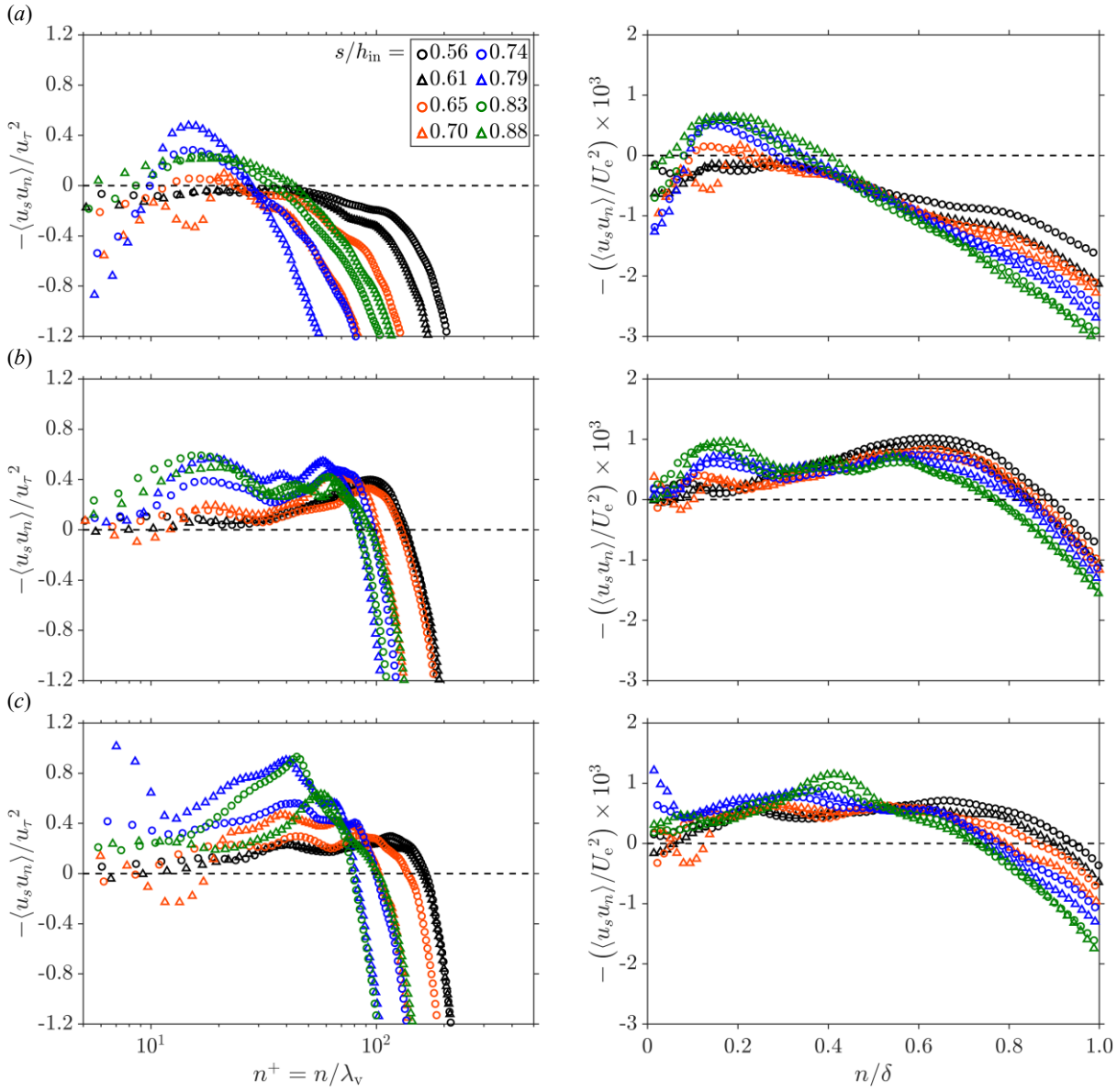

Figure 7-44 Wall-normal variation of the mean Reynolds shear-stress profiles, normalized by the inner (left) and outer scales (right), at eight selected wall-parallel positions for decelerating 200 p.p.m. PAM solution flow over the flat surface of the TG channel's divergence region at (*a*) $Re_{\tau,0}$ = 117, (*b*) $Re_{\tau,0}$ = 141, and (*c*) $Re_{\tau,0}$ = 154.

Figure 7-44(*a*) shows that $-\langle u_s u_n \rangle^+$ is negative over almost the entire BL at s / h_{in} = 0.61. The turbulence production is fully ceased at this position, and flow is no longer turbulent. As flow

advances to $s / h_{in} = 0.74$, $-\langle u_s u_n \rangle^+$ becomes partially positive in the outer layer, exhibiting a weak peak of ≈ 0.3. Similar to this position, the other $-\langle u_s u_n \rangle^+$ profiles downstream shift partially above zero but remain mainly negative. As $Re_{\tau,0}$ increases to 141, $-\langle u_s u_n \rangle^+$ profiles enhance and become positive over a large portion of the BL. Nevertheless, Reynolds shear stress is negative near the edge and acts counter gradient. The turbulence production rate enhances as $Re_{\tau,0}$ increases to 154. At this flow rate, the mean Reynolds shear stress profile at $s / h_{in} = 0.78$ lies above the other profiles and shows a peak at $n^+ \approx 40$.

The outer normalized profiles indicate that as flow advances downstream, $-\langle u_s u_n \rangle / U_e^2$ profiles intensify near the wall under APG. The $Re_{\tau,0} = 117$ flow profiles show noticeable peaks at n / δ at $s / h_{in} > 0.47$. At this flow condition and for almost all the streamwise positions, $-\langle u_s u_n \rangle < 0$ for $(n / \delta) > 0.5$. As the flow with $Re_{\tau,0} = 141$ enters the tested flow region at $s / h_{in} = 0.56$, Reynolds shear stress gradually increases in the wall-normal direction and indicates a peak at $(n / \delta) \approx 0.70$, after which it slowly decreases and gets negative near the edge. As flow advances downstream, a first peak appears near the wall at $(n / \delta) \approx 0.15$, and the second peak relaxes. At $s / h_{in} = 0.88$, the second peak almost vanishes, and the first peak shows a relatively large value. There is no sign of detectable peaks in the Reynolds shear stress profiles of the flow with $Re_{\tau,0} = 154$, except the profiles at $s / h_{in} = 0.83$ and $s / h_{in} = 0.88$, where a peak emerges at $(n / \delta) \approx 0.42$. The combination of the FPG and the viscoelastic effects of the polymer additives makes it challenging to rationalize the reasons behind the emergence of these peaks.

A comparison of the outer-normalized mean Reynolds shear stress profiles of the decelerating 200 p.p.m. solution flow with those under FPG (see Figure 7-27*a-c*) and ZPG (see Figure 7-9*c*) reveals several important physics of these flows. Strong APG intensifies strong Reynolds shear stresses and attenuates the weak ones to the extent that regions of negative $-\langle u_s u_n \rangle / U_e^2$ emerge in the BL that can noticeably spread through the outer layer. While as shown in Figure 7-27(*a-c*), the counter-gradient zones are rare in the FPG flows. The 200 p.p.m. flow enters the divergence region after experiencing a continuous FPG of varying strength over the convergence region, followed by a partial recovery over the throat region. Results show that with this pressure gradient history, APG could not fully recover the strong Reynolds shear stresses and fall at levels lower than the peaks of the ZPG flow. Compared to the decelerating water flow profiles, illustrated in Figure 6-37(*a-c*), it is obvious from Figure 7-44(*a-c*) that polymer additives strongly attenuate the

turbulence production in the 200 p.p.m. flow, even under strong APG, which has a destabilizing effect. Results show polymers cause a maximum reduction of ≈ 58 % in the 200 p.p.m. solution, compared with the decelerating pure water flow.

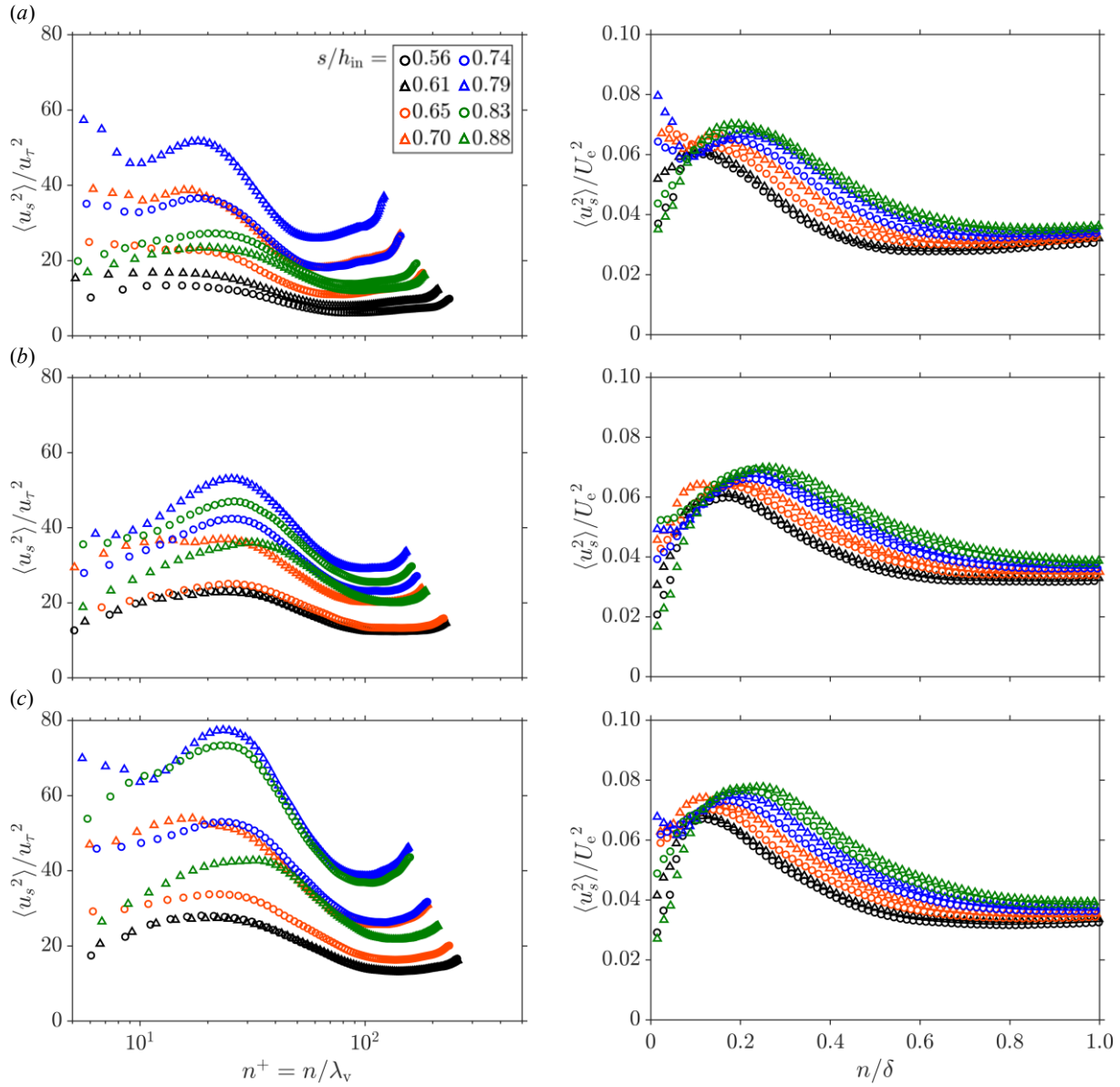

Figure 7-45 Wall-normal variation of the mean wall-parallel Reynolds stress profiles, normalized by the inner (left) and outer scales (right), at eight selected wall-parallel positions for decelerating 200 p.p.m. PAM solution flow over the flat surface of the TG channel's divergence region at (*a*) $Re_{\tau,0}$ = 117, (*b*) $Re_{\tau,0}$ = 141, and (*c*) $Re_{\tau,0}$ = 154.

The $\langle u_s^2\rangle^+$ profiles of the decelerating 200 p.p.m. PAM flow at $Re_{\tau,0}$ = 117 are shown in the left column of Figure 7-45(*a-c*). As flow advances in the divergence region, the wall-parallel turbulence intensity amplifies until s / h_{in} = 0.74, near the local minimum of $c_{f,m}$. After this point, the turbulence intensity attenuates as flow advances. As $\langle u_s^2\rangle^+$ amplifies, a recognizable 'knee

point' at $n^+ \approx 10$ and a peak at $n^+ \approx 20$ appear, which grows for intense $\langle u_s^2 \rangle^+$ profiles. The $\langle u_s^2 \rangle^+$ profiles of the other higher flow rates show similar behavior but at relatively higher levels. Also, the location of the peak seems to drift slightly away from the wall as the flow rate increases.

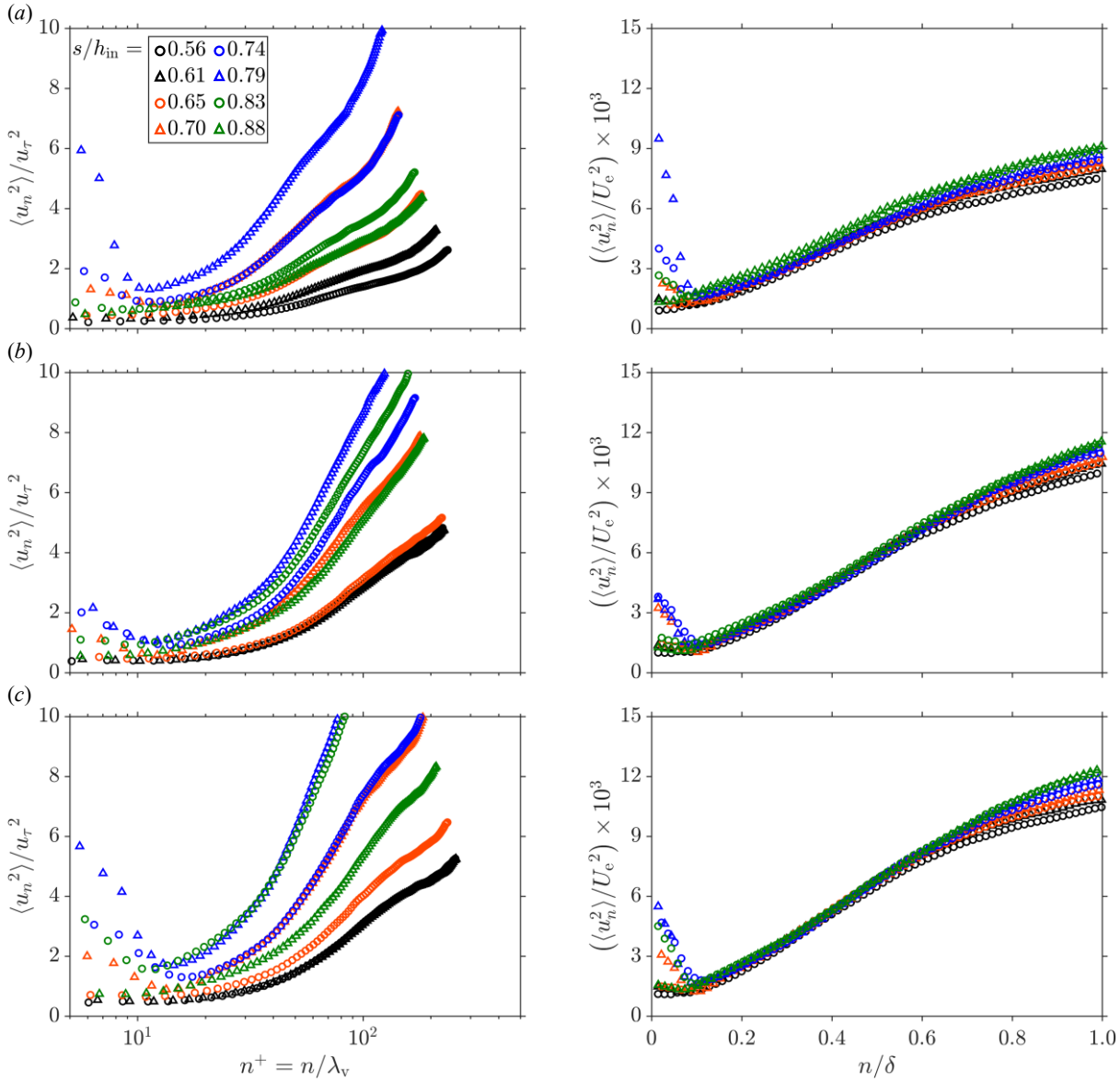

Figure 7-46 Wall-normal variation of the mean wall-normal Reynolds stress profiles, normalized by the inner (left) and outer scales (right), at eight selected wall-parallel positions for decelerating 200 p.p.m. PAM solution flow over the flat surface of the TG channel's divergence region at (*a*) $Re_{\tau,0} = 117$, (*b*) $Re_{\tau,0} = 141$, and (*c*) $Re_{\tau,0} = 154$.

The outer-normalized profiles, shown in the right column of Figure 7-45(*a-c*), show that wall-parallel turbulence intensity slowly amplifies as flow advances in the divergence region. This behavior is recognizable in the outer layer, in $0.2 < (n / \delta) < 0.8$. Near the edge, $\langle u_s^2 \rangle / U_e^2$ profiles

converge to almost an equal value. The results show that increasing the flow rate increases the wall-parallel turbulent activities marginally.

A comparison of the $\langle u_s^2 \rangle / U_e^2$ profiles of the decelerating 200 p.p.m. flow with those of the accelerating flow, shown in Figure 7-28(*a-c*), indicate that under APG, the outer layer's turbulence activities intensify, and variations over the BL are smoother than the FPG flow. Also, over the divergence region, the 200 p.p.m. flow show noticeably enhanced wall-parallel fluctuations compared to the pure water flow (see Figure 6-38*a-c*), and local changes of the profiles are smoother than their counterparts in the decelerating water flow.

Figure 7-46(*a*) shows that as the 200 p.p.m. flow with $Re_{\tau,0} = 117$ advances in the deceleration region, APG amplifies the $\langle u_n^2 \rangle^+$ values and shift the corresponding profiles towards higher levels. As flow passes the position of the local minimum skin friction factor at $s / h_{in} = 0.79$, the $\langle u_n^2 \rangle^+$ profiles relax. The intensification in the $\langle u_n^2 \rangle^+$ is accompanied by the appearance of a knee point at $n^+ \approx 12$, which bends the profile more as turbulence intensity enhances in the wall-normal direction. Increasing the flow rate squeezes the high intensity $\langle u_n^2 \rangle^+$ profiles in the normal direction and increase with a relatively steeper slope after the minimum point. Similar knee points were also observed in the FPG flows of the 200 p.p.m. flows, shown in Figure 7-29(*a-c*). The main difference is that in FPG profiles, the locations of the minimum points are farther from the wall, at $n^+ \approx 35$. Also, both accelerating (see Figure 6-28*a-c*) and decelerating (see Figure 6-39*a-c*) water flows show similar knee points for intense $\langle u_n^2 \rangle^+$ profiles, where they occur at $n^+ \approx 35$.

The outer-normalized profiles of $\langle u_n^2 \rangle / U_e^2$, shown in the right column of Figure 7-46(*a-c*), indicate that for all three tested flow conditions, profiles almost collapse at the median region of the outer layer. As discussed, profiles with $s / h_{in} > 0.65$ show minima in the wall region. Results show that APG enhances the wall-normal turbulent activities closer to the BL edge as flow advances downstream. A comparison of the $\langle u_n^2 \rangle / U_e^2$ profiles of the 200 p.p.m flow subjected to APG with those subjected to FPG (see Figure 7-29*a-c*) indicate that APG enhances the wall-normal fluctuations. Similarly, comparison with the water flow under APG (see Figure 6-39*a-c*) reveals that polymer additives intensify $\langle u_n^2 \rangle / U_e^2$.

The skewness and kurtosis profiles of the 200 p.p.m. flow, subjected to APG, are illustrated in Figure 7-47(*a-c*). In all tested flow rates, skewness is maximum near the wall, reaching values in $\mathcal{O}(1)$. The streamwise velocity fluctuations are negatively skewed in the outer layer, where they

reduce to values as low as ≈ -0.5. Over the BL, the skewness profiles of different positions almost collapse to a similar profile. The kurtosis profiles do not collapse and show deviations from each other. They oscillate in the range of $2.5 < \mu_4 < 4.5$ over the BL and do not converge to the normal value of $\mu_4 = 3$ anywhere in the divergence region.

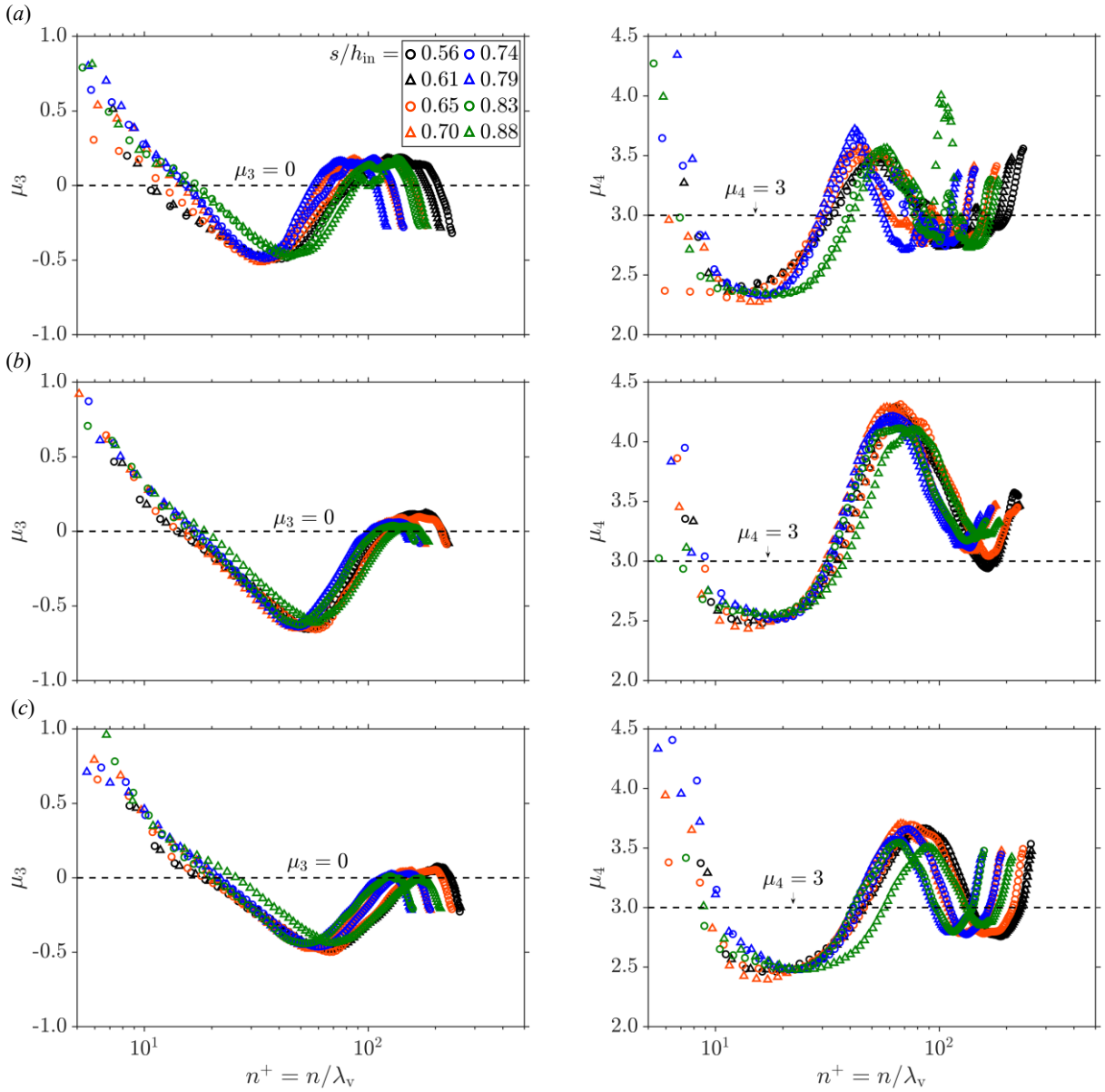

Figure 7-47 Wall-normal variation of the mean skewness, μ_3, profiles (left), and mean kurtosis, μ_4, profiles (right) at eight selected wall-parallel positions for accelerating 200 p.p.m. PAM solution flow over the flat surface of the TG channel's convergence region at (*a*) $Re_{\tau,0} = 117$, (*b*) $Re_{\tau,0} = 141$, and (*c*) $Re_{\tau,0} = 154$.

7.5.3 Mean flow of the 400 p.p.m. PAM solution

The normalized mean velocity profiles of the decelerating 400 p.p.m. flows are shown in Figure 7-48(*a-c*). The figures on the left and rights columns represent the inner- and outer-normalized results. Similarly, Figure 7-49(*a-c*), Figure 7-50(*a-c*), and Figure 7-51(*a-c*) illustrate the mean normalized Reynolds shear stress and wall-parallel and wall-normal Reynolds stress profiles for the same flow conditions. Figure 7-52(*a-c*) shows the skewness and kurtosis profiles.

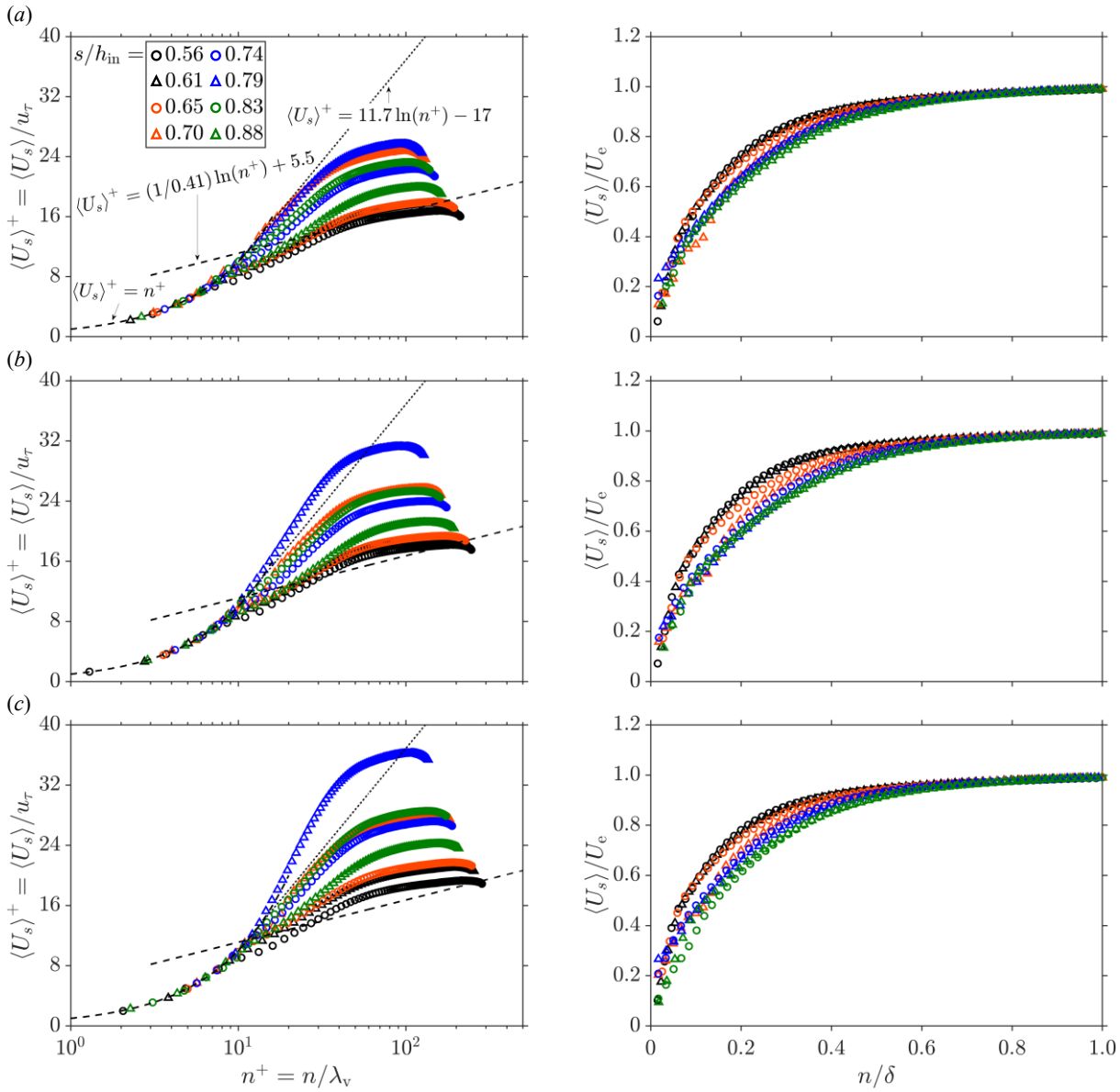

Figure 7-48 Wall-normal variation of the mean wall-parallel velocity profiles, normalized by the inner (left) and outer scales (right), at eight selected wall-parallel positions for decelerating 400 p.p.m. PAM solution flow over the flat surface of the TG channel's divergence region at (*a*) $Re_{\tau,0}$ = 107, (*b*) $Re_{\tau,0}$ = 126, and (*c*) $Re_{\tau,0}$ = 141.

Inner normalized velocity profiles, given in Figure 7-48(*a-c*), show that as the strength of the APG varies over the divergence region, the local velocity profiles deviate above the logarithmic law. A similar behavior was observed for the decelerating 200 p.p.m. flows, shown in Figure 7-43(*a-c*). Results show that as the flow rate increases, the local reduction of the friction factor elevates the velocity profiles toward the ultimate profile of Virk et al. (1970). At $s / h_{in} = 0.79$, where the friction factor is minimum, the velocity profiles of the flows with $Re_{\tau,0} = 126$, and $Re_{\tau,0} = 141$ deviate above the ultimate profile, with a slope higher than 11.7. The profiles do not exhibit logarithmic behavior in the tested flow conditions.

The outer-normalized velocity profiles, shown in the right column of Figure 7-48(*a-c*), denote that as flow advances in the divergence region, the profiles deviate from a canonical ZPG turbulent flow profile. They form smoother shapes in the buffer layer, indicating that the thickness of this layer increases, which is a common characteristic of drag-reduced flows.

Figure 7-49(*a*) shows that, at $Re_{\tau,0} = 107$, deceleration significantly damp the mean Reynolds shear stress over the BL to the extent that a considerable portion of the layer indicates negative $-\langle u_s u_n \rangle^+$ values. At $s / h_{in} = 0.70$, Reynolds shear stress is negative, and turbulent production is completely ceased. As the flow rate increases, only the zones near $s / h_{in} = 0.79$ show footprints of turbulent production in the buffer layer. The flow at this position exhibits a flat peak occurring at $n^+ \approx 25$, which shifts toward the wall to $n^+ \approx 16$, in the flow with $Re_{\tau,0} = 141$.

The outer-normalized profiles show that turbulent production enhances near the wall as flow advances in the divergence region but drifts to larger negative values in almost the entire outer layer. Results show that increasing the flow rate enhances the near-wall turbulence but generates stronger counter-gradient Reynolds shear stresses in the outer layer. In these regions with $-\langle u_s u_n \rangle / U_e^2 < 0$, flow is no longer turbulent.

The results show that compared to the 200 p.p.m. flow (see Figure 7-44*a-c*), the peak of the mean Reynolds shear stress profiles near the wall does not change significantly. Nevertheless, the counter-gradient zones in the wall-normal direction grow rapidly in the 400 p.p.m. solution, where there is no turbulent activity due to full relaminarization.

Figure 7-50(*a-c*) shows that $\langle u_s^2 \rangle^+$ profiles at streamwise positions with stronger APGs, such as at $s / h_{in} = 0.79$, noticeably elevate and deviate from other profiles. A second peak emerges for intensified profiles, which amplifies as the flow approaches the streamwise position $s / h_{in} = 0.79$.

The results show that as flow advances downstream of s / h_{in} = 0.79, APG weakens, friction factor increases, the $\langle u_s^2 \rangle^+$ profiles fall down to relatively lower intensities, and the second peak disappears. Flows at higher rates exhibit similar behavior, only with higher intensities.

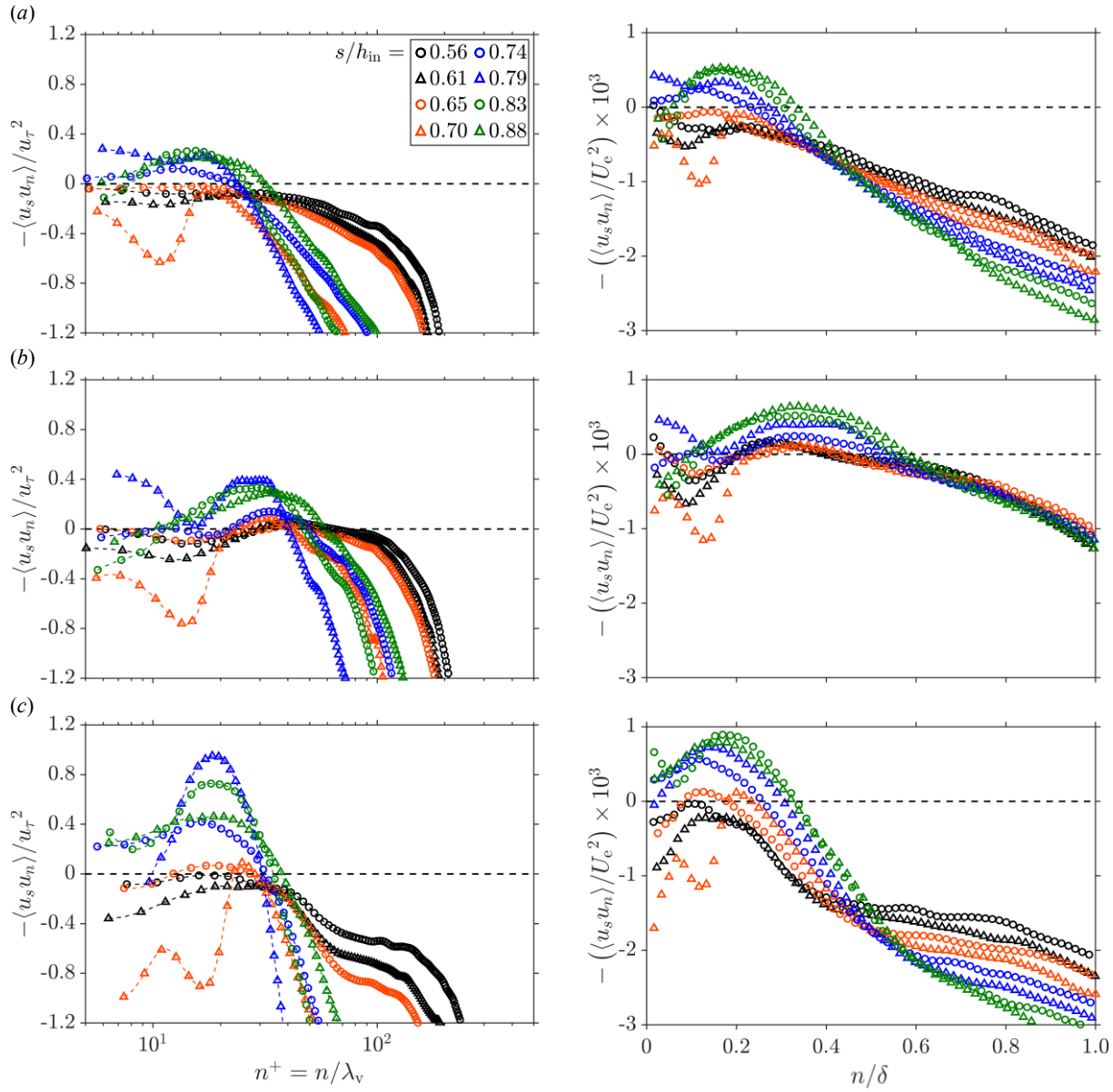

Figure 7-49 Wall-normal variation of the mean Reynolds shear-stress profiles, normalized by the inner (left) and outer scales (right), at eight selected wall-parallel positions for decelerating 400 p.p.m. PAM solution flow over the flat surface of the TG channel's divergence region at (*a*) $Re_{\tau,0}$ = 107, (*b*) $Re_{\tau,0}$ = 126, and (*c*) $Re_{\tau,0}$ = 141.

The outer-normalized wall-parallel Reynolds stress profiles, illustrated in Figure 7-50(*a-c*), denote that as flow advances in the divergence region, the wall-normal velocity fluctuations in the 400 p.p.m. solution flow intensify all over the BL. These profiles show that the maximum near-

wall peak occurs at s / h_{in} = 0.70, which amplifies as the flow rate increases. However, increasing the flow rate enhances $\langle u_s^2 \rangle / U_e^2$ negligibly over the outer layer.

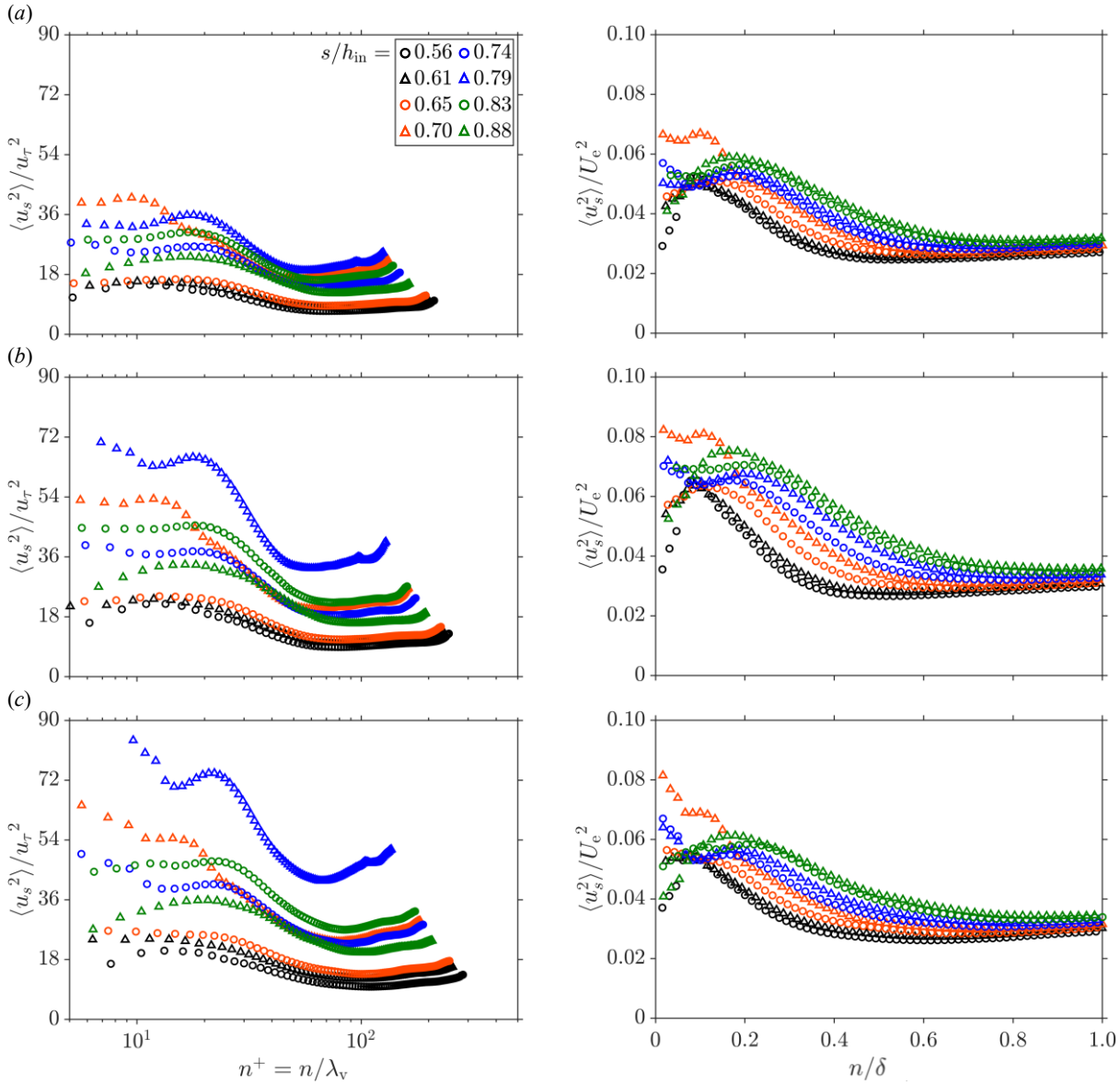

Figure 7-50 Wall-normal variation of the mean wall-parallel Reynolds stress profiles, normalized by the inner (left) and outer scales (right), at eight selected wall-parallel positions for decelerating 400 p.p.m. PAM solution flow over the flat surface of the TG channel's divergence region at (*a*) $Re_{\tau,0}$ = 107, (*b*) $Re_{\tau,0}$ = 126, and (*c*) $Re_{\tau,0}$ = 141.

A comparison of the $\langle u_s^2 \rangle / U_e^2$ profiles of the decelerating 400 p.p.m. flow with those of the decelerating 200 p.p.m. flow, shown in Figure 7-45(*a-c*), elucidates that increasing the polymer concentration has negligible impact on the enhancement of the streamwise fluctuations at different streamwise positions. Conversely, the profiles of the 200 p.p.m. flow indicate slightly higher

intensities than those of the 400 p.p.m. flow at an equal flow rate. Comparing the flows at an equal $Re_{\tau,0} = 141$, shows similar behavior.

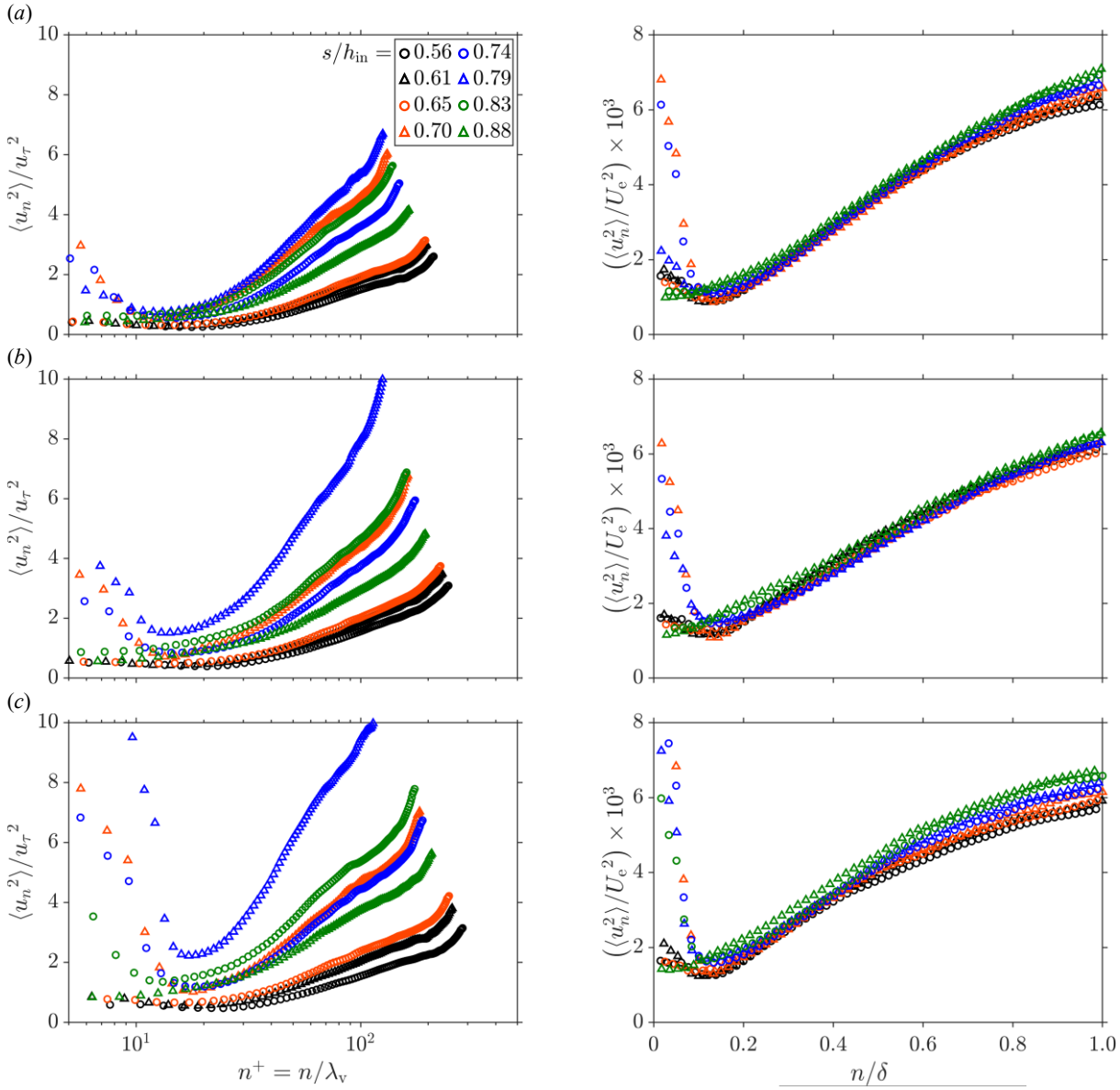

Figure 7-51 Wall-normal variation of the mean wall-normal Reynolds stress profiles, normalized by the inner (left) and outer scales (right), at eight selected wall-parallel positions for decelerating 400 p.p.m. PAM solution flow over the flat surface of the TG channel's divergence region at (*a*) $Re_{\tau,0} = 107$, (*b*) $Re_{\tau,0} = 126$, and (*c*) $Re_{\tau,0} = 141$.

The inner-normalized mean wall-normal Reynolds stress profiles of the decelerating flow of the 400 p.p.m. solution are illustrated in the right column of Figure 7-51(*a-c*). Similar to their counterparts in the 200 p.p.m. flow, shown in Figure 7-46(*a-c*), as the flow approaches the position of the minimum friction factor at $s / h_{\mathrm{in}} = 0.79$, the $\langle u_n^2 \rangle^+$ profiles elevate and knee points emerge at $n^+ \approx 14$. This minimum point does not exist for flows with lower intensities. For instance, the

profiles at $s / h_{in} = 0.61$ or $s / h_{in} = 0.88$ do not exhibit any knee points. The results show that increasing the flow rate squeezes the $\langle u_n^2 \rangle^+$ profiles in the wall-normal direction and causes steeper slopes of changes over the BL.

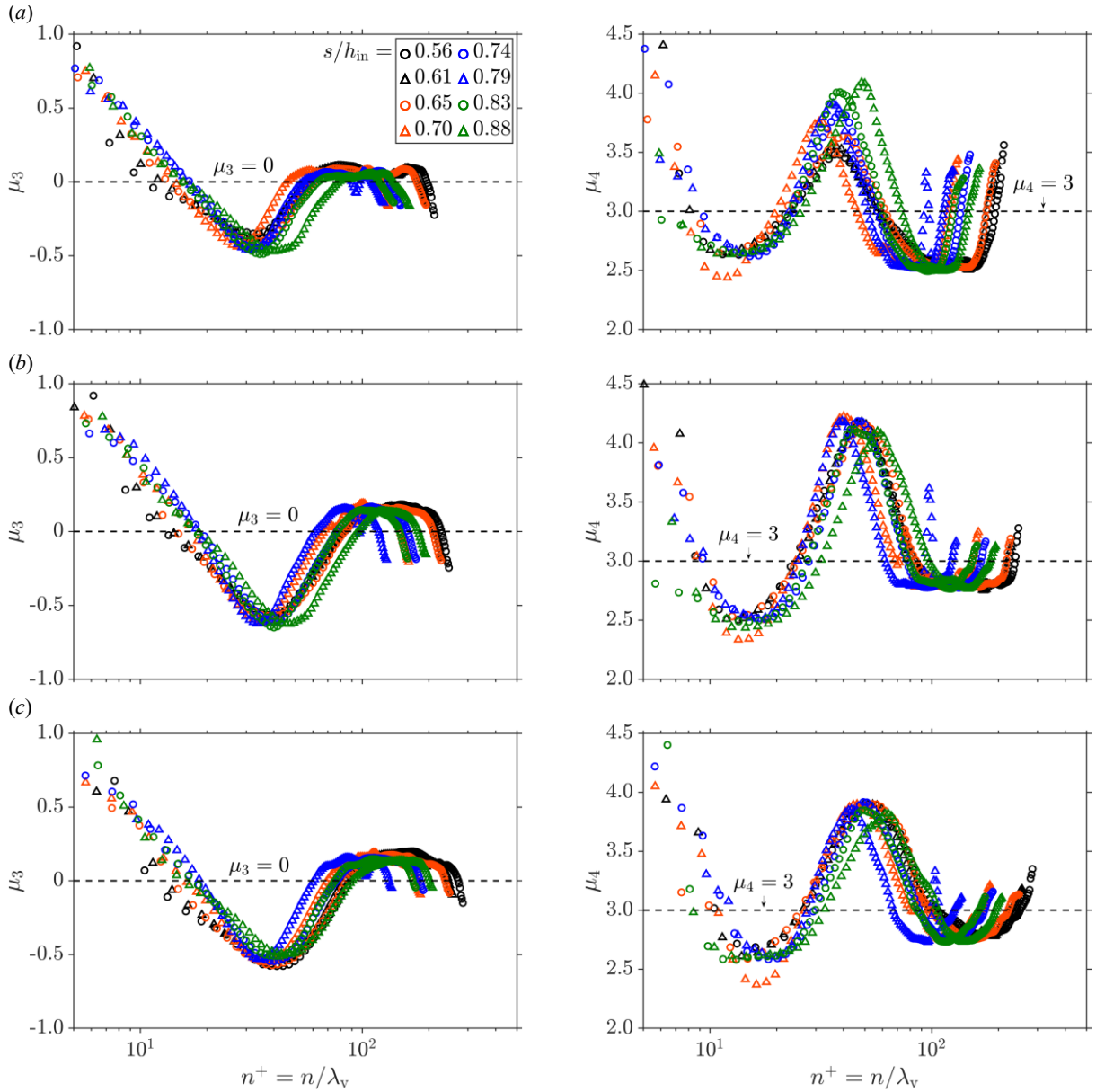

Figure 7-52 Wall-normal variation of the mean skewness, μ_3, profiles (left), and mean kurtosis, μ_4, profiles (right) at eight selected wall-parallel positions for decelerating 400 p.p.m. PAM solution flow over the flat surface of the TG channel's divergence region at (*a*) $Re_{\tau,0} = 107$, (*b*) $Re_{\tau,0} = 126$, and (*c*) $Re_{\tau,0} = 141$.

The outer-normalized wall-normal Reynolds shear stress profiles also exhibit knee points for profiles near $s / h_{in} = 0.79$. The $\langle u_n^2 \rangle / U_e^2$ profiles show relatively similar values over the outer layer for flow with $Re_{\tau,0} = 107$, but they deviate from each other near the BL edge. Flows at higher flow

rates denote a similar trend of changes. As flow advances in the divergence region, APG enhances $\langle u_n^2 \rangle / U_e^2$ in the outer layer.

Compared to the 200 p.p.m. flow under APG (see Figure 7-46*a*-*c*), the 400 p.p.m. solution considerably attenuates the wall-normal fluctuations, even under strong APG. In the 200 p.p.m. flow, almost independent of the flow rate, $\langle u_n^2 \rangle / U_e^2$ at $s / h_{in} = 0.70$ changes from a minimum of $\approx 2.0 \times 10^{-3}$ at the knee point to a maximum of $\approx 12 \times 10^{-3}$ near the edge. At the same streamwise position, $\langle u_n^2 \rangle / U_e^2$ gradually increases from $\approx 1.5 \times 10^{-3}$ to $\approx 6 \times 10^{-3}$ at the edge. The difference is a maximum of $\approx$ 50 % in the wall-normal turbulent activities.

Figure 7-52(*a*-c) shows that in any streamwise position, the skewness profile decreases almost linearly from $\approx$ 1 near the wall to a minimum value of $\approx$ -0.5 at $n^+ \approx 40$. After this point, it increases almost linearly toward relatively small positive values. None of the profiles converges to the standard value of $\mu_3 = 0$ over the BL. The kurtosis profiles indicate a minimum of $\approx$ 2.5 at $n^+ \approx 14$ and a peak of $\approx$ 4.0 at $n^+ \approx 40$ at almost any streamwise position in the divergence region.

7.6. Conclusion

In this Chapter, the combined effects of drag-reducing polymers, pressure gradients of varying strength and sign, and local convex and concave curvatures were experimentally investigated. PIV was utilized to investigate the flow field at three critical regions over the channel's convergence, divergence, and straight regions. Over the convergence region, the non-Newtonian flow was subjected to FPG of varying strength, and in the divergence region, a continuous APG of varying strength was applied to the flow. In the straight channel, a fully developed ZPG flow was investigated. The flow fields were studied at three different flow rates in two semi-dilute PAM solutions with concentrations of 200 p.p.m. and 400 p.p.m. and the dynamics of the mean velocity fields and turbulent statistics are discussed in detail.

In each case, using 11 000 pairs of PIV images in calculating the mean fields ensured statistically converged results. Uncertainty analysis showed that the random noises of the mean Reynolds shear stress could be as high as ≈ 11 % of its local value. Random noises of the wall-parallel and wall-normal Reynolds stresses were at a maximum of 2.5 % of their local value.

A maximum DR of 30.4 % and 38.6 % were obtained in the 200 p.p.m. and 400 p.p.m. solution flows at the highest tested flow rate. The results show that the mean velocity profiles of the ZPG PAM flow deviate above the standard logarithmic law, with slopes relatively higher than $\kappa^{-1} \approx 2.44$. As the flow rate or the solution concentration increases, the velocity profile tends toward the ultimate profile of Virk et al. (1970). Near the wall, the measured velocities follow the linear viscous law, which was resolved for $n^+ > 2$. Maximum drag reduction was not achieved in any of the tested ZPG flows.

The mean Reynolds shear stress and wall-normal Reynolds stress are strongly attenuated in the PAM solutions, and the wall-parallel Reynolds stress remains almost at the same level as the water flow when normalized using the Zagarola-Smits velocity (Zagarola and Smits, 1998). The outer-normalized Reynolds stress profiles show that for the highest flow rate, mean Reynolds shear stress relaxes in the PAM solutions relative to water, and wall-parallel Reynolds stress significantly enhances. The outer-scaled wall-normal Reynolds stress is mitigated near the wall and enhanced in the outer layer, compared to the ZPG water flow.

The acceleration of the non-Newtonian PAM solutions over the convergence region, combined with the local wall curvature effects, modified the skin friction factor over this region. The results

show that, generally, FPG increases the friction factor, convex curvature stabilizes, and concave curvature destabilizes the flow. Nevertheless, the combination of these effects leads to a streamwise varying friction factor profile. The results show that increasing the solution concentration to 400 p.p.m. or increasing the flow rate decreases the local friction significantly.

Evaluation of the non-dimensional pressure gradient parameters K, Δ_p, and β show that their magnitudes vary with position over the acceleration region, where $K \gg 3 \times 10^{-6}$, $\Delta_p \ll -0.025$, and $\beta \ll 0$. Hence, the flow was fully relaminarized in most of the convergence region. Increasing the flow rate or PAM solution resulted in stronger negative β values, which could grow to a negative peak of $\beta \approx -30$ in the highest flow rate of the 400 p.p.m. flow.

Inner-normalized velocity profiles of the 200 p.p.m. accelerating PAM flows show that depending on the local strength of the FPG and wall curvature, the profile deviates partially or fully below or above the logarithmic law, with a slope almost similar to that of the standard log-law. Under strong FPG in the inclined flat wall region, the inner-normalized velocity profiles of the 400 p.p.m. flow were elevated above the ultimate profile. These profiles did not show a logarithmic shape.

Comparing the mean Reynolds shear stress profiles of the accelerating 200 p.p.m. flow with its corresponding ZPG flow indicates that the peak of the outer-normalized Reynolds shear stresses can reduce up to 70 % under FPG. Thee 200 p.p.m. FPG flow shows a maximum reduction of $\approx$ 78 % in the mean outer-normalized Reynolds shear stress compared to the FPG water flow. Under the FPG, parts of the convergence region exhibit negative Reynolds shear stress zones, where flow is no longer turbulent. Apparent attenuation of the turbulence production in the 400 p.p.m. FPG flow generates relatively large zones of negative Reynolds shear stress. Regions of positive shear are significantly smaller than those in the 200 p.p.m. flow, and the wall-parallel and wall-normal Reynolds stresses in the 400 p.p.m. flow are relatively less intense.

The skin friction factor varies over the divergence zone due to the applied APG. The magnitudes of the local friction factors are relatively lower than those in the FPG. In the deceleration region, $K \ll 3 \times 10^{-6}$, $\Delta_p \gg -0.025$, and $\beta \gg 0$, where can rise to values as high as $\beta \approx 12$ in the highest tested flow rate.

The mean velocity profile of the decelerating 200 p.p.m. flow deviates above the log-law at positions where the friction factor is smaller than its ZPG equivalent and indicates slopes almost

equal to that of the ultimate profile. Results indicate that at local positions with the minimum friction factor, the velocity profile collapses to the ultimate profile. At a similar position and the highest flow rate, the velocity profile of the 400 p.p.m. flow elevates above the ultimate profile.

APG intensifies the stronger mean Reynolds shear stresses in both PAM solutions and attenuates the weaker ones to the extent that negative counter-gradient zones emerge over the BL, where turbulence activities are severely ceased. Even under the destabilizing effect of APG, the turbulence production reduces by a maximum of ≈ 58 % in the PAM solutions compared to the water flow at a similar flow rate. Compared to the APG water flow, the semi-dilute solutions indicate intensified wall-parallel and wall-normal fluctuations.

8. Concluding remarks and future work

The design of the next generation of inflow control devices and improving the production efficacy of a SAGD process requires an in-depth understanding of the flow phenomena occurring in these environments. The relatively large pressure drop over the control devices generally leads to a chaotic cavitating turbulent flow that hinders oil production and causes severe damage to the equipment by eroding the material.

In this research study, it was hypothesized that drag-reducing polymer additives could reduce the cavitation intensity by suppressing the chaotic pressure fluctuations in the flow field and modifying the turbulence of the developing BLs over the wall surfaces. To examine this hypothesis, a closed-loop flow facility was developed in the Applied ThermoFluids Lab at the University of Alberta. Two test channels were designed: (1) a converging-diverging channel, with a 60° convergence to 12° divergence and a throat size of 2 mm. (2) a channel with a bump geometry resembling the converging-diverging wall profile with a width-to-height ratio of more than 7.

An optical setup was developed based on high-speed imaging and microscopic PIV. The instantaneous cavitation structures were studied on the central plane of the channel in a wide range of flow conditions, $2 \times 10^4 < Re_{th} < 5 \times 10^4$ and $3 < \sigma < 9$, covering the onset to super-cavitation regimes. Pure water and four different semi-dilute PAM solutions in water, with concentrations of 50 p.p.m. to 400 p.p.m., were tested. The two-dimensional turbulent flow was examined in the bumped channel under zero, favorable, and adverse pressure gradients and local curvature effects using microscopic PIV. Pure water, 200 p.p.m. and 400 p.p.m. PAM solution flows were used as operating fluids. They were tested at three different flow rates, close to the cavitation onset flow rate of the converging-diverging channel.

The results show that the flow statistics were fully converged. A detailed uncertainty analysis was performed on the main instantaneous and mean flow parameters. The bias uncertainty of the instantaneous wall-parallel velocity measurements was ≈ 7 %. The mean uncertainty of the instantaneous velocity fields, determined using the correlation statistics method of Wieneke (2015), showed that near-wall uncertainties could be as high as 4.5 %, and far from the wall, it reduces to values close to 2 % of the mean local wall-parallel velocity. The measurement uncertainties of the mean streamwise velocity field were at most 0.2 % of the local mean velocity.

Rheological measurements were performed on samples taken directly from the flow loop using a rotational rheometer with controlled shear rates. The results suggest that concentrations less than 100 p.p.m. had constant viscosities in the range of the tested shear rates, with viscosities of 5-20 % more than the pure water. Solutions with $C_s \geq 200$ p.p.m. indicated shear-thinning behavior with infinite shear viscosities relatively larger than the pure water flow.

Numerical simulations showed that the wall shear stress at the throat could be as high as 1000 Pa, where the wall shear viscosity is very close to its infinite value. This result suggests that viscosity plays a minor role in the cavitation reduction mechanism of polymer additives. Nevertheless, in the turbulent flow tests over the bump profile, the wall shear stresses estimated from the velocity data were relatively small. Therefore, the Correau-Yasuda model (Yasuda et al., 1981), fitted to the measured viscosity data, was utilized to evaluate the wall shear viscosities of each PAM solution.

8.1. Cavitation reduction phenomenon

Visualization of the temporal evolution of vapor ratio fields on the channel's midspan revealed that adding PAM additives would delay the cavitation onset to higher flow rates. Micro collapsing bubbles densely populated the edge of cloud cavitation in the pure water flow. In contrast, in PAM solutions, wall cavities grew in the form of streaky structures in the direction of the core liquid flow, with relatively smoother interfaces.

Collapse and growth levels in cavitating water and solution flows were determined by calculating the fluctuations of the vapor-ratio time variance. The results indicated that the collapse and growth process of cavitation bubbles in water occurred at relatively higher levels as the flow rate and the pressure drop over the nozzle increased. The maximum level at which the cavitation bubbles collapsed in the flow of the 400 p.p.m. solution was 60 % lower than the collapse level in the pure water at the highest tested Re_{th}. This result elucidates that the attenuation of the extreme collapse and growth fluctuations in a cavitating flow field is one of the main mechanisms polymer molecules reduce cavitation.

Spectral analysis of the measured downstream pressure fluctuations showed that the Strouhal number peaked suddenly at the cavitation inception and gradually reduced for higher Re_{th} and smaller σ. The inception St reduced significantly in the PAM solutions, which is ≈ 70 % relative to the water in the 400 p.p.m. solution.

8.2. Acceleration and deceleration of the Newtonian flow

Microscopic PIV was utilized to investigate developing turbulent BLs subjected to continuous pressure gradients of various signs and strengths over a converging-diverging bump in a rectangular channel flow. The flow was mainly studied in three different regions: (1) straight channel region, sufficiently far from the converging-diverging bump profile, with fully developed ZPG flow, (2) convergence region, where the flow was subjected to a continuous effect of FPG of varying strength and wall curvature, and (3) divergence region with a decelerating flow, where APG of varying strength altered the flow turbulence locally. The mass flow rate was kept constant during each test, and flow fields were studied at three different inlet Reynolds numbers.

The measured mean wall-parallel velocity profiles followed the linear profile in the viscous sublayer and collapsed to the standard logarithmic profile in the outer layer. The applied velocimetry method resolved the mean velocity fields for wall positions with $n^+ > 2$. The $\langle u_s^2 \rangle^+$ profiles exhibited peaks at $n^+ \approx 13$, consistent with previous reports of similar canonical 2D ZPG turbulent channel flow. For the tested flow conditions, the sweep events dominated the ejection events in the near-wall region, and far from the wall, ejection motions dominated.

The evaluated skin friction factor profiles over the convergence and divergence regions showed that overall, FPG increased, and APG decreased the local friction factors. Nevertheless, it was found that the friction factor varied over the studied channel regions, even when the flow was fully under APG or FPG. The K values were at least an order of magnitude larger than the critical value of $K = 3 \times 10^{-6}$, and Δ_p values were significantly lower than $\Delta_p = -0.025$ in the FPG flows. These large magnitudes of pressure gradient parameters signified that the FPG flow might have transferred to a fully relaminarized regime in the convergence region. However, the mean turbulent statistics exhibit damped turbulent activities relative to a ZPG flow but with finite non-zero values.

Conversely, the decelerating flow in the divergence region showed varying negative values of K, which were significantly lower than the critical value of $K = 3 \times 10^{-6}$. Negative K values with large magnitudes indicated that the flow in the divergence region experienced a strong APG of varying strength. Although no separation occurred over the APG region in the tested flow scenarios, over the entire domain, $\Delta_p \gg -0.025$ and its profile exhibited noticeable peaks at positions with strong APG, where flow tended to separate.

All measured inner normalized mean velocity profiles of the pressure gradient flow regions collapsed to the linear line of $\langle U_s \rangle^+ = n^+$ in the viscous sublayer and deviated from the standard logarithmic law in the outer layer. Depending on the local strength of the pressure gradient and wall shear stress, the profile deviated partially or fully below or above the log law. At positions with a stronger FPG in the convergence region or with a weaker APG in the divergence region, the local friction factor increased; as a result, velocity profiles were pushed partially or fully below the logarithmic profile, and their slope became smaller than κ^{-1}. Conversely, for a position with a milder FPG or stronger APG, the local friction factor decreased, which caused the inner-normalized velocity profiles to deviate significantly above the logarithmic law profile. These profiles exhibited slopes similar to that of a ZPG, i.e., $\kappa^{-1} = 2.44$.

The inner normalized mean Reynolds shear stress profiles were amplified as the skin friction factor decreased in the convergence region, even when the flow was fully subjected to a continuous FPG. Compared to a ZPG flow, the peak of the $-\langle u_s u_n \rangle^+$ profiles of the FPG flow were relatively larger at positions with smaller friction factors. Conversely, the outer normalized profiles showed that FPG relaxed the Reynolds shear stresses compared to ZPG flows. This relaxation improved as the flow rate increased or FPG strengthened. Similar to Reynolds shear stress profiles, as FPG strength varied over the convergence region, the mean $\langle u_s^2 \rangle^+$ and $\langle u_n^2 \rangle^+$ profiles showed different levels of intensity levels. The friction factor decreased at positions with a milder FPG, and the resultant normalized profiles were elevated. In contrast, when normalized by the outer scales, wall-parallel and wall-normal Reynolds stress profiles of the FPG flow indicated amplifications in their intensity relative to their corresponding ZPG flows.

When normalized by the local outer scales, the mean Reynolds shear stress profiles showed similar intensity levels to that of a ZPG flow but with comparably flattened profiles over the outer layer. Similar to the Reynolds shear stress profiles, inner normalized profiles of $\langle u_s^2 \rangle$ and $\langle u_n^2 \rangle$ were significantly amplified under strong APG. However, when normalized by outer scales, these stresses showed relatively higher intensities than the ZPG flows, with peak values significantly higher than their counterparts in a ZPG flow at a similar mass flow rate. The $\langle u_n^2 \rangle$ profiles exhibited minimum points at positions subjected to APG in the divergence region, which might indicate the initiation of an internal layer in the inner layer. The minimum peak drifted away from the wall and finally disappeared as the APG weakened and the skin friction factor increased.

8.3. Impact of pressure gradient on semi-dilute PAM flows

A maximum *DR* % of 30.4 % and 38.6 % were obtained in the 200 p.p.m. and 400 p.p.m. solution flows at the highest tested flow rate, but maximum drag reduction was not achieved in any of the tested ZPG flows. The mean velocity profiles of the ZPG PAM flows deviated above the standard log law, with slopes relatively higher than $\kappa^{-1} \approx 2.44$. As the flow rate or the solution concentration increased, the velocity profile approached the ultimate law of Virk et al. (1970).

The mean Reynolds shear stress and wall-normal Reynolds stress were strongly attenuated in the PAM solutions, and the wall-parallel Reynolds stress remained almost at the same level as the water flow when normalized using the Zagarola-Smits velocity (Zagarola and Smits, 1998). The outer-normalized Reynolds stress profiles showed that for the highest flow rate, mean Reynolds shear stress relaxed in the PAM solutions relative to water, and wall-parallel Reynolds stress significantly enhanced. The outer-scaled wall-normal Reynolds stress was mitigated near the wall and enhanced in the outer layer, compared to the ZPG water flow.

Over the acceleration region $K \gg 3 \times 10^{-6}$, $\Delta_p \ll -0.025$, and $\beta \ll 0$. Hence, the flow was fully relaminarized in most of the convergence region. The effects of the acceleration and local wall curvature altered the skin friction factor over this region. The results show that, generally, FPG increased the friction factor, convex curvature stabilized, and concave curvature destabilized the flow. Nevertheless, the combination of these effects led to a streamwise varying friction factor profile. The results showed that increasing the solution concentration to 400 p.p.m. or increasing the flow rate decreased the local friction significantly.

Inner-normalized velocity profiles of the 200 p.p.m. accelerating flows show that depending on the local strength of the FPG and wall curvature, the profile deviated partially or fully below or above the logarithmic law, with a slope almost similar to that of the standard log-law. Under strong FPG in the inclined flat wall region, the inner-normalized velocity profiles of the 400 p.p.m. flow were elevated above the ultimate profile. These profiles did not show a logarithmic shape.

Comparing the mean Reynolds shear stress profiles of the accelerating 200 p.p.m. flow with its corresponding ZPG flow indicated that the peak of the outer-normalized Reynolds shear stresses could reduce up to 70 % under FPG. The 200 p.p.m. FPG flow showed a maximum reduction of $\approx$ 78 % in the mean outer-normalized Reynolds shear stress compared with the FPG water flow. Under the FPG, parts of the convergence region exhibited negative Reynolds shear stress zones,

where the flow was no longer turbulent. Substantial attenuation of the turbulence production in the FPG 400 p.p.m. flow generated relatively large negative Reynolds shear stress zones. Regions of positive shear were significantly smaller than those in the 200 p.p.m. flow, and the wall-parallel and wall-normal Reynolds stresses in the 400 p.p.m. flow were relatively less intense.

The skin friction factor varied over the divergence zone due to the applied APG. The magnitudes of the local friction factors were relatively lower than those in the FPG. In the deceleration region, $K \ll 3 \times 10^{-6}$, $\Delta_p \gg -0.025$, and $\beta \gg 0$. The mean velocity profile of the decelerating 200 p.p.m. flow deviated above the log-law at positions where the friction factor was smaller than its ZPG equivalent and indicated slopes almost equal to that of the ultimate profile, i.e., 11.7. Results indicate that the velocity profile collapsed to the ultimate profile at local positions with the minimum friction factor. At a similar position and the highest flow rate, the velocity profile of the 400 p.p.m. flow elevated above the ultimate profile.

APG intensified the stronger mean Reynolds shear stresses in both PAM solutions and attenuated the weaker ones to the extent that negative counter-gradient zones emerged over the BL, where turbulence activities were severely ceased. Even under the destabilizing effect of APG, the turbulence production was reduced by a maximum of ≈ 58 % in the PAM solutions compared to the water flow at a similar flow rate. Compared to the APG water flow, the semi-dilute solutions indicate intensified wall-parallel and wall-normal fluctuations.

This study elucidated that adding long-chain polymers such as PAM to the flow can be utilized as an efficient passive cavitation-controlling method in industrial applications such as SAGD. The presented novel methodology for quantitative analysis of the cavitation reduction mechanisms from high-speed images was unique. Consistent with previous studies, the PAM additives generated significant reductions in turbulent drag in the fully developed ZPG PAM solutions. Under strong pressure gradients and wall curvature effects, flows indicated significant streamwise dependence. Wall-normal variations of mean flow statistics were reported at different streamwise positions of the accelerating and decelerating Newtonian water, and non-Newtonian PAM flows using microscopic PIV. The high spatial resolution and accuracy of the obtained results make them unique in their type, which can be used to validate newly developed numerical models. Also, for the first time, the viscoelastic polymer solutions were examined under pressure gradient effects, which was another novelty of the current research work.

8.4. Future work

In the past decades, there has been a wealth of studies devoted to understanding the physics of Newtonian cavitating and turbulent flows under various conditions to meet the needs of the growing fluid-based technologies in turbomachinery, marine, and aerospace industries. However, little is known about the dynamics of non-Newtonian flows, such as viscoelastic and viscoplastic flows, in terms of their turbulence drag or cavitation intensity reduction mechanisms. Hence, two suggestions are made here as possible research topics in this area, with the hope that the outcomes will start to fill out the corresponding gap in this part of the knowledge body.

8.4.1 Cavitation growth and collapse process in viscoelastic flows

All large-scale cavitation structures growing or shrinking in a cavitating flow start to emerge at an initial position in the flow domain. It is important to scrutinize the physics of this initial growth and the related length and time scales in non-Newtonian flows when the nuclei appear at the wall surface or in the bulk flow. Studying this phenomenon is challenging both experimentally and numerically. The experiments require ultra-high-speed cameras with speeds of at least millions of frames per second and reasonable resolutions to capture the ultra-fast collapse process synchronized with the flow. Simulation of this phenomenon in a non-Newtonian flow, as a priori, requires a validated constitutive equation to account for the strain-rate dependency of the flow's viscosity. Coupling the compressible solvers and stabilizing the solution would be challenging.

8.4.2 Volumetric study of turbulence under pressure gradient

Newtonian flow fields under a strong favorable and adverse pressure gradient and the effect of strong wall curvatures have been numerically simulated using LES and DNS. See, for instance, Laval et al. (2012) and Balin and Jansen (2021), among others. One interesting aspect of the full 3D results is that complex flow structures, such as large-scale turbulent or low and high momentum structures, can be extracted from high-resolution data. However, numerical setups are mostly affected by assumptions that might not reflect the real physics of the flow. The advent of three-dimensional PIV or particle tracking velocimetry (PTV) methods in the past decade, such as the shake-the-box (STB) method of Schanz et al. (2016), enabled researchers to obtain 3D flow structures out of the velocimetry data. A similar approach can be applied to Newtonian and non-Newtonian flows under a pressure gradient, where, for instance, quiet zones in accelerating regions or stretching eddy structures in decelerating flow can be obtained from the velocity data.

References

ADRIAN, R.J., WESTERWEEL, J., 2011. Particle Image Velocimetry. Cambridge University Press, Cambridge; New York.

ARNDT, R.E.A., 2002. Cavitation in vortical flows. *Annu. Rev. Fluid Mech.* **34**, 143–175.

AROSEMENA, A.A., ANDERSSON, H.I., SOLSVIK, J., 2020. Turbulent channel flow of generalized Newtonian fluids at a low Reynolds number. *J. Fluid Mech.* **908**, A43.

BALANTRAPU, N.A., HICKLING, C., ALEXANDER, W.N., DEVENPORT, W., 2021. The structure of a highly decelerated axisymmetric turbulent boundary layer. *J. Fluid Mech.* **929**, 9.

BALIN, R., JANSEN, K.E., 2021. Direct numerical simulation of a turbulent boundary layer over a bump with strong pressure gradients. *J. Fluid Mech.* **918**, A14.

BANERJEE, S., HASCAKIR, B., 2018. Flow control devices in SAGD completion design: Enhanced heavy oil/ bitumen recovery through improved thermal efficiency. *J. Pet. Sci. Eng.* **169**, 297–308.

BASKARAN, V., SMITS, A.J., JOUBERT, P.N., 1991. A turbulent flow over a curved hill. Part 2. Effects of streamline curvature and streamwise pressure gradient. *J. Fluid Mech.* **232**, 377–402.

BASKARAN, V., SMITS, A.J., JOUBERT, P.N., 1987. A turbulent flow over a curved hill Part 1. Growth of an internal boundary layer. *J. Fluid Mech.* **182**, 47.

BENEDICT, L.H., GOULD, R.D., 1996. Towards better uncertainty estimates for turbulence statistics. *Exp. Fluids* **22**, 129–136.

BERMAN, N.S., 1977. Flow time scales and drag reduction. *Phys. Fluids* **20**, S168.

BIRD, R.B., ARMSTRONG, R.C., HASSAGER, O., 1987. Dynamics of polymeric liquids. Vol. 1, 2nd Ed. : Fluid mechanics. John Wiley and Sons.

BOBKE, A., VINUESA, R., ÖRLÜ, R., SCHLATTER, P., 2017. History effects and near equilibrium in adverse-pressure-gradient turbulent boundary layers. *J. Fluid Mech.* **820**, 667–692.

BRADSHAW, P., 1969. A note on reverse transition. *J. Fluid Mech.* **35**, 387–390.

BRENNEN, C., 1970. Some cavitation experiments with dilute polymer solutions. *J. Fluid Mech.*

44, 51–63.

BRENNEN, C.E., 2013. Cavitation and bubble dynamics, Cavitation and Bubble Dynamics. Cambridge University Press, Cambridge.

BROSS, M., FUCHS, T., KÄHLER, C.J., 2019. Interaction of coherent flow structures in adverse pressure gradient turbulent boundary layers. *J. Fluid Mech.* **873**, 287–321.

BRUJAN, E., 2011. Cavitation in Non-Newtonian Fluids, Cavitation in Non-Newtonian Fluids: With Biomedical and Bioengineering Applications. Springer Berlin Heidelberg, Berlin, Heidelberg.

BUTLER, R.M., 2008. Steam-assisted gravity drainage: Concept, development, performance and future, in: SPE Reprint Series. pp. 44–50.

CASAL, J., 2008. Annex 1 Constants in the Antoine equation. *Ind. Saf. Ser.* **8**, 333–334.

ÇENGEL, Y.A., CIMBALA, J.M., 2013. Fluid Mechanics: Fundamentals And Applications, Third Edition, McGraw-Hill.

CHAHINE, G.L., KAPAHI, A., CHOI, J.-K., HSIAO, C.-T., 2016. Modeling of surface cleaning by cavitation bubble dynamics and collapse. *Ultrason. Sonochem.* **29**, 528–549.

CHATTERJEE, D., ARAKERI, V.H., 1997. Towards the concept of hydrodynamic cavitation control. *J. Fluid Mech.* **332**, 377–394.

CLAUSER, F.H., 1956. The Turbulent Boundary Layer. *Adv. Appl. Mech.* **4**, 1–51.

CLAUSER, F.H., 1954. Turbulent Boundary Layers in Adverse Pressure Gradients. *J. Aeronaut. Sci.* **21**, 91–108.

COLEMAN, G.N., RUMSEY, C.L., SPALART, P.R., 2018. Numerical study of turbulent separation bubbles with varying pressure gradient and Reynolds number. *J. Fluid Mech.* **847**, 28–70.

CURTISS, G.A., LEPPINEN, D.M., WANG, Q.X., BLAKE, J.R., 2013. Ultrasonic cavitation near a tissue layer. *J. Fluid Mech.* **730**, 245–272.

DEAN, R.B., 1978. Reynolds Number Dependence of Skin Friction and Other Bulk Flow Variables in Two-Dimensional Rectangular Duct Flow. *J. Fluids Eng.* **100**, 215–223.

DEN TOONDER, J.M.J., DRAAD, A.A., KUIKEN, G.D.C., NIEUWSTADT, F.T.M., 1995. Degradation

effects of dilute polymer solutions on turbulent drag reduction in pipe flows. *Appl. Sci. Res.* **55**, 63–82.

DEN TOONDER, J.M.J., HÜLSEN, M.A., KUIKEN, G.D.C., NIEUWSTADT, F.T.M., 1997. Drag reduction by polymer additives in a turbulent pipe flow: Numerical and laboratory experiments. *J. Fluid Mech.* **337**, 193–231.

DUBIEF, Y., WHITE, C.M., TERRAPON, V.E., SHAQFEH, E.S.G., MOIN, P., LELE, S.K., 2004. On the coherent drag-reducing and turbulence-enhancing behaviour of polymers in wall flows. *J. Fluid Mech.* **514**, 271–280.

DULAR, M., BACHERT, B., STOFFEL, B., ŠIROK, B., 2004. Relationship between cavitation structures and cavitation damage. *Wear* **257**, 1176–1184.

DURBIN, P.A., 1993. A Reynolds stress model for near-wall turbulence. *J. Fluid Mech.* **249**, 465.

ESCUDIER, M.P., GOULDSON, I.W., PEREIRA, A.S., PINHO, F.T., POOLE, R.J., 2001. On the reproducibility of the rheology of shear-thinning liquids. *J. Nonnewton. Fluid Mech.* **97**, 99–124.

FEBURIE, V., GIOT, M., GRANGER, S., SEYNHAEVE, J.M., 1993. A model for choked flow through cracks with inlet subcooling. *Int. J. Multiph. Flow* **19**, 541–562.

FRUMAN, D.H., 1999. Effects of non-newtonian fluids on cavitation, in: Siginer, D.A., De Kee, D., Chhabra, R.P. (Eds.), Advances in the Flow and Rheology of Non-Newtonian Fluids, Rheology Series. Elsevier, pp. 209–254.

FUCHS, A., KHARCHE, S., PATIL, A., FRIEDRICH, J., WÄCHTER, M., PEINKE, J., 2022. An open source package to perform basic and advanced statistical analysis of turbulence data and other complex systems. *Phys. Fluids* **34**, 101801.

FUJIKAWA, S., AKAMATSU, T., 1980. Effects of the non-equilibrium condensation of vapour on the pressure wave produced by the collapse of a bubble in a liquid. *J. Fluid Mech.* **97**, 481–512.

GANESH, H., MÄKIHARJU, S.A., CECCIO, S.L., 2016. Bubbly shock propagation as a mechanism for sheet-to-cloud transition of partial cavities. *J. Fluid Mech.* **802**, 37–78.

HARUN, Z., MONTY, J.P., MATHIS, R., MARUSIC, I., 2013. Pressure gradient effects on the large-scale structure of turbulent boundary layers. *J. Fluid Mech.* **715**, 477–498.

HASEGAWA, T., USHIDA, A., NARUMI, T., 2009. Huge reduction in pressure drop of water, glycerol/water mixture, and aqueous solution of polyethylene oxide in high speed flows through micro-orifices. *Phys. Fluids* **21**, 052002.

HERSHEY, H.C., ZAKIN, J.L., 1967. A molecular approach to predicting the onset of drag reduction in the turbulent flow of dilute polymer solutions. *Chem. Eng. Sci.* **22**, 1847–1857.

HOLMGREN, M., 2021. X Steam, Thermodynamic properties of water and steam. - File Exchange - MATLAB Central [WWW Document]. *MATLAB Cent. File Exch.*

HOYT, J.W., 1976. Effect of polymer additives on jet cavitation. *J. Fluids Eng. Trans. ASME* **98**, 106–111.

INOUÉ, S., SPRING, K.R., SPRING R., K., SPRING, S.I.K.R., INOUÉ, S., SPRING, K.R., 1997. Video microscopy: the fundamentals, Language of science. Plenum Press, New York.

ISHII, M., HIBIKI, T., 2006. Thermo-fluid dynamics of two-phase flow, Thermo-Fluid Dynamics of Two-Phase Flow. Springer US, Boston, MA.

JONES, M.B., MARUSIC, I., PERRY, A.E., 2001. Evolution and structure of sink-flow turbulent boundary layers. *J. Fluid Mech.* **428**, 1–27.

JONES, W.P., LAUNDER, B.E., 1972. Some properties of sink-flow turbulent boundary layers. *J. Fluid Mech.* **56**, 337–351.

JOSHI, P., LIU, X., KATZ, J., 2014. Effect of mean and fluctuating pressure gradients on boundary layer turbulence. *J. Fluid Mech.* **748**, 36–84.

KADIVAR, E., TIMOSHEVSKIY, M. V., PERVUNIN, K.S., MOCTAR, O. EL, 2020a. Cavitation control using Cylindrical Cavitating-bubble Generators (CCGs): Experiments on a benchmark CAV2003 hydrofoil. *Int. J. Multiph. Flow* **125**, 103186.

KADIVAR, E., TIMOSHEVSKIY, M. V, NICHIK, M.Y., EL MOCTAR, O., SCHELLIN, T.E., PERVUNIN, K.S., 2020b. Control of unsteady partial cavitation and cloud cavitation in marine engineering and hydraulic systems. *Phys. Fluids* **32**, 052108.

KÄHLER, C.J., SCHARNOWSKI, S., CIERPKA, C., 2012. On the resolution limit of digital particle image velocimetry. *Exp. Fluids* **52**, 1629–1639.

KARATHANASSIS, I.K., KOUKOUVINIS, P., KONTOLATIS, E., LEE, Z., WANG, J., MITROGLOU, N.,

GAVAISES, M., 2018. High-speed visualization of vortical cavitation using synchrotron radiation. *J. Fluid Mech.* **838**, 148–164.

KAWANAMI, Y., KATO, H., YAMAGUCHI, H., TANIMURA, M., TAGAYA, Y., 1997. Mechanism and Control of Cloud Cavitation. *J. Fluids Eng.* **119**, 788–794.

KIM, J., MOIN, P., MOSER, R., 1987. Turbulence statistics in fully developed channel flow at low reynolds number. *J. Fluid Mech.* **177**, 133–166.

KITSIOS, V., SEKIMOTO, A., ATKINSON, C., SILLERO, J.A., BORRELL, G., GUNGOR, A.G., JIMÉNEZ, J., SORIA, J., 2017. Direct numerical simulation of a self-similar adverse pressure gradient turbulent boundary layer at the verge of separation. *J. Fluid Mech.* **829**, 392–419.

KOLMOGOROV, A.N., 1941. The local structure of turbulence in incompressible viscous fluid for very large Reynolds numbers. *C. R. Acad. Sci. URSS* **30**, 301–305.

KROGSTAD, P.Å., SKÅRE, P.E., 1995. Influence of a strong adverse pressure gradient on the turbulent structure in a boundary layer. *Phys. Fluids* **7**, 2014–2024.

LAVAL, J.P., MARQUILLIE, M., EHRENSTEIN, U., 2012. On the relation between kinetic energy production in adverse-pressure gradient wall turbulence and streak instability. *J. Turbul.* **13**, 1–19.

LENAERS, P., LI, Q., BRETHOUWER, G., SCHLATTER, P., ÖRLÜ, R., 2012. Rare backflow and extreme wall-normal velocity fluctuations in near-wall turbulence. *Phys. Fluids* **24**, 035110.

LUCHIK, T.S., TIEDERMAN, W.G., 1988. Turbulent structure in low-concentration drag-reducing channel flows. *J. Fluid Mech.* **190**, 241–263.

LUMLEY, J.L., 1973. Drag reduction in turbulent flow by polymer additives. *J. Polym. Sci. Macromol. Rev.* **7**, 263–290.

LUMLEY, J.L., 1969. Drag Reduction by Additives. *Annu. Rev. Fluid Mech.* **1**, 367–384.

MACIEL, Y., WEI, T., GUNGOR, A.G., SIMENS, M.P., 2018. Outer scales and parameters of adverse-pressure-gradient turbulent boundary layers. *J. Fluid Mech.* **844**, 5–35.

MANE, M.B., BHANDARI, V.M., BALAPURE, K., RANADE, V. V, 2020. Destroying antimicrobial resistant bacteria (AMR) and difficult, opportunistic pathogen using cavitation and natural oils/plant extract. *Ultrason. Sonochem.* **69**, 105272.

MEINHART, C.D., WERELEY, S.T., SANTIAGO, J.G., 2000. A PIV Algorithm for Estimating Time-Averaged Velocity Fields. *J. Fluids Eng.* **122**, 285–289.

MELLOR, G.L., GIBSON, D.M., 1966. Equilibrium turbulent boundary layers. *J. Fluid Mech.* **24**, 225–253.

MIN, T., YOO, J.Y., CHOI, H., JOSEPH, D.D., 2003. Drag reduction by polymer additives in a turbulent channel flow. *J. Fluid Mech.* **486**, 213–238.

MITISHITA, R.S., MACKENZIE, J.A., ELFRING, G.J., FRIGAARD, I.A., 2021. Fully turbulent flows of viscoplastic fluids in a rectangular duct. *J. Nonnewton. Fluid Mech.* **293**, 104570.

MORETTI, P.M., KAYS, W.M., 1965. Heat transfer to a turbulent boundary layer with varying free-stream velocity and varying surface temperature-an experimental study. *Int. J. Heat Mass Transf.* **8**, 1187–1202.

MORRISON, F.A., 1998. Understandig Rheology, Understanding Rheology.

MURAKAMI, K., YAMAKAWA, Y., ZHAO, J., JOHNSEN, E., ANDO, K., 2021. Ultrasound-induced nonlinear oscillations of a spherical bubble in a gelatin gel. *J. Fluid Mech.* **924**, A38.

NARASIMHA, R., SREENIVASAN, K.R., 1979. Relaminarization of Fluid Flows, in: Advances in Applied Mechanics. Elsevier, pp. 221–309.

NARASIMHA, R., SREENIVASAN, K.R., 1973. Relaminarization in highly accelerated turbulent boundary layers. *J. Fluid Mech.* **61**, 417–447.

NASERI, H., KOUKOUVINIS, P., MALGARINOS, I., GAVAISES, M., 2018a. On viscoelastic cavitating flows: A numerical study. *Phys. Fluids* **30**, 033102.

NASERI, H., TRICKETT, K., MITROGLOU, N., KARATHANASSIS, I., KOUKOUVINIS, P., GAVAISES, M., BARBOUR, R., DIAMOND, D., ROGERS, S.E., SANTINI, M., WANG, J., 2018b. Turbulence and Cavitation Suppression by Quaternary Ammonium Salt Additives. *Sci. Rep.* **8**, 1–15.

ŌBA, R., ITŌ, Y., URANISHI, K., 1978. Effect of polymer additives on cavitation development and noise in water flow through an orifice. *J. Fluids Eng. Trans. ASME* **100**, 493–499.

OLSEN, M.G., ADRIAN, R.J., 2000. Out-of-focus effects on particle image visibility and correlation in microscopic particle image velocimetry. *Exp. Fluids* **29**, S166–S174.

OWOLABI, B.E., DENNIS, D.J.C., POOLE, R.J., 2017. Turbulent drag reduction by polymer additives in parallel-shear flows. *J. Fluid Mech.* **827**, R4.

OYEKA, O., FELTEN, F., LEAST, B., 2014. Screen-inflow-design considerations with inflow control devices in heavy oil, in: Society of Petroleum Engineers - SPE Heavy Oil Conference Canada 2014. SPE, pp. 1070–1078.

PALLARES, J.D.M., WANG, C., HAFTANI, M., PANG, Y., MAHMOUDI, M., FATTAHPOUR, V., NOURI, A., 2018. Experimental assessment of wire-wrapped screens performance in SAGD production wells, in: Society of Petroleum Engineers - SPE Thermal Well Integrity and Design Symposium 2018, TWID 2018. SPE, p. 193375.

PANDEY, S., CHU, X., WEIGAND, B., LAURIEN, E., SCHUMACHER, J., 2020. Relaminarized and recovered turbulence under nonuniform body forces. *Phys. Rev. Fluids* **5**, 104604.

PARGAL, S., WU, H., YUAN, J., MOREAU, S., 2022. Adverse-pressure-gradient turbulent boundary layer on convex wall. *Phys. Fluids* **34**, 035107.

PATEL, V.C., 1965. Calibration of the Preston tube and limitations on its use in pressure gradients. *J. Fluid Mech.* **23**, 185.

PATEL, V.C., HEAD, M.R., 1968. Reversion of turbulent to laminar flow. *J. Fluid Mech.* **34**, 371–392.

PATEL, V.C., SOTIROPOULOS, F., 1997. Longitudinal curvature effects in turbulent boundary layers. *Prog. Aerosp. Sci.* **33**, 1–70.

PINHASI, G.A., ULLMANN, A., DAYAN, A., 2005. Modeling of flashing two-phase flow. *Rev. Chem. Eng.*

PIROZZOLI, S., 2014. Revisiting the mixing-length hypothesis in the outer part of turbulent wall layers: Mean flow and wall friction. *J. Fluid Mech.* **745**, 378–397.

POPE, S.B., 2000. Turbulent Flows. Cambridge University Press.

PTASINSKI, P.K., BOERSMA, B.J., NIEUWSTADT, F.T.M., HULSEN, M.A., VAN DEN BRULE, H.A.A., HUNT, J.C.R., 2003. Turbulent channel flow near maximum drag reduction: Simulations, experiments and mechanisms. *J. Fluid Mech.* **490**, 251–291.

RAFFEL, M., WILLERT, C.E., SCARANO, F., KÄHLER, C.J., WERELEY, S.T., KOMPENHANS, J., 2018.

Particle Image Velocimetry. Springer International Publishing, Cham.

ROOD, E.P., 1991. Review. Mechanisms of cavitation inception. *J. Fluids Eng. Trans. ASME* **113**, 163–175.

ROTTA, J.C., 1953. On the Theory of the Turbulent Boundary Layer, NACA TM 1344.

SATO, K., TAGUCHI, Y., HAYASHI, S., 2013. High Speed Observation of Periodic Cavity Behavior in a Convergent-Divergent Nozzle for Cavitating Water Jet. *J. Flow Control. Meas. & Vis.* **01**, 102–107.

SCHANZ, D., GESEMANN, S., SCHRÖDER, A., 2016. Shake-The-Box: Lagrangian particle tracking at high particle image densities. *Exp. Fluids* **57**, 70.

SCIACCHITANO, A., WIENEKE, B., 2016. PIV uncertainty propagation. *Meas. Sci. Technol.* **27**, 084006.

SHAH, Y., YARUSEVYCH, S., 2020. Streamwise evolution of drag reduced turbulent boundary layer with polymer solutions. *Phys. Fluids* **32**, 065108.

SIMÕES-MOREIRA, J.R., BULLARD, C.W., 2003. Pressure drop and flashing mechanisms in refrigerant expansion devices. *Int. J. Refrig.* **26**, 840–848.

SITARAMAIAH, G., SMITH, C.L., 1969. Turbulent Drag Reduction by Polyacrylamide and Other Polymers. *Soc. Pet. Eng. J.* **9**, 183–188.

SPALART, P.R., 1986. Numerical study of sink-flow boundary layers. *J. Fluid Mech.* **172**, 307–328.

SPICER, T., MILLER, D., 2018. Quantifying the mass discharge rate of flashing two phase releases through simple holes to the atmosphere. *Process Saf. Prog.* **37**, 382–396.

SREENIVASAN, K.R., 1982. Laminarescent, relaminarizing and retransitional flows. *Acta Mech.*

SREENIVASAN, K.R., WHITE, C.M., 2000. The onset of drag reduction by dilute polymer additives, and the maximum drag reduction asymptote. *J. Fluid Mech.* **409**, 149–164.

STRIDE, E., COUSSIOS, C., 2019. Nucleation, mapping and control of cavitation for drug delivery. *Nat. Rev. Phys.* **1**, 495–509.

STRIDE, E., SEGERS, T., LAJOINIE, G., CHERKAOUI, S., BETTINGER, T., VERSLUIS, M., BORDEN, M.,

2020. Microbubble Agents: New Directions. *Ultrasound Med. Biol.* **46**, 1326–1343.

SYED MUSTAPHA, S.M.F.D., PHILLIPS, T.N., PRICE, C.J., MOSELEY, L.G., JONES, T.E.R., 1999. Viscometric flow interpretation using qualitative and quantitative techniques. *Eng. Appl. Artif. Intell.* **12**, 255–272.

TABOR, M., GENNES, P.G. DE, 1986. A Cascade Theory of Drag Reduction. *Europhys. Lett.* **2**, 519–522.

TAYLOR, G.I., 1938. The Spectrum of Turbulence. *Proc. R. Soc. London. Ser. A - Math. Phys. Sci.* **164**, 476–490.

TAYLOR, M.A., KURIEN, S., EYINK, G.L., 2003. Recovering isotropic statistics in turbulence simulations: The Kolmogorov 4/5th law. *Phys. Rev. E - Stat. Physics, Plasmas, Fluids, Relat. Interdiscip. Top.* **68**, 8.

TING, R.Y., 1978. Characteristics of flow cavitation in dilute solutions of polyethylene oxide and polyacrylamide. *Phys. Fluids* **21**, 898–901.

TOMS, B.A., 1948. Some observations on the flow of linear polymer solutions through straight tubes at large Reynolds numbers, in: Proceedings of the 1st International Congress on Rheology. pp. 135–141.

TONG, Y., CHEN, S., LI, M., LI, Z., KLINGMANN, J., 2017. Experimental study on bluff-body stabilized premixed flame with a central air/fuel jet. *Energies* **10**, 2011.

TOONDER, J.M.J., NIEUWSTADT, F.T.M., KUIKEN, G.D.C., 1995. The role of elongational viscosity in the mechanism of drag reduction by polymer additives. *Appl. Sci. Res.* **54**, 95–123.

TSUJI, Y., MORIKAWA, Y., 1976. Turbulent Boundary Layer with Pressure Gradient Alternating in Sign. *Aeronaut. Q.* **27**, 15–28.

TULAPURKARA, E.G., KHOSHNEVIS, A.B., NARASIMHAN, J.L., 2001. Wake-boundary layer interaction subject to convex and concave curvatures and adverse pressure gradient. *Exp. Fluids* **31**, 697–707.

TURNER, P., HODNETT, M., DOREY, R., CAREY, J.D., 2019. Controlled Sonication as a Route to in-situ Graphene Flake Size Control. *Sci. Rep.* **9**, 8710.

VERHAAGEN, B., FERNÁNDEZ RIVAS, D., 2016. Measuring cavitation and its cleaning effect.

Ultrason. Sonochem. **29**, 619–628.

VERSLUIS, M., STRIDE, E., LAJOINIE, G., DOLLET, B., SEGERS, T., 2020. Ultrasound Contrast Agent Modeling: A Review. *Ultrasound Med. Biol.* **46**, 2117–2144.

VINUESA, R., HOSSEINI, S.M., HANIFI, A., HENNINGSON, D.S., SCHLATTER, P., 2017a. Pressure-Gradient Turbulent Boundary Layers Developing Around a Wing Section. *Flow, Turbul. Combust.* **99**, 613–641.

VINUESA, R., ÖRLÜ, R., SANMIGUEL VILA, C., IANIRO, A., DISCETTI, S., SCHLATTER, P., 2017b. Revisiting History Effects in Adverse-Pressure-Gradient Turbulent Boundary Layers. *Flow, Turbul. Combust.* **99**, 565–587.

VIRK, P.S., 1975. Drag reduction fundamentals. *AIChE J.* **21**, 625–656.

VIRK, P.S., 1971. An elastic sublayer model for drag reduction by dilute solutions of linear macromolecules. *J. Fluid Mech.* **45**, 417–440.

VIRK, P.S., MICKLEY, H.S., SMITH, K.A., 1970. The Ultimate Asymptote and Mean Flow Structure in Toms' Phenomenon. *J. Appl. Mech.* **37**, 488–493.

VOLINO, R.J., 2020. Non-equilibrium development in turbulent boundary layers with changing pressure gradients. *J. Fluid Mech.* **897**, A2.

WALLACE, J.M., ECKELMANN, H., BRODKEY, R.S., 1972. The wall region in turbulent shear flow. *J. Fluid Mech.* **54**, 39–48.

WARHOLIC, M.D., HEIST, D.K., KATCHER, M., HANRATTY, T.J., 2001. A study with particle-image velocimetry of the influence of drag-reducing polymers on the structure of turbulence. *Exp. Fluids* **31**, 474–483.

WARHOLIC, M.D., MASSAH, H., HANRATTY, T.J., 1999. Influence of drag-reducing polymers on turbulence: effects of Reynolds number, concentration and mixing. *Exp. Fluids* **27**, 461–472.

WATMUFF, J.H., WATMUFF, J.H., SPALART, P.R., WATMUFF, J.H., WATMUFF, J.H., 1993. Experimental and numerical study of a turbulent boundary layer with pressure gradients. *J. Fluid Mech.* **249**, 337–371.

WEI, T., WILLMARTH, W.W., 1992. Modifying turbulent structure with drag-reducing polymer additives in turbulent channel flows. *J. Fluid Mech.* **245**, 619.

WERNET, M.P., 1991. Particle displacement tracking applied to air flows, in: Proc. Fourth Int. Conf. on Laser Anemometry. pp. 327–335.

WESTERWEEL, J., SCARANO, F., 2005. Universal outlier detection for PIV data. *Exp. Fluids* **39**, 1096–1100.

WHITE, C.M., DUBIEF, Y., KLEWICKI, J., 2012. Re-examining the logarithmic dependence of the mean velocity distribution in polymer drag reduced wall-bounded flow. *Phys. Fluids* **24**, 021701.

WHITE, C.M., MUNGAL, M.G., 2008. Mechanics and Prediction of Turbulent Drag Reduction with Polymer Additives. *Annu. Rev. Fluid Mech.* **40**, 235–256.

WHITE, F.M., 2011. Fluid Mechanics, 7th ed, Fluid Mechanics. McGraw Hill.

WIENEKE, B., 2015. PIV uncertainty quantification from correlation statistics. *Meas. Sci. Technol.* **26**, 074002.

WILLERT, C.E., CUVIER, C., FOUCAUT, J.M., KLINNER, J., STANISLAS, M., LAVAL, J.P., SRINATH, S., SORIA, J., AMILI, O., ATKINSON, C., KÄHLER, C.J., SCHARNOWSKI, S., HAIN, R., SCHRÖDER, A., GEISLER, R., AGOCS, J., RÖSE, A., 2018. Experimental evidence of near-wall reverse flow events in a zero pressure gradient turbulent boundary layer. *Exp. Therm. Fluid Sci.* **91**, 320–328.

WILLMARTH, W.W., LU, S.S., 1972. Structure of the reynolds stress near the wall. *J. Fluid Mech.* **55**, 65–92.

WU, J., DEIJLEN, L., BHATT, A., GANESH, H., CECCIO, S.L., 2021. Cavitation dynamics and vortex shedding in the wake of a bluff body. *J. Fluid Mech.* **917**, A26.

XI, L., 2019. Turbulent drag reduction by polymer additives: Fundamentals and recent advances. *Phys. Fluids* **31**, 121302.

XU, S., WANG, J., CHENG, H., JI, B., LONG, X., 2020. Experimental study of the cavitation noise and vibration induced by the choked flow in a Venturi reactor. *Ultrason. Sonochem.* **67**, 105183.

YASUDA, K., ARMSTRONG, R.C., COHEN, R.E., 1981. Shear flow properties of concentrated solutions of linear and star branched polystyrenes. *Rheol. Acta* **20**, 163–178.

ZAGAROLA, M. V., SMITS, A.J., 1998. Mean-flow scaling of turbulent pipe flow. *J. Fluid Mech.* **373**, 33–79.

ZENG, Q., GONZALEZ-AVILA, S.R., OHL, C.-D.D., 2020. Splitting and jetting of cavitation bubbles in thin gaps. *J. Fluid Mech.* **896**, A28.

ZHANG, H., ZUO, Z., MORCH, K.A., LIU, S., 2019. Thermodynamic effects on Venturi cavitation characteristics. *Phys. Fluids* **31**, 097107.

ZUPANC, M., PANDUR, Ž., STEPIŠNIK PERDIH, T., STOPAR, D., PETKOVŠEK, M., DULAR, M., 2019. Effects of cavitation on different microorganisms: The current understanding of the mechanisms taking place behind the phenomenon. A review and proposals for further research. *Ultrason. Sonochem.* **57**, 147–165.

Appendix A: Statistics

Here, the analytical and discretized descriptions of the statistical definitions are provided for reference, based on the definitions provided in Pope (2000), with minor modifications. Mean of the instantaneous fields $U(\boldsymbol{x},t)$ is symbolized by the angled brackets as $\langle U\rangle$ and is defined as:

$$\langle U\rangle \equiv \int_{-\infty}^{\infty} U\mathcal{P}(U)dU, \tag{A-1}$$

where $\mathcal{P}(U)$ is the probability density function (PDF) of U, and satisfies the normalization condition:

$$\int_{-\infty}^{\infty} \mathcal{P}(U)dU = 1, \tag{A-2}$$

with $\mathcal{P}(-\infty) = \mathcal{P}(\infty) = 0$. The variance of U is

$$\mathrm{var}(U) = \sigma_u^2 = \langle u^2\rangle = \int_{-\infty}^{\infty} u^2\mathcal{P}(U)dU, \tag{A-3}$$

and its standard deviation is $\mathrm{std}(U) = \sigma_u = \langle u^2\rangle^{1/2}$. The nth *standardized central moment* field is defined as

$$\mu_n = \frac{\langle u^n\rangle}{\sigma_u^n} = \frac{\int_{-\infty}^{\infty} u^n\mathcal{P}(U)dU}{\left[\int_{-\infty}^{\infty} u^2\mathcal{P}(U)dU\right]^{n/2}}. \tag{A-4}$$

Evidently, $\mu_0 = 1$, $\mu_1 = 0$, and $\mu_2 = 1$. Here, μ_3 is called *skewness*, μ_4 is the *flatness* or *kurtosis* and μ_6 is the *superskewness*. If at a position $\boldsymbol{x}_0$, U has a *normal* or *Gaussian* distribution, its PDF is defined as

$$\mathcal{P}(U) = \mathcal{N}(u,\sigma_u) = \frac{1}{\sigma_U\sqrt{2\pi}}\exp\left[-\frac{1}{2}\left(\frac{u}{\sigma_u}\right)^2\right]. \tag{A-5}$$

The odd moments of a Gaussian (or normal) distribution are zero, i.e., $\mu_3, \mu_5, \ldots$ are all zero. Therefore, the skewness of a normal distribution is zero. Accordingly, the kurtosis and superskewness of a Gaussian distribution are $\mu_4 = 3$ and $\mu_6 = 15$.

Let us assume U_1 and U_2 are two random variables fluctuating in time, each one at a particular position in a turbulent flow, i.e., $U_1(t) \equiv U_1(\boldsymbol{x}_1,t)$ and $U_2(t) \equiv U_2(\boldsymbol{x}_2,t)$. The covariance of U_1 and U_2 is defined to be

$$\mathrm{cov}(U_1, U_2) = \langle u_1 u_2 \rangle = \int_{-\infty}^{\infty} \int_{-\infty}^{\infty} u_1 u_2 \mathcal{P}_{12}(U_1, U_2) dU_1 dU_2, \tag{A-6}$$

where, $\mathcal{P}_{12}$ is the *joint* PDF (JPDF) of variables U_1 and U_2. With this terminology, $\mathcal{P}_1$ and $\mathcal{P}_2$ are, respectively, the *marginal* PDFs (MPDF). The correlation coefficient of U_1 and U_2 is defined as

$$r_{12} = \frac{\mathrm{cov}(U_1, U_2)}{[\langle u_1^2 \rangle \langle u_2^2 \rangle]^{\frac{1}{2}}} = \frac{\langle u_1 u_2 \rangle}{\sigma_{u_1} \sigma_{u_2}}, \tag{A-7}$$

and is independent of time for a statistically stationary turbulent flow. Based on the *Cauchy-Schwarz* inequality, $-1 \leq r_{12} \leq 1$. If $r_{12} = 0$, the random variables U_1 and U_2 are uncorrelated and entirely independent of each other. For $r_{12} = 1$, U_1 and U_2 are *perfectly correlated*, and if $r_{12} = -1$, they are *perfectly negatively correlated*.

For N discrete independent repetitions of a measurement conducted at nominally similar conditions, the mean field can be approximated by the ensemble average of the measurements as

$$\langle U \rangle_N (\boldsymbol{x}, t) \equiv \frac{1}{N} \sum_{n=1}^{N} U(\boldsymbol{x}, t_n). \tag{A-8}$$

Here, $\langle U \rangle_N$ is still a random variable with the properties of $\langle \langle U \rangle_N \rangle = \langle U \rangle$ and $\sigma^2_{\langle u \rangle_N} = \sigma_u^2 / N$. The variance of a statistically stationary random variable $U(\boldsymbol{x}, t)$ is

$$\mathrm{var}(U) = \sigma_u^2(\boldsymbol{x}) = \langle u^2 \rangle (\boldsymbol{x}) = \frac{1}{N-1} \sum_{n=1}^{N} u^2(\boldsymbol{x}, t), \tag{A-9}$$

and standard deviation of $U(\boldsymbol{x}, t)$ is $\mathrm{std}(U) = \sigma_u = \langle u^2 \rangle^{1/2}$, which is equal to the root mean square (r.m.s.) of the fluctuation field u for a large number of iterations, i.e., $u_{\mathrm{rms}}(\boldsymbol{x}) = \sigma_u(\boldsymbol{x})$. The n^{th} *standardized central moment* field is defined as (Pope, 2000):

$$\mu_n \equiv \frac{\langle u^n \rangle (\boldsymbol{x})}{\sigma_u^n(\boldsymbol{x})} = (N-1)^{\frac{n}{2}-1} \frac{\sum_{n=1}^{N} u^n(\boldsymbol{x}, t)}{[\sum_{n=1}^{N} u^2(\boldsymbol{x}, t)]^{\frac{n}{2}}}. \tag{A-10}$$

Appendix B: Numerical simulation setup

A series of simulations were performed on the final CG I geometry (see Table 3-1), with a fine mesh for three volumetric flow rates of 8 lit min^{-1}, 10 lit $min^{-1,}$ and 12 lit min^{-1}, using the Flow Simulation toolbox of commercial software (SOLIDWORKS 2021, Dassault Systèmes). The numerical results were used as an approximate guideline to identify the critical flow regions and approximate the longitudinal distribution of the wall shear stress τ_w (x) and the order of magnitude of the strain rate $\dot{\gamma}_w(x)$ over the nozzle wall.

Figure B-1(a) displays the selected computational domain, and Figure B-1(b) shows a zoomed-in view of the mesh structure projected on the midspan plane of the channel. A total of 4.5 million mesh cells, with 1.6 million refined cells in contact with the solid walls, were used for simulations. Navier-Stokes equations and the two-equation k-ε turbulence model were solved simultaneously for a steady incompressible water flow at 20 °C. The variation of the pressure drop over the nozzle $\Delta P_{ch} = \bar{\bar{P}}_{in} - \bar{\bar{P}}_{out}$, and the wall shear stress averaged over the lower wall of the throat $\tau_{w,th}$, highlighted in blue in Figure B-1(a), were monitored during the simulation, and when the variation of ΔP_{ch} and $\tau_{w,th}$ were both less than 1 % of their time-averaged value, the solution was assumed to converge, and simulation was stopped.

Here, the pressure coefficient is defined as $c_p = P_w / 0.5\,\rho\bar{\bar{U}}_{th}$. Figure B-2($a$) shows the variation of c_p in the streamwise direction, x, for three different Re_{th}. The plots were obtained by extracting pressure on the channel's lower wall, on the midspan plane, shown by a blue profile in Figure B-1(a). As the flow enters the convergence region, wall pressure drops sharply for all tested cases. Wall pressure has its minimum value at the throat entrance. For $Re_{th} > 4.76 \times 10^4$, wall pressure drops below the flow's saturation pressure, P_{sat}, and conditions are desirable for the cavitation to initiate. After a subtle increase, c_p is relatively constant through the throat region, after which it starts to recover smoothly to $c_p > 0$ in the divergence region. At a higher flow rate (here, $Re_{th} > 5.71 \times 10^4$), wall pressure stays well below P_{sat}, which increases the chances of a more violent cavitation process.

Figure B-2(a) illustrates the variation of average streamwise throat wall shear stress, $\tau_{w,th}$ with Re_{th}, obtained from the numerical simulations. A Gaussian fit is applied to the results, which was utilized to approximate $\tau_{w,th,}$ and relatively the wall shear strain rate $\dot{\gamma}_w$ for different Re_{th} values.

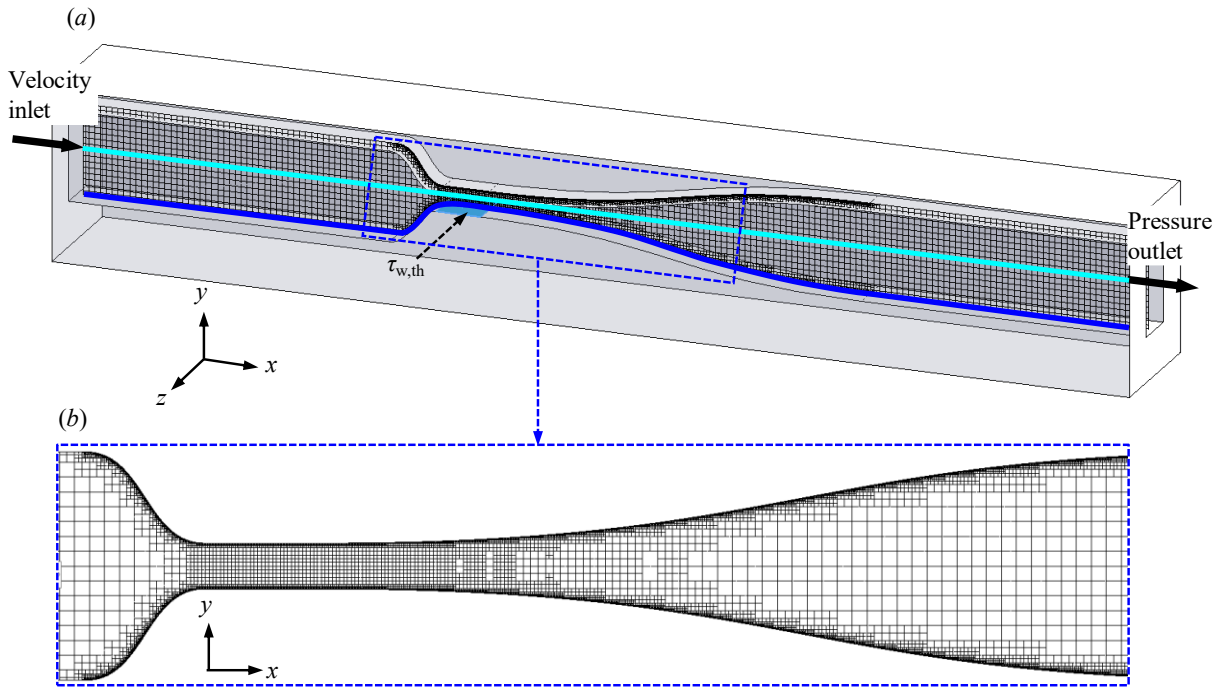

Figure B-1 (*a*) Illustration of the computational domain and the mesh structure at the channel's central (midspan) plane. (*b*) A zoomed-in view of the midspan mesh in the converging, throat, and diverging regions of CG I. The solid blue curve and cyan line shown in (*a*), respectively, highlight the lower nozzle wall and the channel's centerline at the midspan plane.

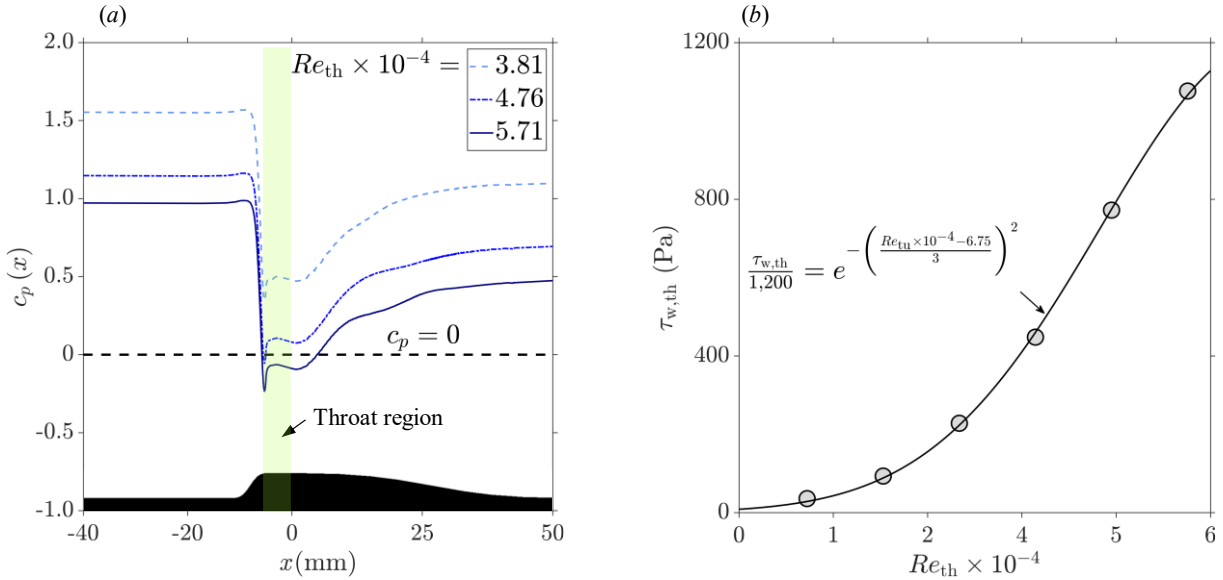

Figure B-2 (*a*) Variation of the pressure coefficient c_p with the streamwise position x on the lower wall at the midspan of the channel. Line $c_p = 0$ is illustrated with a horizontal black dashed line on the plot. A pale green rectangle highlights the throat region. The projection of the lower channel wall on the midspan plane is inserted below the diagram for reference. The black regions show the body of the test section. (*b*) Changes of the average streamwise throat wall shear stress, $\tau_{w,th}$ with the throat Reynolds number Re_{th}. Here, the grey circles show the simulation results, and the black profile is a Gaussian fit on the results, with its equation inserted into the figure. The fit's coefficient of determination is $R = 0.9993$.

Appendix C: Particle image size

The total particle image diameter comprises the geometrical, diffraction, and defocus diameters. As described by Olsen and Adrian (2000), it is formulated as:

$$d_{\mathrm{T}}(z) = \sqrt{d_{\mathrm{geo}}^2 + d_{\mathrm{dif}}^2 + d_{\mathrm{def}}^2} = \sqrt{\left(Md_{\mathrm{p}}\right)^2 + [2.44f_{\#}(M+1)\lambda]^2 + \left(\frac{MzD_{\mathrm{a}}}{s_0 + z}\right)^2}. \quad \text{(C-1)}$$

Here, $d_{\mathrm{T}}(z)$ is the particle's image diameter in microns at a distance z from the focal plane. The subscripts 'geo,' 'dif,' and 'def' stand for geometrical, diffraction, and defocus, respectively. M denotes the magnification factor, d_{p} is the particle's physical diameter (in microns), $f_{\#}$ is the F-number, λ is the light's wavelength (in microns), D_{a} is the lens' aperture diameter (in microns), and s_0 is the object's distance. For a lens with a known numerical aperture NA, $f_{\#}$ can be calculated using the total refractive index n_{t}, as $f_{\#} = n_{\mathrm{tot}} / NA$. For a light ray passing through the air, an acrylic medium, and into the water, $n_{\mathrm{tot}} = n_{\mathrm{wa}} / (n_{\mathrm{ac}} / n_{\mathrm{a}})$. Here, the subscripts 'wa','ac,' and 'a' stand for water, acrylic, and air. For a camera with discrete sensor size e_{d} (in microns) and sensor pixel size of e_{s} with a unit of μm pixel^{-1}, the digital particle diameter D is defined as (Kähler et al., 2012):

$$D\ [\mathrm{pixel}] = \begin{cases} 1, & d_{\mathrm{T}} \le e_{\mathrm{d}} \\ \dfrac{d_T}{e_{\mathrm{s}}}, & d_{\mathrm{T}} > e_{\mathrm{d}} \end{cases}. \quad \text{(C-2)}$$

It is important to note that $|e_{\mathrm{s}}| = |e_{\mathrm{d}}|$. The green light has a wavelength of $\lambda = 0.532$ μm. The refractive indices of water, acrylic, and air are $n_{\mathrm{wa}} = 1.33$, $n_{\mathrm{ac}} = 1.50$, and $n_{\mathrm{ai}} = 1.00$.

Appendix D: Experimental and analytical investigation of mesoscale slug bubble dynamics in a square capillary channel

Click **here** to see the full paper on the publisher's website.

Physics of Fluids ARTICLE scitation.org/journal/phf

Experimental and analytical investigation of meso-scale slug bubble dynamics in a square capillary channel

Cite as: Phys. Fluids 32, 083304 (2020); doi: 10.1063/5.0016241
Submitted: 3 June 2020 • Accepted: 16 July 2020 •
Published Online: 6 August 2020

Reza Azadi, Jaime Wong, and David. S. Nobes[a)]

AFFILIATIONS

Department of Mechanical Engineering, University of Alberta, Edmonton, Alberta T6G 1H9, Canada

[a)]Author to whom correspondence should be addressed: dnobes@ualberta.ca

ABSTRACT

The flow of dispersed gas bubbles in a viscous liquid can create a bubbly, slug bubble, or elongated bubble flow regime. A slug bubble flow, characterized by bubble sizes equal to the hydraulic diameter of the channel, is a transition regime with a complex local flow field that has received little attention in the past. In this study, dynamics of this flow regime in a square capillary with a cross-sectional area of 3×3 mm^2 was studied analytically and experimentally. The main geometric parameters of the flow field, such as film and corner thicknesses and volume fraction, were calculated for different flow conditions based on a semi-empirical approach. Using velocity fields from particle image velocimetry (PIV), combined with the analytical equations derived, local mean variations of the film and corner flow thicknesses and velocity were analyzed in detail. Analysis of the results reveals a linear relation between the bubble speed and the liquid slug velocity that was obtained using sum-of-correlation PIV. Local backflow, where the liquid locally flows in the reverse direction, was demonstrated to occur in the slug bubble flow, and the theoretical analysis showed that it can be characterized based on the bubble cross-sectional area and ratio of the liquid slug and bubble speed. The backflow phenomenon is only contributed to the channel corners, where the speed of liquid can increase to the bubble speed. However, there is no evidence of reverse flow in the liquid film for the flow conditions analyzed in this study.

NOMENCLATURE

Letters

A	cross-sectional area
a	film length
Ca	capillary number, Ca = $\mu U/\sigma$
CV	control volume
D	diameter
d	width of the bubble cross section at distance z_d
$\mathbf{E}$	strain rate tensor, s^{-1}
e	difference
$f_\#$	f-number of the objective lens
fps	frame rate of the camera, s^{-1}
g	gravitational acceleration, 9.81 m/s^2
h	pixel size of the camera, μm
I	intensity matrix
$\mathbf{I}$	unit tensor
$\mathbf{I}$, $\mathbf{J}$, $\mathbf{K}$	unit vectors in the fixed Cartesian coordinate system
$\mathbf{i}$, $\mathbf{j}$, $\mathbf{k}$	unit vectors in the moving Cartesian coordinate system
L	length or perimeter
M_0	total magnification factor
n	refractive index
$\mathbf{n}$	unit normal vector
NA	numerical aperture
p	pressure
Q	volumetric flow rate
$\mathbf{r}$	distance vector
r	radius of curvature
Re	Reynolds number, $\mathcal{R} = UD/\nu$
S	non-dimensionalizing parameter
t	time
U	characteristic velocity magnitude
$\mathbf{U}$	characteristic velocity vector
u	flow velocity magnitude
V	volume
w	width, mm

Appendix E: Determination of fluid flow adjacent to a gas/liquid interface using particle tracking velocimetry (PTV) and a high-quality tessellation approach

Click **here** to see the full paper on the publisher's website.

Experiments in Fluids (2021) 62:48
https://doi.org/10.1007/s00348-020-03103-5

RESEARCH ARTICLE

Determination of fluid flow adjacent to a gas/liquid interface using particle tracking velocimetry (PTV) and a high-quality tessellation approach

Reza Azadi[1] · Jaime Wong[1] · David S. Nobes[1]

Received: 31 July 2020 / Revised: 17 November 2020 / Accepted: 19 November 2020

Abstract

PTV velocity vectors, with high spatial resolution in the flow field, can be used to calculate important flow parameters such as pressure. Determination of such a parameter, which is a function of velocity gradients, entails the velocity vectors to be interconnected by a network of nodes. A tessellated network of the flow field can use the original positions of the PTV particles. This results in a mesh with elements of large aspect ratios, which can produce large numerical errors in the calculation of velocity gradients. In flow scenarios with a moving solid boundary or two-phase interface, a tessellation method is required that can attune to the dynamic topology while capturing the details of the near interface region. Here, we develop a methodology to tessellate two-dimensional (2D) unsteady PTV fields using high quality triangular dynamic meshes, with fine control of the mesh density close to the moving boundaries. To examine the applicability of the method, an experimental setup based on particle shadow velocimetry was conducted, with air and a water/glycerol mixture as the working fluids. Two flow channels of a straight, with a square cross-section of 3×3 mm^2 and wavy, with a throat width of 0.5 mm were utilized to capture the dynamics of relatively large bubbles with quasi-steady and highly deformable moving interfaces. The versatility of the method was successfully demonstrated by the generation of a high-quality mesh, with controlled sizes and determination of the radial and tangential velocity components at the near interface region for different flow conditions.

Graphic abstract

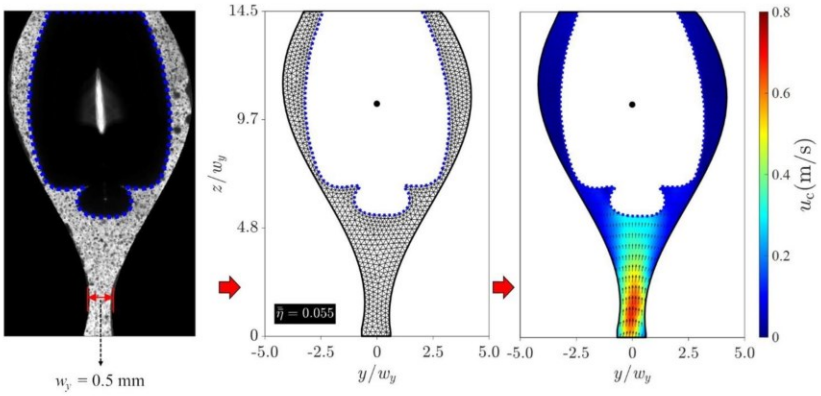

Extended author information available on the last page of the article

Published online: 01 March 2021

Appendix F: On the three-dimensional features of a confined slug bubble in a flowing square capillary

Click **here** to see the full paper on the publisher's website.

Physics of Fluids ARTICLE scitation.org/journal/phf

On the three-dimensional features of a confined slug bubble in a flowing square capillary

Cite as: Phys. Fluids **33**, 033327 (2021); doi: 10.1063/5.0043508
Submitted: 8 January 2021 · Accepted: 19 February 2021 ·
Published Online: 29 March 2021

View Online Export Citation CrossMark

Reza Azadi and David. S. Nobes[a)]

AFFILIATIONS

Department of Mechanical Engineering, University of Alberta, Edmonton, T6G 1H9, Canada

[a)]Author to whom correspondence should be addressed: dnobes@ualberta.ca

ABSTRACT

The motion of long bubbles in tubular capillaries has typically been described by bulk characteristics. However, the dynamics of slug bubbles in square capillaries are more complex due to a corner flow and a thin film flow. The physics can be correctly explained by elucidating local 3D features of the two-phase flow field. To this aim, an experimental study based on particle tracking velocimetry (PTV) and a numerical simulation based on the volume-of-fluid method were conducted to investigate the dynamics of slug bubbles rising in a flowing square capillary with a cross-sectional area of 3×3 mm^2. To precisely analyze the phases' interaction, interfacial flow data were mapped onto a radial-tangential coordinate system on central and diagonal planes. The simulated interface topology and velocity fields show a good agreement with the experimental PTV data on the central plane, with an absolute error of less than 1.2% for terminal bubble speed. Tangential speeds show their maxima occurring in the channel corners, where pressure is maximum. The thin liquid film flow that occurs where the bubble approaches the wall applies noticeable shear stress on the channel walls, where high and low-pressure regions are generated. Structures of vortices inside the bubble were identified using isosurfaces of the Q-criterion, and their cores were detected based on the parallel vector method. Results reveal a dominant vortex ring adjacent to the liquid film flow and two oblique vortex tubes close to the bubble's nose.

I. INTRODUCTION

Two-phase flows with a gas phase dispersed in a continuous liquid phase are complex fluid phenomena, with a wide range of applications in various fields of science and engineering. Rupture of kidney stones by using Lithotripter shockwaves generated from the bubble cavitation,[1,2] efficient drug delivery to tumor cells,[3,4] development of microbubble actuators in microelectromechanical systems (MEMS),[5] reduction of drag in naval hulls,[6] or clustering of air bubbles as foam in breaking sea waves,[7,8] all are industrial or natural phenomena that interact with various scales of gas/liquid two-phase flows as a major part of their existence. The gas phase can coexist with the liquid phase from the start of the process, or it can be produced due to a phase change in the system as a result of a phenomenon such as cavitation[9] or flashing.[10,11] The intricacy of these phenomena aside, the resultant flow field is a gas/liquid two-phase system.[12]

Inclination,[13–15] the shape of the channel cross-sectional area,[16–18] topology of the flow path,[19,20] mass flow rate[21–23] and thermophysical properties[24,25] of each phase, heat transfer, and pressure drop[26–28] are some of the bulk parameters that affect the dynamics of the gas/liquid flow field and results in different two-phase flow regimes. There has been a wide range of studies to identify these flow regimes for conditions, where a combination of the discussed parameters was considered. Limiting the discussion to micro- to mesoscale vertical channels with a rectangular cross section, the most commonly identified gas/liquid two-phase regimes are[21,22,24,27,28] bubbly, slug-bubbly, slug, slug-annular, annular, and parallel flows.

Slug-bubbly flow is a transition regime between the bubbly and slug flow[29] and shares both regimes' main characteristics. In this flow pattern, bubbles are not as long as Taylor bubbles nor as small to be unaffected by the walls, making slug bubble flow a critical transition regime in microchannels. In a tube with a diameter D_c, a Taylor bubble can be characterized with the conditions $L_G/D_c > 1.5$ and $D_G/D_c > 0.6$,[30,31] where L_G and D_G denote the length and equivalent diameter of the bubble. Moreover, the condition of $D_G/D_c < 0.6$ defines a free rising bubble.[30] Hence, in a square channel with a width of w_c, the condition $D_G \sim L_G \sim w_c$ can characterize a slug bubble.

In contrast to tubular channels, a flow path with a rectangular cross section has proven to produce a corner flow field in the surrounding of a slug bubble. The corner flow has been shown to have a key role in creating the reverse flow phenomenon, where the liquid phase locally flows opposite to the direction of bubble rise.[29,32]

Appendix G: Local flow dynamics in the motion of slug bubbles in a flowing mini square channel

Click **here** to see the full paper on the publisher's website.

International Journal of Heat and Mass Transfer 178 (2021) 121588

Contents lists available at ScienceDirect

International Journal of Heat and Mass Transfer

journal homepage: www.elsevier.com/locate/hmt

Local flow dynamics in the motion of slug bubbles in a flowing mini square channel

Reza Azadi, David S. Nobes*

Department of Mechanical Engineering, University of Alberta, Edmonton T6G 1H9, Canada

ARTICLE INFO

Article history:
Received 19 February 2021
Revised 7 April 2021
Accepted 8 June 2021
Available online 26 June 2021

Keywords:
Mini channel
Slug flow
Film flow
Flow visualization
Numerical simulation

ABSTRACT

For a slug flow flowing in a square capillary, the surrounding liquid flows through a thin film between the slug bubble and the wall and the corners of the channel and generates an asymmetric two-phase flow field with significant spatial variations. The current literature mainly discusses the bulk features of such a flow field, while local phenomena in these flows are not well known yet. In this study, the local dynamics of the liquid film and corner flows in a flowing square channel with a width of 3 mm were investigated by experiments and numerical simulations. Instantaneous velocity fields in the liquid flow were measured at the channel's central plane using particle tracking velocimetry (PTV). The obtained data were utilized to calculate the axial variations of the film and corner velocities. Three-dimensional numerical simulations with adaptive mesh refinement of the interface were performed for a series of flow conditions. Comparing the film velocity obtained from PTV and simulations demonstrates an overall good agreement between the results, with discrepancies close to the solid walls, where the PTV data is sporadic. Film and corner flows show rapid velocity changes adjacent to the minimum film area. Both experiments and simulations elucidate the backflow phenomena in the analyzed flow fields, where the liquid locally flows in the opposite streamwise direction. The backflow region shrinks as the liquid flow rate and speed of the bubble increase. Film flow shows significant pressure drops as it passes through the minimum film area. On the contrary, the corner flow does not demonstrate any rapid pressure fluctuations. The vortex structures' identification revealed dominant vortex loops inside the gas and small-scale vortex filaments along the channel walls, generated from the liquid film rupture.

1. Introduction

The two-phase flow that is generated as a result of mixing a flowing gas and liquid can demonstrate different flow regimes based on various parameters: thermophysical properties [1,2] and mass flow rate [3,4] of each phase, scale [5,6], geometry [7,8], and inclination [9,10] of the flow path, surface properties of the channel walls [11,12] and heat, pressure, and velocity conditions of the boundaries of the flow domain [13–15]. These flow regimes can be mainly divided into bubbly, slug, annular, and churn, flows in mini to micro-channels [4,16]. Among these two-phase flow regimes, slug flow in mini- to micro-channels has numerous industrial and health-related applications. Applications such as heat transfer enhancement [17,18], particle removal by cavitation bubbles [19], enhanced oil recovery [20], or localized drug delivery by acoustically active lipospheres [21] require a detailed understanding of the slug flow dynamics to function or to improve the process. A review of the studies available in the literature reveals that recent developments in the experimental apparatus, high-speed imaging systems, and computational resources resulted in: (1) improvements of existing experimental and numerical methodologies and (2) the advent of new techniques to study micro-size flow dynamics in the slug flow fields.

Zhao et al.[2] investigated the mass transfer of a two-phase slug flow in a rectangular microchannel using different non-Newtonian and Newtonian fluids. They used polyacrylamide solutions as shear-thinning non-Newtonian liquids. An aqueous solution of resazurin, glucose, and sodium hydroxide was used as the Newtonian liquid. Air was the working gas phase. The cross-sectional area of the channel was 0.6 mm × 0.3 mm (width × depth). Comparing the slug flows of the shear-thinning solution with the Newtonian solution, the authors reported slim slug bubble shapes, thicker liquid films, and at higher flow rates, smaller mass transfer coefficients. Using an oxygen-sensitive colorimetric method, they found that the mass was mainly transferred in the flow field corresponded to the Taylor bubble's cap (i.e., the bubble's front nose),

* Corresponding author.
E-mail address: dnobes@ualberta.ca (D.S. Nobes).

https://doi.org/10.1016/j.ijheatmasstransfer.2021.121588